"Characterisation and Processing of Carbon-Based Reinforced Al-MMCs for Thermal Management Applications"

A thesis submitted for the degree of Doctor of Philosophy

by

Alberto Torres Miranda

Institute of Materials and manufacturing, Department of Mechanical, Aerospace and Civil Engineering, Brunel University London.

November 2016

Abstract

This thesis examines the possibility of using multi-walled carbon nanotubes (MWCNTs) (as fillers), known for their unusual exceptional high thermal conductivity ($K \sim 3000$ to 3500 W m^{-1} K^{-1}), to produce ultra-high thermal conductivity ($K \geq 400$ W m^{-1} K^{-1}) aluminium matrix composites (Al/MWCNTs). Composites were processed via a combination of rheocasting and equal channel angular extrusion (ECAE) techniques, for use in advanced thermal management applications such as in high power light-emitting diodes (HPLEDs).

Al matrix composites reinforced with Cu-coated pitch-based carbon fibres (Al/Cu-CFs) were first produced to test the processing method selected. Rheocasting allowed the introduction and dispersion of 2 wt.% of Cu-CFs within the Al3Mg matrix. The subsequent ECAE processing of the composites reduced the porosity from 3 to 0.03 % and induced a high degree of fibres alignment ($\emptyset_{ED-DD} \sim 2.69^{\circ}$) within the matrix. However, this resulted in considerable damage on the fibres. The rheocasting alone did not improve the K of the composites as the addition of 2 wt.% of fibres showed a value of $K_{c,C2} = 134.9 \pm 4.1$ W m^{-1} K^{-1}, 9% lower in comparison with the matrix, $K_m = 148.4 \pm 4.5$ W m^{-1} K^{-1}. After ECAE, for 6 iterations in the in-plane direction, composite with the highest degree of fibre alignment, showed a K improvement of ~ 20 % ($K_{c,C1.5,6i,1} = 153.7 \pm 4.6$ W m^{-1} K^{-1}) with respect to the "as-rheocasted" composite ($K_{c,C1.5} = 128.5 \pm 3.9$ W m^{-1} K^{-1}), and a 3.6% increase with respect to the matrix. The improvement is believed to be due to porosity reduction, fibre alignment and forced intimate contact of clean CF surfaces with the matrix.

Rheocasting of the Al/MWCNTs allowed the introduction of up to 0.35 wt.% of MWCNTs (embedded in pure Cu) within the Al matrix. However, the MWCNTs were found in agglomerates. Their introduction within the matrix was aided by the pure Cu, which was further improved after the Cu solubility in Al was reached resulting in the formation of AlCuMg intermetallics which surrounded the agglomerated MWCNTs. ECAE processing reduced the composites porosity (from 1.5 % to 0.03%) and induced a high degree of nanotube bundle alignment ($3.24^{\circ} < \emptyset_{ED-DD} < 3.62^{\circ}$). Aligned individual nanotubes with a good nanotube matrix interface surface contact were also found. However, damage on the nanotubes was also observed.

The SThM+FEM technique developed in this study allowed the acquisition of the K of an individual MWCNT that resulted in a combined (in-and out-of-plane) thermal conductivity value of $K_{MWCNT,1,2} \sim 20$ W m^{-1} K^{-1}. The low value is due the long length and large outer diameter of the nanotube which increases the probability of an increase in the defect content and consequently a lower thermal conductivity.

The K results of the Al/MWCNTs composites processed via rheocasting+ECAE showed an improvement of ~ 5.7 % ($K_{M1,4i,1} = 156.9 \pm 4.7$ W m^{-1} K^{-1}) for an addition of 0.3 wt.% of MWCNTs, in comparison to the matrix ($K_m = 148.4 \pm 4.5$ W m^{-1} K^{-1}). This finding may be related to porosity removal and MWCNTs bundle alignment forming a percolation network. Comparison with various thermal conductivity theoretical models, taking into account the models limitations, the characteristics of the microstructure of the composites, the MWCNTs quality and purity, and the SThM+FEM results, supports the hypothesis that the K of the MWCNTs used for the composite processing is much lower than that claimed by the manufacturer (2000 Wm^{-1} K^{-1}). However, its value is higher than K_m, which is possible as the value obtained by the SThM+FEM is a combined value, and thus its in-plane value is higher than 20 W m^{-1} K^{-1}.

The theoretical models also showed that it should be possible to obtain K values between ~ 351 W m^{-1} K^{-1} to ~ 497 W m^{-1}K^{-1} for Al/MWCNTs composites processed via rheocasting+ECAE with a maximum filler volume content of $v_f = 0.3$. Nevertheless, to process ultra-high ($K \geq 400$ W m^{-1} K^{-1}) thermal conductivity it is critical that the $K_{MWCNTs,1} \geq 2000$ W m^{-1} K^{-1}.

To all my family...

With a special thanks to my sister Susana Torres Miranda

for the endless support and encouragement!

"Don´t only practice your art

But force your way into its secrets

For it and knowledge can

Raise men to the divine."

Ludvig Van Beethoven

Preface

The work described in this thesis was carried out by the author at the Brunel Centre for Advanced Solidification and Technology (BCAST), Institute of Materials and Manufacturing, Brunel University London, from September 2012 to November 2016 under the supervision of Dr. Brian J. McKay. This thesis is submitted for the degree of Doctor of Philosophy at Brunel University London. The research is original and no part of this thesis has been accepted or is being submitted for any other degree or qualification in this university or elsewhere. Where the work of others has been used or reported, it is acknowledged in the text.

Parts of this work have already been presented at the following conferences:

- "Structural and Chemical Characteristics of Cu-CNTs in an Al/Cu-CNTs Composite Processed Using Ultrasonic Cavitation". EUROMAT2013 European Congress and Exhibition on advanced Materials and Processes, Seville, Spain, September 2013.

- "Thermal Stability of Cu-CNTs Powder for High Thermal Conductivity Al Matrix Composites Processing". The World Conference on Carbon (Carbon2014), Carbon Materials for Ubiquitous and Sustainable Life, July 2014 Jeju, South Korea.

- "An SThM Technique to Assess the Thermal Conductivity of Individual Multi-walled Carbon Nanotubes". 7th UK - Japan Symposium on Fundamental Research Advances in Carbon Nanomaterials, Royal Society of Chemistry, Burlington House, London, UK, 13th June 2016.

Acknowledgements

Table of Contents

X

Nomenclature

Symbols

Symbol	Definition
a-C	Amorphous Carbon
Ag	Silver
Al	Aluminium
Al_4C_3	Aluminium Carbide
Al_2O_3	Alumina (Aluminium Oxide)
Ar	Argon
B	Boron
Be	Berylium
C	Carbon
$C_{0.14}Fe_{1.86}$	Martensite
C_{540}	Fullerite
C_{60}	Fullerenes
CO	Carbon Monoxide
CO_2	Carbon Dioxide
Co	Cobalt
Cu	Copper
CuO	Tenorite
Cu_2O	Cuprite

Fe_3O_4	Iron Oxide
Fe_2C	Hexagonal Iron Carbide
Fe_3C	Cementite
He	Helium
Mg	Magnesium
Mo	Molybdenum
Ni	Nickel
O	Atomic Oxygen
O_2	Molecular Oxygen
Pt	Platinum
Si	Silicon
SiC	Silicon Carbide (Carborundum)
SiCp	Silicon Carbide Particles
Ti	Titanium
W	Tungsten
a	Thermal Diffusivity
α-Al	Primary Aluminium
C	Heat Capacity
C_p	Specific Heat Capacity
$\vec{C_h}$	Chiral Vector
D	Nanostructure or Grain Size

d	Interlayer spacing
d	Diameter
d_i	Nanotubes Inner Diameter
d_o	Nanotubes Outer Diameter
d_{MWCNT}	Multi-walled Carbon Nanotube Interplanar Spacing
$d_{spacing}$	Interplanar Spacing
E	Electrical Field
f_s	Solid Fraction
j	Phonon Polarization Branch
K	Thermal Conductivity
K_c	Thermal Conductivity of the Composite
$K_{c,1}$	In-Plane Thermal Conductivity of the Composite
$K_{c,2}$	Out-Of-Plane Thermal Conductivity of the Composite
K_e	Electron Thermal Conductivity Contribution
K_f	Thermal Conductivity of the Filler
K_f^{eff}	Effective Thermal Conductivity of the Filler
K_m	Thermal Conductivity of the Matrix
K_p	Phonon Thermal Conductivity Contribution
l	Fibres/Nanotubes Length
m_r	Residual Mass
P	Electric Dipole Moment

p	Specularity Parameter
q	Heat Flux
Re	Reynolds Number
R_{BD}	Interface Thermal Barrier Resistance
S_{ij}	Thermal Conduction Tensor
t	Time
T	Temperature
T_{end}	End Temperature
Ti	Titanium
T_{in}	Initiation Temperature
T_L	Liquidus Temperature
T_{oxi}	Oxidation Temperature
T_m	Melting Temperature
T_s	Solidus Temperature
T_{ss}	Semi-Solid Processing Temperature
v_f	Filler Volume Fraction
v_f^{corr}	Corrected Filler Volume Fraction
w_f	Filler Weight Fraction
$W(K_x)$	Dispersion Relation
WD	Working Distance
n	Exponent for Cellular Materials

α	Thermal expansion
β	Aspect Ratio
Δ_F	Enthalpy of Formation
ΔT	Temperature Gradient
ΔT_{L-S}	Freezing Range
γ	Surface Energy
υ	Phonon Group Velocity
τ	Phonon Relaxation Time
τ_B	Phonon Lifetime
ω	Phonon Frequency
Λ	Phonon Mean-free Path
φ	Porosity Volume Fraction
θ	Chiral Angle
λ	Electron Wavelength

Abbreviations

Acronym	Definition
ACVD	Aerosol Assisted Chemical Vapour Deposition
AFM	Atomic Force MIcroscopy
AE	Auger Electrons
AMCs	Aluminium Matrix Composites
BF	Bright Field
BSE	Backscattering Electrons
CFs	Carbon Fibres
CCVD	Combustion Chemical Vapour Deposition
CVD	Chemical Vapour Deposition
CNSs	Carbon Nanospheres
CNTs	Carbon Nanotubes
CNFs	Carbon Nanofibres
CTE	Coefficient of Thermal Expansion
DSC	Differential Scanning Calorimetry
DD	Deformation Direction
EBID	Electron Beam Induced Deposition
EBSD	Electron Back-Scattered Diffraction
ECAE	Equal Channel Angular Extrusion
ED	Extrusion Direction
EDS	Energy Dispersive X-Ray Spectroscopy
EELS	Electron Energy-Loss Spectroscopy
FFC	Face-Centred Cubic System
FFT	Fast Fourier Transform
FT	Fourier Transform
FEG	Field Emission Gun
FEM	Finite Elements Method
Gr	Graphite
HAADF	High Angle Annular Dark Field

HIP	Hot Isostatic Pressure
HOPG	Highly Oriented Pyrolytic Graphite
HPLEDs	High Power Light-emitting Diodes
HRTEM	High Resolution Transmission Electron Microscopy /Microscope
HVOF	High Velocity Oxyfuel Spraying
ICDD	International Centre for Diffraction Data
IFFT	Inverse Fast Fourier Transform
LCD	Liquid Crystals Displays
LEDs	Light-emitting Diodes
MFP	Phonon Mean Free Path
MMCs	Metal Matrix Composites
MMNCs	Metal Matrix Nanocomposites
MWCNTs	Multi-walled Carbon Nanotubes
OES	Optical Emission Spectroscopy
PECVD	Plasma Enhanced Chemical Vapour Deposition
PAN	Polyacrylonitrile
PIPS	Precision Ion Polishing System
PMMA	Poly(methyl methacrylate)
PPR	Pulsed Photothermal Reflectance Technique
ROI	Region of Interest
SAED	Selected Area Electron Diffraction
SE	Secondary Electrons
SEM	Scanning Electron Microscopy / Microscope
SG	Specific Gravity
SPD	Severe Plastic Deformation
SPM	Scanning Probe Microscopy
SPS	Spark Plasma Sintering
SSM	Semi-Solid Metal
STA	Simultaneous Thermal Analysis
SThM	Scanning Thermal Microscopy / Microscope
SWCNTs	Single-walled Carbon Nanotubes

TECs	Thermoelectric Coolers
STEM	Scanning Transmission Electron Microscopy
TEM	Transmission Electron Microscopy/ Microscope
TG (A)	Thermogravimmetry / Thermogravimetric Analysis
UTS	Ultimate Tensile Strength
VAMWCNTs	Vertically Aligned Multi-walled Carbon Nanotubes
VGCF	Vapour-grown Carbon Fibre
XRD	X-ray Diffraction

Chapter 1

Introduction

1.1 Chapter Outline

This chapter discusses the background of the thesis with respect to investigating the potential of multi-walled carbon nanotubes (MWCNTS) fillers in producing Al matrix composites with an ultra-high thermal conductivity ($K \geq 400$ W m^{-1} K^{-1}) for thermal management applications. It sets out the aim and objectives of the study and concludes with the thesis outline.

1.2 Background

In past years the rapid development of the electronic industry has greatly benefited the society. Nevertheless, more recently some high-end technological applications have seen their advances limited by the inherent inability to find new materials capable of meeting industrial and consumer demands. One of the most challenging technological barriers that has hindered progress in electronics is the failure to remove excessive heat produced during the operation of the device.[1]

The amount of heat generated in electronics devices has been steadily increasing during the last decades due to the miniaturization of components and the consumption of increasing electrical power in electronic circuits. This heat, if it is not effectively removed, can cause catastrophic failures by overheating or deformation. Therefore, finding materials capable of achieving these functions, in sometimes extreme conditions (fast heating/cooling cycles, high humidity, etc.), is one of today's major challenges for this industry.[1]

For instance, in high power light-emitting diodes (HPLEDs) (see Fig.1.1) thermal dissipation has been a serious issue. Controlled by the internal and the external quantum efficiencies, a non-radiative process in the active layer of the LEDs converts most of the electrical power to heat. Increased drive current means that there is almost 70 W/cm^2 for a 1 W LED with a 1 mm^2 area, which is higher than conventional microprocessor chips. The generated heat will increase the PN junction temperature significantly. This may lead to the damage of the PN junction, which may lower the luminous efficiency, increase forward voltage, or cause wavelength shift, resulting in a reduction in the lifetime of the device.[2]

The degradation of the materials used in HPLEDs is generally caused by long term heating. Therefore, effective heat extraction from the chip to keep the junction temperature below a specific limit is crucial in maintaining LED performance. Applying metal or metal composites with high thermal conductivities as the heat sink is the primary solution for HPLEDs.[2]
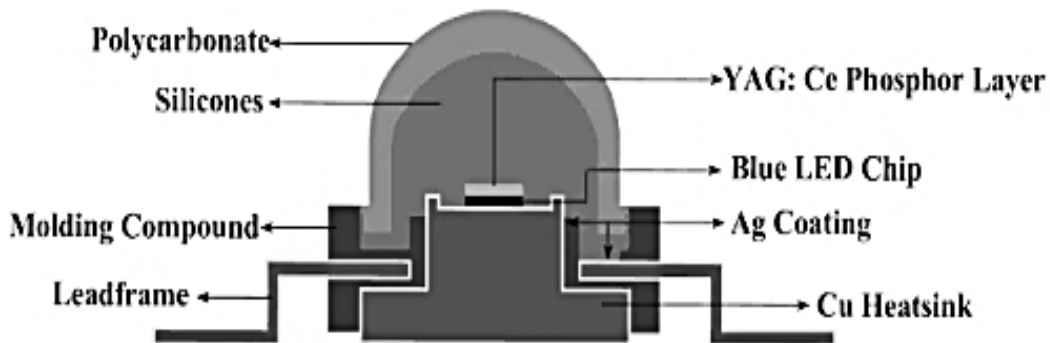
Fig. 1.1 Schematic of high power LED packaging.[2]

Traditional materials have serious deficiencies in meeting the requirements for thermal management especially minimization of thermal stresses in HPLED packaging. Copper (Cu, K = 400 W m^{-1} K^{-1}), the standard material for applications requiring high thermal conductivity, has a coefficient of thermal expansion (CTE = 17 ppm K^{-1}) that is much larger than those of ceramics and semiconductor materials, giving rise to thermal stresses when packages are subjected to thermal loads. Aluminium (Al, K = 237 W m^{-1} K^{-1}) has a lower thermal conductivity and larger CTE (23 ppm K^{-1}) than Cu but it is cheaper and lighter, making it a more attractive option, and when reinforced with high thermal conductivity reinforcements has the potential to be applied as a heat sink for the HPLEDs.[3]

Carbon-based materials, such as pitch-based CFs (1100 W m^{-1} K^{-1}), highly oriented pyrolytic graphite (HOPG) (1700 W m^{-1} K^{-1}) and diamond (2200 W m^{-1} K^{-1}) are already used to manufacture thermal management materials due to their good thermal conductivity and low CTE. However, amongst all the C-based materials, multi-walled carbon nanotubes (MWCNTs) (shown in Fig. 1.2) are reported to have the highest thermal conductivity with a low CTE (-2.5x10^{-6} K^{-1} at room temperature)[4]. This makes this material an excellent filler to manufacture composites with ultra-high thermal conductivity ($K \geq$ 400 W m^{-1} K^{-1}) in order to solve heat dissipation problems such as those found in HPLED applications.[5–7]

Harnessing the thermal conductivity potential of the MWCNTs within metal matrices has yet to be achieved. One of the problems is the low quality of the MWCNTs acquired from commercial sources (see Fig. 1.2) due to the synthetization method used (combustion chemical vapour deposition, CCVD). This technique produces nanotubes with a high defect and impurity content which decreases their thermal conductivity. As a consequence these MWCNTs possibly do not possess the high thermal conductivity required for such applications.[8,9]
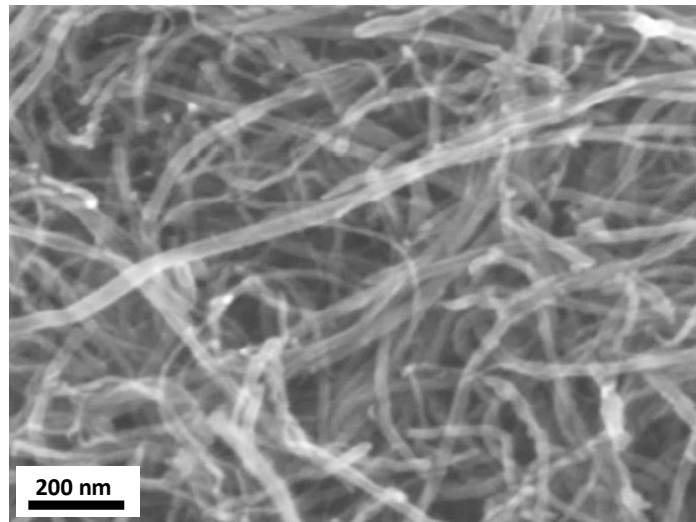
Fig. 1.2 "As-received" combustion chemical vapour deposition (CCVD) MWCNTs.

As nanometrology is still in its infancy, there is no standardized method that enables a quick and effective assessment of the thermal conductivity of MWCNTs to allow the selection of appropriate MWCNTs for composite processing. Currently, thermal conductivity measurements rely on the microfabrication of complex micro-devices. Moreover, the data acquisition for these nanomaterials is time-consuming and extremely expensive with devices having limited availability (as most are still at the research development stage).[10,11]

Another major problem is the difficulty in manufacturing Al matrix composites reinforced with MWCNTs where a high content (i.e. a content that is necessary to manufacture ultra-high thermal conductivity composites) of nanotubes is homogenously and individually dispersed within the metal matrix. The difficulty arises when inserting the

MWCNTs within the Al matrix, especially when using liquid-state processing methods. The density of the MWCNTs is lower than the density of Al and due to the high surface tension of the metal the nanotubes tend to float to the surface of the melt.[12,13]

Also, due to the large surface area of the MWCNTs, and electrostatic and Van der Waals forces, they will naturally agglomerate (see Fig.1.3). It is therefore difficult to obtain a uniform dispersion of individual nanotubes throughout the matrix using most conventional processing methods. This results in a poor composite thermal conductivity. In addition, due to their large surface area and surface dominant characteristics, these materials could also be highly reactive in metal matrices.[14,15]
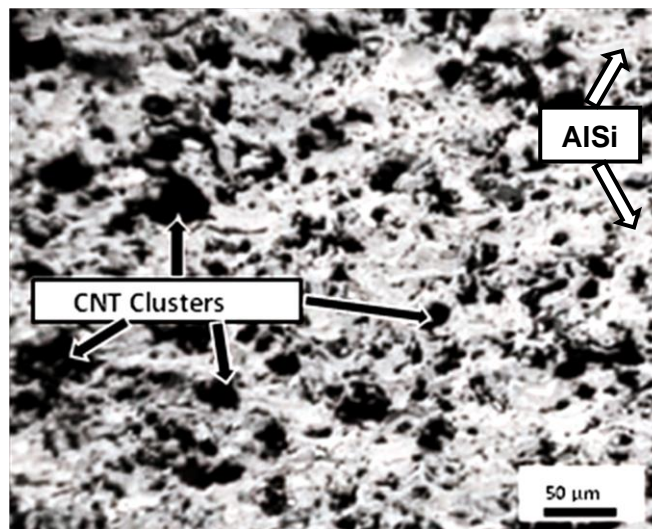
Fig 1.3 Optical micrograph of a plasma-sprayed Al-12 wt.% Si coating containing 10 wt.% MWCNTs clearly showing the presence of MWCNT clusters.[16]

Therefore, it is necessary to develop new approaches to obtain: 1) the thermal conductivity of the MWCNTs prior composite processing; and, 2) alternative composite processing techniques to overcome the limitations addressed above. This will enable the thermal conductivity potential of the MWCNTs to be fully harnessed and allow the processing of Al/MWCNTs composites with ultra-high thermal conductivity ($K \geq 400$ W m^{-1}K^{-1}) for thermal management applications such as HPLEDs.

1.3 Aim of the Study

The aim of this thesis was to study the possibility of using multi-walled carbon nanotubes (MWCNTs) as composite fillers, as these materials are known for their extremely high thermal conductivities ($K \sim$ 3000 to 3500 W m^{-1} K^{-1}). Ultra-high thermal conductivity ($K \geq$ 400 W m^{-1} K^{-1}) materials are required for advanced thermal management applications such as HPLEDs heat sinks.

In order to achieve the aim of the study two critical challenges were identified, they are:

➢ Devising a processing method capable of effectively introducing and dispersing the MWCNTs within the Al matrix composites.

➢ Determining if the MWCNTs used to process the composite have the outstanding thermal conductivity claimed by the manufacturers.

Therefore, this study focused on the assessment of a processing method consisting of a combination of rheocasting and equal channel angular extrusion (ECAE), to overcome the common difficulties found when introducing MWCNTs within Al matrix. The ECAE process promotes the alignment of the anisotropic MWCNTs within the matrix and induces closure of the porosity. Pores are highly detrimental to thermal conductivity, and thus their closure will enable higher thermal conductivity Al/MWCNTs composites to be processed.

This study also evaluates the suitability of using a combination of scanning thermal microscopy (SThM) and finite element method (FEM) as a nanometrology technique. This method can be used to determine the thermal conductivity of the MWCNTs used in the processing of the Al/MWCNT composite, in order to assess if they have the thermal conductivity claimed by the manufacturer and thus their real contribution to the thermal conductivity of the composite can be ascertained.

1.4 Thesis Outline

Following the introduction and aim of this study as outlined in this chapter (Chapter 1), Chapter 2 presents a review of the literature relevant to support the research conducted in this study, and includes:- advanced thermal management materials; C-based materials for thermal management applications; processing of AMCs for thermal management; and, thermal conductivities of composites materials.

Chapter 3 describes: the experimental methods followed to process the Al/CFs and Al/MWCNTs composites; the methods utilized to acquire the experimental thermal conductivity of an individual nanotube and the composites; and, a brief description of the characterisation techniques and respective sample preparation for each technique as required in this study.

Chapter 4 provides the results of this study and is divided in two parts: 1) Al/Cu-CFs composites processing, their characteristics and respective thermal conductivity. 2) Al/MWCNTs composites processing, their characteristics and respective thermal conductivity. It includes rhe results of the MWCNTs morphology, quality and purity study, and the measurement of the thermal conductivity of an individual MWCNT obtained by the SThM+FEM technique.

Chapter 5 offers discussions on the results with respect to the processing and characterisation of the Al/Cu-CFs and Al/MWCNTs composites processed via rheocasting and rheocasting+ECAE; the effect of the MWCNTs morphology, and quality and purity on their thermal conductivity; and, the thermal conductivity of individual MWCNTs in order to assess the possibility of producing ultra-high thermal conductivity ($K \geq 400$ W m^{-1} K^{-1}).

Chapter 6 outlines the conclusions from the results presented in Chapter 4 and discussed in Chapter 5. Suggestions for further work which is required to clarify pending issues and thus bring the study to the next development stage are also outlined in this chapter.

References

1.   Davim, J. P., Metal Matrix Composites: Materials, Manufacturing and Engineering. (Walter de Gruyter GmbH & Co KG, 2014).

2.   Liu, S. & Luo, X., LED Packaging for Lighting Applications: Design, Manufacturing, and Testing. (John Wiley & Sons, 2011).

3.   Zweben, C. H., New Material Options for Light-Emitting Diode Packaging, Proc. SPIE 5366, 173–182 (2004).

4.   Alamusi et al., Prediction of Thermal Expansion Properties of Carbon Nanotubes using Molecular Dynamics Simulations. Comput. Mater. Sci. 54, 249–254 (2012).

5.   Zweben, C., Advanced Thermal Management Materials For Electronics and Photonics. Adv. Microelectron. 37, 14–19 (2010).

6.   ZwebenConsulting. Available at: https://sites.google.com/site/zwebenconsulting/. (Accessed: 15th March 2016)

7.   Lindsay, L., Broido, D. A. & Reinecke, T. L., First-Principles Determination of Ultrahigh Thermal Conductivity of Boron Arsenide: A Competitor for Diamond? Phys. Rev. Lett. 111, (2013).

8.   Collins, P. G., Defects and Disorder in Carbon Nanotubes. Oxf. Handb. Nanosci. Technol. Front. Adv. (2010).

9.   Bifano, M. F. P., Park, J., Kaul, P. B., Roy, A. K. & Prakash, V., Effects of Heat Treatment and Contact Resistance on the Thermal Conductivity of Individual Multiwalled Carbon Nanotubes using a Wollaston Wire Thermal Probe. J. Appl. Phys. 111, 54321 (2012).

10.   Dames, C. et al., A Hot-Wire Probe for Thermal Measurements of Nanowires and Nanotubes inside a Transmission Electron Microscope. Rev. Sci. Instrum. 78, 104903 (2007).

11.   Cahill, D. G., Goodson, K. & Majumdar, A., Thermometry and Thermal Transport in Micro/Nanoscale Solid-State Devices and Structures. J. Heat Transf. 124, 223 (2002).

12.   Barekar, N. et al., Processing of Aluminum-Graphite Particulate Metal Matrix Composites by Advanced Shear Technology. J. Mater. Eng. Perform. 18, 1230–1240 (2009).

13.   Miranda, A. et al., Study of Mechanical Properties of an LM24 Composite Alloy Reinforced with Cu-CNT Nanofillers, Processed Using Ultrasonic Cavitation. Mater. Sci. Forum 765, 245–249 (2013).

14.   Neubauer, E., Kitzmantel, M., Hulman, M. & Angerer, P. Potential and Challenges of Metal-Matrix-Composites Reinforced with Carbon Nanofibers and Carbon Nanotubes. Compos. Sci. Technol. 70, 2228–2236 (2010).

15.   Rohatgi, P. & Schultz, B., Lightweight Metal Matrix Nanocomposites-Stretching the Boundaries of Metals. Mater. Matters 2, 16–20 (2007).

16.   Agarwal, A., Bakshi, S. R. & Lahiri, D., Carbon Nanotubes: Reinforced Metal Matrix Composites. (CRC Press, 2010).

Chapter 2

Literature Review

2.1 Chapter Outline

Multi-walled carbon nanotubes (MWCNTs) are a nanomaterial with outstanding thermal conductivity due to their crystalline structure. If successfully introduced into aluminium matrix composites (AMCs), they could have the potential to produce the next generation of thermal management materials with ultra-high thermal conductivity ($K \geq 400$ W m^{-1} K^{-1}). However, several limitations and challenges regarding MWCNTs synthesis and AMC processing need to be overcome in order to harness their superior thermal properties.

This chapter is divided into four sections discussing: Advanced Thermal Management Materials; C-based Materials for Thermal Management Applications; Processing of AMCs for Thermal Management; and, Thermal Conductivity of Composites.

2.2 Advanced Thermal Management Materials

The demand for advanced thermal management materials has increased exponentially as the current materials struggle to remove the excessive heat generated during the operation of equipment used in microelectronics and optoelectronics applications, such as, microprocessors, power modules, light-emitting diodes (LEDs), plasma and liquid crystals displays (LCD) and thermoelectric coolers (TECs), to name but a few. The amount of heat generated has been steadily increasing during recent years due to the miniaturization of components and the consumption of increasing electrical power in electronic circuits.[1–3]

The heat build-up causes thermal stresses that result in warping and subsequent failure of the components. This occurs primarily due to the coefficient of thermal expansion (CTE) mismatch of the materials used in the manufacture of the components. Advanced composites are a good choice of materials to provide thermal control. The concept of ideal composite material for thermal management applications is based on the following properties:

- The highest thermal conductivity possible
- Identical or similar thermal expansion coefficient
- Low weight.[2,4]

Traditional thermal management materials generally belong to the moderate thermal conductivity (K), $K < 300$ W m^{-1} K^{-1} materials group, apart from Cu which belongs to the high-thermal conductivity, 300 W m^{-1} K^{-1} $\leq K \leq 400$ W m^{-1} K^{-1} group.

Fig. 2.1 illustrates graphically the K values for thermal management materials used in electronic packaging as a function of CTE. The gray band (between 4 to 7 ppm K^{-1}), shows the CTE range that the thermal management material should have to match that of the substrates used in electronic packaging. Traditional thermal management low-CTE materials, like Cu/W, Cu/Mo, Kovar and Invar which are decades old, have high densities and thermal conductivities that are no better than that of Al (see Table 2.1). On the other hand, monolithic Al and Cu despite the good thermal conductivity have

high CTE and the latter also is expensive and has high density. Thus, the traditional materials are no longer suitable and thus impose major packaging design limitations.[1–4]

Advanced thermal management materials, in contrast have a wide range of thermal conductivities spanning from moderate to ultra-high ($K \geq 400$ W m^{-1} K^{-1}) with higher specific thermal conductivities, as shown in Table 1.1, which provide more choices to tackle the heat dissipation problems discussed.[1,2]

Recently, more ultra-high thermal conductivity materials have been produced, with some reaching values as high as 1700 W m^{-1} K^{-1}, e.g. highly oriented pyrolytic graphite (HOPG). As

Fig. 2.1 Thermal Conductivity of thermal management materials used in electronic packaging as a function of their CTE.[6]

the thermal management will continue to be a problem in electronic packaging the search for more materials to face this issue will become more intensive.[1,3]

Monolithic carbonaceous materials and composites reinforced with boron arsenide ($K > 2000$ W m^{-1} K^{-1}), natural graphite platelets ($K = 3000$ W m^{-1} K^{-1}), graphene ($K \approx 5000$ W m^{-1} K^{-1}), or carbon nanotubes (CNTs) ($K > 6000$ W m^{-1} K^{-1}, theoretical value) have the best potential to produce thermal management materials with ultra-high thermal conductivities. The knowledge that CNTs have the highest potential amongst all these materials investigated, motivated this study to attempt to produce Al matrix composites reinforced with CNTs and assess their potential as an ultra-high thermal conductivity material.[1,3,5]

Table 2.1 Thermal properties of the thermal management materials.[1]

	Material/Filler	Matrix	K_{x-y} (W m^{-1} K^{-1})	K_z (W m^{-1} K^{-1})	CTE (ppm K^{-1})	K_{x-y}/SG (W m^{-1} K^{-1})
Traditional Materials	Alloy 42	-	10.5	10.5	5.3	1.3
	Invar	-	11	11	1.3	1.4
	Kovar	-	17	17	5.9	2
	Cu/Invar/Cu	-	88-268	13-31	4-10.6	9-27
	Cu/Mo/Cu	-	220-305	125-160	6.2-6.8	24-33
	Cu/Invar/Cu	-	164	164	8.4	20
	Cu/Mo/Cu	-	182	182	6	18
	Al-40Si	-	126	126	15	50
	Be-Al	-	210	210	13.9	100
	Ti	-	7.2	7.2	9.5	1.6
	W	Cu	157-190	157-190	5.7-8.3	9-13
	Mo	Cu	184-197	184-197	7-7.6	18-20
	Al	-	237	237	23	81
	Cu	-	400	400	17	45
Advanced Materials	Industrial Gr	-	95	-	7.9	53
	Gr Foam	-	45-70	135-245	-1	75-272
	Disc. CFs	Polymer	20-290	3-35	4-7	12-160
	Aramid	Epoxy	0.9	-	1.4	0.6
	Invar	Ag	153	153	6.5	17
	Disc. CFs	Al	190-230	120-150	3-9.5	78-92
	Al-Si	-	120-180	120-180	6.5-17	48-72
	SiC p	Al	150-255	150-255	4.8-16.2	56-82
	Beryllia p	Be	210-230	210-230	6.1-8.7	100-102
	Cont. CFs	Polymer	300	10	-1	183
	Natural Gr	Epoxy	370	6.5	-2.4	190
	Disc. CFs	Cu	300	200	6.5-9.5	44
	Cont. CFs	SiC	340	38	2.5	155
	CVD Diamond	-	500-2200	500-2200	1-2	310-510
	HOPG	-	1300-1700	10-20	-1	740-850
	Pyrolytic Gr Sheet	-	600-1700	~15	0.9	670-690
	Natural Gr	-	140-1500	3-10	-0.4	130-790
	Diamond p	Al	410-530	410-530	7.0-10.0	180
	Diamond p	Cu	465-600	465-600	4.0-7.7	89-114
	Diamond p	Co	>600	>600	3	>145
	Diamond p	SiC	600-680	600-680	1.8	182-206
	Cont. CFs	C	350-400	40	-1	184-200

2.3 Carbon-based Materials for Thermal Management

Carbon materials, which form a variety of allotropes[6], are unique in terms of their thermal properties as illustrated in Fig. 2.2. The different allotropes of carbon span an extraordinarily large range of thermal conductivities, from ≈ 0.01 W m^{-1} K^{-1} in amorphous carbon (*a*-C) to above 2000 W m^{-1} K^{-1} at room temperature in either diamond or graphene. The thermal conductivity of carbon nanotubes (CNTs) ~ 3000 - 3500 W m^{-1} K^{-1} at room temperature exceeds that of diamond, which is the best bulk heat conductor.[8–10]

The heat conduction in carbon materials is usually dominated by phonons, even for graphite, which has metal-like properties. This is attributed to the strong covalent *sp²* bonding resulting in efficient heat transfer by lattice vibrations.[8]
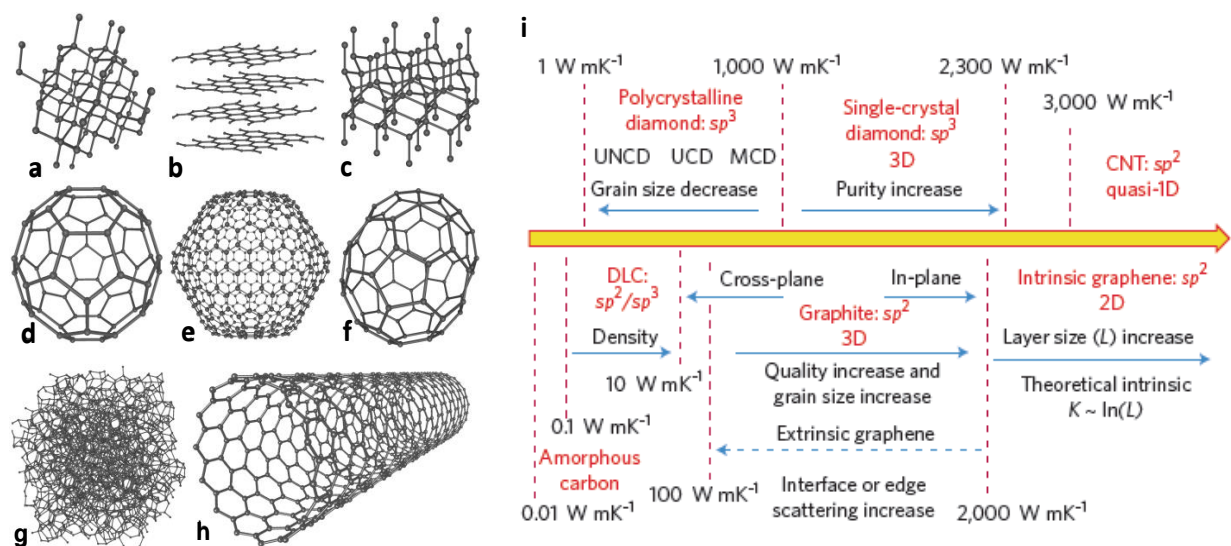
Fig. 2.2 Eight allotropes of carbon: **(a)** Diamond, **(b)** graphite, **(c)** lonsdaleite, **(d)** C_{60} buckminsterfullerene, **(e)** C_{540} fullerite, **(f)** C_{70}, **(g)** amorphous carbon, and **(h)** single-walled carbon nanotubes. **(i)** Thermal properties of carbon allotropes and their derivatives. The diagram is based on average values reported in literature.[8,11]

2.3.1 Pitch-Based Carbon Fibres

A carbon fibre (CF) is defined as a fibre containing at least 92 wt. % carbon, whereas fibres containing at least 99 wt. % carbon are normally referred to as graphite and are fabricated by pyrolysis of an appropriate precursor. Polyacrylonitrile (PAN) and petroleum or coal tar are the precursors of the PAN and mesophase pitch-based fibres, respectively. Carbon fibres are also produced by decomposing gaseous hydrocarbons at high temperatures, also known as vapour-grown carbon fibre (VGCF) processing.[12,13]

The atomic structure of a CF is similar to that of graphite and consists of carbon atom layers (graphene sheets) arranged in a regular hexagonal pattern, as depicted in Fig. 2.3. Depending upon the precursors and manufacturing processes, layer planes in carbon fibres may be either turbostratic, graphitic, or a hybrid structure.[12] In graphitic crystalline regions, the planes are stacked parallel to one another in a regular fashion. The atoms in a plane are covalently bonded through sp^2 bonding while the interaction between the sheets is dominated by weak Van der Waals forces.[12,14]
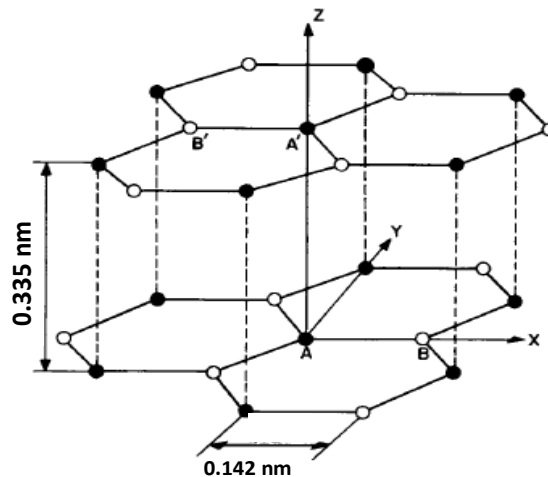
Fig. 2.3 The crystal structure of graphite.[14]

In a single graphitic crystal, the interlayer spacing (d) between two graphene layers (d_{002}) is ~ 0.335 nm. However, the basic structural unit of many carbon fibres consists of a stack of turbostratic layers. In a turbostratic structure, the parallel graphene sheets are stacked irregularly or chaotically folded, tilted, or split. It has been reported that the

irregular stacking and the presence of sp^3 bonding can increase the interatomic spacing to 0.344 nm. Generally, only the mesophase pitch-based and VGCF exhibit a well stacked graphitic crystalline structure, whereas, the turbostratic structure can be observed in carbon PAN fibres.
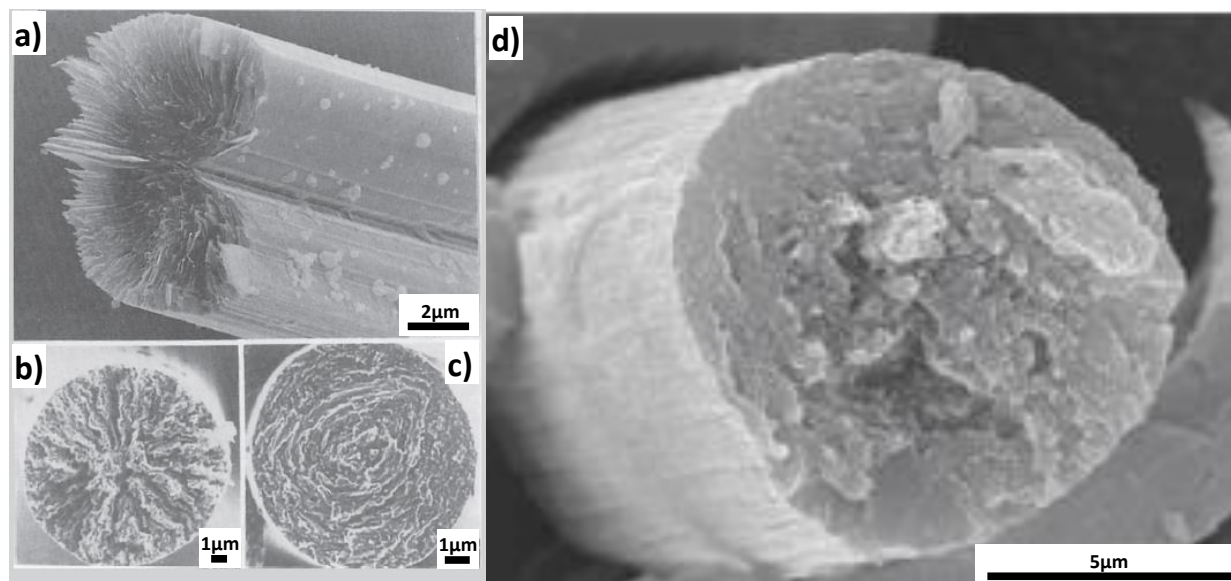
Fig. 2.4 Typical microstructure of CFs: Mesophase pitch-based CFs **(a)** radial with wedge, **(b)** radial, **(c)** concentric and **(d)** PAN CF.[13,15]

It is well known that the microstructure affects the properties. Fig. 2.4 shows the microstructures of various CFs. Due to the formation of micro-domains that can bend and twist, carbon fibres contain defects, vacancies, dislocations, grain boundaries, and impurities. These are the reasons why, as illustrated in Fig. 2.5, PAN fibres are characterised by low electrical and thermal conductivities. Whereas, a small interlayer spacing, large crystallite size, high degree of orientation parallel to the fibre axis, low density of defects, and high degree of crystallinity give mesophase pitch fibres a characteristic high thermal and electrical conductivities.

The pitch-based fibres have an electrical conductivity of 10^5 S/m to 10^6 S/m, thermal conductivity of 20 W m^{-1} K^{-1} to 1100 W m^{-1} K^{-1} and axial coefficient of thermal expansion from -0.4 × 10^{-6}/C to -1.6 × 10^{-6}/C.[12,13]
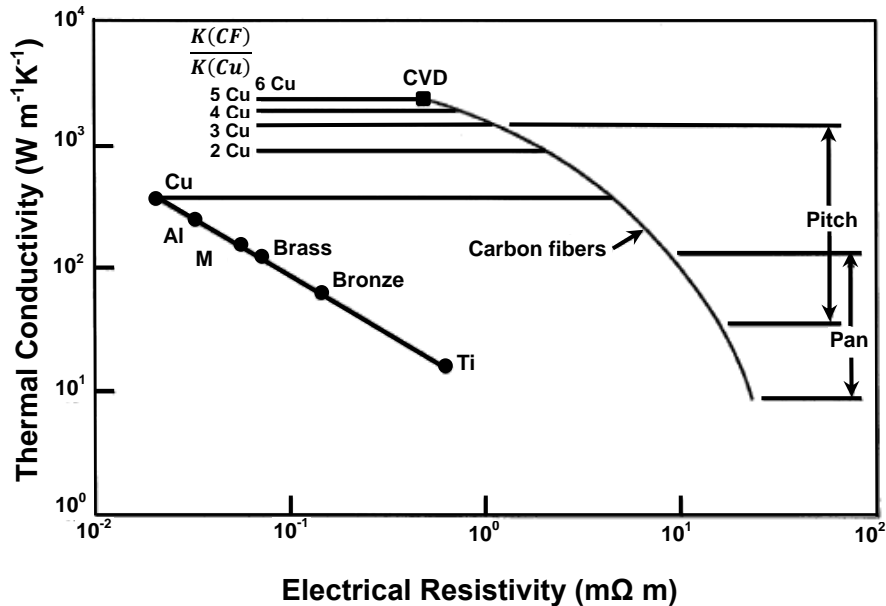
Fig. 2.5 Thermal conductivity and electrical resistivity of CFs compared with common metals.[1,6]

2.3.2 Multi-walled Carbon Nanotubes (MWCNTs)

2.3.2.1 Background

In 1985 a new class of hollow carbon structured materials came to light, with the discovery of fullerenes or buckyballs (C_{60}) by Kroto et al[16]. These materials composed of 60 C atoms, forming a structure resembling a football, gave rise to the subsequent nanomaterials revolution.

In 1991 Iijima et al[17], discovered hollow tubes similar to the buckyballs containing multiple tubes, or shells, one within another (see Fig. 2.6) which were later called multi-walled carbon nanotubes (MWCNTs). Despite Iijima's discovery, Bacon et al[18] was the first to report nanotubes in 1959, however at the time he was not able to identify the tubes internal structure referring to it as filament like graphite with a scroll structure.[6,19,20]

Carbon nanotubes (CNTs) can be thought of as graphitic sheets with a hexagonal lattice (graphene) that have been wrapped up into a seamless cylinder. If the nanotube is comprised of one graphene sheet, as depicted in Fig 2.6 a), then it is a called single-
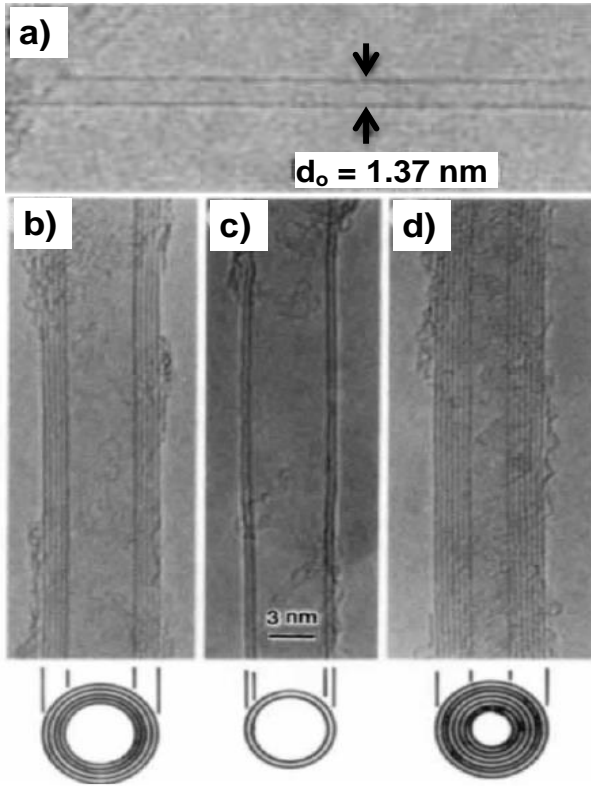
Fig.2.6 High-resolution TEM (HRTEM) images of: **(a)** SWCNTs grown from iron catalyst. MWCNTs with **(b)** 5 walls, **(c)** 2 walls and **(d)** 7 walls.[17,21,22]

walled carbon nanotube (SWCNT). The internal diameter of a SWCNT is in the range of 0.4-3 nm and the thickness of the wall is considered to the same as that of a graphene sheet. However, if the nanotube is comprised of two to fifty coaxial sheets or walls it is called a multi-walled carbon nanotube. Fig. 2.6 b), c) and d) illustrates different CNTs. The distance between MWCNT sheets/walls ($d_{spacing}$) is 0.34 nm.[19,20]

Another way to characterise the nanotube is according to their chirality or helicity. The hexagonal arrangement of atoms in CNTs and graphene sheets can be described in terms of the tube´s chirality or helicity, using the chiral vector, $\vec{C}_h$, or the chiral angle θ, as illustrated in Fig. 2.7. The chiral vector, $\vec{C}_h$, can be defined by the following equation:

$$\vec{C}_h = m\vec{a}_1 + n\vec{a}_2 \qquad \text{(eq. 1)}$$

The integers n and m are the number of steps along the unit vectors $\vec{a}_1$ and $\vec{a}_2$, and the chiral angle θ determines the amount of twist of the carbon nanotube. CNTs are fundamentally classified into three main categories according to their $\vec{C}_h$; chiral, armchair and zigzag.[20,21] A chiral (m,n) nanotube in general has unequal, non-zero m and n integers, i.e. m ≠ n ≠ 0 and the chiral angle θ is between its two limits (0⁰ < θ < 30⁰), whereas for the zigzag nanotubes the chiral angle is θ = 0⁰, where m ≠ n, n = 0 and armchair nanotubes the chiral angle is θ = 30⁰, where m = n ≠ 0.[20,21]
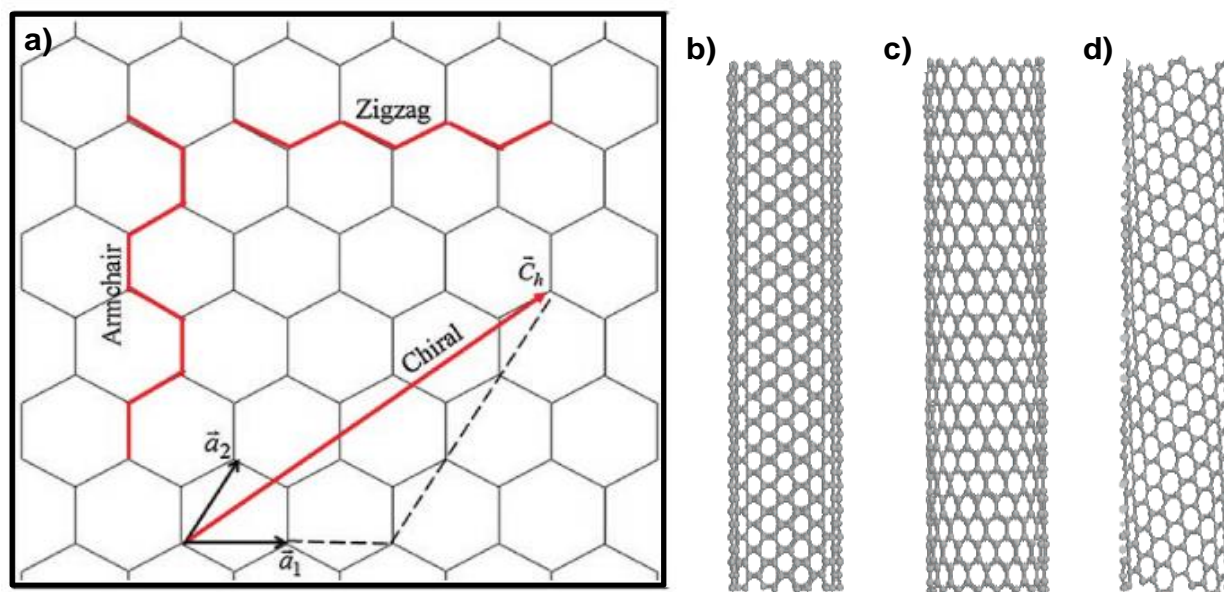
Fig. 2.7. **(a)** Schematic representation of a graphene sheet honeycomb structure and respective SWCNT chiralities. SWCNTs can be formed by folding the sheet along lattice vectors. The two unit vectors $\vec{a}_1$ and $\vec{a}_2$ are shown. Folding of the (8,8), (8,0), and (10,-2) vectors lead to armchair **(b)**, zigzag **(c)**, and chiral **(d)** tubes, respectively.[20,24]

The chiral, armchair and zigzag carbon nanotubes can exhibit different properties. For instance, in terms of electronic properties chiral, and zigzag nanotubes show semiconducting behaviour, whereas armchair carbon nanotubes are categorized as metallic conducting materials.[20,21] This behaviour is depicted in Fig. 2.8 which illustrates the dispersion relation of armchair and chiral CNTs.[25]

Due to this characteristic of the CNTs, a major milestone was reached in separating the metallic and semiconducting nanotubes, since both are created simultaneously during synthesis, therefore, hindering their applications.[26] For further information regarding the physics of carbon nanotubes (which is outside of the scope of this study), the following references are recommended: [6,21,25,26].
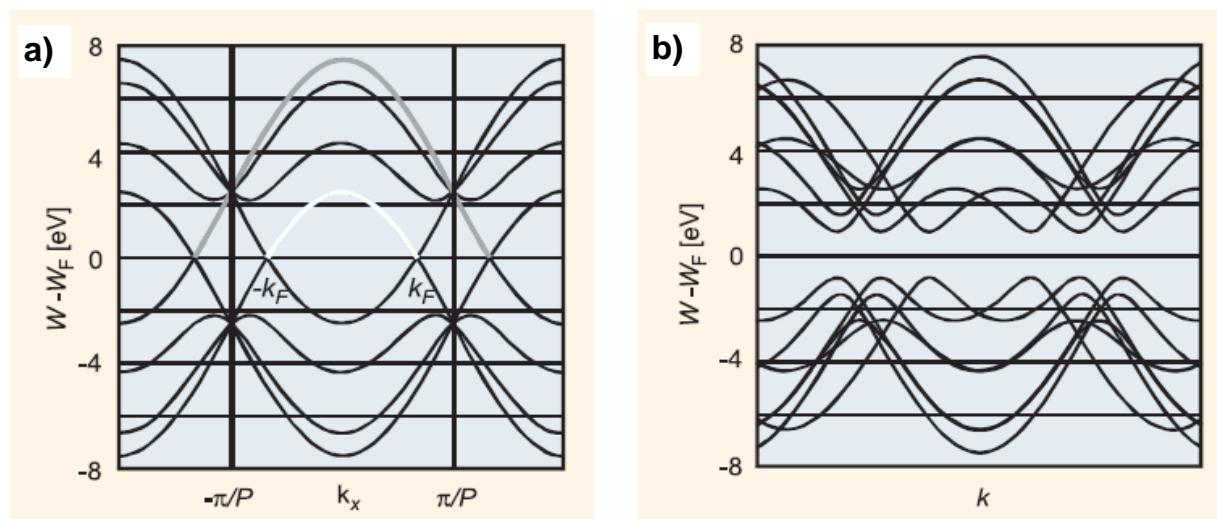
Fig. 2.8 Illustration of the dispersion relation $W(K_x)$ of: **(a)** A (3,3) armchair CNT where the states at the Fermi level indicate a metallic behaviour; and **(b)** A (4,2) chiral tube CNT where the conduction band and the valence band are separated by a bandgap, indicating semiconductor behaviour.[25]

2.3.2.2 Synthesis

Synthesis of MWCNTs can be achieved by several methods. The three most commonly used methods are the arc-discharge, laser ablation, and chemical vapour deposition techniques.[19,24] Also in addition, several non-traditional miscellaneous methods have been developed, such as from amorphous carbon in hydrothermal fluids, the flame synthesis method and a continuously operated arc reactor scheme.[19]

The first two (arc-discharge and laser ablation) employ solid-state carbon precursors to provide carbon sources needed for nanotube growth. This involves carbon vaporization at high temperatures (> 1000 °C). These methods are well established in producing high-quality and nearly perfect nanotube structures, despite large amounts of associated by-products, as illustrated in Fig. 2.9 (e.g. tangled structures and excess amorphous carbon, i.e. low purity). Chemical vapour deposition (CVD) utilizes hydrocarbon gases as sources for carbon atoms and metal catalyst particles as "seeds" for nanotube growth that takes place at relatively lower temperatures (500-1000 °C).[20–22]

2.3.2.3 Quality

The quality of the MWCNTs is of major importance in order to harness their outstanding thermal conductivity. In MWCNTs structural defects such as pentagons, pentagon-heptagon pairs, vacancies, interstitials, edges, disorder (e.g. amorphous carbon, fullerenes and distorted or incomplete mesoscopic graphite shells) and impurities such as metal catalysts are also present, as illustrated in Fig. 2.9.[19] These features have a strong detrimental effect on MWCNT properties in general.[19,24,29–31]
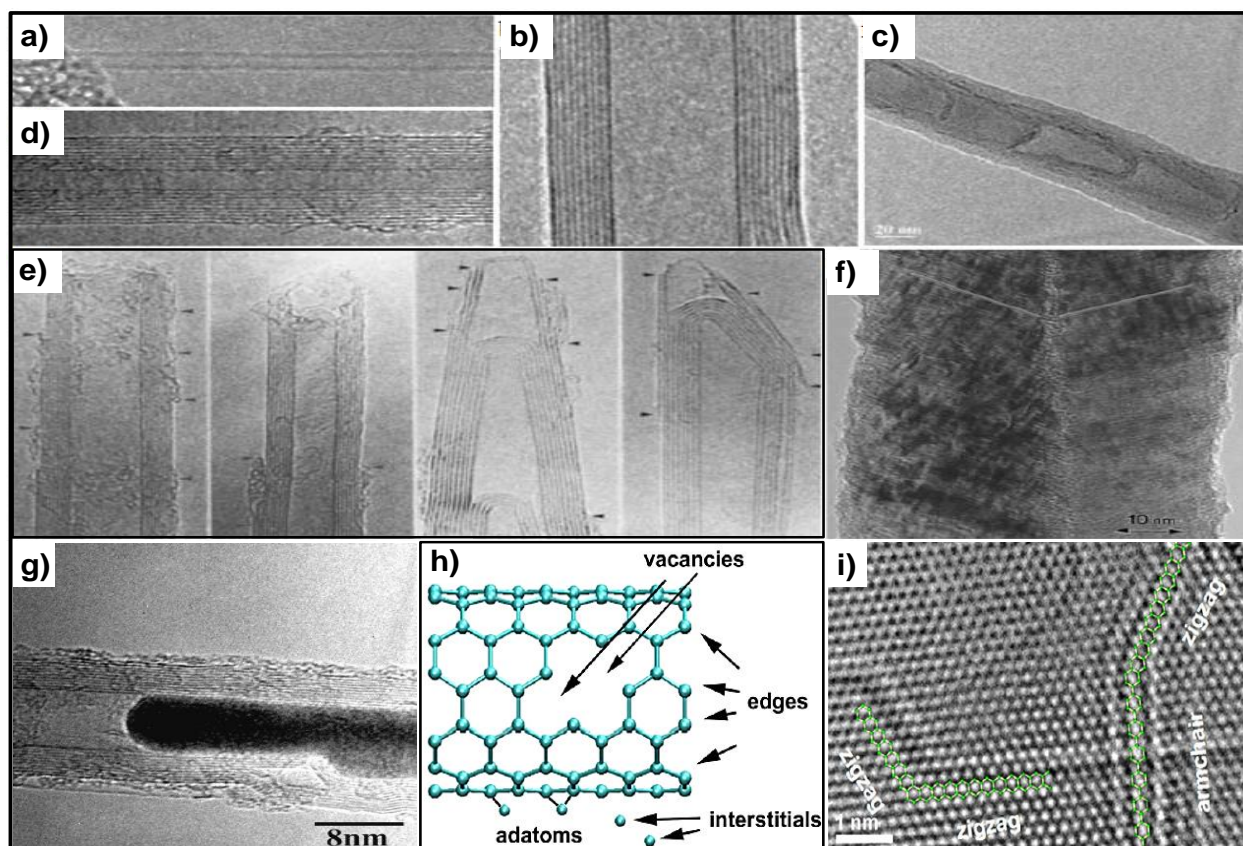
Fig. 2.9: TEM images of: **(a)** a pristine SWCNT; **(b)** a clean-walled MWCNT; and **(c-g)** MWCNTs with varying degrees of disorder. Layers of amorphous carbon, fullerenes, mesoscopic graphitic sheets and metallic catalyst are common MWCNT impurities. Lattice disorder includes: **(c)** "bamboo"; and **(f)** "herringbone" structures. **(g)** Catalysts can be made of different metals and compounds and in this case a Fe catalyst particle was trapped inside. **(h)** Defects caused by reactive carbon atoms such as vacancies, interstitials and edges. **(i)** Graphene edges exhibiting zigzag and armchair edges. [29,34]

MWCNTs can be described as, an intermediate material between graphite and SWCNTs. On closer inspection, though, MWCNTs are more complex than either crystalline graphite or SWCNTs, as subtle forms of disorder exist. For example, the curvature of the tubes applies a force to adjacent layers in a MWCNT (this intrinsic broken symmetry has various consequences)[32], and multilayer scrolls, or MWCNTs composed of both scrolls and cylinders occur, rather than merely the purely cylindrical structure.[29,33] However, the most important contributions to MWCNT disorder include tapering cylinders, variable numbers of carbon layers, and partial interior filling (see Figs. 2.9 c) and g)). The cylindrical crystalline structure can also be severely compromised by certain additives.[29]

2.3.2.4 Purification

Purification is a post processing technique to reduce or eliminate the amount the defects and impurities present in the MWCNTs.[29,35]

One common technique is the chemical method which is based on the concept of: selective oxidation, wherein carbonaceous impurities are oxidized at a faster rate than MWCNTs, and the dissolution of metallic impurities by acids. This method can effectively remove amorphous carbon (*a*-C) and metal particles except for those encaged in polyhedral graphitic particles. However, due to oxidation the chemical method always dictates the structure of MWCNTs.[35]

The physical method (e.g. filtration, centrifugation…) can also be used for purification. It separates the MWCNTs from impurities based on the differences in their physical size, aspect ratio, gravity, and magnetic properties, etc. In general, the physical method is used to remove graphitic sheets, carbon nanospheres (CNSs), aggregates or separate CNTs with different diameter/length ratios. In principle, this method does not require oxidation, and therefore prevents MWCNTs from severe damage. Nevertheless, the physical method is complicated, time-consuming and less effective.[35]

A combination of the physical and chemical methods can also be applied for purification. It can lead to high yield and high-quality MWCNTs. Owing to the diversity of the as-prepared MWCNT samples, such as nanotube type, morphology and structure,

as well as impurity type and morphology, a carefully selected combination of different purification techniques is required to obtain MWCNTs with the desired purity.[29,35,36]

Heat treatment offers another route for purification. Bifano et al[37] demonstrated the importance of purification after increasing on average the thermal conductivity of CVD-grown MWCNTs by 44 ± 29 W m^{-1} K^{-1} to 216 ± 149 W m^{-1} K^{-1} by heat-treating the CNTs at 3000 ºC for 20h. This work clearly shows the importance of performing purification before the use of MWCNTs in order to produce ultra-high thermal conductivity materials for thermal management applications.

2.3.2.5 Thermal Stability

The thermal stability of MWCNTs at different temperatures and in various environments is also very important in order to guarantee that no chemical or structural change occurs (allotropy) leading to a decrease in thermal conductivity, as illustrated in Fig.2.2.

According to the literature[29–31,38] thermal analysis techniques such as thermogravimetric analysis (TGA) is widely employed to measure MWCNTs thermal stability. It involves monitoring sample weight during heating, typically at rates of 1 - 3 °C/min. In air, *a*-C converts to CO and CO_2 at temperatures below 400 °C, whereas MWCNTs burn at higher temperatures of 400 - 750 °C[30,39]. Above 1000 °C, any remaining mass can be attributed to metal contaminants such as transition metal catalysts. The highest quality SWCNTs exhibit relatively sharp weight-loss profiles. In contrast, highly defective or contaminated materials, burn over much wider ranges at lower temperatures.[29]

2.3.2.6 Thermal Conductivity

It is well known that the ability of a material to conduct heat is established by its atomic structure and a knowledge of its thermal properties is of major importance, especially as they alter significantly when they are structured on the nanometre scale.[8]

In the case of MWCNTs the good thermal conductivity reported is attributed to the strong covalent sp^2 bonds. In sp^2 hybridization, three of the valence shell electrons are involved in chemical bondings and hence, there is one free electron, called the π-electron. Materials with extended π-clouds, like carbon nanotubes, are called "π-

electron materials" and these exhibit many exceptional thermal and electrical conductivity properties.[20]

The sp^2 C-C bond is considered to be the strongest in solid materials and it also has a strong harmonic nature resulting in efficient heat transfer by lattice vibrations (phonons). However, due to the MWCNTs graphitic structure (see Fig. 2.3), the sp^2 bonding only occurs along the nanotube sheet/wall (in-plane direction), resulting in very high K (> 3000 W m^{-1} K^{-1}) whereas, in the out-of-plane direction they are connected between walls by weak Van der Waals bonds, resulting in a very low K (10 W m^{-1} K^{-1}) similar to that of graphite. The electrons contribution is so low in comparison to phonons that is considered negligible.[8,20,40]

Thermal conductivity is described by Fourier's law:

$$q = -K\Delta T \hspace{3cm} \textbf{eq. (2)}$$

q is the heat flux, K is the thermal conductivity and ΔT is the temperature gradient. In this expression, K is treated as a constant, which is valid for small temperature (T) variations. In a wide temperature range, K is a function of T. In anisotropic materials, K varies with crystal orientation and is represented by a tensor.[8,41]

In solid materials heat is carried by acoustic phonons that is, ion-core vibrations in a crystal lattice and electrons so that:

$$K = K_p + K_e \hspace{3cm} \textbf{eq. (3)}$$

K_p and K_e are the phonon and electron contributions, respectively. For metals, K_e is dominant due to large concentrations of free carriers. In pure copper, one of the best metallic heat conductors, $K \approx 400$ W m^{-1} K^{-1} at room temperature and K_p is limited to 1-2% of the total.[8]

For carbon materials the heat conduction is governed by phonons (K_p) due to the strong covalent sp^2 bonding. However, in the case of doped materials K_e can become significant.

The phonon thermal conductivity[8] is expressed as

$$K_p \; = \; \Sigma_j \int C_j(\omega) v_j{}^2(\omega) \tau_j(\omega) d\omega \qquad\qquad \textbf{eq. (4)}$$

j is the phonon polarization branch, composed of two transverse acoustic branches and one longitudinal acoustic branch; v is the phonon group velocity, which for many solids, can be approximated by the sound velocity; τ is the phonon relaxation time, ω is the phonon frequency and C is the heat capacity. The phonon mean-free path (Λ)[8] is related to the relaxation time as:

$$\Lambda \; = \; \tau v \qquad\qquad \textbf{eq. (5)}$$

For typical solids, the acoustic phonons, which carry the bulk of the heat, are scattered by other phonons, lattice defects, impurities, conducting electrons and interfaces.[8,41,42]

However, for nanostructures, K is reduced by scattering from boundaries, which can be estimated as:

$$\frac{1}{\tau_B} \; = \; \left(\frac{v}{D}\right)\left(\frac{1-p}{1+p}\right) \qquad\qquad \textbf{eq. (6)}$$

τ_B is the phonon lifetime and $1/\tau_B$ is the phonon scattering rate, D is the nanostructure or grain size and p is the specularity parameter defined as the probability of specular scattering at the boundary.[8]

CNT thermal transport is dominated by the intrinsic properties of the strong sp^2 lattice, rather than by phonon scattering on boundaries or by disorder giving rise to extremely high K values.[8–10,43,44]

The thermal conduction in MWCNTs as described by eqs. 4, 5 and 6 is mainly governed by phonon contribution which is affected by several factors such as the number of the phonon active modes, the length of the mean free path of the phonons and inelastic Umklapp scattering.[45,46] These factors are directly influenced by the following parameters:

- Temperature
- Morphology (chirality, number of walls, length, inner and outer diameter)
- Quality (crystallinity, defects and impurities).
- Tube-tube interaction

Experimental data of the K of CVD-grown MWCNTs for temperatures from 4K to 300K, demonstrate that, because of the larger diameter in comparison to SWCNTs that act as 1-D material, MWCNTs act essentially as 2-D phonon materials. So, at a low temperature (T < 100 K), $K(T)$ increases as ~ T^2, a behaviour similar to graphite $T^{2.3}$. Whereas, at room-temperature K is small, comparable to the less-graphitic carbon fibres, and the MWCNTs do not show a maximum in $K(T)$ due to Umklapp scattering.[47]

Zhang et al[46] calculated the K of three types of SWCNTs, using the homogeneous nonequilibrium Green–Kubo method. They found that K also depends on chirality, despite the fact that the electronic contribution (K_e) was considered negligible. As shown in Fig. 2.10, at room temperature the zigzag nanotube has the maximum value, followed by the armchair and lastly the chiral nanotube.
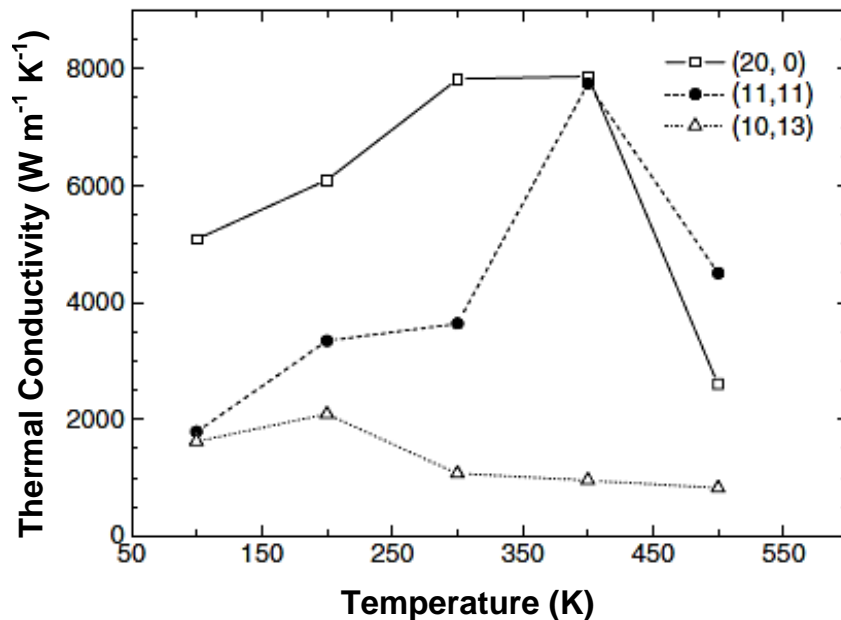
Fig. 2.10 Thermal conductivities of zigzag (20,0), armchair (11,11) and chiral (10,13) SWCNTs as a function of temperature.[46]

However, Zhang and Li[49] claim that unlike the electronic counterpart, the thermal conductivity/conductance of SWCNTs does not depend on the chirality and/or atomic geometry at both low and room temperatures. Therefore, due to the scarce and controversial data it is unclear whether or not chirality plays a role on thermal conductivity. Nevertheless, if it does it will also play a role in MWCNTs.

Depending on their morphology, MWCNTs can be either ballistic or diffusive heat conductors.[46] Ballistic heat transport occurs when phonons rarely scatter along the length of the nanotube resulting in high K. The phonon mean free path (Λ) is longer than the nanotube length and the dominant phonon wavelength is smaller than the nanotube diameter. Diffusive heat transport dominates when the phonons scatter many times within the nanotube, thus the nanotube is much longer than both the Λ and the dominant phonon wavelength, decreasing K.[44] The transition of regime occurs as the nanotube length increases.

Molecular dynamic simulations have estimated that the Λ at room temperature ranges from ~ 50 nm[50] to 1.5 µm[46], although MWCNTs with many defects may have Λ paths as small as 4 nm[46,51]. The increase in length also increases the probability of defect concentration.[46] Song et al[52], found that MWCNTs with lengths < 1 µm increased K, compared to long MWCNTs, due to reduced curving or bending. Pettes and Shi[51] found that the thermal conductivity of MWCNTs decreased with the number of walls, which is believed to be linked with an increased concentration of defects in nanotubes with more walls.

Theoretical work on SWCNTs demonstrated that single vacancy, double vacancies, and Stone-Wales (5,7,7,5) defects significantly reduce K. It was found that K saturated with increasing defect concentrations above ~ 0.5% to ~160 W m^{-1} K^{-1} for all types of defects studied. Despite the fact that the theoretical studies of the effect of defects on carbon nanotubes has been mainly conducted on SWCNTs, the findings suggest that it should also have a strong impact on MWCNTs. Additionally, it is predicted that although individual tubes in a defect-free MWCNT may act independently due to the weak

interwall coupling, the presence of defects can cause scattering in all directions and link together different walls of the MWCNT.[46]

Carbonaceous impurities such as *a*-C resulting from the nanotubes synthesis have a very low K, spanning from 0.1 to 10 W m^{-1} K^{-1}.[8,53] Also, Zhang and Li[49] showed that K decreases as the percentage of ^{14}C impurity increases. With 40%-50% ^{14}C, the K is reduced by ~ 40% compared to a pure ^{12}C SWCNT.

Aliev et al[54] demonstrated that individual nanotubes always possess higher K than bundles/arrays of nanotubes with the same individual characteristics, as illustrated in Fig. 2.11. He showed that tube-tube interaction decreases the room temperature K of the MWCNT bundles, comprised of about 100 nanotubes, by a factor of four relative to that of a single nanotube with a K = 600 W m^{-1} K^{-1}. This phenomenon is also clearly demonstrated in Tables 2.2 and 2.3.
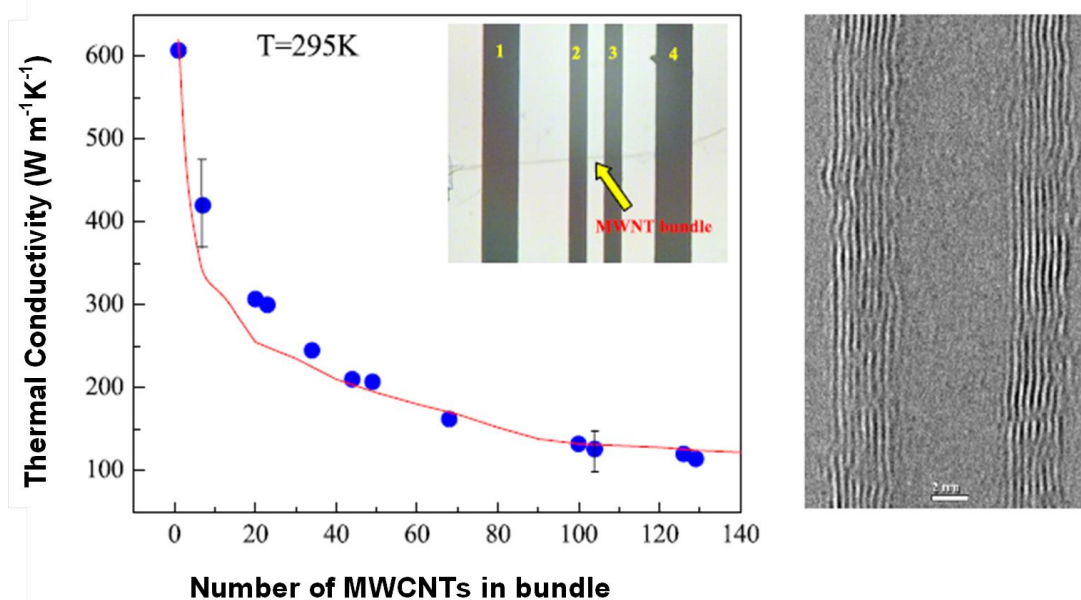
Fig. 2.11 The thermal conductivity of MWCNTs measured by the 3ω method at room temperature as a function of the number of tubes in a bundle. The inset shows an SEM image of a four-probe gold patterned substrate with attached MWNT bundle. Right inset: TEM image of ~10 nm ø MWCNT comprising 7–8 shells.[54]

2.3.2.6.1 Techniques to obtain the thermal conductivity of MWCNTs

MWCNTs are a relatively recent discovery and their overall properties are not yet fully regulated due to the difficulty in controlling their atomic structure during synthesis.[17,19,24] Therefore, despite the fact that considerable work has been conducted in this field, there is still a long way to go until a commercially available material is produced that possesses the "outstanding" thermal properties ($\sim$3000-6600 W m^{-1} K^{-1}) obtained by the theoretical and experimental studies.[8]

The fact that nanometrology is still in its infancy is hindering the development of the thermal properties of the MWCNTs and nanomaterials. As a consequence there are many challenges still to be overcome and understood. These are:

I.   A large thermal resistance of the sample, which requires the probe to have high levels of thermal insulation in order to minimize heat leakage.
II. A need for a stable, repeatable thermal contact to the ends of the sample.
III. A difficulty to align the sample to the thermal probe and to determine the geometry and morphology of the sample and its contacts.

Previous solutions to these challenges have been based on complex microfabrication of the devices, as illustrated in Fig. 2.12. Nevertheless, data acquisition with these devices are time-consuming, extremely expensive and scarcely available (as most are mainly in the research development stage).[53,54] The most common methods to test the thermal conductivity of individual/bundles of CNTs detailed in the literature are as follow:

- 3 ω method [9,37,51,54,56,57]
- Raman shift [56,58,59]
- Pulsed photothermal reflectance (PPR) [54,58,59]
- Scanning thermal microscopy (SThM) [56,62,63]

The experimental studies, as expected, revealed a wide range of K for individual MWCNTs spanning from 17 to >3000 W m^{-1} K^{-1} (see Table 2.2).[8,35,49,52,53,55,57,58,62–64] The large scattering is due to the MWCNTs distinct morphology and the qualities amongst them, as described in the previous Subsection (2.3.2.3). Whereas, bundles of
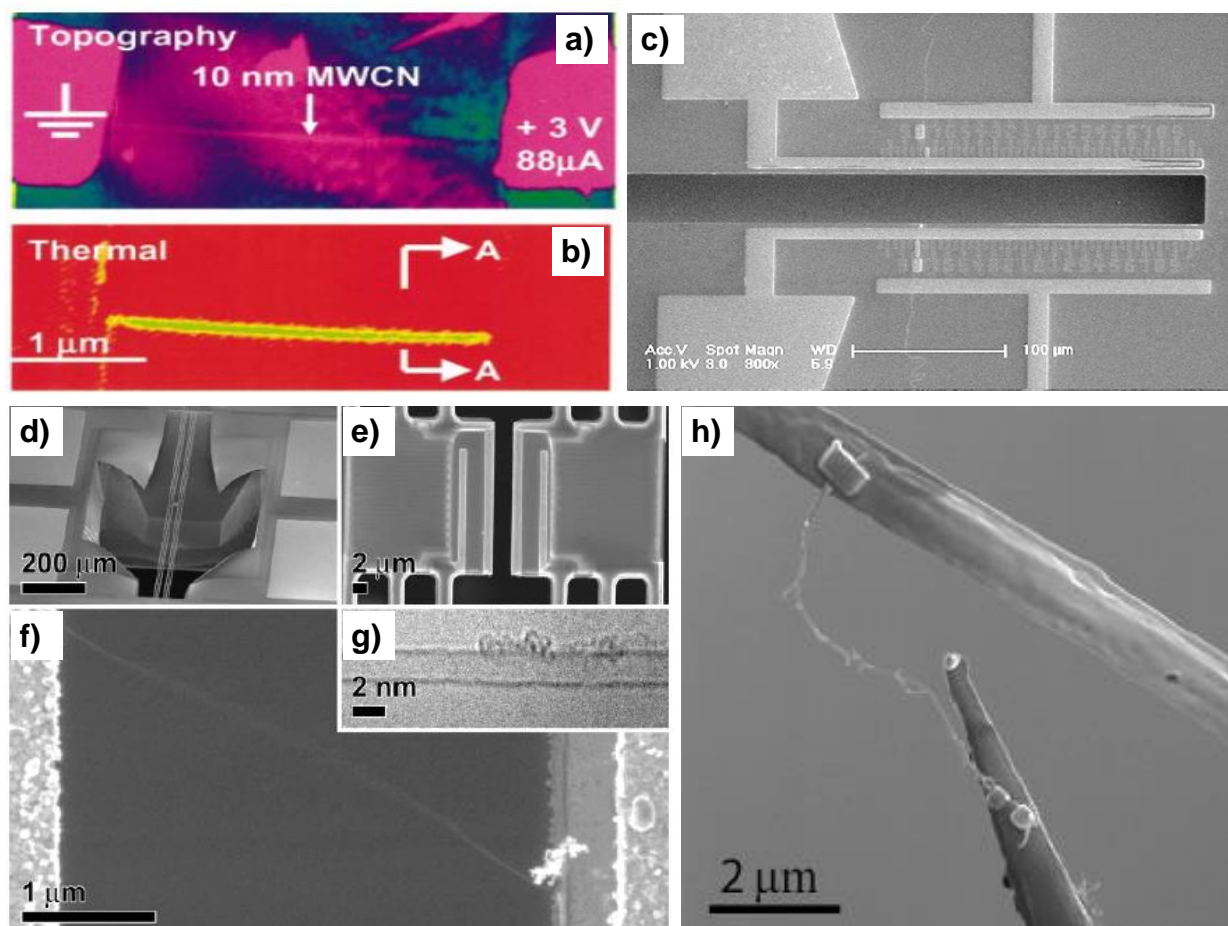
Fig.2.12 Micro-devices employed to acquire the K of MWCNTs: **(a)** Topographical and **(b)** thermal images of a MWCNT obtained by SThM.[67] **(c)** SEM image of an individual CNT grown over a Raman shift method measuring cell.[59] Micro-device used by Pettes and Shi et al[51] where **(d)** and **(e)** show the SEM images of the suspended micro-device and the two central membranes, respectively, **(f)** SEM and **(g)** TEM image of a SWCNT bridging the two membranes. **(h)** The heater/sensor probe wire device connected by a MWCNT attached with Pt by electron beam induced deposition (EBID).[37]

nanotubes exhibited a K ranging from 2.5 to 150 W m^{-1} K^{-1}, i.e. lower values and smaller ranges of K, due to the addition of another factor (tube-tube interaction) in comparison to an individual tube.[52,59,66,67]

The success of the use of MWCNTs and other nanomaterials to develop ultra-high thermal conductivity materials is primarily dependent on the development of cheaper

Table 2.2 Experimental thermal conductivity of individual MWCNTs reported in the literature with the respective technique used.

K (Wm^{-1}K^{-1})	d_o (nm)	d_i (nm)	l (µm)	Technique	Comment	Reference
600	10	---	10	Self-heating 3 ω	CVD	Aliev et al[54]
2586	150	---	2	PPR	PECVD	Samani et al[60]
> 3000	14	---	2.5	Heater Sensor	----	Kim et a[9]l
2069	9.8	---	3.7	T-type sensor	Arc-discharge	Fuji et al[64]
650	46	---	1	3 ω method	---	Choi et al[57]
830	42	---	1.1	3 ω method	---	
269	10.5	7	3.02	Heater Sensor	CVD	Pettes and Shi[51]
178	11.4	6.7	1.97	Heater Sensor	CVD	
42	14	6.6	3.31	Heater Sensor	CVD	
1400	8.2	---	16	Raman Shift	CVD	Li et al[59]
600	20	---	1.08	---	---	Chiu et al[65]
750	105	---	20	Laser Flash	PECVD	Xie et al[66]
17	30	7	0.38	Hot wire	---	Dames et al[53]
765	35	10.15	10.77	T-type Probe	CVD, HT	Bifano et al[37]
228	59	---	10	T-type Probe	CVD, HT	
50	59	---	10	T-type Probe	CVD,HT	
46	41	---	10	T-type Probe	CVD	

HT – The MWCNTs were subjected to a high temperature heat treatment.

Table 2.3 Experimental thermal conductivity of MWCNTs bundles reported in the literature.

K (W m^{-1}K^{-1})	Bundle size (µm)	Technique	Comment	Reference
150	0.1	Self-heating 3 ω	CVD	Aliev et al[54]
50	2	Self-heating 3 ω	CVD	
25	1.5	Self-heating 3 ω	CVD	Yi et al[68]
15	0.07	PPR	Microwave Plasma	Yang et al[59]
2.5	2500	Four - Probe Resistivity	CVD	Jin et al[69]
23	2500	3 ω method	CVD, HT	

HT – The MWCNTs were subjected to a high temperature heat treatment.

and simpler nanometrology techniques. This would allow industries to quickly assess the properties of the nanomaterials purchased from commercial sources, forcing the suppliers to deliver nanomaterials with customized thermal properties to meet the needs of the industry for each given application. Thus, creating a driving force for the fast development of thermal management materials based on nanomaterials.

2.4 Processing of AMCs for Thermal Management

2.4.1 Overview of MMC Processing

Metal matrix composites (MMCs) are defined as a material consisting of two different phases, namely the contiguous metal matrix and the reinforcement or filler material, properly distributed (produced via a physical and chemical (in-situ) combination of pre-existing materials) in order to obtain a new material with improved properties compared to the monolithic material properties.[70,71]

MMCs have been reported to have been used since 7000 BC.[71] Nevertheless, it was only in the 1970s that MMCs started to be more widely studied and developed in order to meet the demands of new materials for space exploration. To face the challenge, these composites needed to have the combined properties of high strength, high-temperature resistance, and low coefficient of thermal expansion so as to withstand the extreme and repeated temperature swings experienced during space missions.[72]

The matrix is a "soft" metal phase that generally provides excellent ductility, formability and thermal conductivity. This matrix is usually a lighter metal such as aluminium (Al), magnesium (Mg), copper (Cu), titanium (Ti) or silver (Ag), which provides a compliant support for the reinforcement. Al and its alloys are the most popular matrix due to their low density, their capability to be strengthened by precipitation hardening, good corrosion resistance, high damping capacity, and high electrical and obviously thermal conductivity.[73]

The reinforcement or filler material, commonly referred as the "hard" phase embedded in the "soft" metal matrix, provides the possibility to tailor and optimize properties (by varying the nature and volume/weight fraction of its constituents) for a given application that are not possible to obtain from the monolithic metal itself, such as, high stiffness, low thermal expansion and high thermal conductivity.[73]

The composites may be categorized according to their microstructure, and the reinforcement used i.e. short fibres, whiskers or particles, as illustrated in Fig. 2.13. This type of composite is commonly referred to as discontinuously reinforced MMCs. Where the reinforcement is in the form of monofilaments or continuous fibres, this is termed as continuously reinforced MMCs.[70,71]

Continuous   **Discontinuous**

Monofilaments   **Whiskers**   **Particulate**
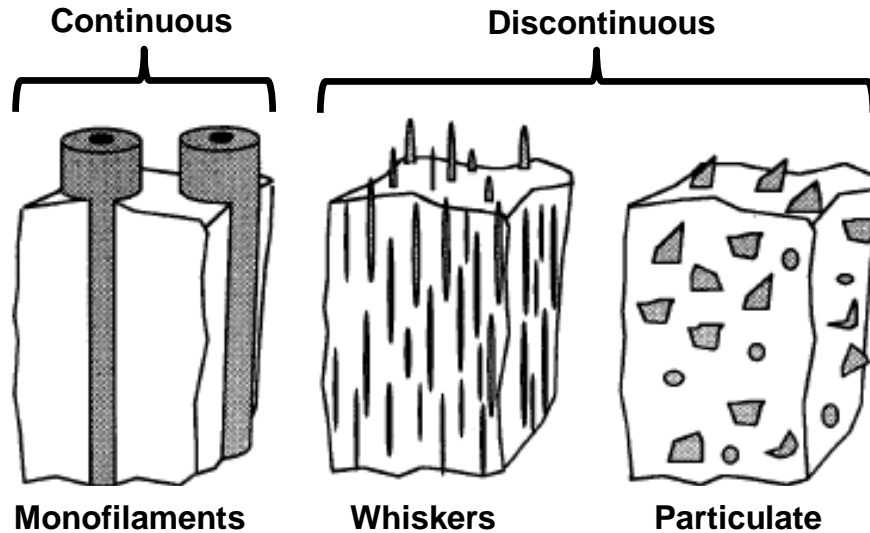
Fig 2.13 Illustration of the types of MMCs classified according to the type of reinforcement. [71]

There are several processing methods used to manufacture MMCs. The methods can be generally classified into three classes:

- Liquid-state processing
- Solid-state processing
- Deposition processes

Fig. 2.14 gives a schematic representation of the MMCs processing methods according to their class and suitability according to the type and shape of the reinforcement.[74,75]
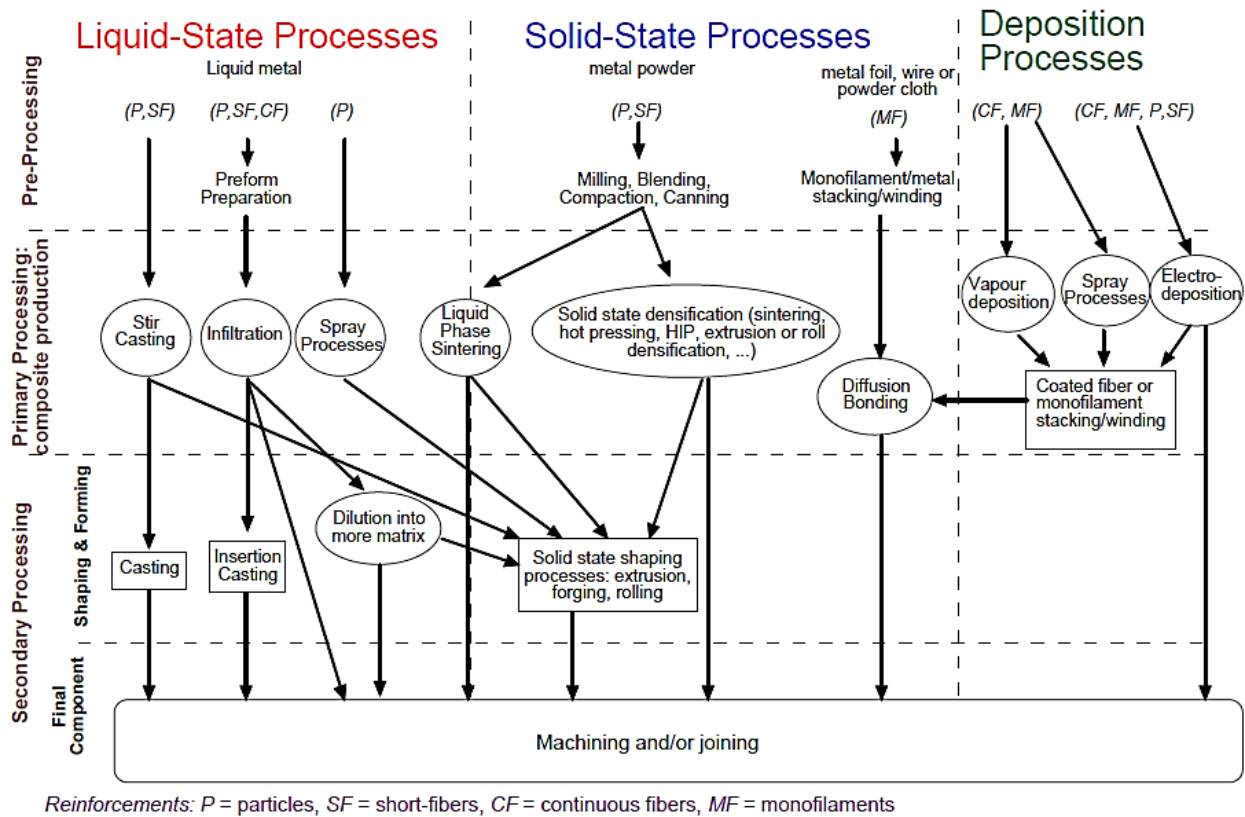
Fig. 2.14 Illustration of general MMC processing routes.[74]

The liquid-phase processes are the most attractive because they are less expensive than solid-state processes and it is possible to select a wider range of materials and processing conditions. Liquid-state processes can be classified into two techniques:

- Vortex and compocasting/rheocasting
- Pressure-assisted and pressureless infiltration.

Vortex and compocasting methods are characterised by the addition of small aspect ratio reinforcements (particles or short fibres) into liquid and semi-solid metals, respectively. However, the efficiency of the processes depends on the wettability of the reinforcements by the metal. Pressure-assisted infiltration and pressureless infiltration are both characterised by liquid metal infiltration into a ceramic porous body. The infiltration routes are the most widely used methods to manufacture MMCs because

they can easily fabricate composites regardless the level of wettability between the liquid metal and the particles.[70,71,75]

The most common solid-state processes to fabricate MMCs are:

- Powder metallurgy
- Diffusion bonding

Powder metallurgy involves a mixture of metal powder and discontinuous reinforcements. The powder mixture can be cold pressed and sintered or hot pressed which then undergo extrusion (rolling, equal channel angular extrusion (ECAE)) or forging. Diffusion bonding, on the other hand is based on the joining with similar and dissimilar metal by interdiffusion at elevated temperatures.[70,71,75]

The deposition processes are outside of the scope of this study, and are therefore not described further. However, for further information on this and other MMCs processing the reader is directed to the following references[76–82].

2.4.2 Processing of Al/MWCNTs

Nowadays, with the advent of nanomaterials and an acknowledgment of the outstanding intrinsic mechanical and physical properties of these materials, the development of MMCs reinforced with nano scale (1 nm = 10^{-9} m) particles is becoming popular. These materials are also referred as metal matrix nanocomposites (MMNCs), and they display novel properties that overcome the limitations of composites reinforced with micron scale fillers.

One important application of these novel nanocomposites is heat removal, especially in the electronics industry where its dissipation is critical due to increasing levels of power usage. In order to tackle this issue, due to their unrivalled thermal properties, carbon based nanomaterials[8], especially CNTs[8,9,46,83], but also carbon nanofibers (CNFs)[84] and graphene[8,43,44] have been studied as a reinforcement of Al and Cu matrices[43,83–88], making their respective composites potential candidates for the next generation of materials for thermal management applications. However, the scope of this study is

focused on Al reinforced composites with MWCNTs (Al/MWCNTs) for the reasons already addressed in Section 2.2, therefore Cu-based composites are only addressed for comparison purposes.

2.4.2.1 Processing Methods

In order to process Al/MWCNTs a wide range of methods can be selected, however certain methods face more challenges than others in order to produce a sound composite with improved properties. Fig. 2.15 shows the classification of the different processes for processing Al/MWCNTs composites and the challenges to be overcome in order to harness the unusual properties of the MWCNTs.[91]
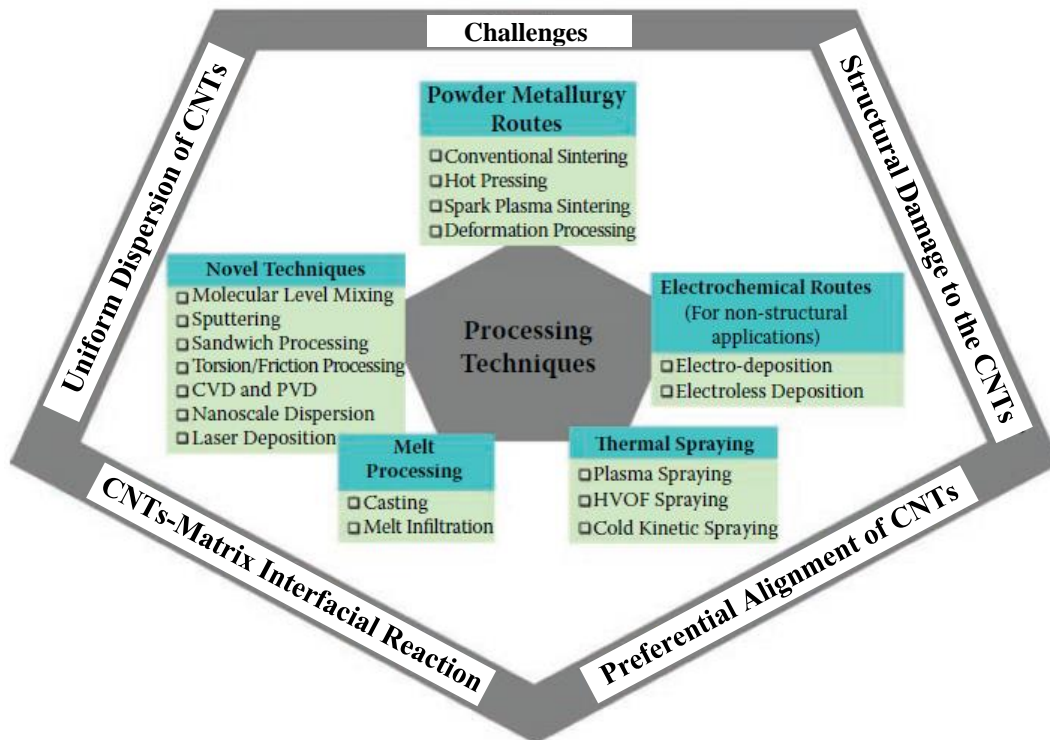
Fig. 2.15 Al/MWCNTs processing methods and the challenges to be overcome in order to harness the MWCNTs properties. (Figure modified from reference[91])

The most widely used methods and their respective advantages and disadvantages to process Al/MWCNTs are given in Table 2.4. More detailed information on these method can be found in the selected literature[45,85,91].

Table 2.4 Description of the most used methods to process Al/MWCNTs**.**

	Methods	Advantages	Disadvantages
Melt processing	**Stir/Vortex Mixing** [45,91,92]	Simple and economical. Can be used to fabricate bulk components. Utilizes conventional casting.	Difficult to introduce MWCNTs into the melt due to difference in density. Difficult to break MWCNTs bundles and disperse them homogeneously in the matrix. Poor wettability. Al_4C_3 formation.
	Compocasting/ Rheocasting [93,94]	Can be used to fabricate bulk components. Utilizes conventional casting equipment. Mixing occurs in highly viscous melt in the semi-solid state that traps nanofillers within the melt.	Difficult to break MWCNTs bundles and disperse them homogeneously in the matrix. Al_4C_3 formation.
	Ultrasonic Cavitation [95,96]	Can be used to fabricate bulk components. High-intensity ultrasonic waves break MWCNTs clusters and disperse them in the metal matrix.	Only efficient for low content of MWCNTs. Al_4C_3 formation.
	Pressure-assisted Pressureless Infiltration [45,74,75,91]	Higher chance of uniform distribution of MWCNTs than casting.	Coarse matrix grain size and undesirable interfacial reactions. Difficult to achieve proper filling of preform pores.
Powder Metallurgy	**Conventional Sintering** [45,85,91]	Simplest conventional method. Near net-shape composites. Homogeneous filler distribution.	Poor compact densification. Long processing time. Longer ball milling mixing for better distribution leads to MWCNTs damage. Al_4C_3 formation.
	Hot Pressing [45,91,97]	Near net-shape composites. Uniform and high densification (> 95%). Isotropic composites. Homogeneous filler distribution.	Long holding times can lead to Al_4C_3 formation. Longer ball milling mixing times for better distribution leads to MWCNTs damage.
	Spark Plasma Sintering [45,85,91,98]	Near net-shape composites. Suitable for consolidation of nano powders. Homogeneous filler distribution. Short processing time restricts grain growth and reactions between the metal matrix and MWCNTs.	Longer ball milling mixing times for better distribution leads to MWCNTs damage.
	Deformation Processing [45,91,98,99]	Improves composites densification. Breaks and aligns MWCNTs bundles.	Damage of the MWCNTs due to high shear forces applied.

Other processes such as thermal spraying, including plasma spraying, HVOF spraying and cold kinetic spraying can be used to produce Al/MWCNTs coatings or free standing structures. However, they will not be discussed further as it is beyond the scope of this study. Electrochemical routes, such as electrochemical and electroless deposition, are only utilized to synthesize composite coatings and thin films and are therefore not relevant with respect to this study. Further descriptions of these methods can be found elsewhere[85,91].

Due to the necessity to overcome the challenges to process Al/MWCNTs other novel processes have been utilized, including molecular level mixing, sputtering, sandwich processing, torsion/friction processing, chemical and physical vapour deposition (CVD and PVD), nanoscale dispersion and Explosive shock wave dispersion.[91,100–103]

2.4.2.2 Challenges

In order to take advantage of the outstanding thermal properties of the MWCNTs several challenges must be overcome during composite processing, such as:

- MWCNTs selection
- Introduction of MWCNTs into the Al matrix
- Dispersion/Wettability
- Alignment
- Structural damage
- Reaction products

The careful selection of appropriate MWCNTs for thermal management materials is crucial, as demonstrated in Subsection 2.3.2.3, the morphology and quality of the nanotubes strongly influence their thermal properties.[19,29,46,86]

The introduction of the MWCNTs within the Al matrix is a real challenge, especially when using liquid-state processing methods. The density of the MWCNTs is lower than the density of Al and Al alloys and due to the metal high surface tension (see Table 2.5) the nanotubes tend to float to the top of the melt surface.[95,104]

As emphasized in the processing methods Subsection (2.4.2.1) achieving uniform dispersion of the MWCNTs during composite processing is imperative in order to achieve the best properties. The dispersion of the filler is dependent on the processing method selected but most importantly depends on wettability. Due to the large surface area of the MWCNTs, and the electrostatic and Van der Waal's forces that arises between them they will naturally agglomerate, making it difficult to obtain a uniform dispersion using most conventional processing methods.[86,105]

In addition, due to their large surface area and surface dominant characteristics, these materials may also be highly reactive in metal matrices. In Al/MWCNT composites, agglomeration has been reported especially when MWCNT contents > 1 wt.% are used. In addition, brittle aluminium carbide (Al_4C_3) phases at the interface could form during processing, impairing the thermal properties of the nanocomposite.[85,106]

Conventional powder metallurgic methods of blending the metal powder and filler and other advanced surface modification processes based on the deposition of various metallic coatings (such as Cu, Ni, Co) onto nanofillers by electrochemical methods such as electroless plating methods, molecular level mixing[86,107], CVD and PVD methods[86] have been used to improve wettability.[108–112]

Table 2.5 Relationship between surface tension and wetting between various metals and CNTs. High surface tension reduces wetting.[91]

Element	Surface Tension (mN/m)	Wetting with CNT
S	61	Yes
Cs	67	Yes
Rb	77	Yes
Se	97	Yes
Te	190	No
Pb	470	No
Hg	490	No
Ga	710	No
Al	860 (750 °C)	No

Alignment of the MWCNTs within the metal matrix is crucial in order to give the best thermal conductivity contribution to the matrix. MWCNTs have a graphite-like structure (see Figs. 2.3 and 2.7), consequently, it also has anisotropic properties like graphite, with thermal conductivity best along the longitudinal axis of the tube (in-plane).[8,113]

Therefore, it is imperative that the nanotubes are aligned within the Al matrix to achieve the best thermal conductivity possible. However, the alignment is normally achieved through deformation processes that can induce serious structural damage on the MWCNTs, which therefore, may be detrimental to the thermal properties.[91,114]

Regarding the processing and development of composites reinforced with MWCNTs, polymer reinforced composites are the most advanced class, in both mechanical and physical properties, however the K improvement due to the MWCNTs is still low in comparison to the theoretical predictions.[53]

For metal matrix composites, the development lags behind its polymer counterpart due to the higher processing temperatures that augment difficulties in processing. In this class of composites most of the studies explore the mechanical properties and only a very limited number focus on the thermal conductivity.[53] For comparison, Table 2.6 gives the thermal conductivity of some of the few AMCs reinforced with MWCNTs and other metal matrices (Cu and Ag) available.

Table 2.6 Published thermal conductivity data for MMCs reinforced with MWCNTs produced using various processing methods.

Matrix	K_c Wm^{-1}K^{-1}	ΔK_c Wm^{-1}K^{-1}	K_m Wm^{-1}K^{-1}	v_f	w_f	Method	References
Al12Si	25.4	- 47.6	73	0.12	0.1	Plasma spraying	Bakshi et al[87]
Pure Al	103	- 53	156	0.05	0.04	PM /Deformation	Shin et al[99]
	172	16	156	0.05	0.04		
Pure Al	199	14	185	0.006	0.005	SPS	Wu et al[113]
	112	- 73	185	0.06	0.05		
Pure Cu	637	298	339	0.02	0.015	Electrochemical co-deposition	Chai and Chen et al[116]
Pure Cu	581	251	330	0.1	0.085	MIM	Muhsan et al[117]
Ag-X	440	15	425	0.006	0.005	HIP	Edtmaier et al[97]

The thermal conductivity improvement of the AMCs due to the addition of MWCNTs is extremely modest (less than 20 W m^{-1} K^{-1}) and in most of the cases the presence of the nanofiller actually decreases this property. The best value reported is from a pure Al matrix composite processed by SPS which resulted in an increase of only 14 W m^{-1} K^{-1} for an addition of 0.5 wt.% of MWCNTs. Whereas, when 5 wt.% of MWCNTs was

added, the K_c decreased to values substantially below that of the matrix (from 185 W m^{-1} K^{-1} to 112 W m^{-1} K^{-1}). This was attributed to the difficulty in achieving a homogeneous nanotubes dispersion and the formation of bundles with increased filler content.

Cu/MWCNT composites are the most commonly studied metal matrix composites in order to improve the thermal conductivity of the matrix for thermal management applications. Nevertheless, the thermal improvement is modest in most cases or negative, just like its Al matrix counterparts, and this effect occurs for the same reasons.[45,88,118,119] However, as shown in Table 2.6, Chai and Chen et al[116] and Muhsan et al[117] managed to achieve substantial K_c improvements, +298 W m^{-1} K^{-1} and +251 W m^{-1} K^{-1}, respectively. Both claim that the improvement was attained due to a good nanotube dispersion and bonding with the Cu matrix.

The limited number of studies that focused on the thermal conductivity of the MMCs, especially AMCs reinforced with MWCNTs clearly demonstrates the undeveloped state of these materials to harness the potential high thermal properties of the MWCNTs. For this reason, a substantial volume of work is still needed to develop processing methods to produce ultra-high thermal conductivity materials for thermal management applications.

2.4.3 Proposed Al/MWCNTs Manufacturing Process

It is clear from the published literature that processing AMCs reinforced with MWCNTs with improved thermal conductivity is no easy task, with many limitations and challenges to be faced regardless of the final processing method selected. With this in mind, in this study a combination of casting and deformation processes were selected to attempt to produce ultra-high thermal conductivity ($K \geq 400$ W m^{-1} K^{-1}) composites reinforced with MWCNTs. The processing consists of two steps, which are:

1st - Rheocasting

The high viscosity melt allows the incorporation and distribution of the fillers into the Al alloy matrix at temperatures below the liquidus temperature (T_L). This avoids Al_4C_3

formation which is detrimental for both the thermal and mechanical properties of the composites.

2nd - Equal Channel Angular Extrusion (ECAE).

This post-processing step allows: 1) the alignment of the fibre/nanotube within the matrix (which is randomly oriented after the rheocasting process) and, 2) porosity closure. This step, is intended to maximize the thermal conductivity of the composite, however, the final resultant composite will also show anisotropic thermal properties due to the resultant aligned microstructure.

2.4.3.1 Rheocasting
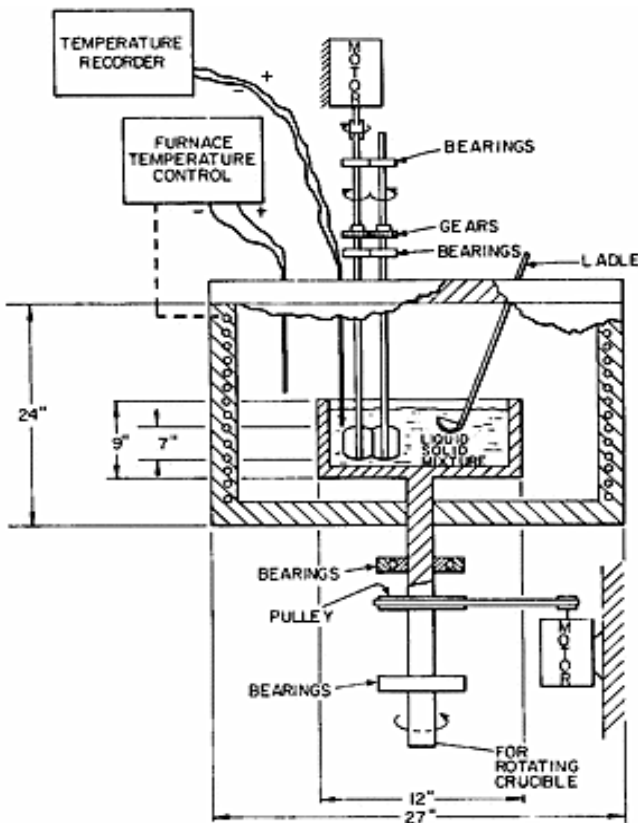
Fig. 2.16 Schematic representation of the Rheocasting method as used by Mehrabian et al[80].

The simplest process available to produce particulate reinforced metal matrix composites is the Vortex method.[120] The reinforcement is incorporated in the form of particles or whiskers into the vortex created during stirring of the molten metal matrix, the mechanical force produced by stirring breaks-up the particle clusters and disperses them within the matrix.

Rheocasting method, depicted in Fig. 2.16, (or Compocasting)[76,81,121,122], works under the same principle but the incorporation of the reinforcements takes place when the melt is in the semi-solid state (i.e. between the liquidus and solidus temperatures).

Semi-solid metal increases the apparent viscosity of the slurry that facilitates the incorporation of the reinforcements and prevents the particles from floating or settling. This problem is more pronounced

when introducing reinforcements with a different density and/or surface energy than the molten metal, as it is the case of the MWCNTs. [76,81,121,122]

Rashad et al[121] and Elshalakany et[92] al used the rheocasting technique to produce Al/MWCNTs and achieved an improvement of 34% and 50% in ultimate tensile strength, and 250% and 280% in elongation, respectively. However, no study using this method was used to examine the thermal conductivity.

2.4.3.2 ECAE

Equal channel angular extrusion (ECAE), depicted schematically in Fig.2.17, is primarily used to obtain high-density nanostructured materials with grains displaying a high degree of homogeneity in billets which have undergone a significant plastic deformation.

The shear deformation of the specimen occurs when the ingot is pressed in a special die through two channels with equal cross-section usually intersecting at an angle 2θ, as illustrated in Fig. 2.17. The repeated iterations of the ECAE procedure produce a systematic increase in deformation, leading to a successive decrease in grain size by the formation of a network of first low-angle and then high-angle grain boundaries.

As the number of iterations increases the angle ø between deformation direction (DD) and extrusion direction (ED) approaches 0°, resulting in an highly aligned microstructure. This feature enables the severe plastic deformation of not only plastic, but also difficult-to-deform metals and alloys. In this technique the intersection angle of the channels in the mould is of great importance. ECAE can, therefore be used to control the crystallographic texture of bulk structural nanostructured materials.[122–124]
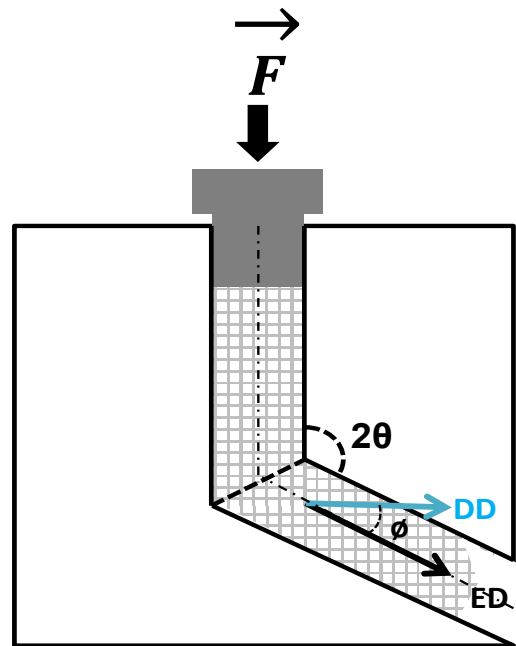
Fig. 2.17 Equal channel angular extrusion (ECAE) method schematic illustration.

As the billet dimensions are unchanged after extrusion, the process can be repeated to generate ultra-high strains. As the strain at each pass is accumulative the total strain can theoretically be unlimited. [122–124]

In powder metallurgy, methods that utilize shear deformation to induce deformation are useful to improve the metal composites density, break-down filler agglomerations and increase dispersion.[91]

2.5 Effective Thermal Conductivity of Composites

The thermal conductivity of metal matrix composites, especially that of particle reinforced composites, has been the primary focus of research for thermal management materials for electronic packaging due to their good thermophysical properties. Although there are many studies on these composites, their thermal conduction mechanisms have not been elucidated and are poorly understood.[125]

The pioneer of thermal conductivity studies for two-phase mixtures was Maxwell.[126] According to Maxwell's theory (mean-field scheme), the effective thermal conductivity of composites with a dispersed spherical phase can determined from:

$$K_c = \frac{K_m\left[2K_m + K_f^{eff} + 2\left(K_f^{eff} - K_m\right)v_f\right]}{2K_m + K_f^{eff} - \left(K_f^{eff} - K_m\right)v_f} \qquad \textbf{eq. (7)}$$

where K is the thermal conductivity, K_f^{eff} is the effective thermal conductivity of the filler, v_f is the volume fraction of filler, and the subscripts c, m, f stand for composite, matrix and filler, respectively.

Generally, it was found that the effective thermal conductivity was a function of the thermal conductivity, the geometric distribution and the volume fraction of each component, but independent of their dimensions. However, several studies indicated that the effective thermal conductivity of composites can be affected by a thermal barrier resistance (R_{Bd}) at the interface between the individual components. The R_{Bd} arises from the combination of a poor mechanical or chemical adherence at the interface and a mismatch in the CTE, such as that which occurs on the cooling of the composite from

the temperatures at which it was manufactured. Consequently, the experimental results tend to be slightly lower than those predicted by the theoretical models that do not take into account this phenomenon.[127]

However, for simplicity, in this study the models discussed assume no R_{BD} at the interface between the filler and matrix, and for this reason the interfacial thermal barrier is not further discussed. More information about R_{BD} can be found in the selected literature[39,73,128–131].

Many studies on this topic have been published after Maxwell's seminal work. For example, eq. 7 is also derived as a bound using a variational approach by Hashin and Shtrikman[132] which relates to the simple spherical-cap-on-a-sphere model of Kerner[133]. Hatta and Taya[134] also derived equation 8 from the Eshelby equivalent inclusion:

$$K_c = K_m \left[1 + \frac{v_f}{\frac{1}{3}(1-v_f)+\frac{K_m}{K_f-K_m}} \right] \qquad \text{eq. (8)}$$

These models have been developed and designed for small concentrations ($v_f < 1$) of second phase particles. Nevertheless, they are also in general, in good agreement with experiments containing higher filler volume fractions.[73,128] Eq. 8 is used in this study to predict the effect of MWCNT bundles on the thermal conductivity of the composites.

The Hatta-Taya Eshelby´s equivalent inclusion model[135,136] can also be used to predict the thermal conductivity of the composites reinforced with short fibres taking into account fibre geometry and orientation. This model is used in this study to predict the effect of the fibres/nanotubes orientation within the matrix on the composite thermal conductivity. For a 2D in-plane aligned short fibre composite, $K_{c,1}$ (see Fig. 2.19), the equation is:

$$K_{c,1} = K_m \left[1 + \frac{v_f}{S_{ij}(1-v_f)+\frac{K_m}{\left(K_f-K_m\right)}} \right] \qquad \text{eq. (9)}$$

where, the S tensor for the thermal conduction, S_{ij} (i and j = 1, 2 or 3) , as a function of fibre aspect ratio (β), is given by:[136]

$$S_{11} = S_{22} = \frac{\beta}{2(\beta^2-1)^{\frac{3}{2}}}\left[\beta(\beta^2-1)^{\frac{1}{2}} - cosh^{-1}\beta\right] \qquad \text{eq. (10)}$$

$$S_{33} = 1 - 2S_{11} \qquad \text{eq. (11)}$$
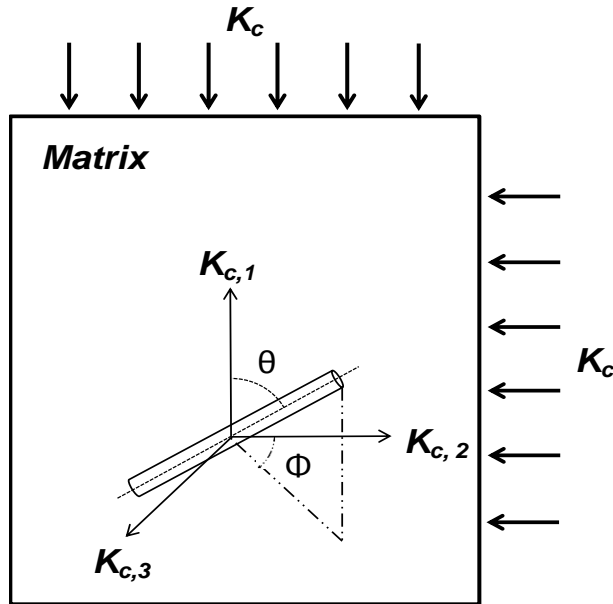
Fig. 2.18 Schematic representation of the relationship between thermal conductivity measurement direction and fibre orientation.

The $K_{c,1}$ assumes that the fibres in the plane 1-2 are all aligned in the thermal conductivity acquisition direction ($K_{c,1}$), in other words θ = 0° (unidirectional) (see Fig. 2.18).

For a 2D random short fibre reinforced composite, the in-plane conductivity ($K_{c,1,r}$) is given by:

$$K_{c,1,r} = K_m\left[1 + \frac{v_f(K_f-K_m)[(K_f-K_m)(S_{11}-S_{33})+2K_m]}{H}\right] \qquad \text{eq. (12)}$$

where H, is:

$$H = 2(K_f - K_m)^2(1 - v_f)S_{11}S_{33} + K_m(K_f - K_m)(2 - v_f)(S_{11} + S_{33})2K_m^2 \quad \textbf{eq. (13)}$$

The $K_{c,1,r}$ assumes that the fibres are aligned in the plane 1-2, parallel to the thermal conductivity measurement direction $(K_{c,1})$, where $\Phi = 0^0$ but the angle between the $K_{c,1}$ and the fibre orientation is random $0^0 \leq \theta \leq 90^0$.

Thermal conductivity along the out-of-plane direction $K_{c,2}$ and $K_{c,2,r}$ are given by eq. 9 and eq. 12, respectively, where S_{ij} is defined by equation eq. 11. $K_{c,2}$, simulates the thermal conductivity of the composite when the fibres are perpendicularly aligned to the thermal conductivity acquisition direction, where $\Phi = 90^0$ and $\theta = 90^0$. $K_{c,2,r}$ assumes $\Phi = 90^0$, however the fibres are randomly aligned in the plane 1-3, $0^0 \leq \theta \leq 90^0$.

MWCNTs have a very high aspect ratio and thermal conductivity. The models referred above are not very accurate for such conditions. Maxwell-Garnett effective medium approach (MG-EMA)[137] considers these conditions. Nevertheless, it also does take into account R_{BD}. For high aspect ratio fibres, over 100, as in the case for the MWCNTs, individually dispersed and randomly orientated in the matrix, the MG-EMA model can be derived as:

$$K_c = K_m \left[\frac{3\left(\frac{K_2}{K_m+1}\right) + v_f\left[2\left(\frac{K_2}{K_m-1}\right) + \left(\frac{K_2}{K_m+1}\right)\left(\frac{K_1}{K_m-1}\right)\right]}{3\left(\frac{K_2}{K_m+1}\right) - 2v_f\left(\frac{K_2}{K_m-1}\right)} \right] \qquad \textbf{eq. (14)}$$

where, due to the anisotropic nature of the MWCNTs, the thermal conductivity along the axis (in-plane) is denoted by K_1, whereas across the axis (out-of-plane) is denoted by K_2.

Nan et al[137] developed an extension of the MG-EMA model in order to improve the fit for materials where the filler has a much greater thermal conductivity than the matrix, i.e. as in the case of Al/MWCNT composites:

$$K_c = \left[\frac{3 + \left(\frac{v_f K_1}{K_m}\right)}{3 - 2v_f} \right] \qquad \textbf{eq. (15)}$$

The models discussed above are used throughout this study in order to predict the thermal conductivity of the composites processed via rheocasting and rheocasting+ECAE processing.

References

1.   Zweben Consulting. Available at: https://sites.google.com/site/zwebenconsulting/. (Accessed: 15th March 2016)

2.   Electronic Materials Handbook: Packaging. (ASM International, 1989).

3.   Zweben, C., Advanced Thermal Management Materials For Electronics and Photonics. Adv. Microelectron. 37, 14–19 (2010).

4.   Davim, J. P., Metal Matrix Composites: Materials, Manufacturing and Engineering. (Walter de Gruyter GmbH & Co KG, 2014).

5.   Lindsay, L., Broido, D. A. & Reinecke, T. L., First-Principles Determination of Ultrahigh Thermal Conductivity of Boron Arsenide: A Competitor for Diamond? Phys. Rev. Lett. 111, (2013).

6.   Dresselhaus, M. S., Dresselhaus, G. & Eklund, P. C., Science of Fullerenes and Carbon Nanotubes: Their Properties and Applications. (Academic Press, 1996).

7.   Balandin, A. A., Thermal Properties of Graphene and Nanostructured Carbon Materials. Nat. Mater. 10, 569–581 (2011).

8.   Kim, P., Shi, L., Majumdar, A. & McEuen, P. L., Thermal Transport Measurements of Individual Multiwalled Nanotubes. Phys. Rev. Lett. 87, (2001).

9.   Pop, E., Mann, D., Wang, Q., Goodson, K. & Dai, H., Thermal Conductance of an Individual Single-Wall Carbon Nanotube above Room Temperature. Nano Lett. 6, 96–100 (2006).

10.   Allotropes of carbon. Wikipedia, the free encyclopedia (2016).

11.   Huang, X., Fabrication and Properties of Carbon Fibers. Materials 2, 2369–2403 (2009).

12.   Minus, M. & Kumar, S., The Processing, Properties, and Structure of Carbon Fibers. Jom 57, 52–58 (2005).

13.   Chung, D. D. L., Carbon Fiber Composites. (Butterworth-Heinemann, 1994).

14.   Wang, L. et al., Effects of Positive and Negative Stretching on the Structure and Properties of Polyacrylonitrile Fibers in the Pre-Oxidation Process. Carbon Lett. 12, 107–111 (2011).

15.   Zweben, C., Advances in Composite Materials for Thermal Management in Electronic Packaging. Jom 50, 47–51 (1998).

16.   Kroto, H. W., Heath, J. R., O'Brien, S. C., Curl, R. F. & Smalley, R. E., C60: Buckminsterfullerene. Nature 318, 162–163 (1985).

17.   Iijima, S., Helical Microtubules of Graphitic Carbon. Nature 354, 56–58 (1991).

18.   Bacon, R. Growth, Structure, and Properties of Graphite Whiskers. J. Appl. Phys. 31, 283 (1960).

19.   Sinnott, S. B. & Andrews, R. Carbon Nanotubes: Synthesis, Properties, and Applications. Crit. Rev. Solid State Mater. Sci. 26, 145–249 (2001).

20.   Rahmandoust, M. & Ayatollahi, M. R., Characterization of Carbon Nanotube Based Composites under Consideration of Defects. (Springer, 2015).

21.   Dresselhaus, M. S., Dresselhaus, G. & Avouris, P., Carbon Nanotubes: Synthesis, Structure, Properties, and Applications. (Springer Science & Business Media, 2003).

22.   Dai, H. Carbon Nanotubes: Synthesis, Integration, and Properties. Acc. Chem. Res. 35, 1035–1044 (2002).

23.   Appenzeller, J., Joselevich, E. & Hönlein, W. Carbon Nanotubes for Data Processing. Nanoelectron. Inf. Technol. Wiley-VCH (2003).

24.   Purifying Carbon Nanotubes for Electronic Devices | Electronics360. Available at: http://electronics360.globalspec.com/article/7186/purifying-carbon-nanotubes-for-electronic-devices. (Accessed: 23rd August 2016)

25.   Endo, M., Iijima, S. & Dresselhaus, M. S., Carbon Nanotubes. (Elsevier, 2013).

26.   Saito, R., Dresselhaus, G. & Dresselhaus, M. S., Physical Properties of Carbon Nanotubes. (World Scientific, 1998).

27.   Collins, P. G., Defects and Disorder in Carbon Nanotubes. Oxf. Handb. Nanosci. Technol. Front. Adv. (2010).

28.   Bom, D. et al., Thermogravimetric Analysis of the Oxidation of Multiwalled Carbon Nanotubes: Evidence for the Role of Defect Sites in Carbon Nanotube Chemistry. Nano Lett. 2, 615–619 (2002).

29.   DiLeo, R. A., Landi, B. J. & Raffaelle, R. P., Purity Assessment of Multiwalled Carbon Nanotubes by Raman spectroscopy. J. Appl. Phys. 101, 64307 (2007).

30.   Lehman, J. H., Terrones, M., Mansfield, E., Hurst, K. E. & Meunier, V., Evaluating the Characteristics of Multiwall Carbon Nanotubes. Carbon 49, 2581–2602 (2011).

31.   Roche, S., Triozon, F., Rubio, A. & Mayou, D., Conduction mMechanisms and Magnetotransport in Multiwalled Carbon Nanotubes. Phys. Rev. B 64, (2001).

32.   Zhou, O. et al., Defects in Carbon Nanostructures. Science 263, 1744–1747 (1994).

33.   Hou, P.-X., Liu, C. & Cheng, H.-M., Purification of Carbon Nanotubes. Carbon 46, 2003–2025 (2008).

34.   Andrews, R., Jacques, D., Qian, D. & Dickey, E. C., Purification and Structural Annealing of Multiwalled Carbon Nanotubes at Graphitization Temperatures. Carbon 39, 1681–1687 (2001).

35.   Bifano, M. F. P., Park, J., Kaul, P. B., Roy, A. K. & Prakash, V., Effects of Heat Treatment and Contact Resistance on the Thermal Conductivity of Individual Multiwalled Carbon Nanotubes using a Wollaston Wire Thermal Probe. J. Appl. Phys. 111, 54321 (2012).

36.   Mahajan, A., Kingon, A., Kukovecz, Á., Konya, Z. & Vilarinho, P. M., Studies on the Thermal Decomposition of Multiwall Carbon Nanotubes Under Different Atmospheres. Mater. Lett. 90, 165–168 (2013).

37.   Dillon, A. C. et al., A Simple and Complete Purification of Single-Walled Carbon Nanotube Materials. Adv. Mater. 11, 1354–1358 (1999).

38.   Clarke, D. R. & Phillpot, S. R., Thermal Transport in Nanostructured Materials.

39.   Tritt, T. M., Thermal Conductivity: Theory, Properties, and Applications. (Springer Science & Business Media, 2006).

40.   Callaway, J., Model for Lattice Thermal Conductivity at Low Temperatures. Phys. Rev. 113, 1046–1051 (1959).

41.   Balandin, A. A. et al., Superior Thermal Conductivity of Single-Layer Graphene. Nano Lett. 8, 902–907 (2008).

42.   Ghosh, S. et al., Extremely High Thermal Conductivity of Graphene: Prospects for Thermal Management Applications in Nanoelectronic Circuits. Appl. Phys. Lett. 92, 151911 (2008).

43.   Tjong, S. C., Recent Progress in the Development and Properties of Novel Metal Matrix Nanocomposites Reinforced with Carbon Nanotubes and Graphene Nanosheets. Mater. Sci. Eng. R Rep. 74, 281–350 (2013).

44.   Marconnet, A. M., Panzer, M. A. & Goodson, K. E., Thermal Conduction Phenomena in Carbon Nanotubes and Related Nanostructured Materials. Rev. Mod. Phys. 85, 1295–1326 (2013).

45.   Hone, J. in Carbon Nanotubes 273–286 (Springer, 2001).

46.   Zhang, W. et al., Chirality Dependence of the Thermal Conductivity of Carbon Nanotubes. Nanotechnology 15, 936–939 (2004).

47.   Zhang, G. & Li, B., Thermal Conductivity of Nanotubes Revisited: Effects of Chirality, Isotope Impurity, Tube Length, and Temperature. J. Chem. Phys. 123, 114714 (2005).

48.   Choi, T.-Y., Poulikakos, D., Tharian, J. & Sennhauser, U., Measurement of the Thermal Conductivity of Individual Carbon Nanotubes by the Four-Point Three-ω Method. Nano Lett. 6, 1589–1593 (2006).

49.   Pettes, M. T. & Shi, L., Thermal and Structural Characterizations of Individual Single-, Double-, and Multi-Walled Carbon Nanotubes. Adv. Funct. Mater. 19, 3918–3925 (2009).

50.   Song, P. C., Liu, C. H. & Fan, S. S., Improving the Thermal Conductivity of Nanocomposites by Increasing the Length Efficiency of Loading Carbon Nanotubes. Appl. Phys. Lett. 88, 153111 (2006).

51.   Han, Z. & Fina, A., Thermal Conductivity of Carbon Nanotubes and Their Polymer Nanocomposites: A Review. Prog. Polym. Sci. 36, 914–944 (2011).

52.   Aliev, A. E., Lima, M. H., Silverman, E. M. & Baughman, R. H., Thermal Conductivity of Multi-Walled Carbon Nanotube Sheets: Radiation Losses and Quenching of Phonon Modes. Nanotechnology 21, 35709 (2010).

53.   Dames, C. et al., A Hot-Wire Probe for Thermal Measurements of Nanowires and Nanotubes Inside a Transmission Electron Microscope. Rev. Sci. Instrum. 78, 104903 (2007).

54.   Cahill, D. G., Goodson, K. & Majumdar, A., Thermometry and Thermal Transport in Micro/Nanoscale Solid-State Devices and Structures. J. Heat Transf. 124, 223 (2002).

55.   Choi, T. Y., Poulikakos, D., Tharian, J. & Sennhauser, U., Measurement of Thermal Conductivity of Individual Multiwalled Carbon Nanotubes by the 3-ω Method. Appl. Phys. Lett. 87, 13108 (2005).

56.   Hsu, I.-K. et al., Optical Absorption and Thermal Transport of Individual Suspended Carbon Nanotube Bundles. Nano Lett. 9, 590–594 (2009).

57.   Li, Q., Liu, C., Wang, X. & Fan, S., Measuring the Thermal Conductivity of Individual Carbon Nanotubes by the Raman Shift Method. Nanotechnology 20, 145702 (2009).

58.   Samani, M. K. et al., Thermal Conductivity of Individual Multiwalled Carbon Nanotubes. Int. J. Therm. Sci. 62, 40–43 (2012).

59.   Yang, D. J. et al., Thermal Conductivity of Multiwalled Carbon Nanotubes. Phys. Rev. B 66, (2002).

60.   Majumdar, A., Scanning Thermal Microscopy. Annu. Rev. Mater. Sci. 29, 505–585 (1999).

61.   Zhou, J. & Shi, L., Scanning Thermal Microscopy of Carbon Nanotube Electronic Devices. In Semiconductor Thermal Measurement and Management IEEE Twenty First Annual IEEE Symposium, 2005. 303–306 (IEEE, 2005).

62.   Fujii, M. et al., Measuring the Thermal Conductivity of a Single Carbon Nanotube. Phys. Rev. Lett. 95, (2005).

63.   Chiu, H.-Y. et al., Ballistic Phonon Thermal Transport in Multiwalled Carbon Nanotubes. Phys. Rev. Lett. 95, (2005).

64.   Xie, H., Cai, A. & Wang, X., Thermal Diffusivity and Conductivity of Multiwalled Carbon Nanotube Arrays. Phys. Lett. A 369, 120–123 (2007).

65.   Cahill, D. G. et al., Nanoscale ThermalTransport. J. Appl. Phys. 93, 793 (2003).

66.   Yi, W., Lu, L., Dian-lin, Z., Pan, Z. W. & Xie, S. S., Linear Specific Heat of Carbon Nanotubes. Phys. Rev. B 59, R9015–R9018 (1999).

67.   Jin, R. et al., The Effect of Annealing on the Electrical and Thermal Transport Properties of Macroscopic Bundles of Long Multi-Wall Carbon Nanotubes. Phys. B Condens. Matter 388, 326–330 (2007).

68.   Chawla, N., Metal Matrix Composites. (Springer, 2006).

69.   Clyne, T. W., An Introduction to Metal Matrix Composites. (New York, NY, USA : Cambridge University Press, 1993).

70.   Palucka, T. & Bensaude-Vincent, B., Composites Overview. Available at: http://authors.library.caltech.edu/5456/1/hrst.mit.edu/hrs/materials/public/composites/Composites_Overview.htm. (Accessed: 19th February 2015)

71.   Cayron, C., TEM Study of Interfacial Reactions and Precipitation Mechanisms in Al_2O_3 Short Fiber in High Volume Fraction SiC Particle Reinforced Al-4Cu-1Mg-0.5Ag Squeeze-Cast Composites. (Swiss Federal Institure of Technology Lausanne (EPFL), 2001).

72.   Evans, A., San Marchi, C. & Mortensen, A., Metal Matrix Composites in Industry. (Springer US, 2003).

73.   Kida, M., HIgh-Temperature Wettability and Thermal Conductivity of Aluminium Nitride Reinforced Metal Matrix composites. (École Polytechnique Fédérale de Lausanne, 2008).

74.   Ejiofor, J. U. & Reddy, R. G., Developments in the Processing and Properties of Particulate Al-Si Composites. Jom 49, 31–37 (1997).

75.   Evans, A., San Marchi, C. & Mortensen, A., Metal Matrix Composites in Industry. (Springer US, 2003).

76.   Garg, H. K., Verma, K., Manna, A. & Kumar, R., Hybrid Metal Matrix Composites and Further Improvement in Their Machinability-A Review. Int. J. Latest Res. Sci. Technol. 1, 36–44 (2012).

77.   Ibrahim, I. A., Mohamed, F. A. & Lavernia, E. J., Particulate Reinforced Metal Matrix Composites - A Review. J. Mater. Sci. 26, 1137–1156 (1991).

78.   Lubin, G. & Peters, S. T., Handbook of Composites. (Chapman & Hall, 1998).

79.   Mehrabian, R., Riek, R. G. & Flemings, M., Preparation and Casting of Metal-Particulate Non-Metal Composites. Metall. Trans. 5, 1899–1905 (1974).

80.   Miserez, A., Müller, R., Rossoll, A., Weber, L. & Mortensen, A., Particle Reinforced Metals of High Ceramic Content. Mater. Sci. Eng. A 387–389, 822–831 (2004).

81.   Hone, J., Whitney, M., Piskoti, C. & Zettl, A., Thermal Conductivity of Single-Walled Carbon Nanotubes. Phys. Rev. B 59, R2514 (1999).

82.   Mayhew, E. & Prakash, V., Thermal Conductivity of Individual Carbon Nanofibers. Carbon 62, 493–500 (2013).

83.   Bakshi, S. R., Lahiri, D. & Agarwal, A., Carbon Nanotube Reinforced Metal Matrix Composites - A Review. Int. Mater. Rev. 55, 41–64 (2010).

84.   Neubauer, E., Kitzmantel, M., Hulman, M. & Angerer, P., Potential and Challenges of Metal Matrix Composites Reinforced with Carbon Nanofibers and Carbon Nanotubes. Compos. Sci. Technol. 70, 2228–2236 (2010).

85.   Bakshi, S. R., Patel, R. R. & Agarwal, A., Thermal Conductivity of Carbon Nanotube Reinforced Aluminum Composites: A Multi-Scale Study using Object Oriented Finite Element Method. Comput. Mater. Sci. 50, 419–428 (2010).

86.   Cho, S. et al., Multiwalled Carbon Nanotubes as a Contributing Reinforcement Phase for the Improvement of Thermal Conductivity in Copper Matrix Composites. Scr. Mater. 63, 375–378 (2010).

87.   Oh, S.-I. et al., Fabrication of Carbon Nanofiber Reinforced Aluminum Alloy Nanocomposites by a Liquid Process. J. Alloys Compd. 542, 111–117 (2012).

88.   Chang, S.-W., Nair, A. K. & Buehler, M. J., Geometry and Temperature Effects of the Interfacial Thermal Conductance in Copper- and Nickel-graphene Nanocomposites. J. Phys. Condens. Matter 24, 245301 (2012).

89.   Agarwal, A., Bakshi, S. R. & Lahiri, D., Carbon Nanotubes: Reinforced Metal Matrix Composites. (CRC Press, 2016).

90. Lim, J.-Y. et al., Effects of CNF Dispersion on Mechanical Properties of CNF Reinforced A7xxx Nanocomposites. Mater. Sci. Eng. A 556, 337–342 (2012).

91. Abbasipour, B., Niroumand, B. & Monir Vaghefi, S. M., Compocasting of A356-CNT Composite. Trans. Nonferrous Met. Soc. China 20, 1561–1566 (2010).

92. Elshalakany, A. B., Osman, T. A., Khattab, A., Azzam, B. & Zaki, M., Microstructure and Mechanical Properties of MWCNTs Reinforced A356 Aluminum Alloys Cast Nanocomposites Fabricated by Using a Combination of Rheocasting and Squeeze Casting Techniques. J. Nanomater. 2014, 1–14 (2014).

93. Miranda, A. et al., Study of Mechanical Properties of an LM24 Composite Alloy Reinforced with Cu-CNT Nanofillers, Processed Using Ultrasonic Cavitation. Mater. Sci. Forum 765, 245–249 (2013).

94. Donthamsetty, S., Damera, N. R. & Jain, P. K., Ultrasonic Cavitation Assisted Fabrication and Characterization of A356 Metal Matrix Nanocomposite Reinforced with SiC, B_4C, CNTs. Asian Int. J. Sci. Technol. Prod. Manuf. Eng. 2, 27–34 (2009).

95. Edtmaier, C., Steck, T., Hula, R. C., Pambaguian, L. & Hepp, F., Thermo-Physical Properties and TEM Analysis of Silver Based MMCs utilizing Metallized Multiwall-Carbon Nanotubes. Compos. Sci. Technol. 70, 783–788 (2010).

96. Kwon, H., Estili, M., Takagi, K., Miyazaki, T. & Kawasaki, A., Combination of Hot Extrusion and Spark Plasma Sintering for Producing Carbon Nanotube Reinforced Aluminum Matrix Composites. Carbon 47, 570–577 (2009).

97. Shin, S., Choi, H. & Bae, D., Electrical and Thermal Conductivities of Aluminum-Based Composites Containing Multi-Walled Carbon Nanotubes. J. Compos. Mater. 47, 2249–2256 (2013).

98. Izadi, H. & Gerlich, A. P., Distribution and Stability of Carbon Nanotubes During Multi-Pass Friction Stir Processing of Carbon Nanotube/Aluminum Composites. Carbon 50, 4744–4749 (2012).

99. Lim, D. K., Shibayanagi, T. & Gerlich, A. P., Synthesis of Multi-Walled CNT Reinforced Aluminium Alloy Composite Via Friction Stir Processing. Mater. Sci. Eng. A 507, 194–199 (2009).

100. Salas, W., Alba-Baena, N. G. & Murr, L. E., Explosive Shock-Wave Consolidation of Aluminum Powder/Carbon Nanotube Aggregate Mixtures: Optical and Electron Metallography. Metall. Mater. Trans. A 38, 2928–2935 (2007).

101. Noguchi, T. et al., Carbon Nanotube/Aluminium Composites with Uniform Dispersion. Mater. Trans. 45, 602–604 (2004).

102. Barekar, N. et al., Processing of Aluminum-Graphite Particulate Metal Matrix Composites by Advanced Shear Technology. J. Mater. Eng. Perform. 18, 1230–1240 (2009).

103. Rohatgi, P. & Schultz, B., Lightweight Metal Matrix Nanocomposites-Stretching the Boundaries of Metals. Mater. Matters 2, 16–20 (2007).

104. Esawi, A. M. K., Morsi, K., Sayed, A., Taher, M. & Lanka, S., Effect of Carbon Nanotube (CNT) Content on the Mechanical Properties of CNT-Reinforced Aluminium Composites. Compos. Sci. Technol. 70, 2237–2241 (2010).

105. Wang, F., Arai, S. & Endo, M., The Preparation of Multi-Walled Carbon Nanotubes with a Ni–P Coating by an Electroless Deposition Process. Carbon 43, 1716–1721 (2005).

106. Xing, H., Sun, L., Song, G., Gou, J. & Hao, Y. W., Surface Coating of Carbon Nanofibers/Nanotubes by Electrodeposition for Multifunctionalization. Nanotechnology 19, 25704 (2008).

107. Chen, C.-Y., Lin, K.-Y., Tsai, W.-T., Chang, J.-K. & Tseng, C.-M., Electroless Deposition of Ni Nanoparticles on Carbon Nanotubes with the Aid of Supercritical CO_2 Fluid and a Synergistic Hydrogen Storage Property of the Composite. Int. J. Hydrog. Energy 35, 5490–5497 (2010).

108. Chen, X., Xia, J., Peng, J., Li, W. & Xie, S., Carbon-Nanotube Metal-Matrix Composites Prepared by Electroless Plating. Compos. Sci. Technol. 60, 301–306 (2000).

109. Chin, K. C. et al., Gold and Silver Coated Carbon Nanotubes: An Improved Broad-Band Optical Limiter. Chem. Phys. Lett. 409, 85–88 (2005).

110. Liu, Z.-J. et al., A simple Method for Coating Carbon Nanotubes with Co–B Amorphous Alloy. Mater. Lett. 57, 1339–1344 (2003).

111. Che, J., Çagin, T. & III, W. A. G., Thermal Conductivity of Carbon Nanotubes. Nanotechnology 11, 65 (2000).

112. Pham, Q., Jeong, Y. G., Hong, S. H. & Kim, H. S., Equal Channel Angular Pressing of Carbon Nanotube Reinforced Metal Matrix Nanocomposites. Key Eng. Mater. 326–328, 325–328 (2006).

113. Wu, J., Zhang, H., Zhang, Y. & Wang, X., Mechanical and Thermal Properties of Carbon Nanotube/Aluminum Composites Consolidated by Spark Plasma Sintering. Mater. Des. 41, 344–348 (2012).

114. Chai, G. & Chen, Q., Characterization Study of the Thermal Conductivity of Carbon Nanotube Copper Nanocomposites. J. Compos. Mater. 44, 2863–2873 (2010).

115. Muhsan, A. S., Ahmad, F., Mohamed, N. M., Yusoff, P. S. M. M. B. & Raza, M. R., Effect of CNTs Dispersion on the Thermal and Mechanical Properties of Cu/CNTs Nanocomposites. AIP Conf. Proc. 1621, 643–649 (2014).

116. Chu, K. et al., Thermal Properties of Carbon Nanotube–Copper Composites for Thermal Management Applications. Nanoscale Res. Lett. 5, 868–874 (2010).

117. Chu, K. et al., Fabrication and Effective Thermal Conductivity of Multi-Walled Carbon Nanotubes Reinforced Cu Matrix Composites for Heat Sink Applications. Compos. Sci. Technol. 70, 298–304 (2010).

118. Rohatgi, P. K., Asthana, R. & Das, S., Solidification, Structures, and Properties of Cast Metal-Ceramic Particle Composites. Int. Met. Rev. 31, 115–139 (1986).

119. Fundamentals of Metal-Matrix Composites. (Butterworth-Heinemann, 1993).

120. Balasubramanian, P. K., Srinivasa Rao, P., Pai, B. C., Satyanarayana, K. G. & Rohatgi, P. K., Casting and Extrusion Characteristics of an Al-Zn-Mg Alloy Composite Containing TiO_2 Dispersions. Compos. Sci. Technol. 39, 245–259 (1990).

121. Rashad, R. M., Awadallah, O. M. & Wifi, A. S., Effect of MWCNTs Content on the Characteristics of A356 Nanocomposite. J. Achiev. Mater. Manuf. Eng. 2, 74–80 (2013).

122. Valiev, R., Nanostructuring of Metals by Severe Plastic Deformation for Advanced Properties. Nat. Mater. 3, 511–516 (2004).

123. Prokofiev, E. A., Jorge, A. M., Botta, W. J. & Valiev, R. Z. In Comprehensive Materials Processing 187–209 (Elsevier, 2014).

124. Valiev, R. Z. et al., Producing Bulk Ultrafine-Grained Materials by Severe Plastic Deformation: Ten Years Later. JOM 68, 1216–1226 (2016).

125. Zhang, Y., Shen, Z. & Tong, Z., Thermal Conductivity and Interfacial Thermal Barrier Resistance of the Particle Reinforced Metal Matrix Composites. In Electronic Packaging Technology, 2007. ICEPT 2007. 8th International Conference on 1–4 (IEEE, 2007).

126. Maxwell, J. C., A Treatise on Electricity and Magnetism. (Clarendon Press, 1873).

127. Hasselman, D. P. H. & Johnson, L. F., Effective Thermal Conductivity of Composites with Interfacial Thermal Barrier Resistance. J. Compos. Mater. 21, 508–515 (1987).

128. Pietrak, K. & Wisniewski, T. S., A Review of Models for Effective Thermal Conductivity of Composite Materials. J. Power Technol. 95, 14 (2015).

129. Swartz, E. T. & Pohl, R. O., Thermal Boundary Resistance. Rev. Mod. Phys. 61, 605–668 (1989).

130. Nan, C.-W., Birringer, R., Clarke, D. R. & Gleiter, H., Effective Thermal Conductivity of Particulate Composites with Interfacial Thermal Resistance. J. Appl. Phys. 81, 6692 (1997).

131. Little, W. A., The Transport of Heat Between Dissimilar Solids at Low Temperatures. Can. J. Phys. 37, 334–349 (1959).

132. Hashin, Z. & Shtrikman, S. , A Variational Approach to the Theory of the Effective Magnetic Permeability of Multiphase Materials. J. Appl. Phys. 33, 3125–3131 (1962).

133. Kerner, E. H., The Elastic and Thermo-elastic Properties of Composite Media. Proc. Phys. Soc. Sect. B 69, 808 (1956).

134. Hiroshi, H. & Minoru, T., Equivalent Inclusion Method for Steady State Heat Conduction in Composites. Int. J. Eng. Sci. 24, 1159–1172 (1986).

135. Hatta, H., Taya, M., Kulacki, F. A. & Harder, J. F., Thermal Diffusivities of Composites with Various Types of Filler. J. Compos. Mater. 26, 612–625 (1992).

136. Hatta, H. & Taya, M. Effective Thermal Conductivity of a Misoriented Short Fiber Composite. J. Appl. Phys. 58, 2478 (1985).

137. Nan, C.-W., Shi, Z. & Lin, Y., A Simple Model for Thermal Conductivity of Carbon Nanotube-Based Composites. Chem. Phys. Lett. 375, 666–669 (2003).

Chapter 3

Experimental Techniques and Procedures

3.1 Chapter Outline

The experimental methods relevant to this study are described in this chapter. In Section 3.2, the materials, carbon fibres (CFs), multi-walled carbon nanotubes (MWCNTs) and the metal matrix utilized with their respective properties are described. Section 3.3 gives a detailed description of the aluminium matrix composites (AMCs), both Al/Cu-CFs and Al/MWCNTs, with their associated processing methods steps and parameters. Section 3.4, describes briefly the microscopy and spectroscopy techniques required in the study and respective sample preparation for each technique. Section 3.5 describes the methods utilized to acquire the experimental thermal conductivity of individual nanotubes and the composites. The parameters used to predict the theoretical thermal conductivities calculated using the models given in Chapter 2, Section 2.5 are also described.

3.2 Materials

In this section, the materials utilized in the study and their respective properties are described.

3.2.1 Matrix

In processing of aluminium matrix composites, the alloy selection is of major importance due to the fact it has to be suitable for semi-solid metal (SSM) processing, which requires an alloy with a large freezing range (ΔT_{L-S}). In addition it should also be alloyed with an element that decreases the Al surface energy in order to facilitate wettability and incorporation of the fillers within the matrix.

In this study, an Al3Mg alloy was used. Commercially pure (CP) Al LM0 (BS 1490:1988) was purchased from NORTON ALUMINIUM (United Kingdom) and its nominal composition and physical properties are given in Table 3.1 and 3.2, respectively. The Al was alloyed with an addition of 3 wt.% of commercially pure Mg purchased from MAGONTEC (Germany). The nominal chemical composition of the Mg is given in Table 3.3 and the typical physical and mechanical properties of unalloyed Mg are shown in Table 3.4.

Table 3.1. Nominal chemical composition of LM 0 [wt.%] BS 1490:1988 [1]

	Cu	Mg	Si	Fe	Mn	Ni	Zn	Pb	Sn	Al	others
Max.	0.03	0.03	0.30	0.40	0.03	0.03	0.07	0.03	0.03	99.5	0.50

Table 3.2. LM0 physical properties as given by the manufacturer.

Thermal Expansion α (per ºC 20-100 ºC)	Thermal Conductivity K (W m^{-1}K^{-1} at 100 ºC)	Density ρ (g cm^{-3})	Freezing Range (ºC)	0.2% Proof Stress $R_{p0.2}$ (N/mm^2)	Young's Modulus E (N/mm^2)
0.000024	214	2.7	657-643	30	69

Table 3.3. Nominal chemical composition of commercially pure Mg [wt.%] EN10204 3.1

	Al	Zn	Mn	Si	Fe	Cu	Ni	ppm Be
Max.	0.04	0.00	0.02	0.013	0.002	0.001	<0.001	1

Table 3.4. Typical physical and mechanical properties of unalloyed sand casted Mg at 20ºC [2].

Thermal Expansion α, (per ºC 20-100 ºC)	Thermal Conductivity K, (Wm^{-1}K^{-1} at 20ºC)	Density ρ (g cm^{-3})	Melting Point T_m (ºC)	0.2% Proof Stress $R_{p0.2}$ (N/mm^2)	Young's Modulus E, (N/mm^2)
0.000024	154.1	1.738	650	21	40

3.2.2 Fillers

The ever increasing demand for novel heat dissipation materials with superior thermal conductivity, driven by the electronics and lighting industry, for high temperature applications such as high power LEDs is the driving force of this study. Therefore, this study explores the possibility of improving the thermal properties of Al alloys, namely thermal conductivity (K), for thermal management applications. Some carbon (C) based materials exhibit high thermal conductivity, such as carbon fibres (CFs) and multi-walled carbon nanotubes (MWCNTs). As a result, these two materials were acquired to be embedded within the Al3Mg matrix in order to investigate their effect on the composites thermal conductivity. In this section, the details of the mechanical and physical properties of the fillers as provided by the manufacturers are outlined.

3.2.2.1 Carbon Fibres

Mesophase pitch-based, short CFs designated as Raheama R-A201 purchased from Teijin Limited, Japan[3], were the selected CF filler. According to the manufacturer the CFs have an average diameter of 8 µm, length of 50 µm and possess a thermal conductivity that ranges between 500 to 600 W m^{-1} K^{-1} (data given in Table 3.5). The fibres are ideal to be used in the production of heat-radiation components of almost any shape. The thermal expansion coefficient is as low as that of some ceramics, so materials produced using the fibres have exceptional dimensional stability and high electrical conductivity[3]. The fibres were coated with Cu via electroless deposition at the Korean Institute of Industrial Technology (KITECH), Incheon, South Korea.

Table 3.5. Mesophase pitch CFs designation and properties according to the suppliers.

Thermal Conductivity K (W m^{-1} K^{-1})	diameter d (μm)	Length (μm)	Young's Modulus E (N/mm2)	Tensile Strength UTS (N/mm^2)
500-600	~8	50	NP	NP

NP – Not Provided

3.2.2.2 Multi-walled Carbon Nanotubes

Multi-walled carbon nanotubes (MWCNTs) processed via combustion chemical vapour deposition (CCVD) and purchased from Applied Carbon Nano Technology Co., Ltd., Korea, defined as source 1 (nomenclature - S1) was selected to be added to the Al-3Mg alloy. Two other sources (S2 and S3) of MWCNTs were studied, however, these were only used for the quality comparison studies with the S1 filler and therefore were not used as filler due to the restricted amount of material acquired.

Source 2 (S2) MWCNTs were also synthesised by CCVD and provided by EMFUTUR, Spain, whilst source 3 (S3) are vertically aligned multi-walled carbon nanotubes (VAMWCNTs) synthetized via the aerosol assisted chemical vapour deposition (ACVD) method, supplied by Dr. Seyyed Shayan Meysami from the Department of Materials of Oxford University, UK. The mechanical and physical properties of the S1, S2 and S3 MWCNTs studied are given in Table 3.6.

Table 3.6. MWCNTs designation and properties according to the suppliers.

Source	Description	Thermal Conductivity K (Wm^{-1}K^{-1})	Purity (wt.%)	Outer diameter d_o (nm)	Length l (μm)	Young's Modulus E (N/mm^2)	Tensile Strength UTS (N/mm^2)
S1	CCVD MWCNTs	2000	85-97	5-20	10	1.28×10^6	0.1×10^6
S2	CCVD MWCNTS	2000	95	5-20	1-10	NP	NP
S3	ACVD VAMWCNTS	NP	NP	NP	NP	NP	NP

NP – Not provided.

Previously, in Chapter 2 Subsection 2.4.2.2, the challenges of introducing MWCNTs into the Al melt were addressed, such as, negligible wettability and large variations in density between matrix and fillers.

To facilitate the addition of the filler to the matrix, the S1 MWCNTs were mixed with pure Cu powder, 99.9 wt.% with an average particle size of 45 μm purchased from Kojundo Chemical Laboratory Co., Ltd., Japan. The mixing process was performed by means of a high energy ball milling technique at the Korean Institute of Industrial Technology (KITECH), Incheon, South Korea. This resulted in Cu-10MWCNTs composite powder also referred in this study as Cu10S1 with a mesh size of 325 μm, comprised of 90 wt.% pure Cu mixed with 10 wt.% of MWCNTs. The powder flakes had a size distribution ranging from ~1-100 μm.

3.3 Composites Processing

In this section (3.3) the processing of the matrix alloy and the aluminium matrix composites reinforced with multi-walled carbon nanotubes and carbon fibres is described. The composites were processed via rheocasting. However, carbon based materials such as MWCNTs and CFs show anisotropic thermal behaviour and the rheocasting method distributes the filler randomly within the matrix, therefore it is necessary to align the fillers to harness their full potential and to achieve this, an equal channel angular extrusion (ECAE) post processing method is utilized.

3.3.1 Rheocasting

Rheocasting, one of the simplest processes available to produce particulate reinforced metal matrix composites was used to produce the AMCs in this study. The principle of the processing methods is described in Chapter 2 Subsection 2.4.3.1.

In this study, in order to aid introduction to the matrix, two different modified fillers were produced, labelled as C (Cu-CFs) and M (containing a Cu10wt.%MWCNT filler denoted as Cu10S1). For the MWCNTs composite powders the nanofillers are from source 1, (S1 MWCNTs). The designation of the modified fillers, processing conditions and parameters are given in Tables 3.7 and 3.8. The schematic representation of the rheocasting set-up used in this study is shown in Fig. 3.1.

In order to process the composites, an aluminium–magnesium (Al3Mg) based alloy was selected as the matrix. For each composite, 2500 g of Al3Mg containing 2427.2 g of

commercial pure Al LM0 (see composition in Table 3.1) and 72.8 g of commercially pure Mg (Table 3.3) was placed in an A7 salamander clay graphite bonded crucible and transferred to a Carbolite resistance furnace at 700 ℃. The modified fillers were weighed and placed in containers in a fume cabinet; FUMAIR LTD., Herts, UK, equipped with a nanoparticles filter. The modified fillers were then placed in an ELITE box furnace, Italy, at 100 ℃ in an argon atmosphere for 2 hours to remove moisture and avoid Cu oxidation.

Table 3.7 Composites nomenclatures with respective materials and processing conditions.

Sample	Material	Condition	Cu-CFs (g)	Cu10S1 (g)	MWCNTs (g)	Fillers (wt.%)
C0	Al3Mg	Rheocasting	_ _ _	_ _ _	_ _ _	_ _ _
C0.5	Al3Mg + Cu-CFs	Rheocasting	12.5	_ _ _	_ _ _	0.5
C1	Al3Mg + Cu-CFs	Rheocasting	25	_ _ _	_ _ _	1
C1.5	Al3Mg + Cu-CFs	Rheocasting + ECAE	37.5	_ _ _	_ _ _	1.5
C2	Al3Mg + Cu-CFs	Rheocasting	50	_ _ _	_ _ _	2
M0	Al3Mg	Rheocasting	_ _ _	_ _ _	_ _ _	_ _ _
M1	Al3Mg + Cu- MWCNTs	Rheocasting + ECAE	_ _ _	75	7.5	0.3
M2	Al3Mg + Cu-MWCNTs	Rheocasting	_ _ _	87.5	8.75	0.35

Table 3.8 Composites processing parameters.

Alloy	Filler heat treatment	Mixing				Heating Belt	Cover Gas
T (℃)	T (℃)	T (℃)	Speed (rpm)	Time (s)	Feeding rate (g/min)	T (℃)	
700	100 / in Argon	633	1200	600	~ 15	550	Argon

The fillers were then placed in an ELITE electric resistance box furnace at 100 ℃ in an argon (Ar) atmosphere for 2 hours to remove moisture whilst avoiding Cu oxidation.

Once the alloy was melted, the crucible was transferred to a heating belt (a heating element that wrapped around the crucible) at 550 ℃, and Ar gas was immediately purged throughout the furnace to protect the melt from forming Al oxides. Thermocouples were then also submerged in the melt to record the temperature.

With increasing melt viscosity (increasing of solid fraction (f_s)) in a semi-solid metal, the flow induced by conventional turbine impellers that promotes turbulent flow (beneficial for filler bundle break-up and dispersion) becomes useless and hence the flow velocities rapidly decay to low values away from the impeller. Therefore, in this study, in order to promote good filler mixing and dispersion a laminar flow was created in the slurry.[4] For this, a high viscosity stainless steel mixing paddle (Berg model RR85 S, see Fig. 3.1), 85 mm in diameter and 400 mm in length was coated with boron nitride to avoid Fe contamination of the melt and connected to a digital stirrer, IKA Eurostar 200.

The mixing system was then positioned above the surface of the melt, where the paddle was preheated, whilst the melt temperature dropped. When the melt temperature was just above the liquidus temperature (T_L = ~ 643 ºC) the paddle was inserted into the melt and placed 5 mm from the base of the crucible where it was rotated at 300 rpm.

The particles delivery system made of a steel tube (450 mm in length and 15 mm in diameter), was positioned above the shallow vortex in the melt surface. Once, the melt reached 633 ºC (semi-solid temperature (T_{SS}) ~ 30 % of solid fraction (f_s), the paddle speed was increased to 1200 rpm, and the introduction and mixing of the particles in the melt commenced. The whole system was covered with glass wool to reduce the heat loss. The fillers were introduced onto the melt surface at a rate of 15 g/min (with the amounts added as given in Table 3.7) and mixed for 10 minutes in total, after which the paddle was retracted from the melt and the crucible removed from the heating belt. A 5 kg ceramic block was then placed directly on the surface of the mushy melt to remove porosity created by the rotating paddle and the semi-solid melt left to cool down in the crucible at room temperature.

Some filler segregation was observed in the composites, especially the Al/Cu-CFs, Therefore, for both composite systems (C and M) all the samples extracted for characterisation, ECAE and thermal conductivity studies were extracted from the bottom of the castings.
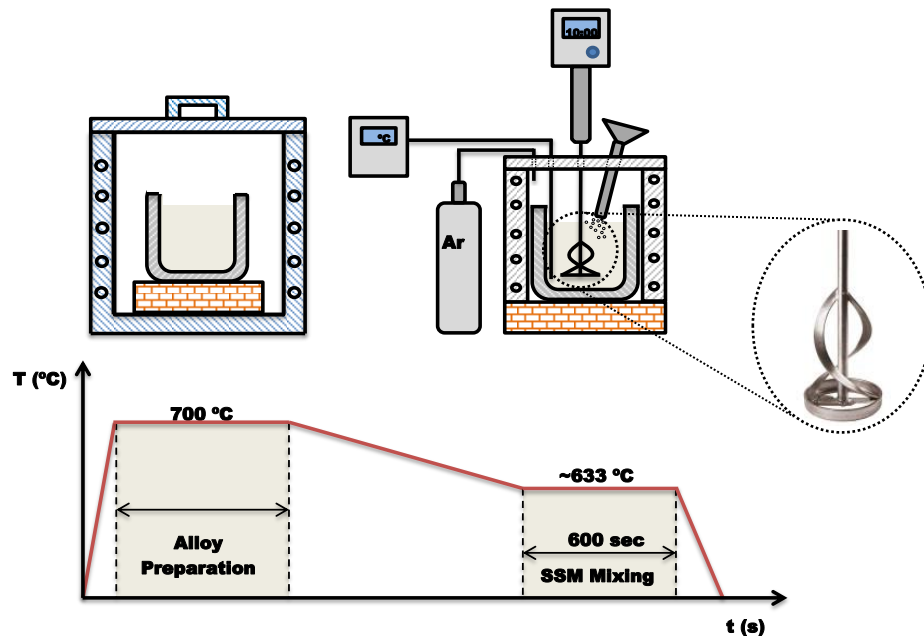
Fig. 3.1 Schematic representation of the rheocasting set-up to process the composites.

3.3.2 Equal Channel Angular Extrusion (ECAE)

Two composites C1.5 (Al3Mg alloy reinforced with 1.5 wt.% of Cu-CFs) and M1 (Al3Mg alloy reinforced with Cu10S1 (0.3 wt.% of MWCNT fillers) were subjected to ECAE for fibre/nanotube alignment and porosity reduction.

Two specimens for each composite sample were produced with dimensions 100mm x 15mm x 15mm, lubricated with graphite and pre-heated to 350 ºC prior extrusion. The heated specimens were then pushed by a ram at low speed (≈ 0.75 mm/s) through the die with an angle $2\theta = 120º$ at room temperature. The process was repeated and specimens from both composites with 4 and 6 iterations were produced.

The initial plan for the experimental work included the ECAE processing with 4 and 6 iterations of the Al3Mg matrix without fillers and all the C-based and M-based composites. This would have allowed a complete study of the effect of ECAE on the composites with increasing filler content and type to be conducted, resulting in a better understanding of the effect of the process on the composites thermal properties.

Unfortunately, due to limited funds and access to the facilities it was only possible to post-process the C1.5 and M1 composites.

3.4 Characterisation Techniques

3.4.1 Microscopy

3.4.1.1 Optical Microscopy (OM)

A Zeiss Axio Scope.A1 AX10 optical microscope (O.M.) supported with AxioVision 40 V 4.8.2.0 software, was used to perform microstructural studies of polished and etched, resin-embedded, composite samples. The microstructure of the composites was studied to reveal the filler distribution in the matrix, agglomeration, final morphology and determine if reaction products formed at the CF/matrix interface.

- **Sample Preparation**

The samples obtained from the composites processed by both, rheocasting and rheocasting followed by ECAE, were sectioned using a Struers Acutom-50 equipped with high speed silicon carbide (SiC) cut-off wheel (code: 10S15). The cut samples were mounted in a thermosetting phenolic resin with carbon filler using a BUEHLER Simplimet 1000 mounting press.

After mounting, samples were ground with SiC paper to obtain a flat surface. Grinding of the composite samples was performed in the following sequence: paper grade P240 for ~ 30 s with a force of 9 N, grade P600 for ~ 30s at 9 N, grade P800 for 1 minute and 9 N and finally grade P1200 for 3 minutes at 9 N. The final polishing was performed in two steps, in the first step, 1 µm KEMET diamond suspension type K std with KEMET diamond compound (grade 1-W-C2) was placed on a KEMET MSFL polishing cloth and used to polish the samples for ~ 3 minutes at a force of 13 N. The second and last step involved using a standard colloidal silica suspension OP-S 0.04 µm, on a MD-chem Struers polishing cloth for 5 minutes at 15 N. On completion of every step, the samples were rinsed with water and ethanol, and then blown with compressed air to remove small foreign particles from the sample surface and checked with an optical microscope.

3.4.1.2 Scanning Electron Microscopy (SEM)

Scanning Electron Microscopy (SEM) is an electron microscopy technique based on a focused electron beam generated by an electron gun than scans over a surface to create an image.[5]

A Zeiss Supra 35VP ultra-high performance field emission gun scanning electron microscope (FEG-SEM), as shown in Fig 3.2 with both high-vacuum and variable operating pressure (VP) capability was used. It was equipped with a suite of micro-chemical analysis techniques, such as, energy-dispersive spectroscopy (EDS) analysis, back-scattered electron detection (BSE) and electron back-scattered diffraction (EBSD) which enabled topographical and compositional characterisation of the MWCNT and CF fillers, and their respective composites.

Fig. 3.2 FEG-SEM Zeiss Supra 35VP used in this study.

The use of the SEM allowed the characterisation of the "as-received fillers", such as length, diameter, surface appearance and chemical composition. In the case of the metallic samples, it allowed the microstructural observation of the composites, filler shape, distribution and dispersion within the matrix. It was also used to identify the different phases present in the matrix and the CF/filler interfaces for reaction products.

SE, BSE and In-lens detectors were employed. The SE and BSE were operated at accelerating voltage of 20 kV and working distance (WD) of 12 mm. The In-Lens mode detector was operated at an accelerating voltage of 3 kV and WD of 3 mm.

- **Sample Preparation**

The MWCNT and CF powder samples were prepared by using aluminium pin stubs with carbon tape attached, the stubs were submerged in the powder where it became attached to the tape, after which any excess powder were removed to avoid contamination of the microscope chamber.

Metallic samples were prepared prior to SEM examination in a manner identical to that described for the optical microscope in Subsection 3.4.1.1. However, for SEM investigation the samples were also plasma cleaned for 120 s (see Subsection 3.4.1.3, Table 3.9)

3.4.1.2.1. EDS

Energy-dispersive X-ray spectroscopy (EDS) is an analytical technique widely used in conjunction with a scanning or transmission electron microscope (SEM or TEM). It is based on the detection of emitted characteristic X-rays when a high-energy beam of charged particles such as electrons is focused on the sample being studied, thus allowing its elemental analysis or chemical charactersation. The technique is based on the fundamental principle that each element has a unique atomic structure resulting in a unique set of characteristic peaks in the X-ray emission spectrum.[6]

EDS spectrums were collected using TEAM EDAX v4.2.1 software and the technique used to verify the composition of the CF and the Cu fibre coating (Subsection 4.2.1.1). It was also employed to study the fibre/matrix interface reaction products using elemental maps (Subsection 4.2.1.2). This enabled the identification of different phases in the Al/MWCNTs composites and their evolution with increasing Cu content (Subsections 4.3.4.2.1 and 4.3.4.2.2).

3.4.1.3 Transmission Electron Microscopy (TEM)

Transmission electron microscopy (TEM) is a microscopy technique that permits the characterisation of the materials structure and properties down to the atomic scale. Similar to SEM, in a TEM, the interaction between the electrons from the electron beam and the specimen generates several signals from which an image can be generated. In a conventional TEM, the transmitted electrons or the forward scattered electrons are collected on a fluorescent screen to generate a bright-field image.[7]

In this study a JEOL TEM 2100 field emission gun transmission electron microscope (FEG-TEM) shown in Fig. 3.3, supported with 64-bit Gatan Digital Micrograph software version 2.32.888.0, was used. The TEM was used to overcome the SEMs limited magnification which was not adequate to observe the MWCNTs internal structure (inner concentric hole, nanotube walls, etc…) and the possible formation of nano-sized Al_4C_3 at the nanotube/matrix interface.

Fig. 3.3 JEOL TEM-2100F (FEG-TEM) used in this study, located at the Experimental Techniques Centre (ETC), Brunel University London.

However, to achieve this it was necessary to first understand the nanotubes behaviour when irradiated with the high energy electron beam. Therefore, the 3 different MWCNTs

sourced were placed under an electron beam at operation voltages of 80 kV and 200 kV to test their stability (see Subsection 4.3.3.2), after which an operating voltage of 80 kV was selected and employed for the remainder of the study in order to avoid nanotube damage and erroneous results.

The TEM was utilized to quantify the "as-received" MWCNTs, specifically the average length and average inner and outer diameter of the nanotubes (Subsection 4.3.1). It also enabled the investigation of the crystallinity, structural and lattice defects and composition of impurities present on the nanotubes from different sources, as shown in Subsections 4.3.2.4.1 and 4.3.2.4.2

For the metallic composite samples produced, the TEM was used to identify the presence of the MWCNTs and the intermetallic within the composites matrix using EDS and EELS techniques (see Subsection 3.4.1.3.2). EELS was utilized as it is more accurate in detecting low atomic number elements such as carbon (see Subsection 4.3.4.2.2). High resolution phase contrast imaging also enabled lattice information to be acquired from the matrix/nanotube interface to assess the possible formation of Al_4C_3 and also observe the damage induced in the nanotubes due to the composite processing as described in Subsection 4.3.4.3.

- **Sample preparation**

The MWCNTs from the various sources were all prepared in a similar manner. Very small amounts (~ 0.05 mg) of powder were placed in a small 10 ml glass vial with ~5 ml of ethanol (C_2H_5OH), and then placed in an ultrasonic bath (SHESTO ultrasonic cleaner model UT8031/EUK, 100W, 40 kHz) until the liquid turned light grey (~ 2 minutes), as shown in Fig. 3.4 a).

Using a pipette, one drop of the nanotube solution was placed onto the lacey C film with H7 Cu finder support grid (Agar Scientific), as shown in Fig. 3.4 b). This was left to dry (~15 minutes) as the ethanol quickly evaporates. Then the dried sample was then immediately examined in the TEM to verify if a good dispersion (Fig. 3.4 c)) of the nanotubes was attained on the grid in order to facilitate a more detailed study.
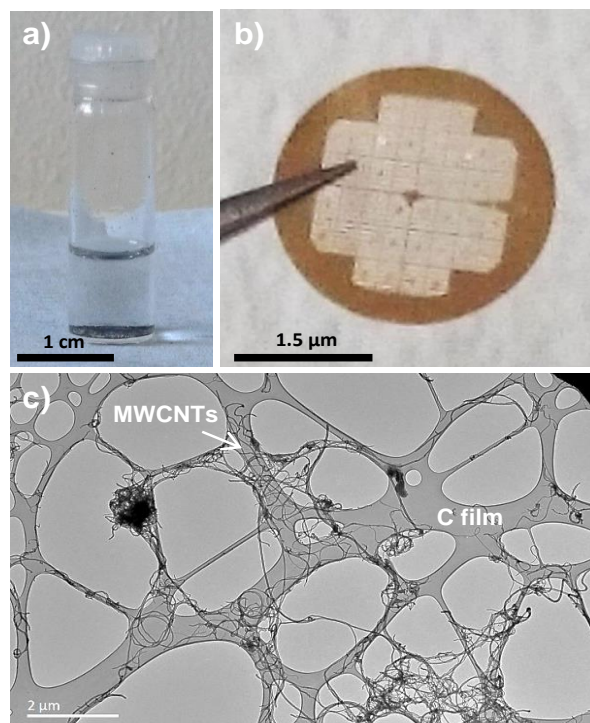
Fig. 3.4 As-received MWCNTs sample preparation for TEM studies: **(a)** container with MWCNTs dispersed in ethanol after ultrasonication. **(b)** Lacey carbon film supported on an H7 copper finder grid and **(c)** TEM bright-field image showing the lacey C film with nanotubes dispersed on it.

<u>TEM foils from the metallic composite samples</u> were prepared as follows: a slice of metal (1cm x 1cm x 150 µm) was sectioned from the composites using a Struers Acutom-50 equipped with a high speed silicon carbide (SiC) cut-off wheel (code: 10S15), after which 3 mm ø discs were produced from the slice using a gatan disc punch system. These discs were subsequently thinned to ~ 50 µm using conventional grinding methods and subsequently placed in a Gatan 691 Precision Ion Polishing System (PIPS), as shown in Fig. 3.5 a) for approximately 4 hours with the steps and milling parameters followed, as detaild in Table 3.9.
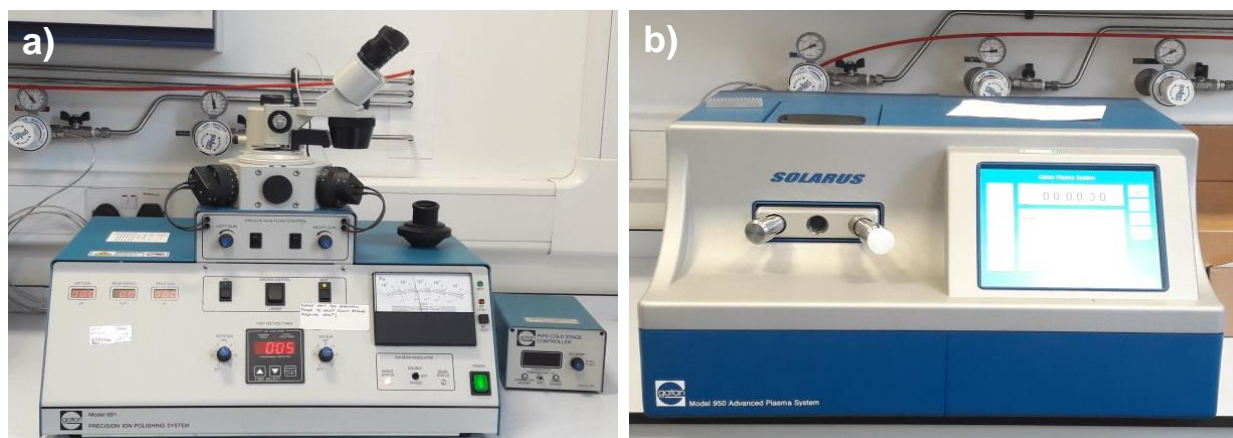
Fig. 3.5 Equipment used for metallic TEM sample preparation: **(a)** Gatan 691 Precision Ion Polishing System (PIPS) and **(b)** Solarus model 950 Advanced Plasma Cleaning System.

The metallic TEM foils were then transferred to a Solarus model 950 Advanced Plasma Cleaning System, as pictured in Fig 3.5 b), to clean the hydrocarbons from the surface.

Table 3.9 PIPS milling steps and corresponding parameters.

Steps	Gun Energy keV	Gun Angle (⁰)	Beam Modulation	Rotation (rpm)	Time (min)
1st	5	6 top and bottom	Dual Beam	3	60
2nd	5	4 top and bottom	Dual Beam	3	Until perforation
3rd	2.5	3 top and bottom	Dual Beam	3	5
4th	0.5	3 top and bottom	Dual Beam	3	2 (cleaning)

The Solarus advanced plasma cleaning system is a low power hydrogen and oxygen radical generator producing glow-discharge plasma within the generator housing that by convection, passing over and around the specimen, cleans the hydrocarbons contaminants from the sample.

The parameters used for the plasma cleaning are given in Table 3.10, which takes ~ 30 s for the TEM samples. Immediately after cleaning the samples were then placed in either, a single tilt beryllium analytical holder for use with EDS as it eliminates stray x-ray signals or a double tilt holder for diffraction analysis.

The plasma cleaning device was also used to determine the stability of the MWCNTs under the plasma discharge after 30 s and 120 s in order to assess its effect on CNT

structure prior to TEM and SEM characterisation. The sample preparation is described in Subsection 3.4.2.2 and the results are shown in Chapter 4, Subsection 4.3.3.1.

Table 3.10 Advanced Plasma Cleaning parameters used to study their effect on the structural characteristics of the MWCNTs.

Sample	Power (W)	Gas	Characterisation Device	Time (s)	Comment
Al/MWCNTs	50	H_2/O_2	TEM	30	_ _ _
Al/MWCNTs	50	H_2/O_2	SEM	120	_ _ _
S1 MWCNTs	50	H_2/O_2	Raman	30 / 120	Stability Test
S2 MWCNTs	50	H_2/O_2	Raman	30 / 120	Stability Test
S3MWCNTs	50	H_2/O_2	Raman	30 / 120	Stability Test

3.4.1.3.1 Selected Area Electron Diffraction (SAED)

Diffraction is based on the elastic scattering of electrons in a crystalline material and selected area electron diffraction (SAED) is an important technique that can be used to yield information on phase identification such as sample crystallinity, crystal structure and orientation and structural defects via measuring+calculating interplanar (d) spacings.[7]

If the electrons from an incident electron beam are scattered through an angle 2θ at the specimen then the distance between the direct and diffracted beams spots (R) as measured on the TEM screen is determined by the camera length (L), as demonstrated in eq.16.[7]

$$\frac{R}{L} = \tan 2\theta \sim 2\theta \qquad\qquad \textbf{eq. (16)}$$

Then according to the Bragg equation:

$$\frac{\lambda}{d} = 2\sin\theta \sim 2\theta \qquad\qquad \textbf{eq. (17)}$$

Where, λ is the electron wavelength, any distance between the direct beam and a specific diffraction spot or the radius of a diffraction ring, R, is related to a specific spacing (d) (eq. 16 and 17) between planes in a crystal. Since λL is constant, if the lattice parameter of the crystal is known then the allowed reflections are known and only certain d-spacings will be associated with diffraction spots. **Thus, the ratio of any two**

R values gives the inverse ratio of the d-spacings (reciprocal lattice 1/nm), as follows:

$$R = \frac{\lambda L}{d}$$ **eq. (18)**

SAED was used in this study to identify the MWCNTs by the comparison of diffraction parameters obtained from corresponding diffraction rings by comparing calculated d values with XRD results. The data could also be used to determine if nano Al_4C_3 were formed at the nanotube/matrix interface.

According to the XRD studies of the "as-received" MWCNTs, the d-spacing of the studied MWCNTs are given in Table 3.11 (see Subsection 3.4.2.1 for XRD methodology). The SAED results are shown in Figs. 4.16, 4.17 and 4.32, and are observed in Chapter 4 Subsections 4.3.2.4.1 and 4.3.4.2.2, accordingly.

Table 3.11 MWCNTS crystallographic information according to the international centre for diffraction (ICCD), and Al_4C_3 according to Cox and Pidgeon et al[8].

Material	2θ Angle (º)	{h,k,i,l} Planes	d (Å)	d/d_{0002}	Reference 2015 ICDD
MWCNTs	25.9188	0002	3.434760	1	00-058-1638
	42.957	$10\bar{1}0$	2.103680	0.61	
	53.2886	0004	1.717650	0.50	
	78.7221	$11\bar{2}0$	1.214560	0.35	
Al_4C_3		105	2.49	0.72	Cox and Pidgeon et al
		107	2.24	0.65	
		0012	2.08	0.605	
		201	1.44	0.418	

The SAED patterns were analysed using Gatan Digital Micrograph software version 2.32.888.0 and using the line profile tool the average of five R measurements (in nm) for each ring was taken. The obtained R values were used to calculate the ratio of the R_n/R_1, where n is the ring number, that were compared with the ratios given by the XRD data (Table 3.11). All the data is given in Table 3.12.

Table 3.12 Average diffraction ring/spots radii (R) and ratios (R_n/R_1), of the MWCNTs from Figs. 4.16, 4.17 and 4.32 (Chapter 4).

R	Fig. 4.16 Average Radius (nm)/Plane	Fig. 4.17 Average Radius (nm)/Plane	Fig. 4.32 Average Radius (nm)/Plane
R_1	0.35 ± 0.002 / d_{0002}	0.40 ± 0.006 / d_{0002}	0.30 ± 0.004 / d_{0002}
R_2	0.21 ± 0.002 / $d_{10\bar{1}0}$	0.25 ± 0.001 / $d_{10\bar{1}0}$	0.22 ± 0.004 / d_{105}
R_3	0.17 ± 0.001 / d_{0004}	0.20 ± 0.0003 / d_{0004}	0.18 ± 0.002 / $d_{10\bar{1}0}$
R_4	0.12 ± 0.002 / $d_{11\bar{2}0}$	0.14 ± 0.001 / $d_{11\bar{2}0}$	0.15 ± 0.001 / d_{0004}
R_5	$---$	$---$	0.13 ± 0.002 d_{201}
R_6	$---$	$---$	0.11 ± 0.002 / $d_{11\bar{2}0}$
R_7	$---$	$---$	0.20 ± 0.001 / d_{107}
R_8	$---$	$---$	0.18 ± 0.002 / d_{0012}
R_2 / R_1	0.61	0.61	0.71
R_3 / R_1	0.50	0.50	0.60
R_4 / R_1	0.36	0.36	0.50
R_5 / R_1	$---$	$---$	0.42
R_6 / R_1	$---$	$---$	0.36
R_7 / R_1	$---$	$---$	0.66
R_8 / R_1	$---$	$---$	0.605

3.4.1.3.2 Electron Energy-Loss Spectroscopy (EELS)

Electron energy-loss spectroscopy (EELS) is an analytical technique that deals directly with the primary process of electron excitation, a process that results in the fast electrons losing a characteristic amount of energy. [9]

The energy resolution is typically 1 eV but can approach 0.1 eV if an electron-beam monochromator is used. The energy-loss events detected with this technique give important data about the chemistry and the electronic structure of the specimen atoms, from which their bonding/valence state, the nearest-neighbour atomic structure, the free-electron density, the band gap and the specimen thickness can be determined. The technique is also well suited to the detection of light elements, which can be challenging to analyse with EDS. It can detect and quantify all the elements in the periodic table.[7,9]

EELS is capable of giving structural and chemical information about a solid, with a spatial resolution down to the atomic level in favourable cases. For example, different C allotropes (the same elemental but have different crystalline structures) can be distinguished in an EELS spectrum as the plasmon peaks occur at different energies, i.e. 33 eV in diamond, 27 eV in graphite, and 25 eV in a-C). [9]

The EELS method was used in this study for elemental analysis of the MWCNTs due to its superior power of detection of light elements such as C and its allotropes in comparison with the EDS technique. The results using this technique are shown in Subsections 4.3.4.2.2 and 4.3.4.3.

3.4.1.3.3 Fast Fourier Transform (FFT) and Inverse Fast Fourier Transform (IFFT)

In transmission electron microscopy, the fast Fourier transform (FFT) also named Fourier transform (FT) is a crystallographic experimental technique analogous to SAED, based on the image processing of a TEM lattice image using the following Fourier transform equation:

$$F\{f(x)\} = \int_{-\infty}^{+\infty} f(x)\, e^{-2i\pi qx}\, dx \qquad \text{eq. (19)}$$

Mathematically, the objective lens performs a FT that creates the diffraction pattern of the object in the back focal plane and the inverse fast Fourier transform, IFFT or simply FT^{-1}, makes the interference of the diffracted beams back to a real space image in the image plane (lattice image).[7,10]

Whereas, the image processing method calculates the FT of a HRTEM image, where periodic structures in the image give rise to diffraction patterns comprised of sharp spots. A filtered image of the area analysed can then be generated using the FT^{-1}.

The mechanics of the FFT and IFFT routine and other simulations approach are complex and beyond the scope of this study. They are therefore not outlined here but further information can be found in the given selected literature[7,10–12]

The FFT images, contain similar information to diffraction patterns, and the IFFT retrieves the lattice image of the area studied. This method has the advantage of generating diffraction patterns from very small areas from a good lattice image, thus simplifying the task in comparison to SAED, as in the latter the area selected is limited to the aperture size. With this in mind, FFT and IFFT were used to study the crystallinity and d-spacings of the MWCNTs from the various sources and identify the phases

present in the metallic composites (matrix and filler) and their respective interface as illustrated in Chapter 4, Subsections 4.3.2.4.2 and 4.3.4.3.

The microscope was operated at 80 kV and the lattice images were acquired in the bright-field mode at magnifications > 400000 x. In order to generate the FFT and IFFT from the lattice image the image processing software used was Gatan Digital Micrograph software version 2.32.888.0 using the function: Line profile – Process – FFT – IFFT.

3.4.2 Spectroscopy

3.4.2.1 X-ray Diffraction (XRD)

X-ray diffraction (XRD) is a characterisation method that allows identification of unknown phases on crystalline materials by studying their internal structure using X-ray monochromatic electromagnetic radiation. When the interaction of the incident X-rays with the sample satisfy Bragg´s Law (see eq. 17) constructive interference occurs and a ray is diffracted from the sample. This law gives the relationship between the wavelength of electromagnetic radiation, the diffraction angle and the lattice spacing (d-spacing) in a crystalline sample. If a sample is scanned for a range of 2θ angles, all possible diffraction directions of the lattice should be obtained from which d-spacings can be calculated and the material identified as this property is intrinsic of each material.[13,14]

The XRD technique was required to study the chemical composition and crystallinity of the three different MWCNTs powders and Cu10S1 composite powder (see Subsection 3.2.2) to assess their quality and purity.

The device used in this study Bruker D8 Advance X-ray diffractometer with filtered Cu Kα1 (λ: 1.5406 Å) operated at a generator voltage of 40 kV and a current of 50 mA. The powders were placed in an poly(methyl methacrylate) (PMMA) holder, until it filled the holder cavity, levelled with a glass slab and transferred to the machine. In order to obtain the XRD traces, angles (2θ) between 20º and 80º were scanned using a step size of 0.009º at a speed of 0.01º s^{-1}. The observed crystalline phases were identified

with the help of the DIFFRAC.EVA V4 software updated with the international centre for diffraction data (2015 ICDD) database (see Chapter 4 Subsection 4.3.2.2 Tables 4.9 and Subsection 4.3.4.1, Fig. 4.15).

3.4.2.2 Raman Spectroscopy

Raman spectroscopy is a spectroscopic technique based on the Raman effect, and is named after Sir C. V. Raman who discovered it in 1928, even though it had been predicted theoretically by Smekal et al in 1923.[15]

This effect is based on the phenomenon of a change of frequency when light is scattered by molecules, in other words due to the inelastic scattering of monochromatic light, usually from a laser source[15,16]. The photons of the laser light are absorbed by the sample and then re-emitted. The frequency of the re-emitted photons can be shifted up or down in comparison with original monochromatic frequency. This shift provides information about vibrational, rotational and other low frequency transitions in molecules. Raman spectroscopy can be used to study solid, liquid and gaseous samples.[16]

Raman spectroscopy is one of the most common techniques to study MWCNTs as it is relatively simple and quick to yield information on characteristics such as purity, defects and tube alignment. The technique assists in distinguishing the presence of MWCNTs relative to other carbon allotropes.[17]

In order to study the quality of the "as-received" MWCNTs from the three different sources a Renishaw's inVia confocal Raman microscope with a spectrophotometer with excitation energy of 2.54 eV and an acquisition range of 100 to 3000 cm^{-1} was used, and is shown in Fig. 3.6. The parameters used for each source of MWCNTs are given in Table 3.13.

The preparation of the MWCNTs powder for Raman characterisation is in part similar to the powder sample preparation for the TEM study (see Subsection 3.4.1.3). Small amounts (1 mg) of powder were placed in a small, 10 ml glass vial with ~5 ml of ethanol

(C_2H_5OH), and then placed (~2 minutes) in an ultrasonic bath (SHESTO ultrasonic cleaner model UT8031/EUK, 100W, 40 kHz) until the liquid turned light grey.

Fig. 3.6 Renishaw's inVia confocal Raman microscope used in this study.

Using a pipette, the liquid was transferred drop-by-drop to a paper filter until it formed a dense and homogeneous MWCNT mat, with a nearly circular shape and about 1 cm in diameter, which was left to dry. Finally, the mat was transferred to a glass strip using tweezers and placed in the Raman device. Each MWCNT powder sample was analysed 10 times, with each measurement comprising of 2 acquisitions each last 10s.

Table 3.13 Raman spectroscopy parameters.

Measurements	Objective Mag.	Time (s)	Acquisitions	Power (%)	Laser energy (ev)
10	20x	10	2	5	2.54

3.4.3 Simultaneous Thermal Analysis (STA)

Simultaneous thermal analysis is a combination of a Differential Scanning Calorimetry (DSC) and Thermogravimetry (TG). In heat-flux DSC (principle of device used in this study), the temperature difference between the sample and the reference is measured as a function of temperature or time, under controlled temperature conditions. The temperature difference is proportional to the change in heat flux (energy input per unit of time). During a phase change heat is absorbed or emitted by the sample, altering the

heat flux. This technique provides information such as heat capacity (C_p), that in turn allows the study of phase transformations.[18] The technique can thus be used to compare materials and examine purities.

However, TG examines the mass change of a sample as a function of temperature. TG is used to characterize the decomposition and thermal stability of materials under a variety of conditions and to examine the kinetics of the physicochemical processes occurring in the sample. Not all thermal events result in a change in mass of the sample, but some important phenomena do, such as, desorption, absorption, sublimation, vaporization, oxidation, reduction and decomposition.[18] Therefore, the combination of both thermal analysis methods allows a more detailed analysis of the material under investigation.

The STA thermal analysis method was used to study the thermal stability and catalyst content of the three varieties of "as-received" MWCNTs and the Cu10S1 filler, as described in Chapter 4, Subsections 4.3.2.3 and 4.3.4.1.

The STA study was performed with a heat-flux NETZCH STA 409 PC Luxx device using alumina crucibles + lids. Before each material was tested, a baseline correction curve was obtained in order to remove noise caused by crucible contamination or vibrations from the surroundings. The reference sample (empty crucible) and the sample (in this case also an empty crucible) were placed in the microbalance and the chamber closed, after which the balance was set to 0. The chamber was then cleared of unwanted gases by purging the enclosed environment with either O_2 or He, and then extracting it using a rotary vane pump, the process was repeated four times, after which the chamber was left open and the flow rate set to 40 mL/min, at an atmospheric pressure of 1.01325 bar.

The test was then started according to the thermal cycle illustrated in Fig. 3.7. The powder samples were initially handled in a fume cabinet where they were weighed in a micro-balance, ~ 8 mg for the "as-received" MWCNTs and ~ 50mg for the Cu10S1 sample. Once the baseline was obtained, the crucible was filled with the weighed powder and the baseline subtracted following the same procedure and parameters. Table 4.14 gives the designation and conditions of the samples analysed. Each powder

source was tested five times under the corresponding atmosphere, either O_2 or He (only for S1 MWCNTs and Cu10S1 powders) to ensure the repeatability of the results.
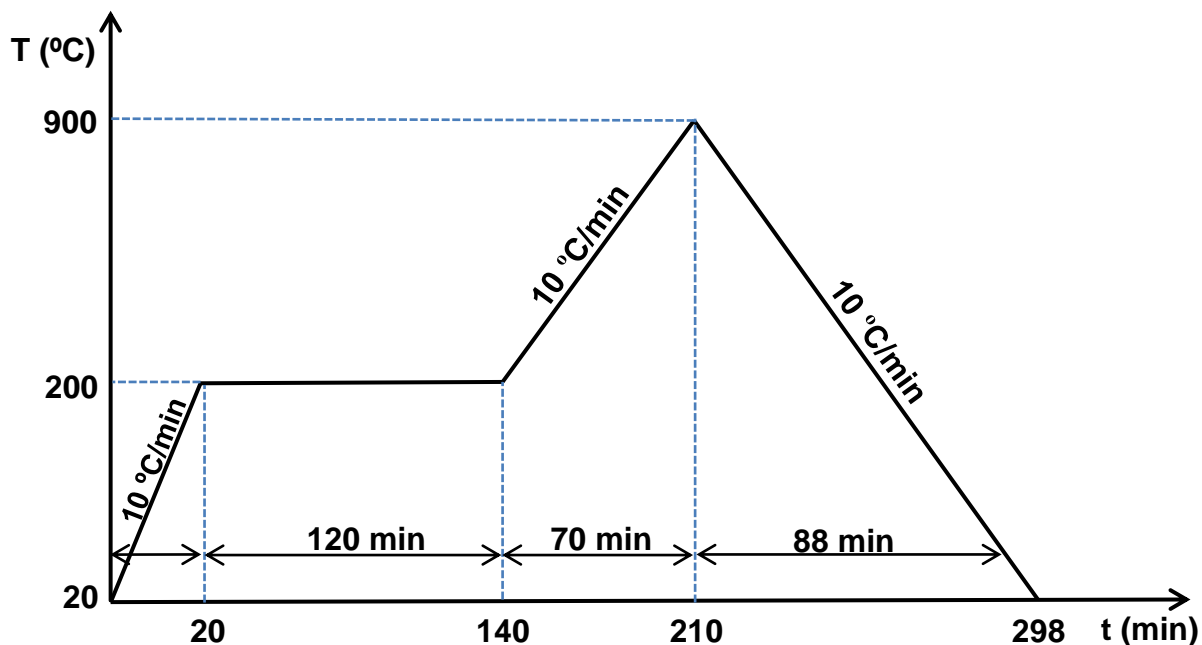
Fig. 3.7 STA thermal cycle for MWCNTs and Cu10S1 powders.

Table 3.14 Sample designation and conditions.

Samples	Nr. of measurements	Atmosphere
S1 MWCNTs	5 / 5	O_2 / He
S2 MWCNTs	5	O_2
S1 MWCNTs	5	O_2
Cu10S1	5 / 5	O_2 / He

3.4.4 Image Analysis

The thermal conductivity of the composites is strongly dependent on the content of the constituent phases. The quantification of these phases is useful in order to predict their thermal contribution to the composite by employing these values in the thermal conductivity theoretical models. These theoretical values can then be compared to the

experimental, as described in Chapter 4, Subsection 4.2.2.3 for the Al/Cu-CFs, and Subsection 4.3.5.4 for Al/MWCNTs composites. The porosity and the volume fraction of the fillers within the composites, were assessed via the surface area analysis technique using the image analysis software, Image J version 1.45s.

For each composite sample, ten optical micrographs were taken with a 5x magnification objective to assess the porosity content whilst another 10 micrographs were taken with a 20x magnification objective to determine the filler content. If the phases are randomly dispersed, then it can be assumed that the volume fraction will be equal to the areal fraction. Thus, by comparing the area of a given phase to the overall area of the image, as illustrated in Fig. 3.8 (a) and (b) the average volume fraction of the porosity/fillers can be determined.

The volume fraction of the MWCNTs in the matrix was not assessed as this technique is not reliable as the are MWCNTs too small. Despite, the fact that the MWCNTs were found in the matrix in micron sized bundles, also small nano sized clusters and in some cases individually dispersed were found which are difficult to account for using this method.
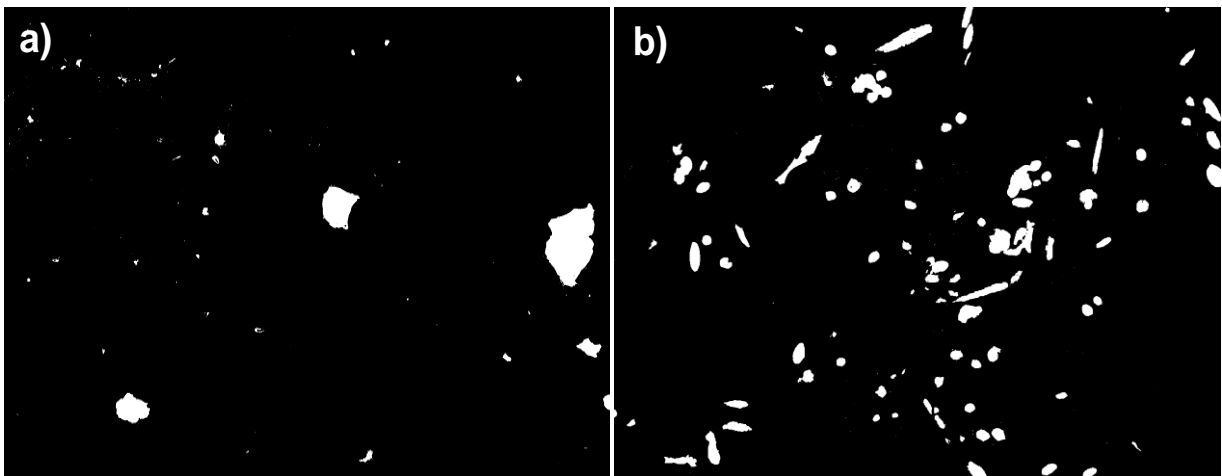

Fig. 3.8 Image analysis of Al/Cu-CFs C1.5 composite using Image J software: **(a)** porosity and **(b)** CF content.

3.5 Thermal Conductivity Measurements

In this section the techniques used to obtain the thermal conductivity of the composites and the thermal conductivity of an individual S1 MWCNT are described. In order to validate the experimental thermal conductivity values obtained, these were compared with the theoretical thermal conductivity models described in Chapter 2 Section 2.5 and the parameters used are given in this section.

3.5.1 Laser Flash Analysis

The laser-flash is a transient technique developed originally for measurements in solids but which can occasionally be used also for liquids, particularly at high temperatures. Fig. 3.9 shows a schematic representation and picture of the apparatus used in this study.

The sample is illuminated on one face with a laser pulse of very short duration and high intensity. The absorption of the laser energy on the front face of the sample causes the generation of heat at that front surface, which is subsequently transmitted throughout the sample to the back face where the temperature rise is detected with an infrared remote sensor. The interpretation of measurements is based on a one-dimensional solution of eq. 20 subjected to an initial condition of an instantaneous heat pulse at one location.
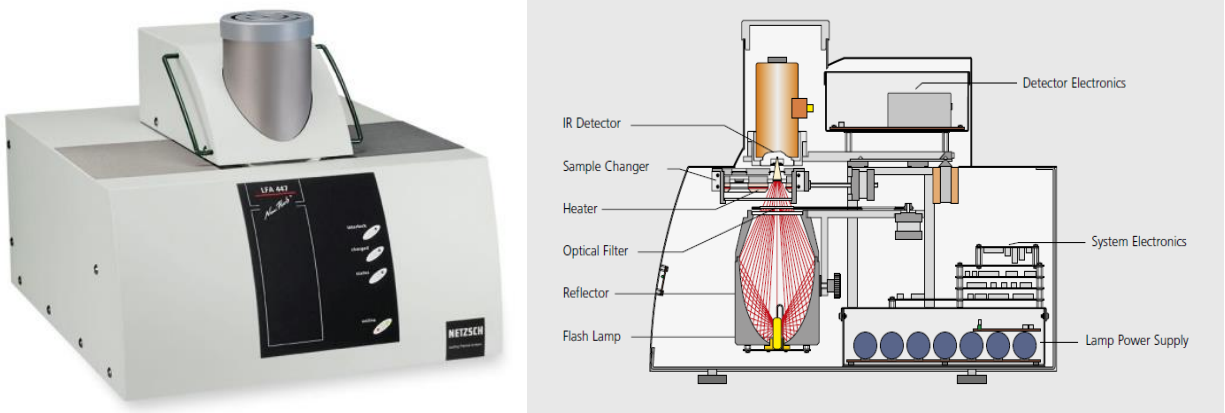

Fig. 3.9 The LFA 447 apparatus with its respective schematic representation.[19]

The temperature increase at the back face of a sample with thickness l, radius r and density ρ is given by:

$$\Delta T(1,t) = \frac{Q}{\rho C_p / \pi r^2}\left[1 + 2\sum_{n=1}^{\infty}(-1)^n exp\left(-\frac{n^2\pi^2 at}{l^2}\right)\right] \qquad \textbf{eq. (20)}$$

ΔT is the thermal gradient, t is the time, C_p is the specific heat capacity and Q is the energy absorbed at the front surface at time zero. The thermal diffusivity of the sample, a, is often deduced from the measurement of the time taken for the back face temperature of the sample to reach one half of its maximum value.

The technique has the distinct advantage that it does not require physical contact between the test sample and the heater or detector. For this reason, it is a particularly appropriate technique for use at high temperatures or in aggressive environments. Nevertheless, the method has seen widespread application to a wide range of materials including composites, polymers, glasses, metals, refracting materials, insulating solids and coatings.[20]

The thermal conductivity measurements were obtained using a NETZSCH LFA 447 NanoFlash device and conducted at the Korean institute of Industrial Technology (KITECH). Each measurement requires a set of 3 specimens, two specimens with dimensions 10 x 10 x ~1-2 mm and one with dimensions of 3 x 3 x 1 mm. Five measurements were taken for each material: Al3Mg (reference alloy); Al/Cu-CFs and Al/Cu10S1 composites processed via rheocasting and rheocasting followed by ECAE. The obtained results are shown in Chapter 4, Subsections 4.2.2 and 4.3.5.

3.5.2 Scanning Thermal Microscopy (SThM) + Finite Elements Method (FEM)

Scanning thermal microscopy (SThM) is a technique primarily based on atomic force microscopy (AFM) as it allows the use of a wider variety of samples and is also very versatile allowing the use of various types of sensors at the tip of the AFM probe. SThM is a promising technique for nanometer-scale thermal measurements, imaging, and the study of thermal transport phenomena.[21]

Fig. 3.10 illustrates the typical set-up of an AFM-based SThM system. When scanning the sample surface the cantilever deflection generates an electrical signal that is detected. In the imaging mode, the deflection signal is used in a feedback control loop to maintain a constant tip-sample contact force while the tip scans laterally. Piezoelectric scanners are used to move the sample vertically and to scan the sample surface laterally. The combination of the X-Y scan position data, the force feedback signal and the thermal signal measured by the sensor located either at the tip or on the cantilever gives the raw data for both the topography image and the "thermal" image of the surface.
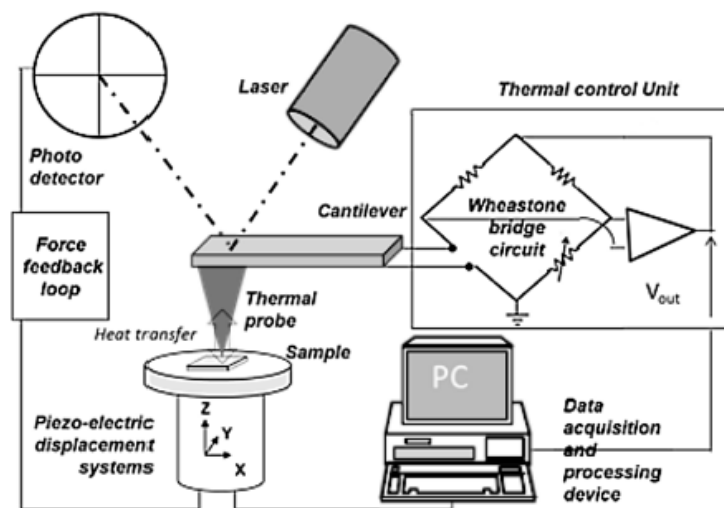
Fig. 3.10 Schematic representation of an AFM-based SThM system. [21]

The thermal image contrast reflects the change in the amount of heat locally exchanged between the tip and the sample. Usually real-time thermal signal analysis is performed with the help of a thermal control unit. Various thermal methods based on the use of different thermosensitive sensors or phenomena have been developed and can be classified according to the temperature-dependent mechanism that is used: thermovoltage, change in electrical resistance, fluorescence or thermal expansion.[21]

The SThM technique, in combination with the finite element method (FEM) was employed to attempt to measure the thermal conductivity of individual MWCNTs to verify whether or not the nanotubes in the "as-received" condition do have the

outstanding properties claimed by the manufacturers, and thus assess their real thermal contribution as filler used in the Al matrix.

The study was possible thanks to a collaboration with the Czech Institute of Metrology (CMI) based in Brno, Czech Republic. The principle of the study was to measure the average thermal conductivity values of individual nanotubes for each of the three "as-received" MWCNTs sources (S1, S2 and S3) and assess if the values obtained are in agreement with the quality studies performed using the TEM, XRD, Raman and STA methods.

Obtaining the thermal conductivity of individual nanotubes is a difficult task and only a few research groups in the world have the know-how and facilities to obtain representative data. Unfortunately, due to the complexity of the measurements most tests yielded unreliable data, mostly due to the nanotube movement during scanning. In fact only a single measurement from the S1 MWCNT sample was deemed reliable (see Chapter 4, Subsection 4.3.5.1), and therefore it was impossible to perform the comparison as first proposed.

The device utilized to perform the experiments was a Bruker AFM Dimension Icon ScanAsyst, which is depicted Fig. 3.11 a). Fig 3.11 b) shows the Bruker VITA thermal control unit that generates the real-time thermal signal and Fig. 3.11 c) illustrates the cantilever used. The experiments were performed in contact mode.

The procedure to prepare the multi-walled carbon nanotubes sample is similar to that performed for TEM observations (see Subsection 3.4.1.3) but following dispersion in ethanol they were distributed on a mica substrate and scanned by the SThM probe in order to obtain sufficient information to determine the thermal conductivity of the individual nanotubes.
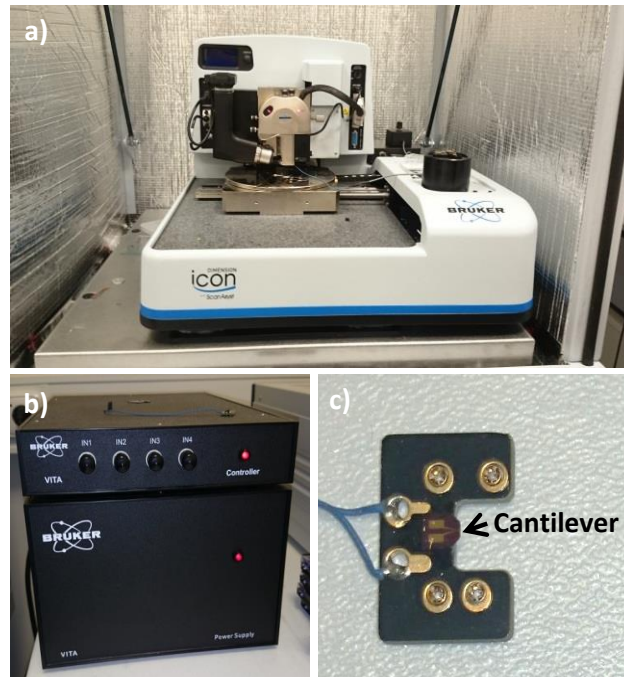
Fig. 3.11 AFM-based SThM at the Czech Metrology Institute (CMI), Brno, Czech Republic, used in this study. (a) Bruker AFM Dimension Icon ScanAsyst. (b) Bruker VITA thermal control unit and (c) ScanAsys-Air probe with a silicon nitride cantilever.

- **Schematics and estimated electrical and thermal parameters**

The SThM measurement device consists of a Wheatstone bridge as depicted in Fig. 3.12.

The bridge voltage was set to a value U_{in} = 1.2 V. Two upper resistors, R_1 and R_2 are both fixed with a resistance of 1kΩ. The R_{TIP} represents the probe resistance, which was 400 Ω at room temperature and the temperature coefficient was 0.00165 K^{-1}. R_{ADJ} is the resistance of an adjustable resistor, whose goal is to adjust the bridge so that the voltage difference U_{DIFF} is within the limits of the subsequent amplifier (A = 1000) and analog-to-digital (AD) convertor (not shown in figure).

Fig. 3.12 Schematic representation of the Wheatstone bridge of the SThM device.

The left branch of the bridge remains constant throughout the whole measurement. The temperature of the tip changes with the tip resistance, which in turn changes the current in the right branch along with the measured voltage and the heatin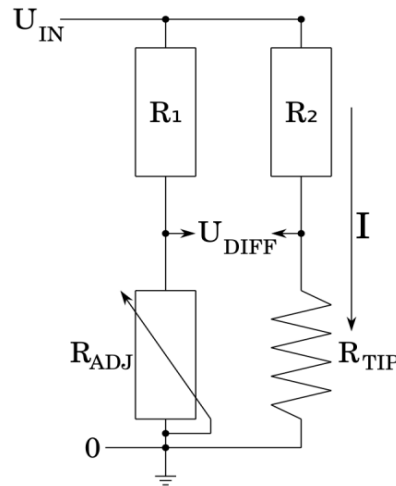g power of the tip. Every change in the measured voltage can be expressed as a change of temperature and heating power. The ratio between the temperature and heating power gives us the temperature resistance in ($K\ W^{-1}$), but only the change is known, not the actual value.

- **FEM modelling**

Two different geometries were designed to simulate the conditions during the SThM measurements and are illustrated in Fig. 3.13, and by applying the finite element method (FEM) the difference in temperature resistance was calculated.

FEM was used to find the conditions that were present during the SThM measurements. The model is based on the following principles:

- In order to avoid computation with very small numbers, the problem size was increased 5 million times to achieve numerical stability. All the properties have been recalculated with respect to this scale.

- The tip of the probe was modelled as a heat source in the shape of a hemisphere, with constant volumetric heat power density in $W\ m^{-3}$. It was made of platinum (Pt), so the thermal conductivity was set to 71.6 $W\ m^{-1}\ K^{-1}$ [22,23].

- The radius of the tip was modelled four times larger than the radius of the tube. This ratio comes from AFM measurement of the tube diameter (40 nm) and an assumption that the tip diameter could be roughly 160 nm.

- There is one heat source (the tip) and two heat sinks. The heat flows from the tip to the surroundings in two ways – mostly downwards through the substrate and upwards through the upper part of the tip. The latter represents the partial heat flow through the mechanical construction of the device. However, the actual fraction of heat dissipation from each route is unknown and must be found as a model parameter.

- Two different cases were calculated (Fig. 3.13), a) one in which the tip touches the substrate without being influenced by the nanotube and the other position b) with the probe on top of the tube. These two positions differ in thermal resistance and the goal is to achieve the same thermal resistance difference as measured by SThM.
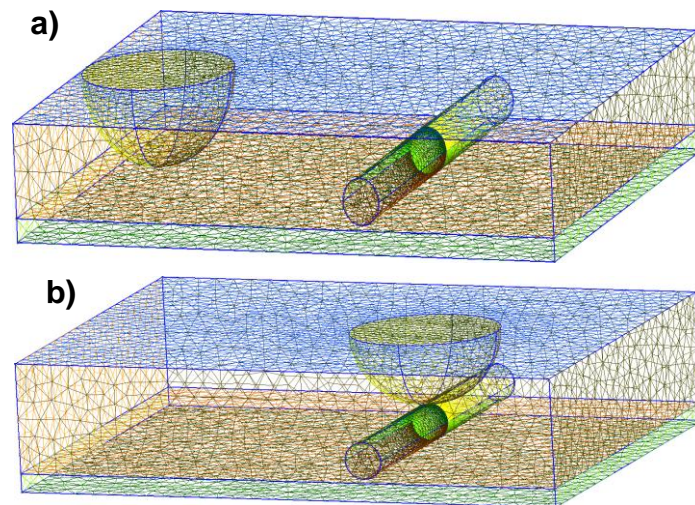

Fig. 3.13 FEM geometries used to measure the thermal resistance between**: (a)** probe and substrate and **(b)** probe and substrate with the nanotube in between them.

3.5.3 Effective Thermal Conductivity Modelling

In this Section, the description of how the effective thermal conductivity models described in Chapter 2, Section 2.5 were used in order to compare the predicted thermal conductivity of the composites with that obtained experimentally in this study. The predicted thermal conductivity of the composites was assessed in two different conditions, the theoretical and corrected conditions that are systematically described hereafter with the utilized parameters outlined.

The thermal conductivity of the composites (K_c) produced, Al/Cu-CFs and Al/MWCNTs was predicted using various theoretical models for two conditions, named in this study as the theoretical condition and the corrected condition. The models selected to predict K_c for each composite are given in Table 3.15 and are described in Chapter 2 Section 2.5.

Table 3.15 Models selected to predict the thermal conductivity of the Al/Cu-CF and Al/MWCNT composites.

Material	Models	Comment
Al/Cu-CFs	Eshelby's	Thermal conductivity of composite reinforced with fibre-shaped filler with anisotropic thermal properties, in-plane ($K_{c,1}$) > out-of-plane ($K_{c,2}$), and individually aligned within the matrix (Eqs. 9, 10, 11 and 12 and Table 3.16).
Al/MWCNTs	Eshelby's	Thermal conductivity of composite reinforced with an isotropic spherical filler (simulate bundles of MWCNTs) (see eq. 8 and Table 3.17). Thermal conductivity of composite reinforced with fibre-shaped filler with anisotropic thermal properties ($K_{c,1}$ > $K_{c,2}$), individually aligned within the matrix (Eqs. 9, 10, 11 and 12 and Table 3.17).
	MG-EMA	Thermal conductivity of composite reinforced with a fibre-shaped filler with anisotropic thermal properties ($K_{c,1}$ > $K_{c,2}$) and high aspect ratio, β > 100, randomly and individually dispersed within the matrix. (Eq. 14 and Table 3.17).
	NAN	Thermal conductivity of composite reinforced with a fibre-shaped filler with anisotropic thermal properties ($K_{c,1}$ > $K_{c,2}$), high aspect ratio, β > 100 and high phase contrast (K_f/K_m), randomly and individually dispersed within the matrix (Eq.15 and Table 3.17).

The theoretical condition, assumes that the fibres/nanotubes diameter and length are constant, however, this is not real as the rheocasting + ECAE method does break and

reduce it. It also assumes that no porosity is present, the fibres/nanotubes are individually and homogeneously dispersed throughout the metal matrix and their volume fraction is the same as initially introduced during processing. Futhermore, it does not account for the presence of interfacial barriers, it assumes that the Cu coating on the fibres and surrounding the MWCNTs dissolves in the Al matrix.

The parameters used for the modelling of the K_c reinforced with CFs and MWCNTs are given in Tables 3.16 and 3.17, respectively. The thermal conductivity (K_m) and density of the matrix (ρ_m) were obtained by laser flash technique (Subsection 3.5.1) from the reference material (Al3Mg, see Table 3.7). The density of the CFs is ρ_f = 2.23 g cm^{-3}, since the manufacturer did not provide the value, it was obtained from another manufacturer[24] that produces the same type of fibres which have similar properties. The length (l_f) and diameter (d_f) of the fillers, in this case CFs, were obtained using SEM (see Subsection 3.4.1.2).

The in-plane thermal conductivity of the fibres ($K_{f,1}$) was given by the manufacturer (see Table 3.5), whereas, the out-of-plane thermal conductivity of the fibres ($K_{f,2}$), due to their anisotropic nature, is assumed to be the same as that of graphite (see Chapter 2, Fig. 2.2).

Table 3.16 Modelling parameters for the Al/Cu-CFs composites.

Matrix			Carbon Fibres			
K_m (W m^{-1} K^{-1})	ρ_m (g cm^{-3})	$K_{f,1}$ (W m^{-1} K^{-1})	$K_{f,2}$ (W m^{-1} K^{-1})	l_f (µm)	d_f (µm)	ρ_f (g cm^{-3})
148.4 ± 4.6	2.65	500	10	285.41 ± 177.27	8.79 ± 203	2.23

In the case of the Al/MWCNTs composites, the reference material is the same as for Al/Cu-CFs, thus the K_m and ρ_m are also the same. As they were found in bundles (Chapter 4, Subsection 4.3.4.2) and also individually (Chapter 4, Subsection 4.3.4.3), it was important to calculate the K_c taking into account the bulk density (takes into account the air between nanotubes) and the real density (takes into account only the nanotubes).

The density values were not provided by the actual manufacturers but according to various manufacturers[25–27], the common density values given for the CCVD MWCNTs, 95 % purity, outer diameter and length ranging from 20-30 nm and 10-30 µm, respectively, are: - Bulk density $\rho_{f,b}$ = 0.28 g cm^{-3} and real density, $\rho_{f,r}$ = 2.1 g cm^{-3}. The S1 MWCNTs length and diameter were obtained using the TEM (see Subsection 3.4.1.3).

The S1 MWCNTs in-plane thermal conductivity ($K_{f,1}$) value given by the manufacturer is 2000 W m^{-1} K^{-1} (see Table 3.6) and used as a best case scenario. In this study also the value 20 W m^{-1} K^{-1} was used as the worst case scenario, which is the value of an S1 MWCNT acquired by the SThM+FEM method (see Subsection 3.5.2 and Chapter 4 Subsection 4.3.5.1). In the out-of-plane direction, analogous to the CFs, the nanotubes walls are connected between walls by the week Van der Waals bonds, resulting in very low K (10 W m^{-1} K^{-1}) similar to graphite (see Chapter 2 Subsection 2.3.2.3).

Table 3.17 Modelling parameters for the Al/MWCNTs composites.

Matrix		S1 MWCNTs							
K_m (Wm^{-1}K^{-1})	ρ_m (gcm^{-3})	$K_{f,1,2000}$, (Wm^{-1}K^{-1})	$K_{f,2,2000}$, (Wm^{-1}K^{-1})	$K_{f,1,20}$, (Wm^{-1}K^{-1})	$K_{f,2,20}$, (Wm^{-1}K^{-1})	l_f (µm)	d_f (µm)	$\rho_{f,b}$ (gcm^{-3})	$\rho_{f,r}$ (gcm^{-3})
148.4±4.6	2.65	500	10	20	10	4.55±2.75	26.32±8.12	0.28	2.1

For the corrected condition, all the parameters used in the theoretical conditions are applied. However, in this case it accounts for the effect of porosity volume faction (φ) which was obtained using the surface area analysis technique (see Subsection 3.4.4). The φ of the Al/Cu-CFs and Al/MWCNTs composites are given in Chapter 4, Tables 4.5 and 4.20, respectively.

In order to do this, it was assumed that the composites were metallic foams. It is expected that the normalized thermal conductivity (K) of the foam scales with density, according to the following scaling relation:

$$K \approx K_s \left(\frac{\rho}{\rho_s}\right)^n \qquad\qquad \text{eq. (21)}$$

ρ is the density of the foam, K_s and ρ_s are the thermal conductivity and density of the solid metal (in this case the composite) of which the foam is made and n is the exponent for cellular metals, which is normally in the range between 1.65 - 1.8.[28] However, Solórzano et al[29] showed an exponent slightly lower than the previously proposed (1.54±0.03), therefore, in this study n = 1.5 was considered.

When using a 2D case, from the definitions of ρ as the solid mass per total volume of the foam and ρ_s as the solid mass per solid volume, their ratio ρ / ρ_s is the complement of φ, so that:

$$\varphi = 1 - \left(\frac{\rho}{\rho_s}\right) \qquad \text{eq. (22)}$$

Therefore, if considering that K_s is the thermal conductivity of the composite according to the corrected condition (K_c^{corr}) and K is the experimental thermal conductivity of the composite denoted in this study as K_c, then in order to deduct the effect of the φ on the K_c, one can rewrite eq. 21 using eq. 22 where K_c^{corr} becomes:

$$K_c^{corr} = \frac{K_c}{(1-\varphi)^n} \qquad \text{eq. (23)}$$

In the corrected condition, the real filler volume fraction (v_f^{corr}), i.e. the real content of fibres present in the composite matrix after processing (obtained using the surface area analysis technique (see Subsection 3.4.4)), was also accounted. However, this property was only accounted for in the Al/Cu-CFs composites as this method is not reliable to account for the volume fraction of the nanotubes due to their nano size, therefore, for the Al/MWCNTs the volume fraction added during processing (v_f) was used.

The corrected condition was then applied to the thermal conductivity experimental values and also to the models as it was necessary to account the porosity present on the reference material (Al3Mg). The results for both composites, the Al/Cu-CFs and Al/MWCNTs are given in Chapter 4, Subsections 4.2.2.3 and 4.3.5.4.

3.6 Alloy Simulation

The chemical composition of the Al/MWCNTs composites, M1 and M2 (see Table 4.16) was obtained using OES and inputted in the PANDAT 8 (Pan Al.database) software in order to simulate their phase diagrams and predict the volume fractions of the phases formed under non-equilibrium conditions.

References

1.   Primary & Secondary Foundry Alloys - LM0. Available at: http://www.nortal.co.uk/lm0/. (Accessed: 3rd October 2016)

2.   Avedesian, M. M. & Baker, H. ASM Specialty Handbook: Magnesium and Magnesium Alloys. (ASM International, 1999).

3.   Raheama Carbon Fiber Filler offers High Thermal Conductivity. Available at: http://www.ledsmagazine.com/ugc/2009/05/raheama-carbon-fiber-filler-offers-high-thermal-conductivity.html. (Accessed: 25th January 2016)

4.   Paul, E. L., Atiemo-Obeng, V. A. & Kresta, S. M. Handbook of Industrial Mixing: Science and Practice. (John Wiley & Sons, 2004).

5.   Reimer, L. Scanning Electron Microscopy: Physics of Image Formation and Microanalysis. (Springer, 2013).

6.   Goldstein, J. Scanning Electron Microscopy and X-ray Microanalysis: Third Edition. (Plenum, 2003).

7.   Williams, D. B. & Carter, C. B. Transmission Electron Microscopy: A Textbook for Materials Science. (Springer, 2009).

8.   Cox, J. H. & Pidgeon, L. M. The X-ray Diffraction Patterns of Aluminum Carbide Al_4C_3 and Aluminum Oxycarbide Al_4O_4C. Can. J. Chem. 41, 1414–1416 (1963).

9.   Egerton, R. Electron Energy-Loss Spectroscopy in the Electron Microscope. (Springer Science & Business Media, 2011).

10.   Fourier Transform. Available at: http://www.microscopy.ethz.ch/TEM_mathe.htm. (Accessed: 25th September 2016)

11.   Walker, J. S. Fast Fourier Transforms, Second Edition. (CRC Press, 1996).

12.   Reimer, L. & Kohl, H. Transmission Electron Microscopy: Physics of Image Formation. (Springer Science & Business Media, 2008).

13.   Cullity, B. D. Elements of X-ray Diffraction. (Addison-Wesley Publishing Company, 1978).

14.   X-ray Powder Diffraction (XRD). Techniques Available at: http://serc.carleton.edu/research_education/geochemsheets/techniques/XRD.html. (Accessed: 19th January 2016)

15.   Szymanski, H. A. Raman Spectroscopy: Theory and Practice. (Springer Science & Business Media, 2012).

16.   Marouf, A. A. R. S. Characterization of Polymethyl Methacrylate and Silicon Photovoltaic Cells after Processing by Laser Direct Writing Technique. (Sudan University of Science and Technology, 2015).

17.   Lehman, J. H., Terrones, M., Mansfield, E., Hurst, K. E. & Meunier, V. Evaluating the Characteristics of Multiwall Carbon Nanotubes. Carbon 49, 2581–2602 (2011).

18.   Hatakeyama, T. & Quinn, F. X. Thermal analysis: Fundamentals and Applications to polymer science. (Wiley, 1999).

19.   LFA447_Brochure.pdf.   Available   at: https://pec.engr.wisc.edu/Assets/Machines/LFA/LFA447_Brochure.pdf. (Accessed: 17th February 2016)

20.   Wakeham, W. A. & Marc J. Thermal Conductivity Measurement. (CRC Press LLC, 2000).

21.   Gomès, S., Assy, A. & Chapuis, P.-O. Scanning Thermal Microscopy: A review: Scanning Thermal Microscopy. Phys. Status Solidi A 212, 477–494 (2015).

22.   Platinum. Wikipedia, the free encyclopedia (2016).

23.   Bhatta, R. P. et al. High Temperature Thermal Conductivity of Platinum Microwire by 3ω Method. Rev. Sci. Instrum. 81, 114904 (2010).

24.   Cytec Thornel® P-120 2K Carbon Fiber, Pitch Precursor. Available at: http://www.matweb.com/search/datasheet.aspx?matguid=2ffe51d7ff0d48b08c5e 8738d558e61b&ckck=1. (Accessed: 17th February 2016)

25.   Multi-Walled Carbon Nanotubes 20-30nm. Cheap Tubes Available at: https://www.cheaptubes.com/product/multi-walled-carbon-nanotubes-20-30nm/. (Accessed: 17th February 2016)

26.   MWCNTs (>95%, OD: 20-30 nm). Available at: http://www.us-nano.com/inc/sdetail/228. (Accessed: 17th February 2016)

27.   Nanomaterials, S. Nano Powder, Copper Nanoparticles, Lanthanum Oxide, Nano Powders,   Titanium   Nanoparticles.   Available   at: http://www.ssnano.com/inc/sdetail/mwnts/876. (Accessed: 17th February 2016)

28.   Ashby, M. F. et al. Metal Foams: a design guide. (Elsevier, 2000).

29.   Solórzano, E., Rodriguez-Perez, M. A. & de Saja, J. A. Thermal Conductivity of Cellular Metals Measured by the Transient Plane Sour Method. Adv. Eng. Mater. 10, 371–377 (2008).

Chapter 4

Results

4.1 Chapter Outline

In this chapter the results of the study are described. The chapter is divided in two main sections:

1) Al/Cu-CFs composites - In this section the characterization results of the fibres and the composites manufactured by rheocasting and rheocasting+ECAE are outlined. Also, the composites experimental thermal conductivity results are presented and compared with the Hatta-Taya's theoretical thermal conductivity model.

2) Al/MWCNTs composites - This section includes the results of a comprehensive characterization of MWCNTs from different sources in order to assess their morphology, quality, purity and stability. It also includes the characterization results of the composites processed via rheocasting and rheocasting+ECAE and their respective experimental thermal conductivity. In order to assess the real thermal conductivity of the nanotubes used to process the Al/MWCNTs composites, the thermal conductivity result of an individual MWCNT was acquired using the SThM+FEM method and its value included in the theoretical thermal conductivity models. Finally, the results of the comparison between the composites experimental thermal conductivity and the thermal conductivity obtained by the theoretical models are outlined.

4.2 Al/Cu-CFs Composites

Carbon fibres are, in many aspects similar to MWCNTs, they share the same chemical composition, and as a consequence, both are unstable when in contact with molten Al resulting in the formation of Al_4C_3. They also exhibit similar reinforcing geometries and anisotropic thermal properties. For that reason, CF is a good reinforcement or filler choice to test the selected processing route selected in this study (rheocasting and rheocasted+ECAE) described in Chapter 2 Subsection 2.4.3, and assess the composites thermal conductivity prior to conducting experimental studies with MWCNTs which are much more expensive and difficult to handle.

In this section (4.2), the characterisation of the as-received CFs and the Al/Cu-CFs composites processed by both the rheocasting and post-processing ECAE techniques, with their respective thermal conductivity are presented.

4.2.1 Composite Processing and Characterisation

4.2.1.1 CF Filler characterisation

The copper (Cu) coated mesophase pitch-based carbon fibres (Cu-CFs) (see Chapter 3 Subsection 3.2.2.1) were characterised using a FEG-SEM Zeiss Supra operated at 20 kV in secondary electron (SE), backscatter electron (BSE) and In-Lens detector modes.

Fig. 4.1 a) shows a low magnification SE image of the as-received Cu-CFs, and the inset reveals the corresponding high energy dispersive spectrum from the characteristic x-rays detected from the image area, revealing C peaks from the CFs and the Cu peaks from the coating.

Fig.4.1 b) shows a higher magnification SE image of the Cu-CFs. Fig. 4.1 c) shows a low acceleration voltage (3 kV) In-lens high magnification image of a fibre from a batch of uncoated CFs, that reveals the well-aligned graphitic layers arranged almost parallel to the fibre axis. This is a characteristic of mesophase pitch-based carbon fibres (see Fig. 2.4) corroborating the information about the nature of the fibres given by the manufacturer. Finally, Fig. 4.1 d) shows the BSE (atomic (Z) contrast) image of a fibre

cross-section where the fibre (with low atomic number is dark) and the uniform Cu coating (with high atomic number is bright) of ~ 0.25 µm are easily discerned.
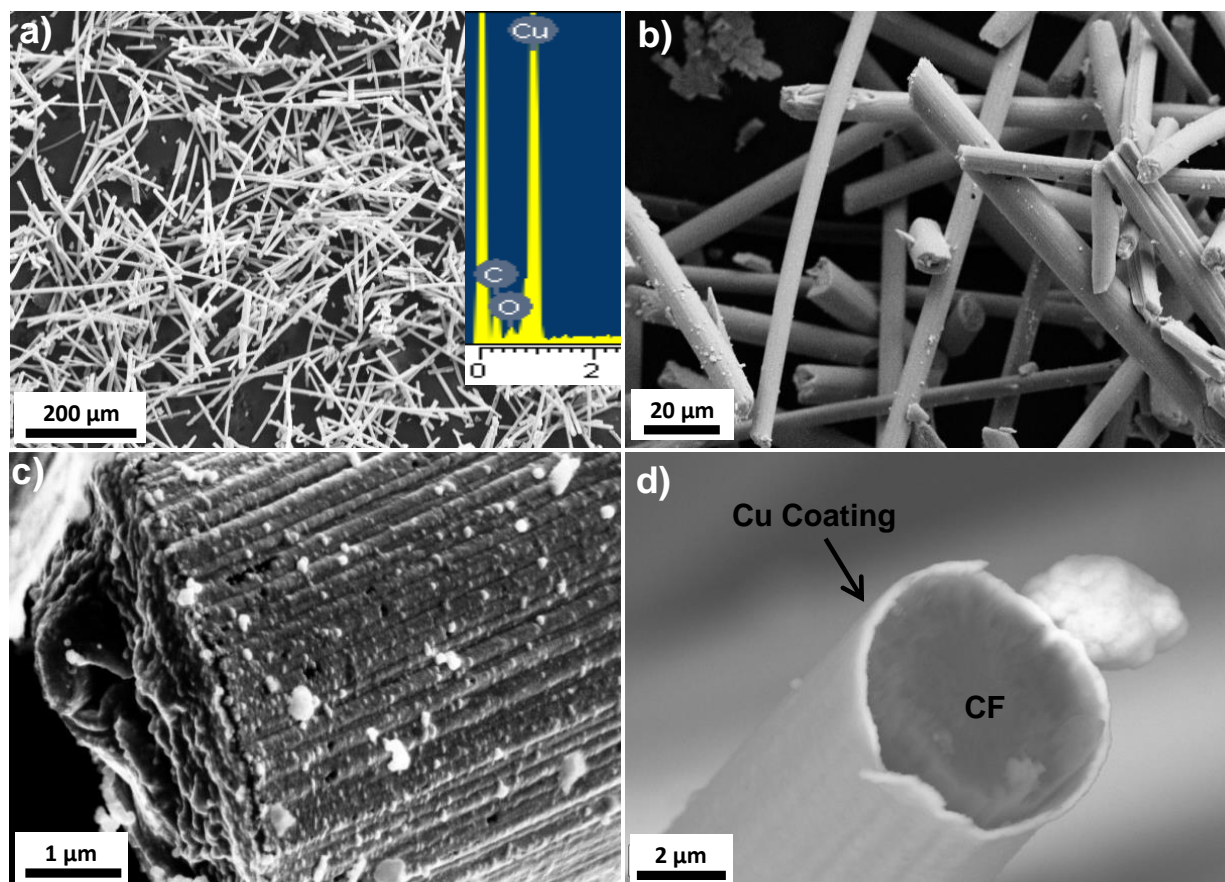
Fig 4.1 SEM micrographs of the Cu-CFs: **(a)** SE low mag. image of the fibres and EDS chemical composition from the field-of-view image area shown in the spectrum (Inset) **(b)** SE high mag image of the fibres. **(c)** High mag. In-Lens image of uncoated fibre revealing the characteristic surface of mesophase pitch-based CFs, and **(d)** High resolution BSE image of cross-section of a CF revealing a uniform Cu coating in bright contrast.

The geometry of the fibres, diameter and length distribution, was obtained from the SEM images using the Image J 1.45s open source software. Five different micrographs were used to obtain 60 diameter and length measurements. The results are displayed in the histograms as shown in Fig. 4.2.

Figs. 4.2 a) and b) show the histograms giving the Cu-CFs diameter and length size distribution, respectively. The fibres show diameter size distribution between 5.48 μm to 15.58 μm with a mean diameter of 8.79±2.03 μm. The length of the CFs was found to vary from 28 μm to 825.88 μm with a mean length of 285.41±177.27 μm. The diameter and length of the Cu-CFs diverge marginally from the values given by the manufacturer, $d_{CFs} \sim 8μm$ and $l_{CFs} \sim 50 - 200μm$ (see section 3.2.2.1, Table 3.5). The increment in diameter (~ 0.8 μm) is justified by the Cu coating.
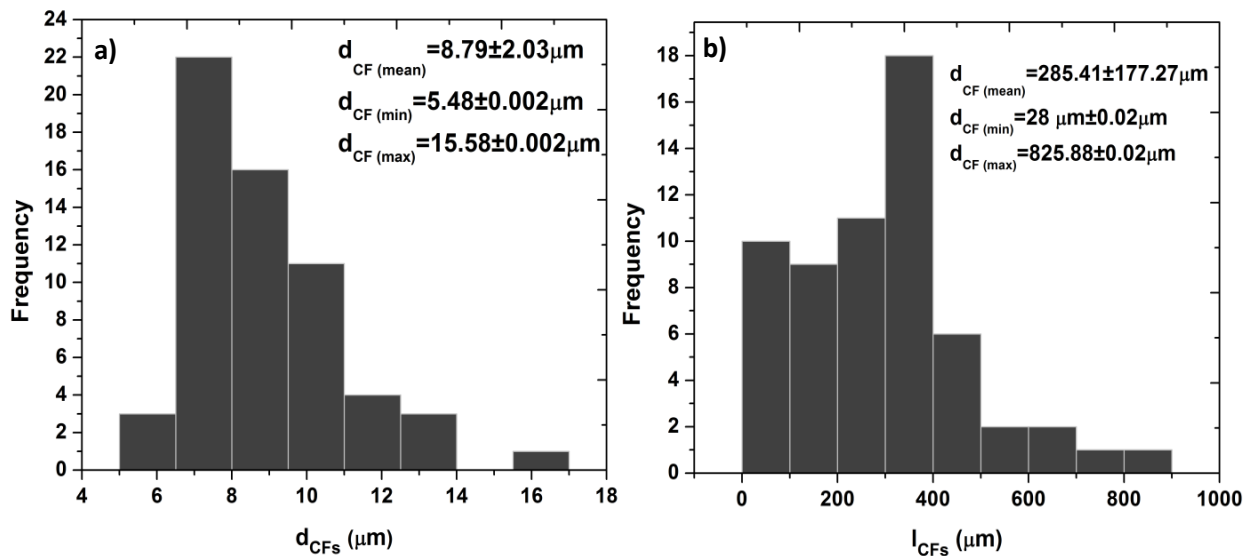
Fig. 4.2 Histograms showing the geometric distribution of the Cu-CFs: **(a)** diameter size distribution and **(b)** length size distribution.

4.2.1.2 Rheocasting

The aluminium matrix composites reinforced with the Cu-CFs fillers were processed using the rheocasting semi-solid metal (SSM) processing method. The processing procedure is a described in Chapter 3, Subsection 3.3.1.

Table 4.1 gives the designation of the Al/Cu-CFs composites (also designated in this study as C system composites) produced. Their final chemical compositions were acquired by means of the optical emission spectroscopy (OES) technique. Sample C0 (Al3Mg, no filler added) has a trace Cu content of 0.002 wt.%, whereas, sample C2 (Al3Mg, w_f = 0.02, 2 wt.% filler added) has a total Cu content of 2.04 wt.%. The analysis

of the composite chemical composition clearly demonstrates the increase in Cu content with increasing filler addition to the matrix (also illustrated in Fig. 4.7).

Table 4.1 Al3Mg/Cu-CFs composites with corresponding respective average chemical composition (wt.%) measured using OES.

Sample	Designation	CFs addition		Measured Composition (wt%)					
		w_f	v_f	Al	Si	Fe	Cu	Mn	Mg
C0	Reference (Al3Mg)	0	0	96.5	<0.003	0.13	**0.002**	0.01	**3.35**
C0.5	Al3Mg/0.5wt%Cu-CFs	0.005	0.006	95	0.09	0.9	**0.33**	0.01	**3.23**
C1	Al3Mg/1wt%Cu-CFs	0.01	0.012	94.3	0.1	1.04	**0.78**	0.01	**3.40**
C1.5	Al3Mg/1.5wt%Cu-CFs	0.015	0.019	93.8	0.14	1.22	**1.21**	0.01	**3.38**
C2	Al3Mg/2wt%Cu-CFs	0.02	0.025	93.3	0.08	0.95	**2.04**	0.01	**3.33**

Figure 4.3, shows the microstructure evolution of the composites with increasing additions of CFs. In Fig. 4.3 a), the microstructure of the sample C0 (no CF addition), reveals a globular grain structure which is a common characteristic of semi-solid metal processing.

Fig. 4.3 b), c), d) and e) depicts the microstructure evolution of the composites, C0.5, C1, C1.5 and C2 respectively, when increasing the CF weight fraction (w_f). The number of fibres (black features) in the matrix is clearly visible and the micrographs also reveal that the fibres are well distributed along the grain boundaries together with AlFe (grey features) based intermetallics. Porosity is also observed and is mainly due to the SSM process employed that tends to trap air inside the melt during the mixing of the fibres. However, some porosity, to a much lesser degree, is originates from CF agglomeration.

Fig. 4.3 f) shows a higher magnification (100x) micrograph of the C2 composite microstructure where the CF are readily discernible and do not show any clear evidence of Al_4C_3 formation. However, it should be noted that good bonding appears to occur between the fibres and surround Al matrix. In order to assess the matrix/filler bonding the interface was studied using SEM and shown in Fig.4.4. Fig. 4.4 a), a low magnification (300x) SEM BSE micrograph from the composite C1.5, which shows individual fibres randomly dispersed along the grain/cell boundaries. The results indicate that good wetting occurred between the matrix and the fibres.
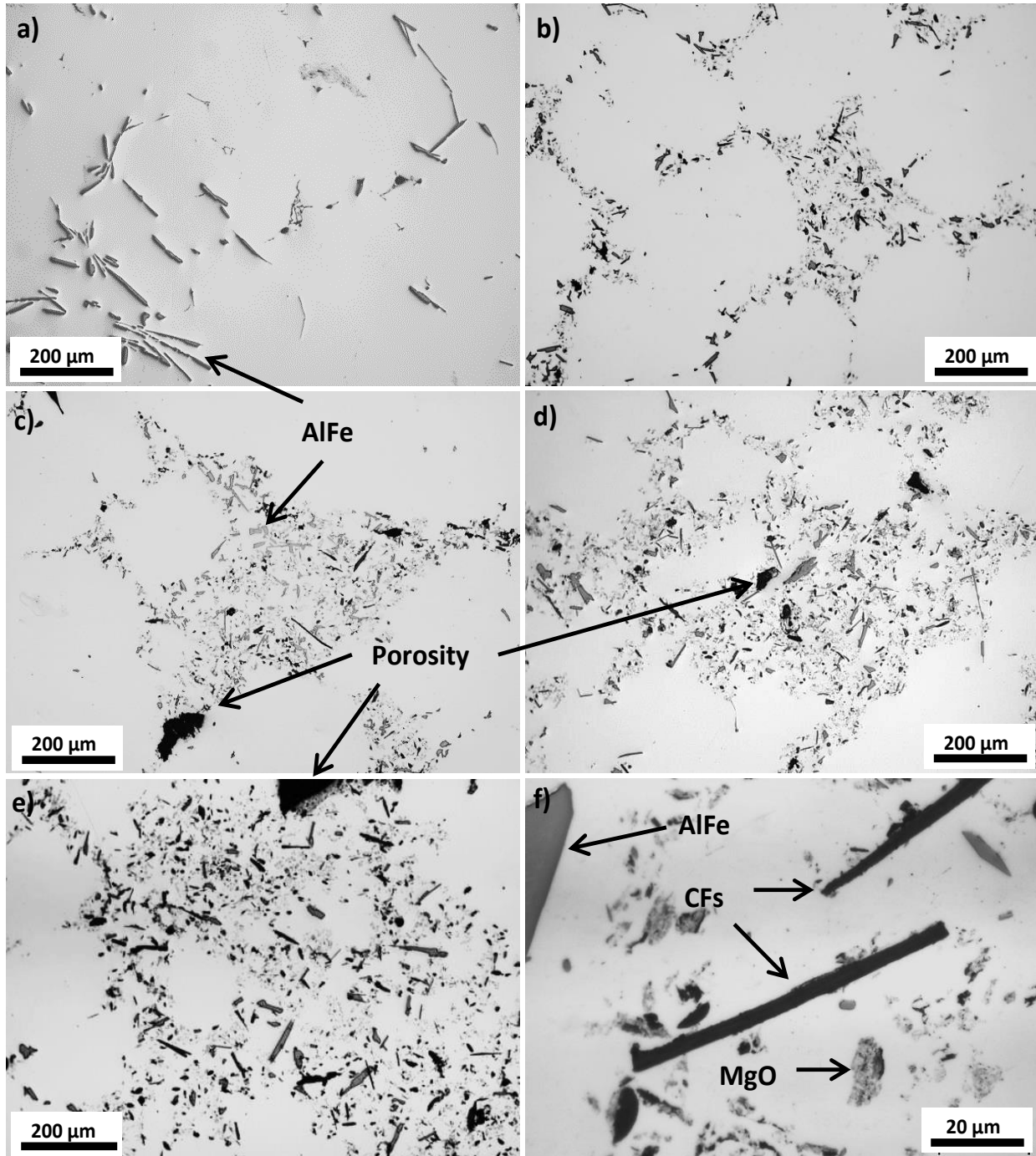
Fig. 4.3 Optical micrographs illustrating the microstructure evolution of the Al3Mg/Cu-CFs composites with increasing filler addition: **(a)** C0, no CF addition (10x Mag.), **(b)** C0.5, 0.5wt.% CF (10x Mag.), **(c)** C1, 1 wt.% CF (10x Mag.), **(d)** C1.5, 1.5 wt.% CF (10x Mag), **(e)** C2, 2 wt.% CF (10x Mag.). **(f)** C2, 2 wt.% CF (100x) revealing the CFs and MgO.
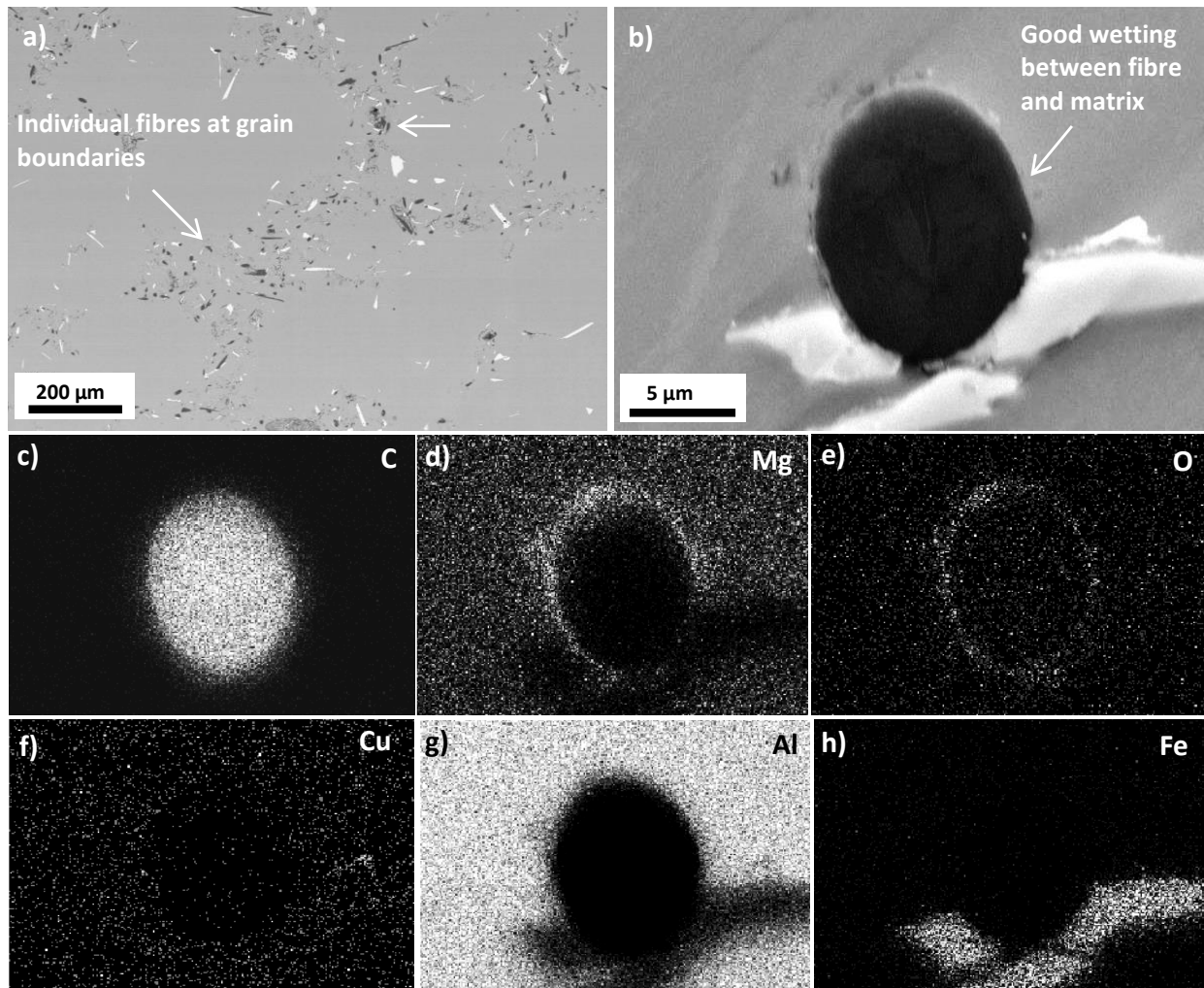
Fig. 4.4 SEM micrographs of C1.5 composite microstructure: **(a)** BSE low magnification (300x) Z (atomic) contrast image showing CF distribution, **(b)** high magnification (14000x) of a CF cross-section showing the interface between the Al matrix and CF and the respective EDS elemental map for: **(c)** C, **(d)** Mg, **(e)** O, **(f)** Cu, **(g)** Al and **(h)** Fe.

Fig. 4.4 b) shows the cross section of a CF embedded in the Al matrix, and the respective EDS elemental map of the Al and CF interface reveals that the improvement in wetting of the CFs with the Al melt could be predominantly driven by the reaction of the Mg (Fig. 4.4 d)) from the matrix with the O (Fig. 4.4 e)) present at the surface of the fibre. Mg was found to react with the CuO and form MgO thereby forcing Cu to diffuse away from the fibre, however, in some cases small traces of Cu are still found around the filler (Fig. 4.4 f)). The CFs are primarily located at the α-Al grain boundaries and in

some cases associated with the AlFe intermetallic possibly inducing the nucleation of the secondary phases (Fig. 4.4 g) and h)). SEM analysis of the CFs showed no evidence of carbon reaction products (Al_4C_3).

4.2.1.3 Equal Channel Angular Extrusion (ECAE)

In order to test the effect of fibre alignment and reduced porosity on the thermal conductivity of the Al/Cu-CFs composites, the C1.5 (Al3Mg, 1.5 wt.% filler added) composite was subjected to the ECAE post-processing method. Due to the limited access to the ECAE facilities, only the C1.5 composite was processed using this technique. The processing details are described in Chapter 3, Subsection 3.3.2.

The composite was subjected to four and six iterations as illustrated in Fig. 2.17. Fig 4.5 shows the microstructure evolution of the C1.5 composite due to the ECAE post-process after 0 iterations (Fig.4.5 a)), 4 iterations (Fig. 4.5 b)) and 6 iterations (Fig. 4.5 c)). After 4 iterations, a high degree of microstructure alignment is already observed as $8.51^0 < \emptyset_{ED-DD} < 9.32^0$, being further improved after 6 iterations as $\emptyset_{ED-DD} \sim 2.69^0$. Fig. 4.5 d), a Z contrast micrograph of the composite after 6 iterations, clearly shows the high degree of CF (dark) and intermetallic (bright) alignment. No porosity was evident in the samples after ECAE post-processing with 6 iterations.

Despite the successful production of a highly aligned Al/Cu-CFs composite microstructure, it is crucial that the ECAE method does not induce substantial damage on the CFs during extrusion as this may reduce the fibres thermal conductivity capability.

Fig. 4.6, shows the damaged induced on the fibres due to the ECAE post-processing. The structure of the fibres, studied using SEM in secondary electron (SE) mode as shown in Fig. 4.6 a) reveal the extent of the damage that can be induced on the fibres after 6 passes, where the fibre is completely destroyed. However, not all the fibres suffer damage to the same extent, which may be due to the fibres initial orientation prior to deformation (the worst case scenario resulting for those fibres with a 90^0 angle between their orientation and the deformation direction).
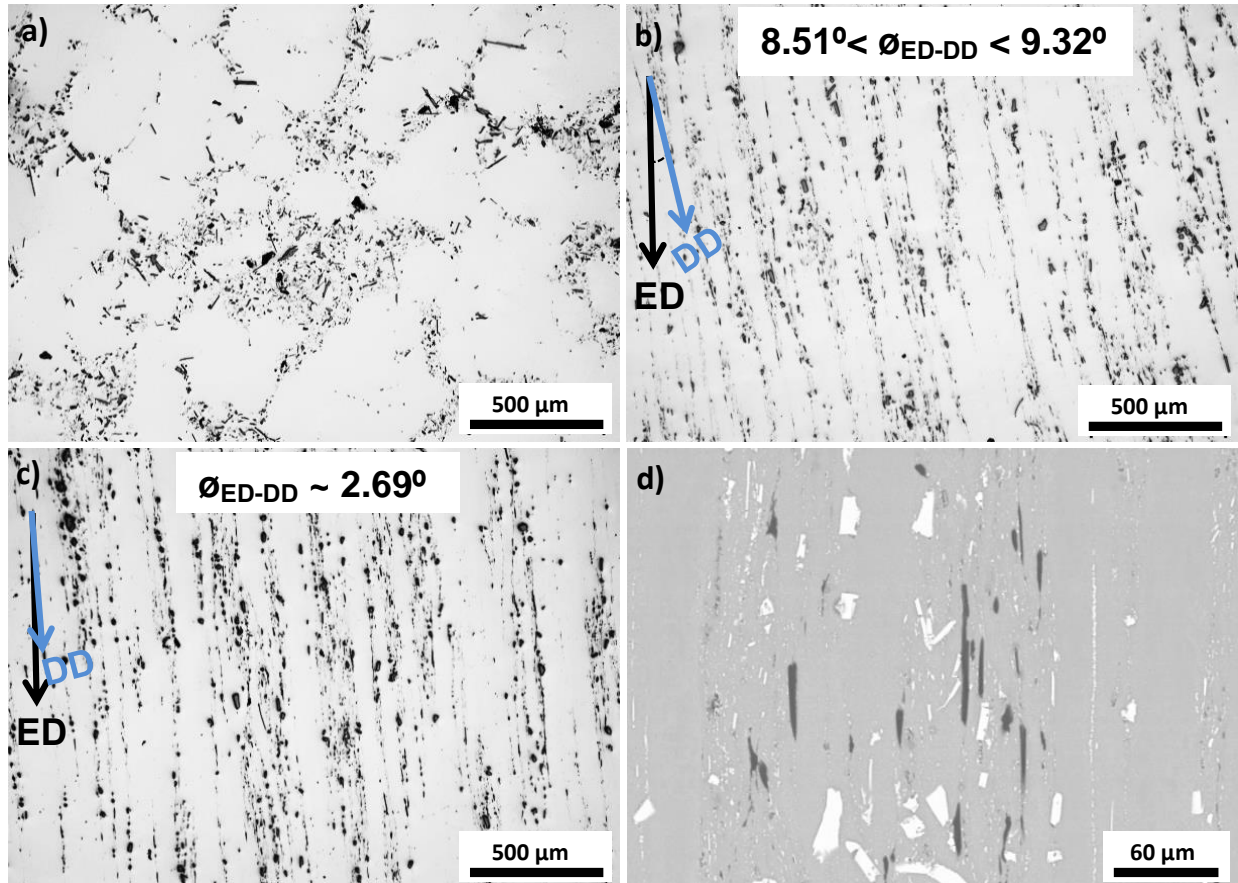
Fig. 4.5 C1.5 composite micrographs displaying the microstructure evolution due to ECAE post-processing: **(a)** O.M. (5x), 0 iterations, **(b)** O.M. (5x) 4 iterations, $8.51^0 <$ $\emptyset_{ED-DD} < 9.32^0$, **(c)** O.M. (5x) 6 iterations, $\emptyset_{ED-DD} \sim 2.69^0$ and **(d)** SEM BSE low magnification (1000x), 6 iterations displaying a high alignment between CFs (dark) and intermetallics (bright) within the Al matrix.

Fig. 4.6 b) shows another fibre with less damage evident, however, higher magnification micrographs of the selected areas of the damaged CF (Fig. 4.6 c) and d)) reveals the extent of the internal damage as the fibre becomes aligned with the deformation direction (DD).
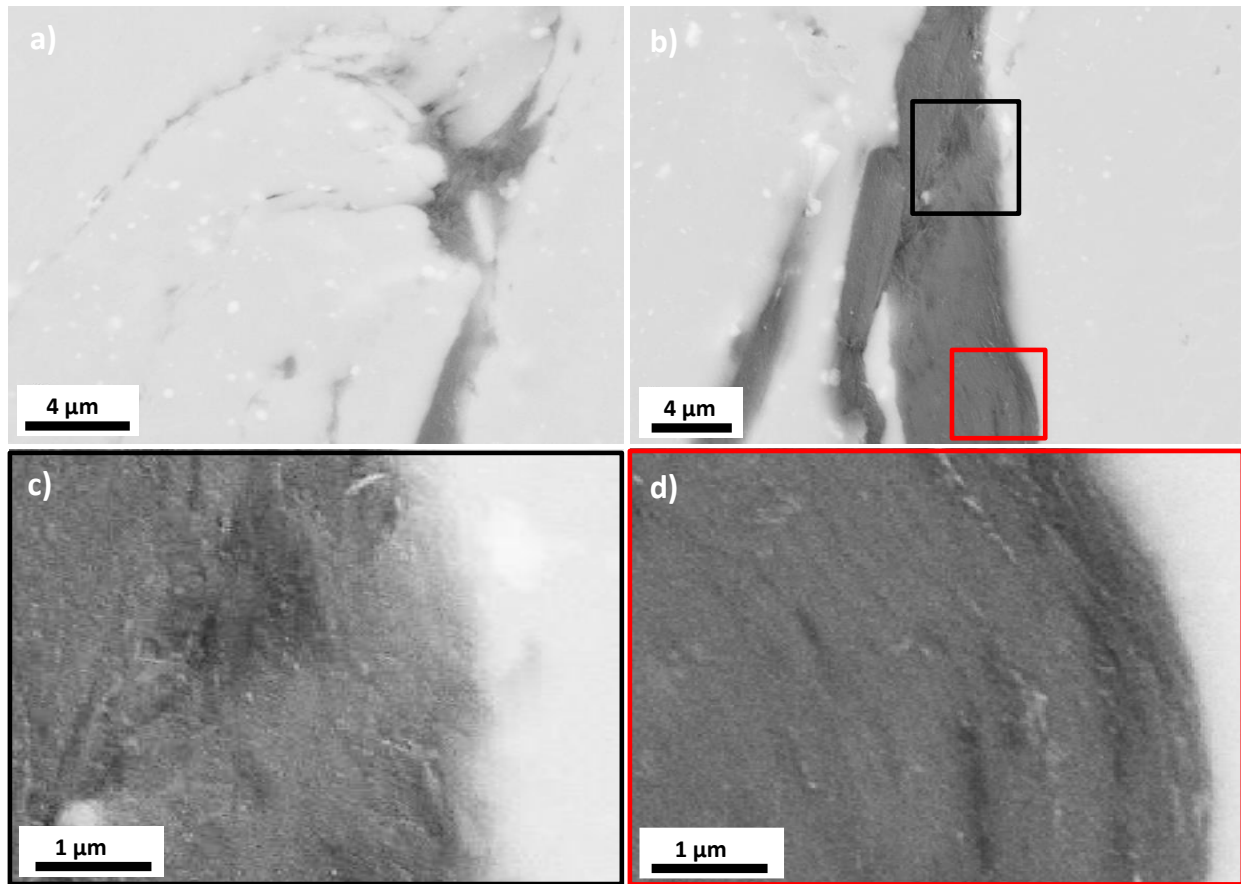
Fig. 4.6 SEM SE micrographs revealing the damage induced on the CF after 6 iterations: **(a)** Completely destroyed CF and **(b)** damaged CF. High magnification micrographs of selected areas of the damaged CF where its structure has fractured **(c)** or aligned **(d)** in the deformation direction.

4.2.2 Al/Cu-CFs Effective Thermal Conductivity

The thermal conductivity of the Al3Mg/Cu-CFs composites produced via rheocasting and rheocasting followed by ECAE post processing, was measured using the laser flash technique (see Chapter 3 Subsection 3.5.1). In order to verify the composites thermal conductivity efficacy, the experimental values were compared with the theoretical calculated from Eshelby´s equivalent inclusion model (see Chapter 2 Section 2.5). The results obtained, are described hereafter in this chapter whilst the thermal conductivity testing details are described in Chapter 3, Subsection 3.5.1.

4.2.2.1 Rheocasting

Fig.4.7 illustrates the thermal conductivity evolution for the Al3Mg/Cu-CFs composite system produced via rheocasting, as a function of increasing CF volume fraction (v_f) content. It also demonstrates the measured Mg and Cu alloying content for each composite. Table 4.2 provides the data used in the plot illustrated in Fig. 4.7.
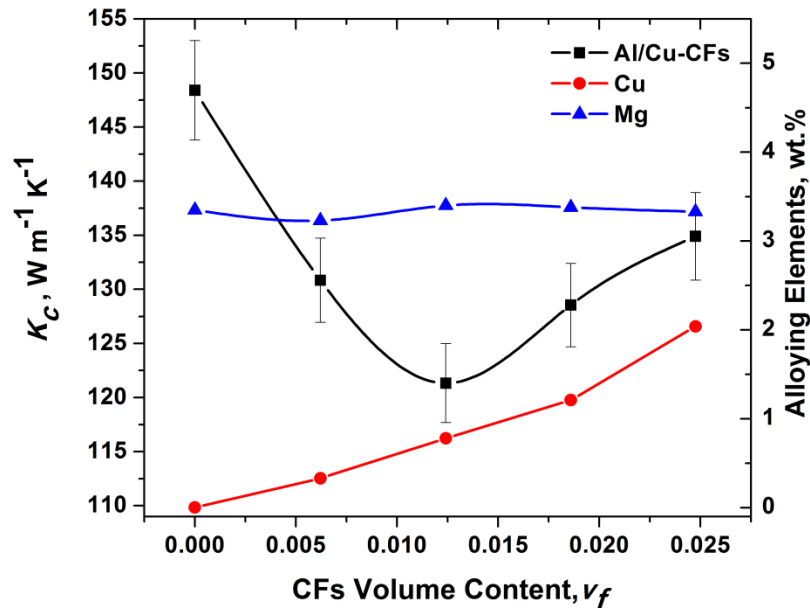
Fig.4.7. Thermal conductivity of the Al3Mg/Cu-CFs composite produced via rheocasting versus CFs volume content (v_f). For reference the comparative Cu and Mg alloying content for the different composites is also indicated.

Table 4.2 Al3Mg/Cu-CFs composites samples with respective average chemical composition (wt. %) measured by OES and corresponding thermal conductivity, K_c, measured with laser flash technique.

Sample	CFs add.	Composition (wt%)						K_c
	v_f	Al	Si	Fe	Cu	Mn	Mg	(W m^{-1} K^{-1})
C0	0	96.5	<0.003	0.13	0.002	0.01	3.35	148.4 ± 4.5
C0.5	0.006	95	0.09	0.9	0.33	0.01	3.23	130.8 ± 3.9
C1	0.012	94.3	0.1	1.04	0.78	0.01	3.40	121.3 ± 3.6
C1.5	0.019	93.8	0.14	1.22	1.21	0.01	3.38	128.5 ± 3.9
C2	0.025	93.3	0.08	0.95	2.04	0.01	3.33	134.9 ± 4.1

The thermal conductivity results show that the introduction of CFs, up to 2 wt.% (v_f = 0.025) within the Al3Mg alloy, decreases the thermal conductivity, $K_{c,C2}$ = 134.9 ± 4.1 W m^{-1} K^{-1}, in comparison with the reference C0 ($K_{c,C0}$ = K_m),which thermal conductivity is $K_{c,C0}$ = 148.4 ± 4.5 W m^{-1} K^{-1}.

The addition of CFs to the Al3Mg matrix decreases the thermal conductivity even for the lowest level of filler addition, as observed for C0.5 (v_f = 0.006) $K_{c,C0.5}$ = 130.8 ± 3.9 W m^{-1} K^{-1}, reaching the lowest value when adding 1wt.% (v_f= 0.012), $K_{c,C1}$= 121.3 ± 3.6 W m^{-1} K^{-1}. For higher filler addition contents, the CFs started to counteract the detrimental effect on thermal conductivity as observed for the C1.5 composite (v_f = 0.019) with $K_{c,C1.5}$ = 128.5 ± 3.9 W m^{-1} K^{-1}. Nevertheless, even the maximum filler addition of CFs, $K_{c,C2}$= 134.9 ± 4.1 W m^{-1} K^{-1}, within the Al3Mg matrix was not sufficient to reach the thermal conductivity of the reference alloy C0, $K_{c,C0}$ = 148.4 ± 4.5 Wm^{-1} K^{-1}.

Fig. 4.7 and Table 4.2 also illustrate the content of Mg (main alloying constituent) and Cu (arising from the fibre coating). Mg and Cu elements have a detrimental effect on the thermal conductivity of the matrix (K_m), therefore any increase on the content of these elements will decrease this property value substantially[1]. The Mg content is relatively constant for the different composites. Whereas, the Cu content increases proportionally with the rise of CF content reaching a maximum of 2.04 wt.% for the C2 composite. This indicates that despite the random orientation of the fibres in the matrix, the thermal contribution from the fillers is starting to overcome the negative effect of Cu indicating that for higher CF contents (> 2wt.%) the thermal conductivity of the composite could overcome the thermal conductivity of the reference alloy (C0).

4.2.2.2 Rheocasting followed by ECAE

In order to study the degree of contribution from the CF alignment within the Al alloy matrix to the composite thermal conductivity (K_c), the C1.5 composite was processed by means of rheocasting + equal channel angular extrusion (ECAE) post-processing. The ECAE alters the alignment of the fibres and the resultant K_c of the sample was measured using the laser flash technique. Unfortunately, due to limited funds and access to the facilities only the C1.5 sample was subjected to ECAE.

Fig. 4.8 shows the thermal conductivity evolution of the composite C1.5 as a function of the number of iterations. The data used to plot the graph is shown Table 4.3.
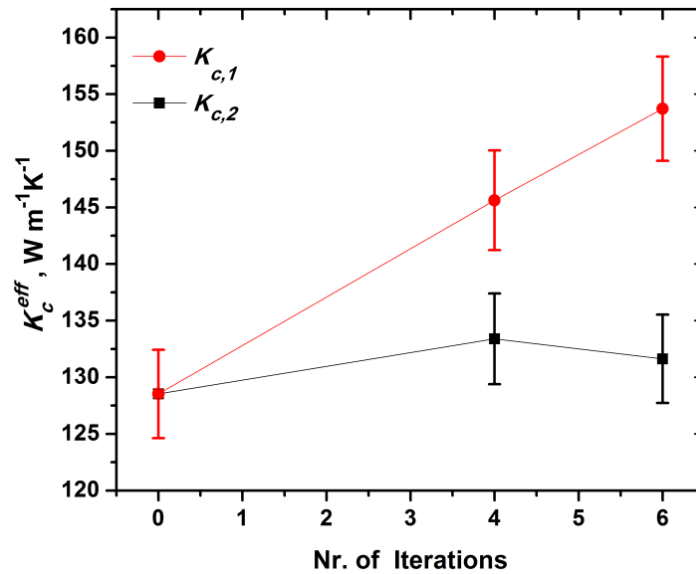
Fig. 4.8. Effect of ECAE post-processing in terms of induced deformation on the effective thermal conductivity of the C1.5 (1.5 wt.% CFs) Al3Mg/Cu-CF composite. Results are given for the direction parallel to ED ($K_{c,1}$) and in the direction perpendicular to ED ($K_{c,2}$) as a function of the number of ECAE iterations.

Table 4.3 Thermal conductivity of the ECAE post-processed C1.5 composite (Al3Mg/Cu-CFs, 1.5 wt.% CFs).

$K_{c,C1.5}$ (W m^{-1} K^{-1})		
Iterations	$K_{c,1}$	$K_{c,2}$
0	128.5 ± 3.9	128.5 ± 3.9
4	145.6 ± 4.4	133.4 ± 4
6	153.7 ± 4.6	131.6 ± 3.9

The thermal conductivity results for the C1.5 composite showed that the deformation induced to align the fibres (see Fig. 4.5), resulted in a continuous thermal conductivity improvement in the ED ($K_{c,1}$) as the number of iterations increased, reaching the maximum value after 6 iterations, $K_{c,C1.5,6i,1}$ = 153.7 ± 4.6 W m^{-1} K^{-1}. This is an increment of 19.6% when compared with the 0 iterations sample, $K_{c,C1.5,0i,1}$= 128.5 ± 3.9 W m^{-1} K^{-1}

(+ 25.17 W m^{-1} K^{-1}). It also exhibited a higher thermal conductivity than the reference alloy, K_m = 148.4 ± 4.5 W m^{-1} K^{-1} (+ 5.31 W m^{-1} K^{-1}) an increase of ~ 3.6%. The improvement in thermal conductivity by fibre alignment was observed despite the damage induced on the fibres (see Fig. 4.6) and the overall microstructure deformation, which both have a detrimental contribution with respect to the composite thermal conductivity.

$K_{c,2}$ increased marginally, reaching its peak after 4 iterations, $K_{c,C1.5,4i,2}$ = 133.4 ± 4 W m^{-1} K^{-1} and after 6 iterations it marginally decreased again, $K_{c,C1.5,6i,2}$ = 131.6 ± 3.9 W m^{-1} K^{-1}. Nevertheless, the thermal conductivity of the C1.5 composite after ECAE was always higher than for the C1.5 composite not processed by ECAE, $K_{c,C1.5,0i}$ = 128.5 ± 3.9 W m^{-1} K^{-1}. The increment in thermal conductivity is believed to be due to porosity closure, however, the improvement is limited due to the low thermal conductivity of the CFs through their cross-section.

4.2.2.3 Effective Thermal Conductivity of Composite

In order to study the thermal conductivity efficacy of the Al/Cu-CFs composites produced by rheocasting and rheocasting followed by ECAE, it is important to compare the obtained results with the thermal conductivity values of the "ideal composite". In other words, with values which are very close to those the composites would have if optimized for every parameter (i.e. no porosity, homogeneous dispersion, no interface reactions, etc…).

The theoretical Eshelby´s equivalent inclusion model developed by Hatta-Taya et al[2,3] for 2D short fibre reinforced composites, which accounts for the composite filler geometry and orientation, was used for this effect. This model does not take into account the interfacial thermal barrier, therefore the thermal conductivity of the fibre is equal to the effective thermal conductivity of the fibre (K_f = K_f^{eff}). For the model description and boundary conditions, see Chapter 2 Section 2.5.

The thermal conductivity comparison was performed according to two circumstances referred to as the "theoretical" and "corrected" conditions, described in Chapter 3,

Subsection 3.5.1. The composites porosity and real v_f of the CFs from each composite were obtained by analysing 10 micrographs from each composite sample using the image processing software ImageJ, using the procedure as described in Chapter 4 Subsection 3.4.4, and the data accounted in the "corrected" condition.

The effect of the increasing Cu content (see Fig. 4.7) on the thermal conductivity of the composite was not accounted for the modelling as it was not possible to obtain experimental data, i.e. Al3Mg+Cu addition (same Cu content as that for the composites but without the CFs).

The characterisation of the Al/Cu-CFs composites processed via rheocasting show that the fibres are introduced and randomly dispersed at the Al matrix grain boundaries, as shown in Fig. 4.4 a). However, ECAE post-processing, begins to align the CFs (see Fig. 4.5) in the deformation direction.

Fig. 4.9 gives the composite´s thermal conductivity boundary conditions calculated for both, "theoretical" and "corrected" conditions using the Hatta-Taya Eshelby´s equivalent inclusion model, in order to consider the effect of the fibre orientations observed in the composite characterization results. The modelling parameters used are given in Table 3.16. Also the data used and obtained for both conditions, "theoretical" and "corrected" are given in table 4.4 and 4.5, respectively.

Fig. 4.9 a) shows the experimental thermal conductivity of the composites K_c processed via rheocasting and rheocasting+ECAE as a function of CF content and the Hatta-Taya's model boundary conditions according to the "theoretical" condition. The thermal conductivity of the reference material (i.e. sample C0 with no filler addition), obtained experimentally using the laser flash technique, was used as the matrix value in the model. ($K_{c,C0} = K_m = 148.4 \pm 4.5$ W m^{-1}K^{-1}).
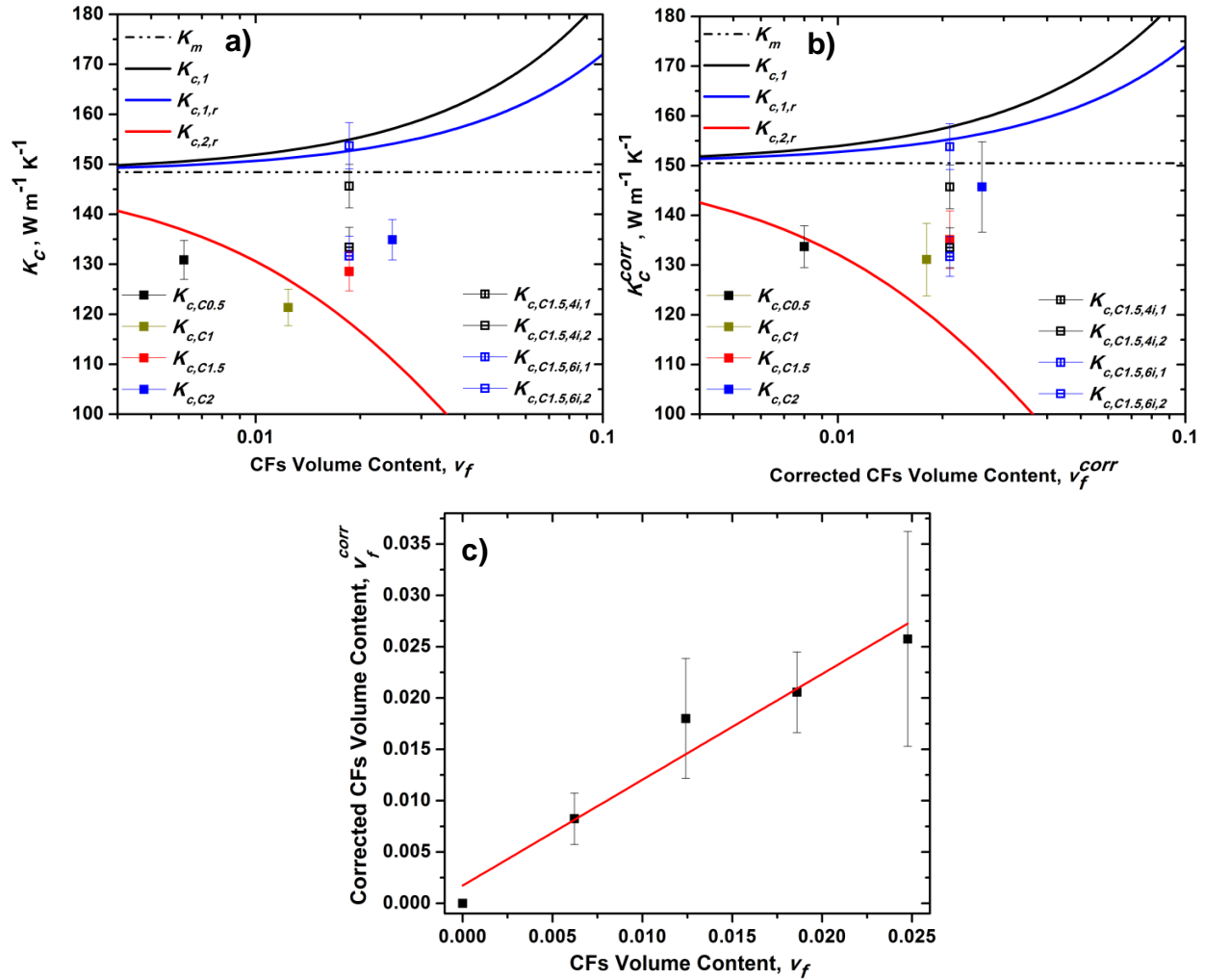
Fig. 4.9 Hatta-Taya Eshelby´s equivalent inclusion model for effective thermal conductivity as a function of fibre content of the Al/Cu-CFs composites. **(a)** "Theoretical" condition simulation. **(b)** "Corrected" condition simulation accounting for the porosity and CFs v_f^{corr} content. **(c)** Linear relationship between the theoretical v_f and corrected v_f^{corr} CFs volume fraction content.

According to the CF manufacturer the in-plane thermal conductivity of the fibres range from 500 W m^{-1}K^{-1} $\leq K_{f,1} \leq$ 600 W m^{-1} K^{-1} (see table 3.5), and for this study the lower value (500 W m^{-1}K^{-1}) was used However, CF have very low thermal conductivity in the out-of-plane direction, i.e. a value closest to that of amorphous carbon (a-C), which is considered to be $K_{f,2}$ = 10 W m^{-1}K^{-1} in this study.

Ideally, due to the CFs anisotropic thermal behaviour, the composites produced via rheocasting should have K_c between the in-plane $K_{c,1}$, (also referred to as the higher boundary in this study) and out-of-plane $K_{c,2,r}$, (lower boundary). Whereas, in the case of the composites processed by rheocasting+ECAE, K_c should be close to the higher boundary and lower boundary values due to the induced fibre alignment. Table 4.4 gives the Al/Cu-CF composites thermal conductivity values obtained experimentally, and calculated for the "theoretical" condition taking into account fibre orientation.

Table 4.4 Thermal conductivity values of Al/Cu-CF composites obtained experimentally and calculated for the "theoretical condition" taking into account fibre orientation.

Sample	v_f	K_c W m^{-1} K^{-1}	$K_{c,1}$ (in-plane) W m^{-1} K^{-1}	$K_{c,1,r}$ (in-plane) W m^{-1} K^{-1}	$K_{c,2,r}$ (out-of-plane) W m^{-1} K^{-1}
C0	- - -	148.4 ± 4.5	148.4	148.4	148.4
C0.5	0.006	130.8 ± 3.9	150.5	149.8	137.2
C1	0.012	121.3 ± 3.6	152.6	151.2	127.5
C1.5	0.019	128.5 ± 3.9	155.1	152.8	117.8
C1.5$_{4i,\,1}$	0.019	145.6 ± 4.4	155.1	152.8	- - -
C1.5$_{4i,\,2}$	0.019	133.4 ± 4	- - -.	- - -	117.8
C1.5$_{6i,\,1}$	0.019	153.7 ± 4.6	155.01	152.8	- - -
C1.5$_{6i,\,2}$	0.019	131.6 ± 4	- - -.	- - -	117.8
C2	0.025	134.9 ± 4.1	157.2	154.2	110.6

The description of the nomenclature used to designate the thermal conductivity for the different samples according to their conditions is given in Chapter 3, Subsection 3.5.3.

The thermal conductivity experimental value for the C0.5 composite sample is $K_{c,C0.5}$ = 130.8 ± 3.9 W m^{-1} K^{-1}, whereas the modelling for the theoretical condition predicts in and out-of-plane K_c values of: $K_{c,C0.5,1}$ = 150.5 W m^{-1} K^{-1}, $K_{c,C0.5,r}$ = 149.8 W m^{-1} K^{-1}, $K_{c,C0.5,2,r}$ = 137.2 W m^{-1} K^{-1}, respectively. The C0.5 composite experimental value $K_{c,C0.5}$ does not lie between the boundary conditions as expected, in fact it is lower than the lower boundary condition $K_{c,0.5,2,r}$ (- 6.4 W m^{-1} K^{-1}).

The experimental thermal conductivity of the composite C1 sample is $K_{c,C1}$ = 121.3 ± 3.6 W m^{-1} K^{-1}, whilst modelling shows that $K_{c,C1,1}$= 152.6 W m^{-1} K^{-1}, $K_{c,C1,1,r}$ = 151.2 W m^{-1} K^{-1} $K_{c,C1,2,r}$ = 127.5 W m^{-1} K^{-1}. Again the experimental value lies below the lower boundary condition $K_{c,C1,2,r}$ (- 3.3 W m^{-1} K^{-1}).

The experimental thermal conductivity of the C1.5 composite sample is $K_{c,C1.5} = 128.5 \pm$ 3.9 W m^{-1} K^{-1}, while modelling shows that $K_{c,C1.5,1} = 155.1$ W m^{-1} K^{-1}, $K_{c,C1.5,1,r} = 152.8$ W m^{-1} K^{-1} and $K_{c,C1.5,2,r} = 117.8$ W m^{-1} K^{-1}. In this case, the experimental value $K_{c,C1.5}$ therefore lies between the boundary conditions values, however, still close to the lower limit $K_{c,C1.5,2,r}$ and below the thermal conductivity of the matrix, K_m. However, the composite sample C1.5 processed by the ECAE technique (the only batch of samples processed using this technique) shows good agreement with Eshelby´s model.

As the number of iterations increase the experimental in (1) and out-of-plane (2) thermal conductivity values become closer to the higher and lower boundaries. The experimental in-plane thermal conductivity values with increasing iterations are $K_{c,C1.5,4i,1} = 145.6 \pm 4.4$ W m^{-1} K^{-1} for 4 iterations and $K_{c,C1.5,6i,1} = 153.7 \pm 4.6$ W m^{-1} K^{-1} for 6 iterations, whereas the respective simulated values using the Eshelby model are $K_{c,C1.5,1} = 155.1$ W m^{-1} K^{-1}, $K_{c,C1.5,1,r} = 152.8$ W m^{-1} K^{-1} (see Table 4.4). After 4 iterations, the experimental composite thermal conductivity increased in comparison to the as-rheocasted C1.5 composite but still well below the value predicted by the model However, the value after 6 iterations is in good agreement with the model for the in-plane condition and proves that fibre alignment does improve composite thermal conductivity.

The experimental out-of-plane thermal conductivity values with increasing iterations are $K_{c,C1.5,4i,2} = 133.4 \pm 4$ W m^{-1} K^{-1} for 4 iterations and $K_{c,C1.5,6i,2} = 131.6 \pm 4.6$ W m^{-1} K^{-1} for 6 iterations. Using the Eshelby model the respective simulated out-of-plane thermal conductivity is $K_{c,C1.5,2,r} = 117.8$ W m^{-1} K^{-1}. Despite the decreasing K_c with increasing number of ECAE iterations, as was expected, it did not follow the same magnitude observed in the in-plane condition and experimental values obtained were still above the value given for by the model, + 15.6 W m^{-1} K^{-1} in comparison with the 4 iterations, and + 13.8 W m^{-1} K^{-1} in comparison with the 6 iterations composite.

Finally, the experimental thermal conductivity of composite sample C2 is $K_{c,C2} = 134.9 \pm$ 4.1 W m^{-1} K^{-1}, whilst the modelling gives a value of $K_{c,C2,1} = 157.2$ W m^{-1} K^{-1}, $K_{c,C2,1,r} =$

154.2 W m^{-1} K^{-1} and $K_{c,C2,2,r}$ = 110.6 W m^{-1} K^{-1}. In this case, the experimental value lies between the lower, $K_{c,C2,2,r}$, and the higher , $K_{c,C2,1}$, boundary conditions as expected.

Fig. 4.9 b) shows the comparison of K_c from the Al/Cu-CFs composites (processed using both rheocasting and ECAE as a function of increasing CF content), with the Eshelby´s equivalent inclusion model for effective thermal conductivity. However, in this case the "corrected" condition is applied. Fig. 4.9 c) shows a linear relationship between the theoretical (v_f) and real/corrected (v_f^{corr}) CFs v_f and proves that, in this case, using image analysis method to determine the real v_f (see Table 4.5) of the fibres is viable.

The porosity volume fraction (φ) present in the composite samples was calculated using image analysis (see Chapter 3, Subsection 3.4.4) and the "corrected" thermal conductivity of the composite (K_c^{corr}) calculated using eqs. 22 and 23, in order to remove the effect of porosity content on K_c. This resulted in a thermal conductivity increase for all samples. The corresponding φ and K_c^{corr} values are given in Table 4.5.

Table 4.5 Al/Cu-CF composites thermal conductivity values calculated for the "corrected" condition taking into account fibre orientation.

Sample	φ	v_f^{corr}	K_c^{corr} W m^{-1} K^{-1}	$K_{c,1}^{corr}$ W m^{-1} K^{-1}	$K_{c,1,r}^{corr}$ W m^{-1} K^{-1}	$K_{c,2,r}^{corr}$ W m^{-1} K^{-1}
C0	0.01 ± 0.005	- - -	150.5 ± 4.8	150.5	150.5	150.5
C0.5	0.014 ± 0.007	0.008 ± 0.003	133.7 ± 4.2	153.2	152.3	135.4
C1	0.05 ± 0.02	0.018 ± 0.006	131.1 ± 7.3	156.7	154.6	120.4
C1.5	0.03 ± 0.01	0.021 ± 0.004	135.1 ± 5.8	157.8	155.3	116.5
C1.5$_{4i, 1}$	0.0003 ± 3.21E-05	0.021 ± 0.004	145.7 ± 4.4	157.8	155.3	- - -
C1.5$_{4i, 2}$	0.0003 ± 3.21E-05	0.021 ± 0.004	133.5 ± 4	- - -	- - -	116.5
C1.5$_{6i, 1}$	0.0003 ± 0.0001	0.021 ± 0.004	153.8 ± 4.6	157.8	155.3	- - -
C1.5$_{6i, 2}$	0.0003 ± 0.0001	0.021 ± 0.004	131.7 ± 4	- - -	- - -	116.5
C2	0.05 ± 0.01	0.026 ± 0.01	145.7 ± 9.1	159.5	156.4	110.6

The thermal conductivity of the reference material C0 (i.e. no filler addition) obtained experimentally with a porosity content φ_{C0} = 0.01 ± 0.005, was corrected and used as the matrix value in the "corrected" model giving a value of. $K_{c,C0}^{corr}$ = 150.5 ± 4.8 W m^{-1} K^{-1}.

The corrected experimental thermal conductivity value for the C0.5 composite sample with $\varphi_{C0.5}$ = 0.014 ± 0.007 and $v_{f,C0.5}^{corr}$ = 0.008 ± 0.003 is $K_{c,C0.5}^{corr}$= 133.7 ± 4.2 W m^{-1} K^{-1},

whereas the modelling for the corrected condition predicts in and out-of-plane values of: $K_{c,CO.5,1}^{corr}$ = 153.2 W m^{-1} K^{-1}, $K_{c,CO.5,1,r}^{corr}$ = 152.3 W m^{-1} K^{-1} and $K_{c,CO.5,2,r}^{corr}$ = 135.4 W m^{-1} K^{-1}. For the corrected condition, the C0.5 composite experimental value $K_{c,CO.5}^{corr}$ does not lie between the boundary conditions, however it is close to the lower boundary condition $K_{c,CO.5,2,r}^{corr}$ (- 1.7 W m^{-1} K^{-1}).

In the case of the C1 composite with φ_{C1}= 0.05 ± 0.02 and $v_{f,C1}^{corr}$ = 0.018 ± 0.006 the $K_{c,C1}^{corr}$= 131.1 ± 7.3 W m^{-1} K^{-1}, whereas the modelling for the corrected condition predicts in and out-of-plane values of: $K_{c,C1,1}^{corr}$ = 156.7 W m^{-1} K^{-1}, $K_{c,C1,1,r}^{corr}$ = 154.6 W m^{-1} K^{-1} and $K_{c,C1,2,r}^{corr}$ = 120.4 W m^{-1} K^{-1}. The correction factor thus brought the composite experimental value of C1, $K_{c,C1}^{corr}$, between the boundary condition values.

C1.5 composite with $\varphi_{C1.5}$ = 0.03 ± 0.01 and $v_{f,C1.5}^{corr}$ = 0.021 ± 0.004 has $K_{c,C1.5}^{corr}$= 135.1 ± 5.8 W m^{-1} K^{-1}, whereas the modelling for the corrected condition predicts in and out-of-plane values of: $K_{c,C1.5,1}^{corr}$ = 157.8 W m^{-1} K^{-1}, $K_{c,C1,1,r}^{corr}$ = 155.3W m^{-1} K^{-1} and $K_{c,C1,2,r}^{corr}$ = 116.5 W m^{-1} K^{-1}. The corrected composite C1.5 thermal conductivity experimental value, $K_{c,1.5}^{corr}$, also lies between the boundary conditions values as expected.

The experimental thermal conductivity of the composite C1.5 processed by the ECAE technique using the corrected condition is also in good agreement with the Eshelby´s model. The experimental in-plane thermal conductivity values with increasing iterations are $K_{c,C1.5,4i,1}^{corr}$ = 145.7 ± 4.4 W m^{-1} K^{-1} ($\varphi_{C1.5,4i,1}$ = 0.0003 ± 3.21E-05 and $v_{f,C1.5,4i,1}^{corr}$ = 0.021 ± 0.004) for 4 iterations and $K_{c,C1.5,6i,1}^{corr}$ = 153.8 ± 4.6 W m^{-1} K^{-1} ($\varphi_{C1.5,6i,1}$ = 0.0003 ± 0.0001 and $v_{f,C1.5,6i,1}^{corr}$ = 0.021 ± 0.004) for 6 iterations, whereas the respective simulated values are $K_{c,C1.5,1}^{corr}$ = 157.8 W m^{-1} K^{-1}, $K_{c,C1.5,1,r}^{corr}$ = 155.3 W m^{-1} K^{-1}. After 4 iterations, despite the correction factor the composite thermal conductivity is still below the higher boundary values (-12.1 W m^{-1} K^{-1} and -9.6 W m^{-1} K^{-1}) predicted by the model. The value after 6 iterations, according to the theoretical condition, in the corrected condition is again in good agreement with the model in the in-plane direction or higher boundary values (-4 W m^{-1} K^{-1} and -1.5 W m^{-1} K^{-1}).

The corrected experimental out-of-plane thermal conductivity values with increasing iterations are $K^{corr}_{c,C1.5,4i,2} = 133.5 \pm 4$ W m^{-1} K^{-1} ($\varphi_{C1.5,4i,2} = 0.0003 \pm 3.21E^{-5}$ and $v^{corr}_{f,C1.5,4i,2} = 0.021 \pm 0.004$) for 4 iterations and $K^{corr}_{c,C1.5,6i,2} = 131.7 \pm 4$ W m^{-1} K^{-1} ($\varphi_{C1.5,6i,2} = 0.0003 \pm 0.0001$ and $v^{corr}_{f,C1.5,6i,2} = 0.021 \pm 0.004$) for 6 iterations. The respective simulated out-of-plane corrected thermal conductivity is $K^{corr}_{c,C1.5,2,r} = 116.5$ W m^{-1} K^{-1} and shows that as for the theoretical condition the corrected experimental values are again above the lower boundary value given by the model, + 17 W m^{-1} K^{-1} in comparison with the 4 iterations and + 15.2 W m^{-1} K^{-1} in comparison with the 6 iterations composites.

Finally, the corrected experimental thermal conductivity of the composite C2 with $\varphi_{C2}= 0.05 \pm 0.01$ and $v^{corr}_{f,C2} = 0.026 \pm 0.01$ is $K^{corr}_{c,C2}= 145.7 \pm 9.1$ W m^{-1} K^{-1}, whereas the modelling for the corrected condition predicts in and out-of-plane values of: $K^{corr}_{c,C2,1} = 159.5$ W m^{-1} K^{-1}, $K^{corr}_{c,C2,1,r} = 156.4$ W m^{-1} K^{-1} and $K^{corr}_{c,C2,2,r} = 110.6$ W m^{-1} K^{-1}. The corrected composite C1.5 thermal conductivity experimental value, $K^{corr}_{c,2}$, still lies between the boundary conditions values as expected.

The thermal conductivity modelling of the composite fits better with the experimental results for the corrected condition rather than the theoretical condition. It demonstrates the importance of porosity content and the real volume fraction of the fibres present on the composite thermal conductivity.

4.3 Al/MWCNTs Composites

This section (4.3) is divided in five subsections where the results of the study to understand if multi-walled carbon nanotubes (MWCNTs) can be used to produce ultra-high thermal conductivity Al matrix composites via rheocasting+ECAE processing techniques are outlined. These subsections are:

> ➢ Morphology of MWCNTs.
> ➢ MWCNTs Quality and Purity
> ➢ MWCNTs Stability
> ➢ Composite Processing and Characterization
> ➢ Effective Thermal Conductivity of Composite.

4.3.1 Morphology of Multi-Walled Carbon Nanotubes

The morphology of multi-walled carbon nanotubes (MWCNTs) plays a key role on the properties they exhibit, and thermal conductivity is no exception, therefore an extensive characterisation of the morphology and geometry of these fillers is of major importance.

Scanning and transmission electron microscopy techniques (SEM and TEM) were employed to characterise the morphology of all three "as-received" MWCNTs from different sources, S1 and S2 MWCNTs synthetized via combustion chemical vapour deposition (CCVD) and S3 vertically-aligned multi-walled carbon nanotubes (VAMWCNTs) synthetized via aerosol-assisted chemical vapour deposition (ACVD) (see table 3.5). Powder (agglomerations) shape, nanotube length, and inner and outer diameter were observed and the results obtained outlined hereafter.

4.3.1.1 Powder Morphology

The fillers were observed using the SEM secondary electron (SE) imaging in order to reveal their topography.

S1 when compared with S2 and S3 showed the finest powder of all, as can be seen in Figs. 4.10 a), e) and i). The low magnification images, Figs. 4.10 a) (x90) and 4.1 b) (x500), show that the powder is comprised of rounded low sphericity particles, with a particle size distribution range between ~5µm to ~110µm and an average particle size of ~31 ± 26.1µm. At high magnifications, Figs. 4.10 c) (x15000) and 4.1 d) (x100000), the surface of the particles reveal highly entangled tubular MWCNTs.

S2 sample presents an intermediate powder size, bigger than S1 but smaller than S3. Fig. 4.10 e) and f) clearly shows that the particles have an equant shape and a distribution size range between ~180 µm to ~900 µm (average size of 554.97±178.69 µm). The observation of the particles or nanotube bundles surface at high magnification, Figs. 4.10 g) (x15000) and 4.10 h) (x100000), reveal entangled MWCNTs however the nanotube diameter is substantially smaller than S1 which is synthetized using the same technique (CCVD).
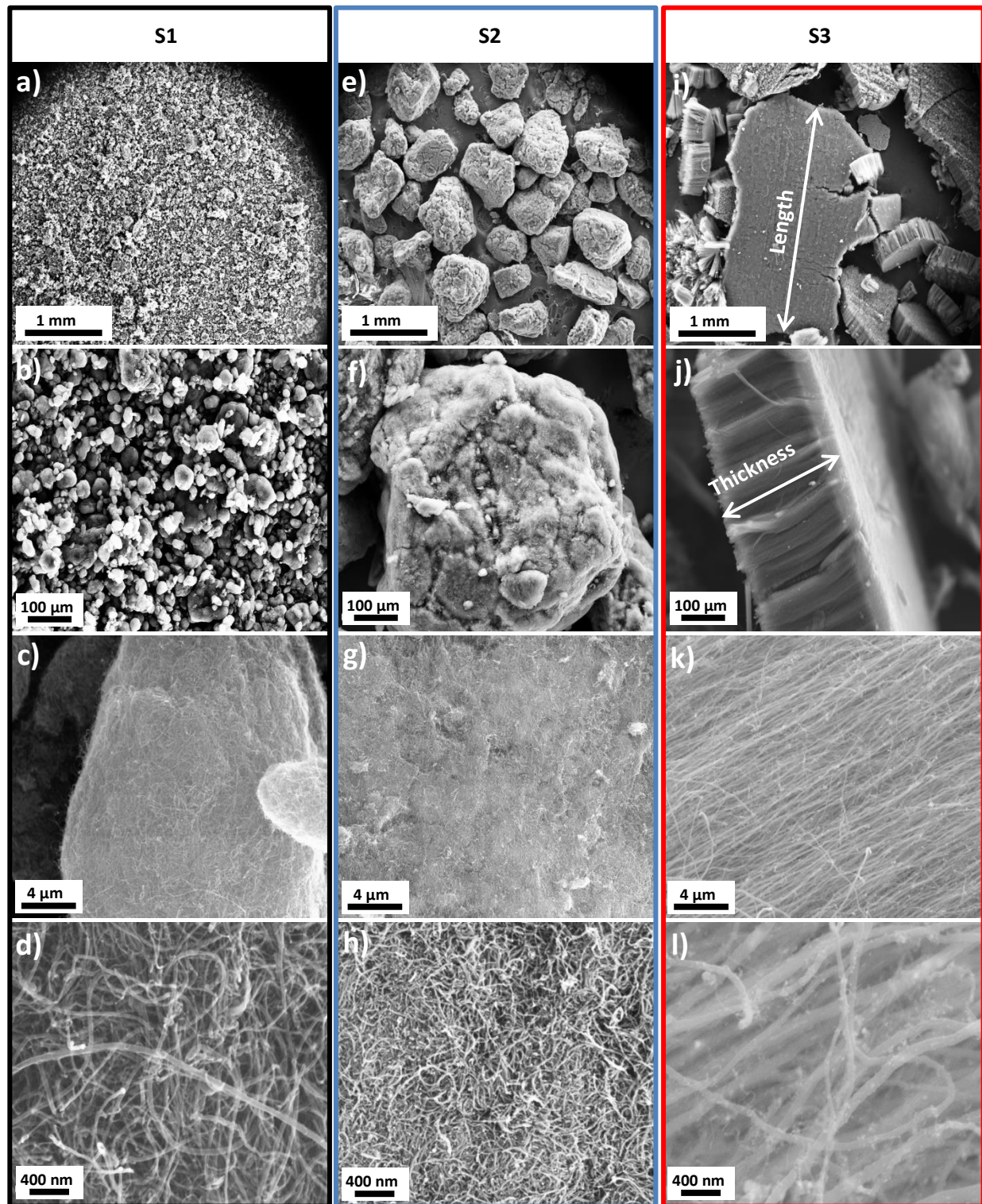
Fig. 4.10 SEM SE images showing various morphologies for the 3 different types of "as-received" MWCNTs studied. **(a)**, **(b)**, **(c)** and **(d)** S1 (CCVD MWCNTs); **(e)**, **(f)**, **(g)** and **(h)** S2 (CCVD MWCNTs); **(i)**, **(j)**, **(k)** and **(l)** S3 (ACVD VAMWCNTs).

Sample S3, revealed that the VAMWCNTs powder is in the form of large carpets, Fig. 4.10 i) (x90), with a highly aligned tube structure, as shown in Fig. 4.10 j) (x500). These features are commonly observed for these types of nanotubes.

The carpets are found to have an average length of 968.04 ± 673.48 µm with length distribution ranging from ~170µm to ~2800µm. The thickness distribution size of the carpets ranges between ~150µm and ~300µm and average thickness of 222.21 ± 34.81 µm. Additionally, according to Figs. 4.12 j) (x900) and 4.12 k) (x15000), the thickness of the carpets is also believed to be close to the VAMWCNTs length. Fig. 4.10 l) (x100000) corroborates the high degree of nanotube alignment, however, some unaligned nanotubes are observed. Their diameter is clearly the largest among the samples studied.

4.3.1.2 MWCNTs Length

The length of the S1 and S2 MWCNTs was obtained by analysing their respective TEM images using the Gatan Microscopy Suite Digital Micrograph software. The length of S3 VAMWCNTs in this study is assumed to be similar to the thickness of the carpets. Fig.4.11 shows the size distribution of the nanotubes length for the three sources of MWCNTs and values are given in Table 4.6.
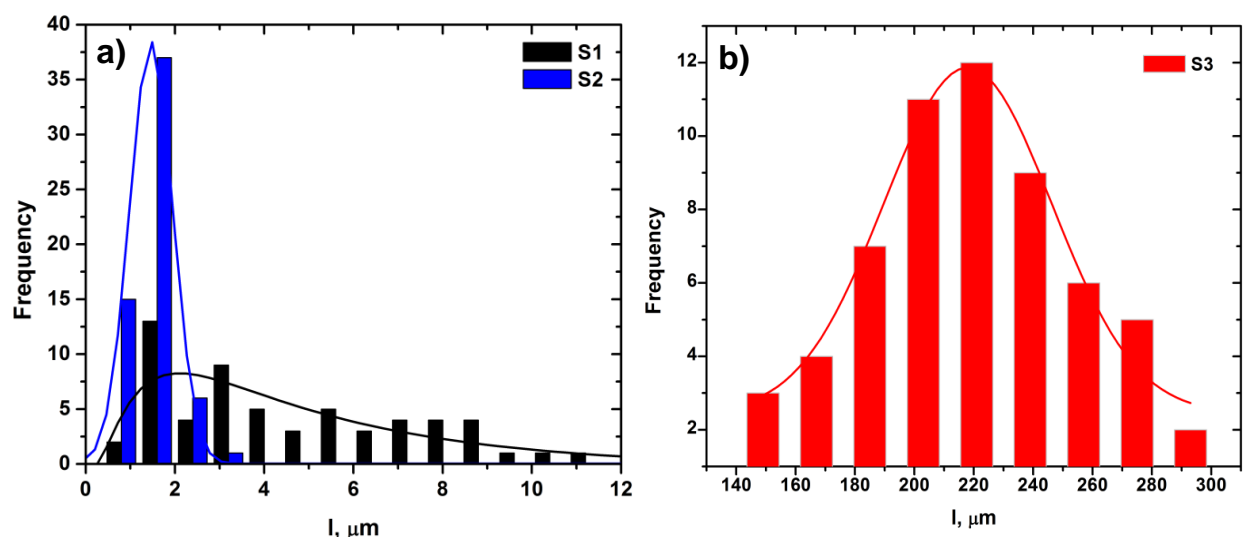

Fig. 4.11 Graphs illustrating the observed MWCNTs length (l) distribution: **(a)** S1 and S2, and **(b)** S3.

Fig. 4.11 a) shows the nanotube length distribution of S1 and S2 MWCNTs. S2 MWCNTs are the shortest, with an average length of 1.5±0.52 μm, they also exhibit the shortest length distribution ranging from 0.47 μm (min) to 3 μm (max).

Table 4.6 Observed length distribution of S1, S2 and S3 MWCNTs

Source	$l_{(min)}$ (μm)	$l_{(max)}$ (μm)	$l_{(mean)}$ (μm)
S1	0.98	11.3	4.6±2.75
S2	0.47	3	1.50±0.52
S3	153.7	297.6	219.9±36.1

Whereas S1 MWCNTs, despite being synthetized by the same method as S2 (CCVD), show an average nanotube length of 4.6 ± 2.75 μm and length distribution ranging from 0.98 μm to 11.3 μm, clearly longer than S2. Finally, Fig. 4.11 b) depicts the length distribution of the S3 MWCNTs. These nanotubes are the longest of all three sources, with an average length of 219.9 ± 36.1 μm and length distribution ranging from 153.7 μm to 297.6 μm. The comparison of the length of the nanotubes show: $l_{S2} < l_{S1} < l_{S3}$.

4.3.1.3 MWCNT Diameters

The study of the nanotubes inner and outer diameter was performed by analysing high resolution images acquired with TEM using Gatan Microscopy Suite Digital Micrograph software. Fig. 4.12 illustrates the MWCNTs inner (d_i) and outer (d_o) diameter size distribution and the values are provided in Table 4.7.

Fig. 4.12 a) shows the inner diameter size distribution for the MWCNTs from the different sources. S2 MWCNTs have the smallest inner diameter, with an average size of 4.80±1.48 nm, they also exhibit the narrowest range of inner diameters amongst the three sources, ranging from 2.03 nm (min) to 9.26 nm (max). S1 MWCNTs, exhibit an average inner diameter of 6.84±2.45 nm and size distribution ranging from 1.57 nm (min) to 12.49 nm (max). S3 MWCNTs have the largest inner diameter, an average of 10.87± 4.66 nm and size distribution with the widest range, from 3.14 (min) nm to 22.27 nm (max). Thus a comparison of the inner diameter of the nanotubes shows: $d_{i,S2} < d_{i,S1} < d_{i,S3}$.
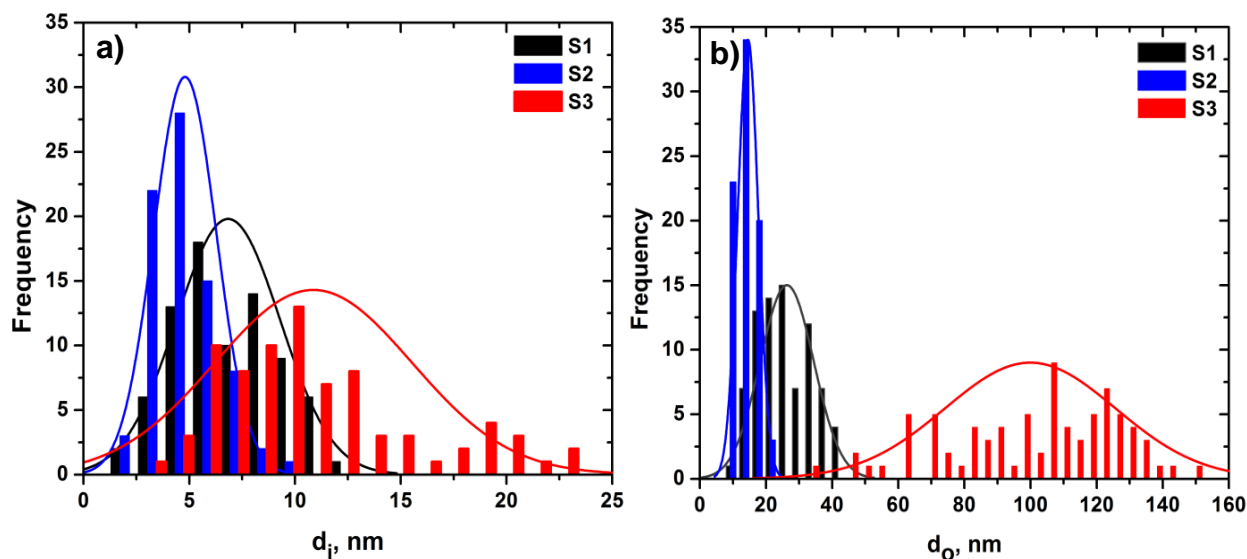
Fig. 4.12 Graphs illustrating the observed MWCNTs inner and outer diameter distribution size: **(a)** S1 and S2, and **(b)** S3.

Table 4.7 Observed inner (d_i) and outer (d_o) diameter distribution of S1, S2 and S3 MWCNTs

Source	d_i (nm)			d_o (nm)		
	min	max	mean	min	max	mean
S1	1.57	12.49	**6.84±2.45**	11.85	42.66	**26.3±8.12**
S2	2.03	9.26	**4.80±1.48**	9.98	23.93	**14.55±3.11**
S3	3.14	22.27	**10.87± 4.66**	34.32	150.14	**99.93 ± 25.79**

Fig. 4.12 b) depicts the outer diameter size distribution of the S1, S2 and S3 MWCNTs. The outer diameter of the nanotubes from the different sources followed a similar trend as in the inner diameter, with $d_{o,S2} < d_{o,S1} < d_{o,S3}$.

S2 MWCNTs have the smallest outer diameter, with an average of 14.55±3.11 nm and size distribution ranging from 9.98 nm to 23.93 nm. S1 MWCNTs have a marginally higher outer diameter than S2, with an average of 26.32±8.12 nm and also wider size distribution, ranging from 9.98 nm (min) to 23.93 nm (max). Whilst, S3 MWCNTs have the largest outer diameter, 99.93 ± 25.79 nm and also the largest distribution size, from 34.32 nm (min) to 150.14 nm (max).

4.3.2 MWCNTs Quality and Purity

The synthesis of MWCNTs, regardless of the method used, always produces a significant amount of defects and metallic and carbonaceous impurities which are detrimental for their physical and mechanical properties, as has been discussed in the literature review (Chapter 2 Subsection 2.3.2).

Here, the results of the quality and purity study of the 3 "as-received" MWCNTs sources are presented. For this purpose, no single technique is able to achieve a thorough study of the MWCNTs. Instead, a combination of techniques are required to fully characterise the quality and purity of the MWCNTs. The techniques used are: Raman spectroscopy, x-ray diffraction (XRD), thermogravimetry (TG) + differential scanning calorimetry (DSC) also known as simultaneous thermal analysis (STA) and lastly transmission electron microscopy + energy dispersive spectroscopy (TEM+EDS).

4.3.2.1 Raman Spectroscopy

Raman spectroscopy was employed to assess and compare the quality of the MWCNTS powders. The procedures and parameters used are described in Chapter 3, Subsection 3.4.2.2. Fig. 4.13 reveals the Raman spectra obtained from S1, S2 and S3 MWCNTs normalized to the D band. The respective Raman ratios and band positions are given in Table 4.8.

The Raman spectra gives an insight into the quality and purity of the nanotubes by providing a somewhat quantitative approach by means of the I_D/I_G, $I_{G'}/I_G$ and $I_{G'}/I_D$ ratios. The D band indicates the presence of impurities and defects such as carbonaceous impurities with sp^3 bonding and broken sp^2 bonds in the sidewalls. The G band indicates the crystallinity present in a MWCNT sample. Whereas, G' band reveals the degree of metallicity of the nanotubes and also reveals the presence of long-range order.[4,5]

According to the data shown in Table 4.8 obtained using the Raman spectrometer, the S2 MWCNTs synthetized via CCVD shows the highest amount of impurities and defects. This is evident when comparing the intensity of the D band (defects) with the G band (crystallinity), which exhibit the highest ratio $I_D/I_G=1.38\pm0.11$.
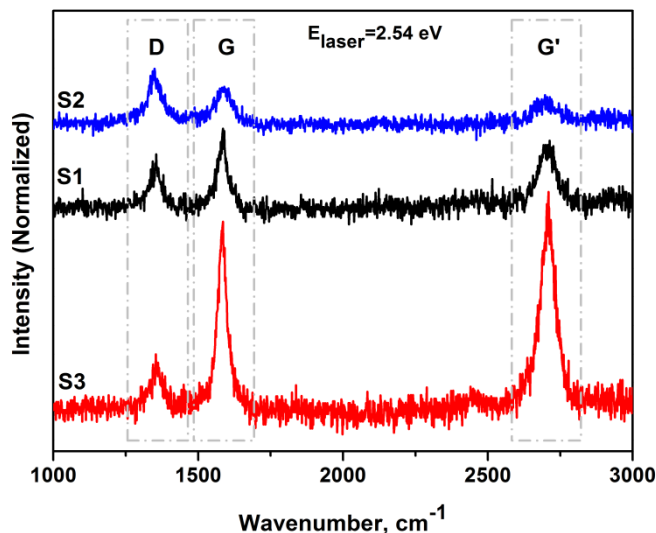
Fig. 4.13 Raman spectroscopy signature of S1 and S2 CCVD MWCNTs, and S3 ACVD VAMWCNTs. The spectrums are normalized to the D band.

Table 4.8 Raman band ratios and band positions of S1, S2 and S3 MWCNTs.

Sample	$\dfrac{I_D}{I_G}$	$\dfrac{I_{G'}}{I_G}$	$\dfrac{I_{G'}}{I_D}$	D (cm^{-1})	G (cm^{-1})	G' (cm^{-1})
S1	0.7 ± 0.03	0.93 ± 0.06	1.33 ± 0.07	1354.32 ± 3.22	1582.26 ± 1.85	2705.11 ± 5.22
S2	1.38 ± 0.11	0.75 ± 0.05	0.54 ± 0.03	1352.66 ± 5.01	1585.84 ± 4.94	2697.27
S3	0.31 ± 0.03	1.16 ± 0.01	3.72 ± 0.29	1353.16 ± 3.64	1582.04 ± 2.55	2709.27 ± 1.08

However, it also shows the lowest $I_{G'}/I_D$=0.54±0.03, as one would expect, as this indicates the metallicity of the material that decreases as the material becomes less ordered. The S1 MWCNTs, also synthetized via the CCVD method, show an intermediate quality when compared to the powders studied. The Raman ratios are I_D/I_G=0.7±0.03 and $I_{G'}/I_D$=1.33±0.07.

Finally, the S3 VAMWCNTs, processed via ACVD, have the highest quality, with an I_D/I_G=0.31±0.03 and $I_{G'}/I_D$=3.72±0.29 revealing the lowest amount of disordered material amongst the 3 powders studied. Nevertheless, it must be noted that Raman spectroscopy does not take into account all the impurities present in the powder samples, such as the Fe-based catalysts used to synthetize the nanotubes. These impurities can strongly affect the thermal stability and thermal conductivity of the nanotubes and must also be quantified.

4.3.2.2 X-Ray Diffraction (XRD)

X-ray diffraction (XRD) is a useful technique to examine the atomic structure and crystalline phases present in a material. The MWCNTs powders were placed in a BRUKER D8 ADVANCED XRD device and examined (see Chapter 3, Subsection 3.4.2.1 for the methodology).

Fig. 4.14 shows the XRD traces for each MWCNT powder, the traces are calibrated to the (0002) peak.
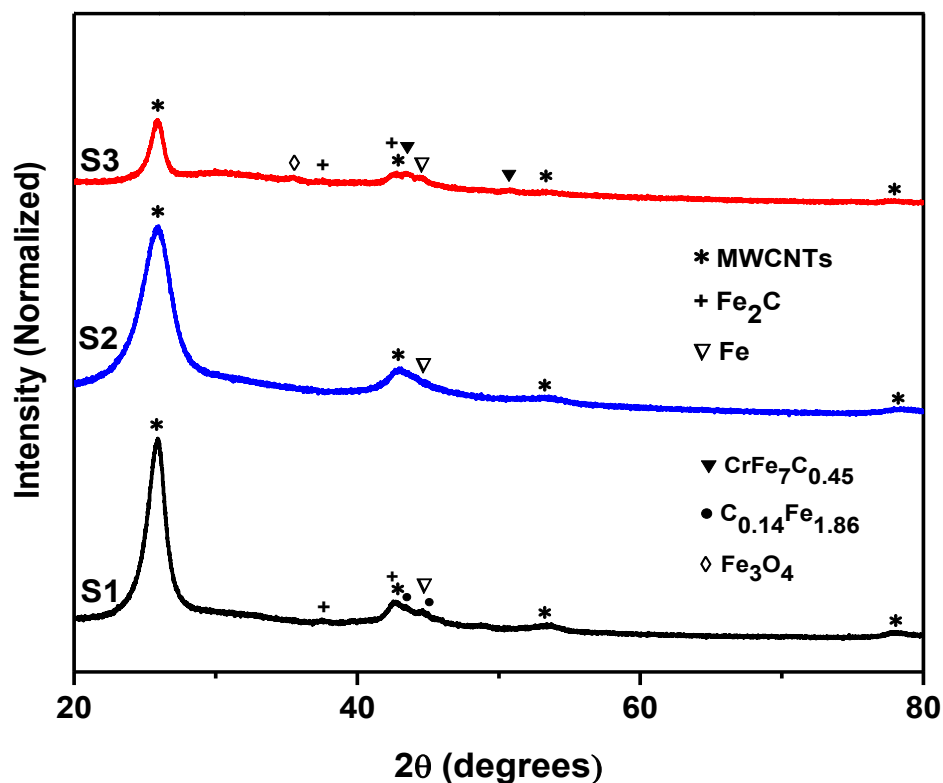
Fig. 4.14 The XRD traces for the S1, S2 and S3 MWCNT powders.

Table 4.9 gives the crystallographic information of the crystalline phases as found in the international centre for diffraction data (ICDD). The traces illustrate the peaks generated by the common MWCNT diffraction planes, namely the (0002), (10$\bar{1}$0), (0004) and (11$\bar{2}$0) planes. In this study, only the (0002) peak is discussed further as this is the most important. Peaks generated by the Fe and Fe-based compounds are also observed.

Table 4.9 Crystallographic information obtained from the international centre for diffraction data on the phases found in the XRD study of the MWCNT powders.

Elements	2θ Angle (º)	{h,k,i,l} {h,k,l} Planes	d(Å)	Reference 2015 ICDD
MWCNTs	25.9188	0002	3.434760	00-058-1638
	42.957	$10\bar{1}0$	2.103680	
	53.2886	0004	1.717650	
	78.7221	$11\bar{2}0$	1.214560	
Fe_2C	37.0407	101	2.425000	00-037-0999
	42.7590	111	2.113000	
Fe	44.6732	110	2.026800	00-006-0696
$C_{0.14}Fe_{1.86}$	43.4408	101	2.081400	00-044-1289
	45.0221	110	2.011900	
$CrFe_7C_{0.45}$	43.5054	222	2.078460	03-065-9781
	50.6730	400	1.800000	
Fe_3O_4	35.4941	122	2.527040	01-076-0957

The S1 MWCNT powder shows the peak corresponding to the (0002) plane at an angle 2θ = 25.908º (which is congruent with the ICDD database, 2θ = 25.918º), with its onset angle 2θ = 21.978º and the offset angle 2θ = 28.563º.

In the case of the S2 MWCNT powder, the peak related to the (0002) occurs at an angle 2θ = 25.961º. However, this peak is broader when compared with the S1 sample, having an angle 2θ = 21.101º and offset angle 2θ = 29.715º. The S3 MWCNT powder reveals the (0002) plane peak at an angle 2θ = 25.916º. This peak is the narrowest of those observed having an onset angle 2θ = 23.915º and offset at the angle 2θ = 27.383º. For this powder, the intensity of the peak is substantially lower than the S1 and S2 powders which is related to their high degree of alignment (see Fig. 4.10), as shown by the work carried by Cao et al[6].

The presence of catalysts was detected in all the three powders. In the S1 MWCNT powder, elemental Fe was observed at an angle 2θ = 44.69º. Results also appears to indicate the presence of Fe-C based compounds, such as $C_{0.14}Fe_{1.86}$, also known as martensite at the angles 2θ = 43.462º and 2θ = 45.018º, which are both in good agreement with the data obtained from the ICDD as given in Table 4.9. The other compound is Fe_2C, observed at the angles 2θ = 37.11º and 2θ = 42.717º, again close

to the theoretical values given in Table 4.9. However, it is important to note that the accuracy of the identification of the compounds observed is low as not all the main peaks were observed during compound identification using the DIFFRAC.EVA software, due to their low quantity.

The presence of catalyst in the S2 MWCNT, according to the XRD trace is almost non-existent and indicates that its content is probably close to the XRD limit (1wt. %) Nevertheless, a discrete peak for the elemental Fe is found at the angle $2\theta = 44.71^0$.

Finally, results indicate that the S3 MWCNT powder contains the largest amount of catalyst in different Fe-base forms. Iron Oxide Fe_3O_4 is observed at the angle $2\theta = 35.48^0$, elemental Fe is found at the angle $2\theta = 44.657^0$, Fe_2C (also observed in S1 powder) is found at the angles $2\theta = 37.085^0$ and $2\theta = 42.714^0$ and $CrFe_7C_{0.45}$ at the angles $2\theta = 43.522^0$ and $2\theta = 50.721^0$. Again the peaks observed are in good agreement with the data obtained from the ICDD database, nevertheless, the accuracy of the catalyst composition is low, for the same reason as stated for the S1 powder.

4.3.2.3 Simultaneous Thermal Analysis (STA)

The MWCNTs powders from all 3 sources were tested in a simultaneous thermal analysis (STA), also known as simultaneous thermogravimetry (TG) + differential scanning calorimetry (DSC) NETZCH STA 409 PC Luxx device. Five samples from each MWCNT source were, heated from 100ºC to 900ºC at a rate of 10ºC/min under an O_2 atmosphere. The full description of the methodology followed to perform the study is given in Chapter 3, Section 3.4.3.

This technique allows the quantification of the metal-based catalyst present in a MWCNT sample by exposing the sample to high temperatures under a molecular oxygen (O_2) based atmosphere, thereby promoting oxidation of the C-based material, leaving behind a residue which is mainly composed of metal catalyst. The residual mass is quantified using the TG scale. The combination of TG + DSC also allows an effective study of the MWCNTs thermal stability by assessing the mass (TG) and/or heat flow (DSC) change per Celsius degree (ºC).The results are illustrated in Fig. 4.15 and the data is provided in Table 4.10.
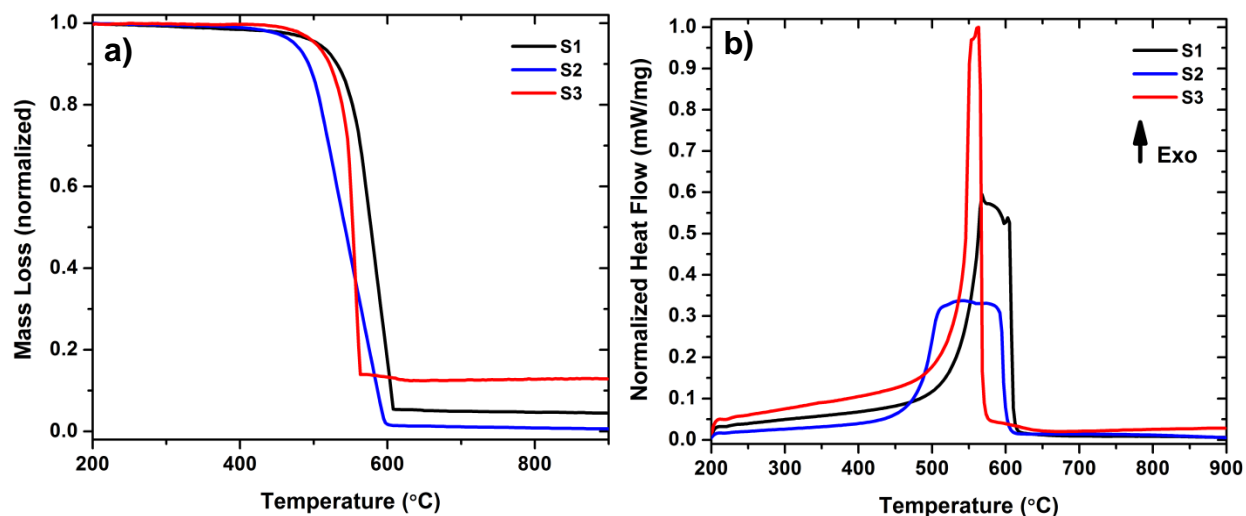
Fig. 4.15 Normalized thermogravimetry (TG), weight-loss **(a)** and differential scanning calorimetry (DSC), heat flow **(b)** curves of S1, S2 and S3 MWCNTs under an O_2 atmosphere, at a heating rate of 10 ºC/min.

Table 4.10 Parameters measured from TG weight-loss and DSC heat flow curves obtained from S1, S2 and S3 MWCNTs samples.

Sample	T_{in} (onset) (ºC)	T_{oxi} (peak) (ºC)	T_{end} (offset) (ºC)	m_r (wt.%)	Width (ºC)	Height (mW/mg)	ΔH_{oxi} (J/g)	ΔC_p (J/gK)
S1	434.56±19	569.28±7.6	607.69±7.5	3.68±1.59	173.13±20.4	54.78	20440	42.48
S2	369.56±10	540.47±5	599.57±15	1.96±1.04	230.01±18	30.8	20088	19.26
S3	413.24±4	560.66±2.6	563.24±2.5	11.55±1.25	150±4.2	102.3	15493	78.22

Fig. 4.15 a) and b) shows the TG weight-loss and DSC heat flow curves, respectively, of the S1, S2 and S3 MWCNTs samples. In order to assess the thermal stability and quality/purity of the samples, important parameters such as: initiation temperature (T_{in}) defined as the temperature at which the material starts to decompose; oxidation temperature (T_{oxi}) which is the point of maximum weight loss; end temperature (T_{end}), temperature at which the all the material has decomposed; and residual mass (m_r), defined as the remaining mass after heating must be analyzed.[5] The parameters data is given in Table 4.10.

According to the observed thermographs, the S1 MWCNTs start to decompose at T_{in} = 434.56±19 ºC, reaching the maximum oxidation at T_{oxi} = 569.28±7.6 ºC and ending at T_{end} = 607.69±7.5 ºC. The decomposition of the S1 CCVD MWCNTs took place over 173.13±20.4 ºC. Whereas, the S2 MWCNTs started to decompose at a lower

temperature than S1, T_{in} = 369.56±10 °C, reaching the maximum oxidation at 540.47±5 °C and ending at T_{end} = 599.57±15 °C. In this case the decomposition process took 230.01±18 °C to complete. Finally, the S3 MWCNTs started to oxidise at T_{in} = 413.24±4 °C (slightly lower temperature than S1), reaching the maximum oxidation at T_{oxi} = 560.66±2.6 °C, and ending at, T_{end} = 563.24±2.5 °C. Hence, the oxidation process of the S3 VAMWCNTs processed via ACVD occurred over a temperature range of only 150±4.2 °C.

Both width of a DSC peak and the slope of the TG curve give an indication of the purity and quality of the material, the narrower the peak or the steeper the negative slope of the curve the purer the material.[5] Therefore, one can conclude that the S2 MWCNTs have the highest amount of carbonaceous impurities amongst all samples, followed by the S1 MWCNTs and the S3 exhibiting the lowest content of carbonaceous impurities. These results corroborate those of the Raman findings shown in section 4.3.2.1. However, despite the higher quality of the S3, the S1 MWCNTs show the highest thermal stability under the O_2 atmosphere.

Furthermore, the residual mass after heating shows that S3 has the highest amount of catalyst, m_r = 11.55±1.25 wt.%, followed by S1, m_r = 3.68±1.59 wt.%, and S2 showing the lowest amount, with only m_r = 1.96±1.04 wt.%. These findings are in good agreement with the XRD results (see Fig. 4.14).

4.3.2.4 Transmission Electron Microscopy (TEM)

Transmission electron microscopy is a powerful tool to identify the types of defects and impurities present in the MWCNTs sample. It also can be used to assess the crystallinity of the material. With this in mind, in this section, the common defects and impurities present in the MWCNTs from the three sources are revealed. The crystallinity of the samples is also obtained and compared by analysing their respective fast Fourier transform (FFT). The device used for this purpose was the JEOL 2100 field emission gun transmission electron microscope (FEG-TEM). For more information about this technique and the methodology behind the study described in this section, see Chapter 3, Subsection 3.4.1.3.

4.3.2.4.1 Defects and Impurities

The common defects and impurities for each MWCNT source observed using the TEM technique has been documented hereafter.

Fig. 4.16 shows a TEM image of a S1 MWCNT and its characteristics. Fig. 4.16 a) reveals the lattice image of a carbon nanotube that represents the best quality (clearly evident by less defects and impurities) observed in the S1 sample. Fig. 4.16 b) illustrates the diffraction pattern obtained from the nanotube. Four diffraction rings are observed and indexed using the Miller-Bravais indexing system. The planes are the (0002), $(10\bar{1}0)$, (0004) and $(11\bar{2}0)$ which are in agreement with the data obtained from the XRD study (see Table 4.9 and Chapter 3, Subsection 3.4.1.3).

In order to obtain the interplanar spacing $(d_{spacing})$ of the MWCNT, Gatan Digital Micrograph software was used as shown in Figs. 4.16 c) and d). Fig. 4.16 c) shows the inverse fast Fourier transform (IFFT) from the area represented by the white dashed line in a) where the multiple carbon nanotube layers are observed. Using the line profile tool, as depicted in Fig. 4.16 d), 14 peaks are observed corresponding to the number of layers present in the nanotube over a distance of 4.845 nm. The average MWCNT interlplanar spacing can be computed by dividing the distance over the number of peaks and the value obtained is d_{MWCNT} = 0.346 nm. This value is in good agreement with the theoretical value obtained from the XRD (d_{MWCNT} = 0.343 nm, see Table 4.9).

Fig. 4.17 illustrates the common defects and impurities observed in nearly all the nanotubes observed during TEM investigations of the S1 CCVD MWCNTs sample. Structural defects, namely pentagons and heptagons can be seen as shown in Fig. 4.17 a) (arrowed). Other types of defects present include lattice disorder defects such as, bamboo structures, tapering cylinders and graphite shells as shown in Fig. 4.17 b).
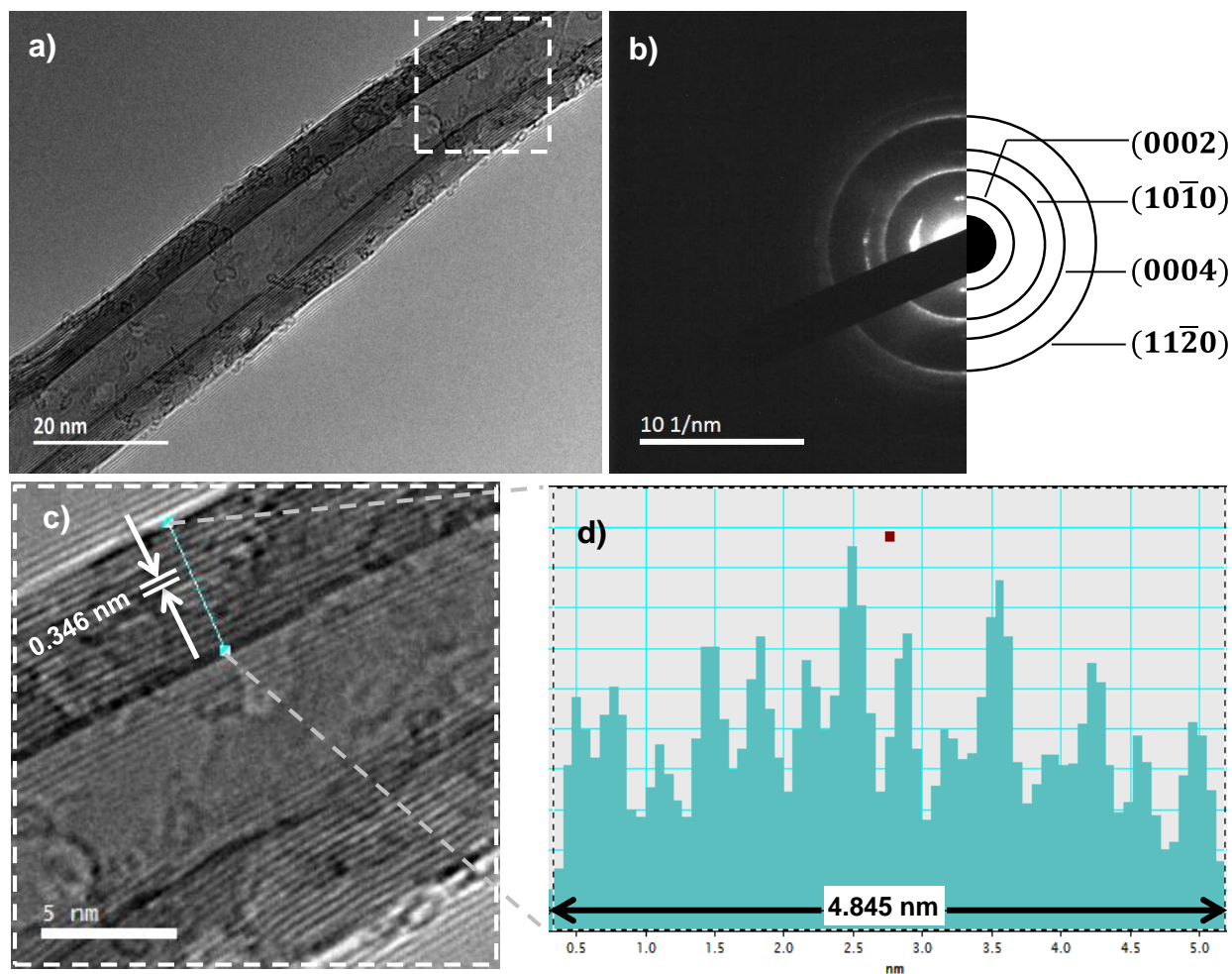
Fig. 4.16 TEM study of a S1 MWCNT: **(a)** lattice image of a good quality MWCNT from the S1 sample. **(b)** Correspondiing SAD pattern obtained from nanotube depicted in (a). **(c)** IFFT lattice image of the area within dashed frame in (a), and **(d)** line profile from which the interplanar spacing was obtained, d_{MWCNT} = 0.346 nm.

The presence of a catalyst is also common, which is mainly trapped inside of the tubes. In order to obtain more information about the nature of the catalyst, an individual nanotube with a catalyst entrapped was selected and studied, as shown in Fig.4.17 c). The chemical composition, according to the energy dispersive spectroscopy (EDS) results, shown in Fig. 4.17 d), confirms the presence of Fe, which is commonly used in nanotubes processed via the chemical vapour deposition (CVD) method. This indicates that it may be pure Fe, Fe-C or Cr-Fe-C compounds, which corresponds with the possible compounds identified according to the XRD results.
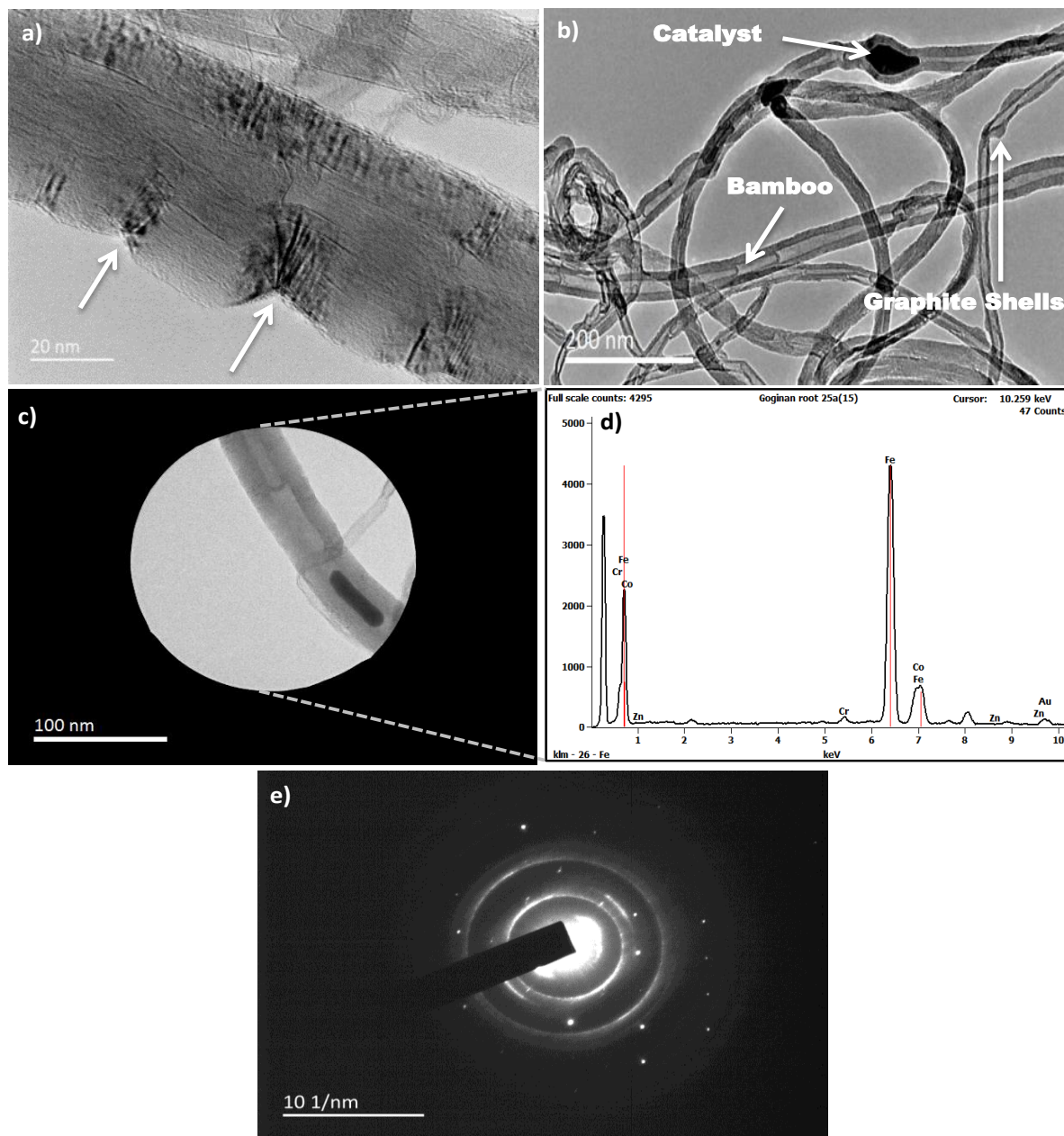
Fig. 4.17 TEM images of the S1 MWCNTs defects and impurities: **(a)** structural defects such as heptagons and pentagons (arrowed). **(b)** Common lattice disorder defects present such as, bamboo structures, graphite shells, tapering cylinders and catalyst impurities, **(c)** a MWCNT with catalyst entrapped and respective **(d)** chemical composition obtained using the EDS technique revealing the Fe-based nature of the catalyst. **(e)** MWCNT SAD pattern obtained from (c) displaying diffraction rings corresponding to the MWCNT and the discrete spots associated with the crystalline nature of the catalyst.

The SAD pattern of the individual nanotube filled with catalyst was also obtained and is shown in Fig. 4.17 e). The diffraction pattern is similar to that illustrated in Fig. 4.16 b), indicating that it is in fact a MWCNT. Discrete spots originated from the catalyst are also observed, this indicates that it has a crystalline structure. However, unfortunately it was not possible to index as the quality of the pattern is not sufficient. This is partly due to the nanotubes movement caused by the transmission beam. Indexing of the pattern would enable the identification of the catalyst compound and provide a direct comparison with that obtained from the XRD results.

Fig. 4.18 shows the TEM characterisation results of the CCVD S2 MWCNTs sample revealing their associated defects and impurities. Fig. 4.18 a) shows a MWCNT BF image, in this case, it is evident structural and lattice defects, the same type of defects observed in S1 MWCNTs. However the major difference observed is the high amount of amorphous material on the surface of the nanotubes as demonstrated in Fig. 4.18 b), c) and d). The FFT pattern from the amorphous material is taken from the region indicated by the dashed box (Fig. 4.18 d)), and shown in Fig. 4.18 e). The diffraction pattern reveals diffuse rings instead of discrete spots, thus confirming amorphous carbon (*a*-C).

The TEM observation from the S2 MWCNTs verifies that the higher I_D/I_G Raman ratio (see section 4.3.2.1), the larger base of the X-ray (0002) peak (see section 4.3.2.2) and larger base of the DSC (see section 4.3.2.3) peak in comparison with S1 and S3 MWCNTs samples are mainly due to the presence of *a*-C. However, only a small number of Fe-based catalyst particles were observed which may explain why the residual mass (m_r) obtained from the TG curve of the S2 MWCNT is the lowest of the 3 samples, $m_r = 1.96 \pm 1.04$ wt.%.

Fig. 4.19 shows the S3 ACVD VAMWCNTs common defects and impurities observed. Fig. 4.19 a) shows a nanotube representative of the highest quality of those found in this sample. It reveals an interplanar spacing of $d_{VAMWCNT} = 0.328$ nm, which is marginally smaller than the theoretical value obtained from the XRD ($d_{MWCNT} = 0.343$ nm, see table 4.9). In this sample, the amount of the high quality nanotubes observed was significantly larger than the S1 and S2 samples respectively.
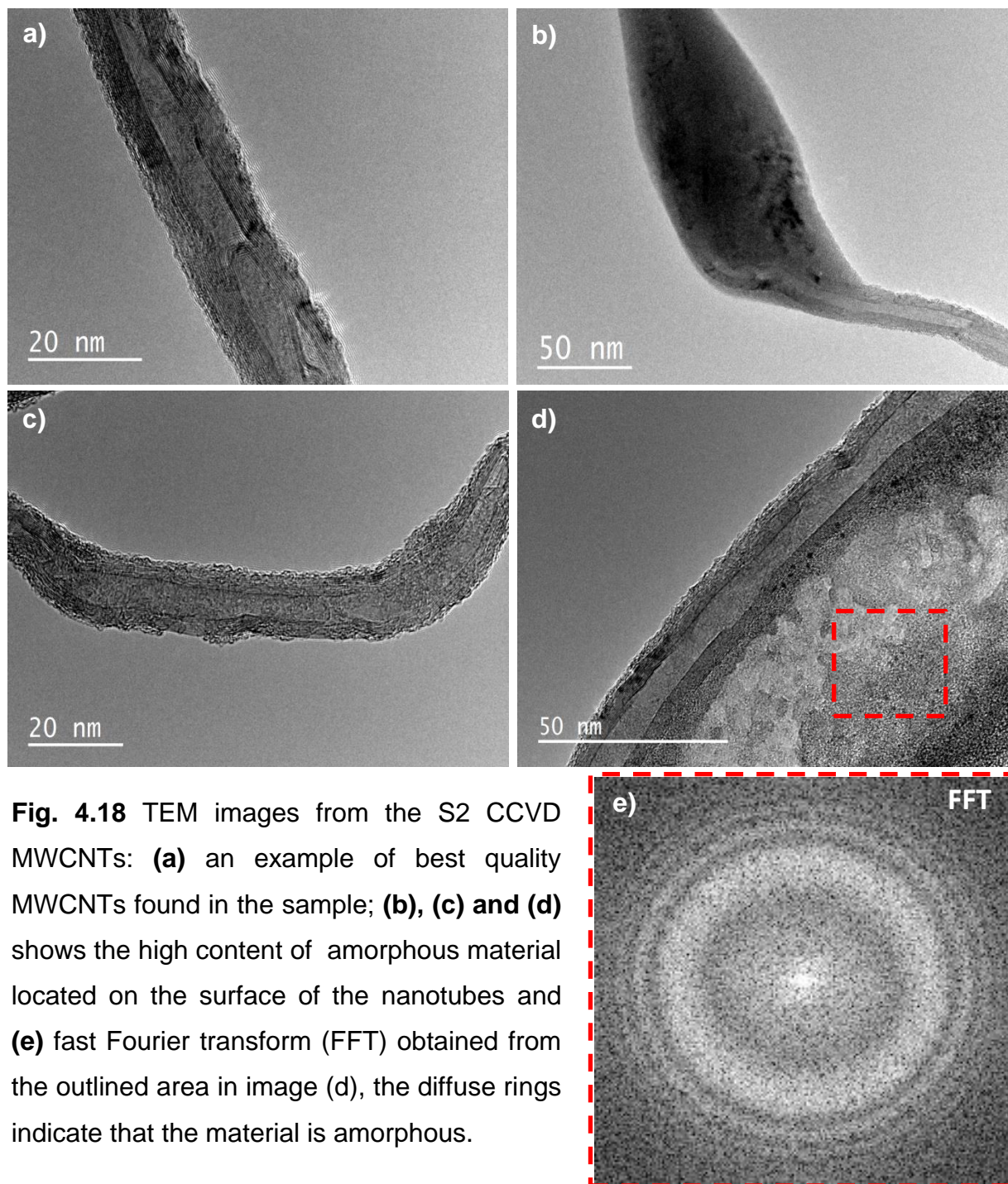
Fig. 4.18 TEM images from the S2 CCVD MWCNTs: **(a)** an example of best quality MWCNTs found in the sample; **(b), (c) and (d)** shows the high content of amorphous material located on the surface of the nanotubes and **(e)** fast Fourier transform (FFT) obtained from the outlined area in image (d), the diffuse rings indicate that the material is amorphous.

In other words, in terms of quality (i.e. nanotubes without or having few *a*-C, catalysts, and/or structural and lattice defects), it was found that S3 >S1>S2.

Nevertheless, the same types of defects observed in both the S1 and S2 samples are also observed in S3. Fig. 4.19 b), c) and d), show these defects, and as before they are
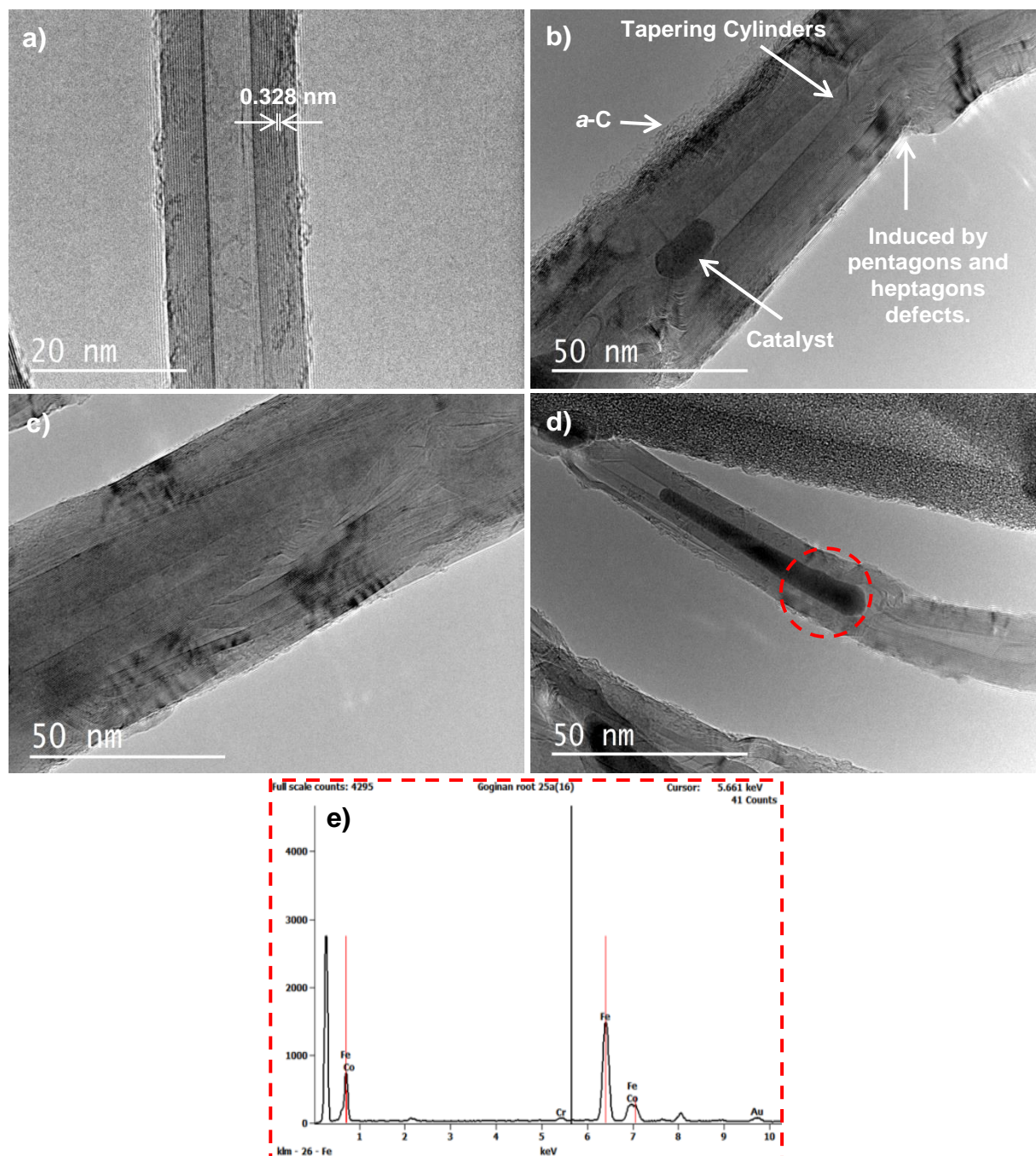
Fig. 4.19 TEM images of the S3 ACVD VAMWCNTs showing commonly observed defects and impurities: **(a)** example of a high quality MWCNT observed. **(b)** common structural (pentagons and heptagons) and lattice defects (tapering cylinders) (arrowed) and impurities (*a*-C and catalyst). **(c)** Large diameter nanotube with almost no inner concentric hole. **(d)** Nanotube with a large catalyst particle entrapped within its cone and **(e)** EDS spectrum revealing the Fe-based nature of the catalyst.

the common structural defects such as pentagons and heptagons which lead to nanotube distortion and lattice defects, mainly tapering cylinders. The *a*-C was found on the surface of the nanotubes in very low amounts, significantly less than in S1 and S2 samples.

The main characteristics that sets apart this sample from the others, besides the obvious longer length (see Fig. 4.11) and larger outer diameter (see Fig. 4.12), is the presence of nanotubes with near or fully closed inner concentric cores, and higher amounts (both quantity and size) of catalyst particles as shown in Fig. 4.19 c) and d).

It was observed that nanotubes with a very large outer diameter also tend to have smaller inner concentric holes and in some cases the hole is completely closed resembling a nanofibre instead. The high amount of catalyst corroborates the TG results which revealed the highest residiual mass of, m_r = 11.55 ± 1.25 wt.% for these samples. Fig. 4.19 e) shows the EDS spectrum obtained from the catalyst in the area within the dashed circle as depicted in Fig. 4.19 d). Again the Fe nature of the catalyst was confirmed which is used to nucleate the nanotube.

4.3.2.4.2 Crystallinity

Lehman et al[5], proposed the use of high resolution transmission electron microscope (HRTEM) to assess the crystallinity of the MWCNTs by calculating the fast Fourier transform (FFT) of a tube segment. If the FFT is comprised of sharp spots (narrow peaks) the material is highly crystalline, however, if it reproduces diffuse spots (broad peaks) the material is less crystalline. Using this approach, the crystallinity of the nanotubes from the three sources was assessed and compared.

Fig. 4.20 shows the TEM results used to study the crystallinity and compare the nanotubes from the different sources. In order to achieve this, a nanotube representing the "average" quality found for each sample source, was selected.

Figs. 4.20 a), b) and c) show the lacey *a*-C film FFT diffraction pattern exhibiting diffuse rings, indicative of an amorphous material, taken from the area demarked in the lattice image, which is reproduced by generating the inverse fast Fourier transform (IFFT). The

line profile that displays the image contrast along the line reveals no sharp peaks confirming the amorphous nature of the film. The amorphous film was also used to align astigmatism before each nanotube was studied. Figs. 4.20 d), e) and f) show the results for the S1 MWCNT sample. The FFT diffraction pattern reveals clear discrete spots arising from the (0002) plane. The IFFT image indicates the area from which the diffraction was taken. The line profile was placed along the (0002) plane and generated two narrow peaks at a distance of 3.031 nm^{-1} from the middle peak (transmitted beam). The sharp peaks indicate that the S1 MWCNT is highly crystalline.

The S2 MWCNT also synthetized via CCVD (as for the S1 MWCNTs), does not show the same degree of crystallinity as is shown in Figs. 4.20 g), h) and i). The FFT diffraction pattern revealed diffused spots together with visible diffuse rings that are indicative of the presence of amorphous material. The IFFT (Fig. 4.20 h)) shows the lattice image from a S2 MWCNT. The image show a distortion in the tube walls and a change in inner diameter due to a lattice defect, known as bamboo defect. In addition, the line profile along the (0002) plane shows broader or diffused peaks at a distance of 3.017 nm^{-1}, indicating a low degree of crystallinity within the S2 MWCNT.

Finally, the crystallinity assessment of the S3 VAMWCNT synthetized via ACVD is given in Figs. 4.20 j), k) and l). The FFT diffraction pattern shows sharp spots from the (0002) plane which occurs as a result of the highly crystalline nature as shown in the IFFT lattice image. The line profile of the (0002) plane shows two very sharp and narrow peaks at a distance of 3.017 nm^{-1} from the middle peak.

The distance between the middle and adjacent peaks in the line profile generated from the reciprocal lattice also gives the interplanar spacing ($d_{spacing}$), Therefore the interplanar spacing of the S1 MWCNT is $d_{spacing,S1}$ = 0.329 nm, S2 MWCNT is $d_{spacing,S2}$ = 0.328 nm and S3 VAMWCNT is $d_{spacing,S3}$ = 0.331 nm.

The crystallinity study clearly shows that, in terms of crystallinity, S3 > S1 >S2.
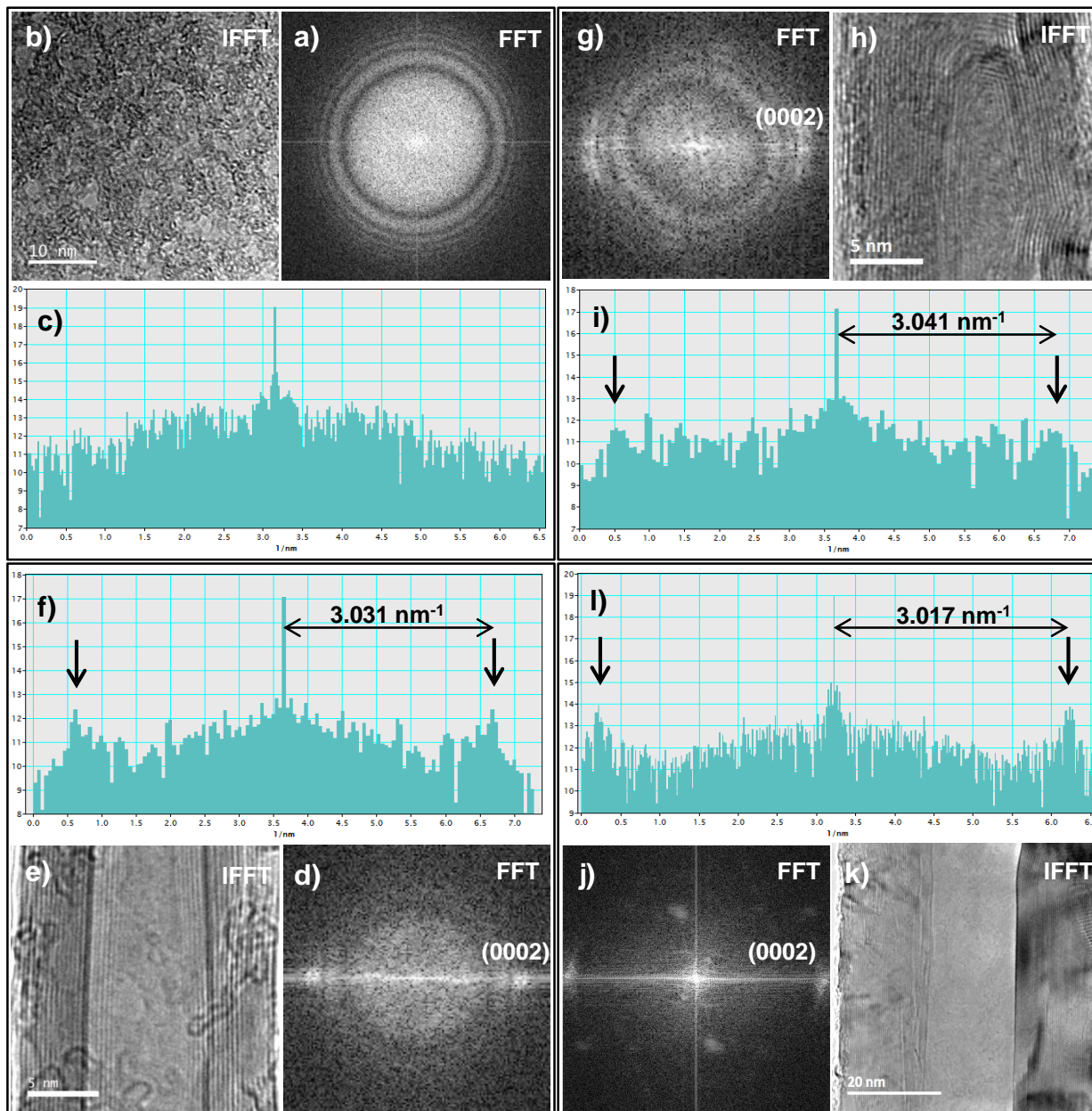
Fig. 4.20 HRTEM crystallography study of the lacey *a*-C film, S1, S2 and S3 MWCNTs: **Lacey *a*-C fillm** used for astigmatism calibration **(a)** FFT generated diffraction pattern, **(b)** IFFT image revealing the area from which the diffraction pattern was taken and **(c)** line profile taken from diffraction pattern, exhibiting no sharp peaks away from transmitted beam (amorphous nature). **S1 MWCNT (d)** FFT diffraction pattern exhibiting the (0002) plane spots, **(e)** IFFT image showing the tube segment from which the diffraction pattern was taken and **(f)** line profile showing narrow peaks corresponding to

the (0002) plane. **S2 MWCNT (g)** FFT diffraction pattern exhibiting the diffuse spots corresponding to the (0002) plane, **(h)** IFFT image showing the tube segment from which the diffraction pattern was taken and **(i)** line profile showing diffuse peaks corresponding to the (0002) plane. **S3 VAMWCNT (j)** FFT diffraction pattern revealing the spots from the (0002) plane, **(k)** IFFT image showing the tube segment from which the diffraction pattern was taken and **(l)** line profile from (0002) plane showing very narrow and well defined peaks.

4.3.3 MWCNTs Stability

In order to study the carbon nanotubes properties and its use in metal composites, it is important to understand how its characteristics can change whilst processing samples. This section investigates the stability of this material.

4.3.3.1 Stability under Plasma Atmosphere

The most common characterization techniques used to study individual, blended powders or embedded carbon nanotubes is via using electron microscopy techniques such as SEM and TEM. These techniques involve sample preparation prior to its examination. This includes plasma cleaning, which involves the use of a plasma atmosphere which is known to ablate C in the form of hydrocarbons in order to improve image quality.

In order to study the effect of plasma cleaning on the MWCNTs, a comparison of Raman spectra obtained from the three MWCNT sources in the as-received, plasma-cleaned state were performed. The plasma cleaned samples were cleaned for 30 s and 120s under a plasma atmosphere composed of H_2/O_2 in a Gatan Advanced Plasma System Solarus, Model 950. See Chapter 3, Subsection 3.4.1.3, Table 3.10 section for full methodology. Cleaning times of 30s and 120s was selected because these are standard times for this device to clean TEM and SEM samples, respectively.

The Raman spectra were normalized to the D band and are given in Fig. 4.21. The I_D/I_G ratio of the samples from the three MWCNT sources during plasma cleaning as a function of time are given in Table 4.11.
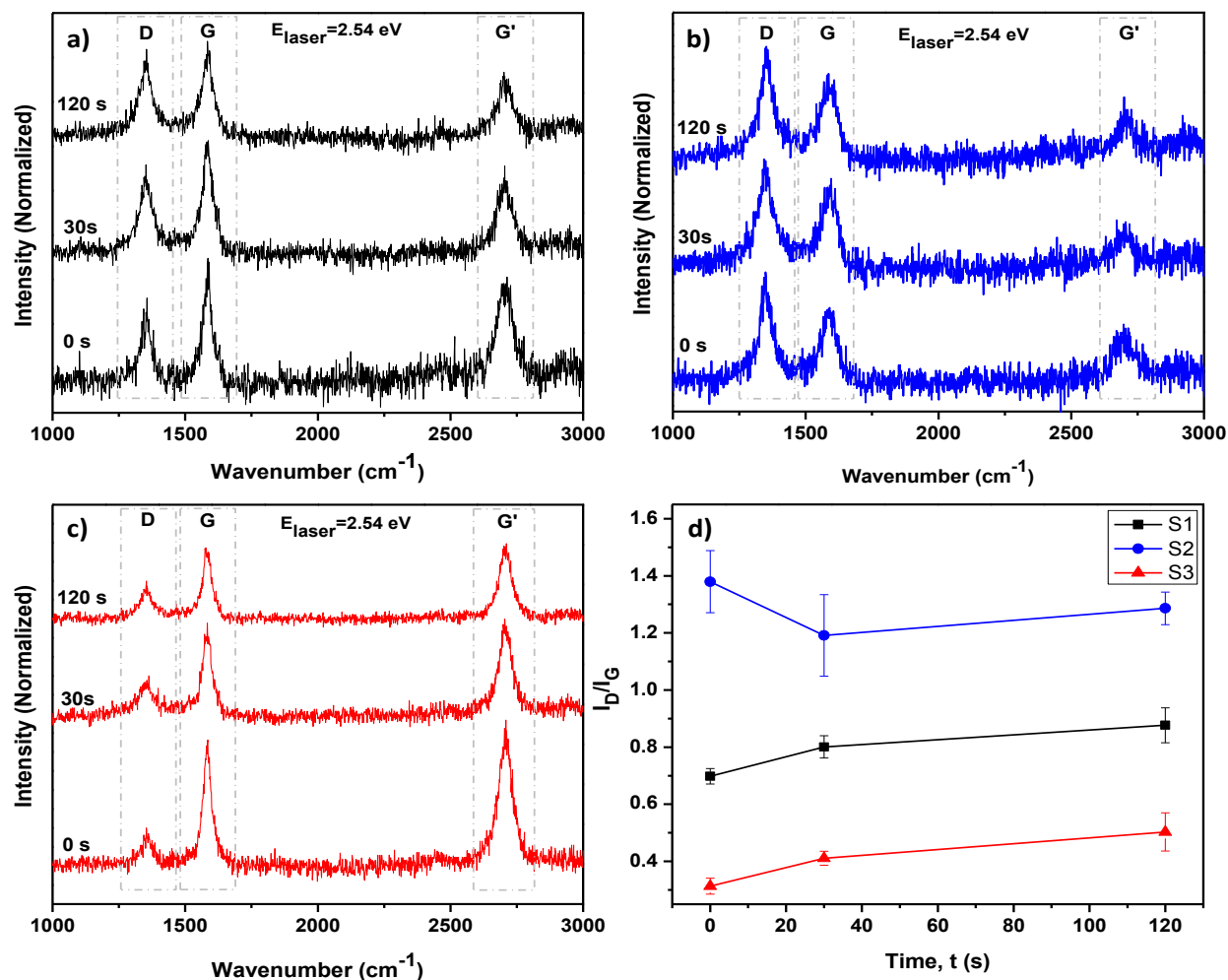
Fig. 4.21 Raman assessment of MWCNTs stability during plasma cleaning over time: 0, 30 and 120 s. Spectra normalized to the D band. **(a)** S1 MWCNTs, **(b)** S2 MWCNTs, **(c)** S3 MWCNTs and **(d)** Raman I_D/I_G ratio of the three MWCNT sources over time.

Table 4.11 Raman I_D/I_G ratio of the samples from the three MWCNT sources during plasma cleaning as a function of time.

	S1	S2	S3
t (s)	I_D/I_G	I_D/I_G	I_D/I_G
0	0.70±0.03	1.38±0.11	0.31±0.03
30	0.80±0.04	1.19±0.14	0.41±0.03
120	0.87±0.06	1.29±0.06	0.50±0.07

Fig. 4.21 a), b) and c), shows the Raman spectra evolution as a function of cleaning time for the S1, S2 and S3 MWCNTs samples, respectively. It was observed that S1 and S3 suffered induced damage due to the plasma cleaning, whereas, the S2 sample revealed an overall increase in quality of the MWCNTs.

Fig. 4.21 d) shows the graph of the Raman I_D/I_G ratio evolution with increasing plasma cleaning time. Samples S1 and S3 showed an increase in defects (damage) of 11%, from $I_D/I_G = 0.70 \pm 0.03$ to 0.80 ± 0.04, and 10%, from $I_D/I_G = 0.31 \pm 0.03$ to 0.41 ± 0.03, after 30 s, respectively. The damage observed in S1 and S3 samples increases with time, however, the rate at which the damage occurs decreases, i.e. over the next 90 s the damage increases 7% of (18% in total) for S1 MWCNTs, and 9 % (19% in total) for the S3 MWCNTs.

In contrast, S2 showed a 19% decrease in defect content, from $I_D/I_G = 1.38 \pm 0.11$ to 1.19 ± 0.14. This may be attributed to the ablation of the high content of *a*-C on the surface of the nanotubes as observed in the TEM (see Fig. 4.18). After which, an increase of 10% in damage was observed with 120s of cleaning, this may be due to nanotube walls becoming exposed and starting to ablate.

4.3.3.2 Stability under the Electron Beam

TEM is a useful technique to study CNTs, however, high operation voltages may cause damage by disrupting the crystalline arrangement of the nanotubes. This could cause erroneous results, for example when studying the crystallinity of the nanotubes (such as the study described in section 4.3.2.4.2), as a higher degree of disorder will be observed which do not correspond to the real crystallinity of the as-received material. Thus, images must be taken with minimum exposure of the material to the beam without compromising image quality+clarity.

According to the literature, damage of the nanotubes walls is expected to be observed for operation voltages higher than 120 kV. Studies indicate that the damage can be avoided for operation voltages less than 86 kV[5]. In this section, a S1 MWCNT sample was exposed to the TEM electron beam at operation voltages of 200 kV and 80 kV as shown in Fig. 4.22.
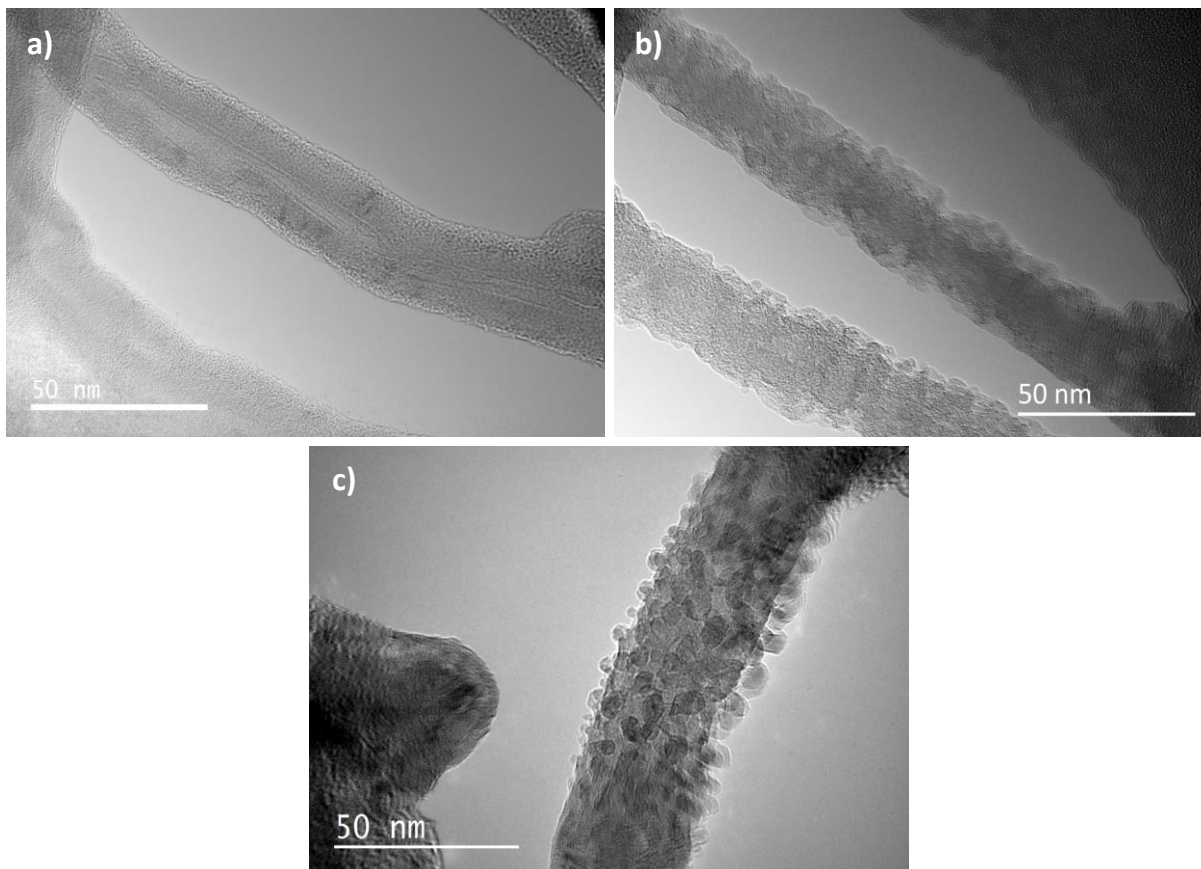
Fig. 4.22 Damage of the S1 MWCNTs under a TEM electron beam using an operation voltage of: **(a)** 200 kV, 0 s; **(b)** 200 kV, 1800s and **(c)** 80 kV, 1800s.

In order to obtain the images the beam was aligned close to but outside the region of interest (ROI) in order to minimize the damage whilst not compromising the image quality. Fig. 4.22 a) and b) illustrates the damaged induced by the electron beam at 200 kV to the S1 MWCNT after 0s and 1800s (30min), respectively. After a long exposure, it is clear that the operating voltage at 200 kV does damage the nanotubes as observed in Fig. 4.22 b), where the nanotubes are visibly disrupted.

Interestingly, damage was also observed at 80 kV in contrast with results published in the literature. Fig. 4.22 c) shows a damaged S1 MWCNT after beam exposure of 1800s. Nevertheless, if the beam position is carefully chosen for alignment and focus, and exposure time reduced, damage can be avoided.

The effect of the electron beam energy at an operating voltage of 80 kV on the other two sources of MWCNTs, S2 and S3 was also observed. It showed that "parking" the beam on top of the nanotubes does cause damage regardless the source of nanotubes. However, of the 3 samples, S3 showed the highest stability followed by S1 and finally S2 under these conditions. As for sample S1, damage in S2 and S3 samples could also be avoided by careful beam positioning and imaging.

4.3.4 Composite Processing and Characterisation

Al/Cu-CFs composites (Section 4.2) processed by rheocasting+ECAE methods, demonstrated good filler distribution, dispersion and alignment of the fillers with an increase of thermal conductivity. Therefore, the same processing method was applied for the Al/MWCNTs with the results outlined in this section. The optical microscopy (O.M), scanning and transmission electron microscopy (SEM and TEM) were also used to characterize the composite.

4.3.4.1 Filler Thermal Stability

To take advantage of the remarkable thermal properties of the CNTs, it is critical to ensure that the MWCNT chemical and structural properties remain unchanged during composite processing. The composites were produced using the S1 MWCNTs, therefore, only this MWCNTs sample was studied further.

In order to perform this study, the S1 MWCNTs powder and the Cu10S1 (Pure Cu ball-milled with 10% of S1 MWCNTs) powder composite were placed in a simultaneous thermal analysis (STA) device, under two atmospheres, either O_2 or He, and heated up to 900 °C and left to cool down to room temperature, (see Chapter 3 Subsection 3.4.3, for STA methodology), the heat-treated powder was then transferred to an XRD device (see Chapter 3 Subsection 3.4.2.1 for XRD methodology) and analysed.

The S1 MWCNTs were also investigated using the Raman technique in the as-received condition (no heating) and after heating to 900 °C in He (see Chapter 3 Subsection 3.4.2.2, for Raman spectroscopy methodology). The Cu10S1 powder was not studied using Raman spectroscopy as the presence of Cu gives unpredictable results.

Fig. 4.23 shows the morphology of the filler used in the production of the composite. Figs. 4.23 a) and b) reveal the S1 MWCNTs morphology at low and high magnifications, respectively. The morphology (powder size, tube length, inner and outer diameter is given in Subsection 4.3.1).

To aid wetting the as-received S1 MWCNTs were also mechanically alloyed via ball-milling with Cu. Fig. 4.23 c) shows the Cu10S1 composite powder which was comprised of 90 wt.% pure Cu and 10 wt.% of S1 MWCNTs. The resultant powder has a mesh size of 325 µm and the powder flakes exhibited a size distribution ranging from ~1 to 100 µm.

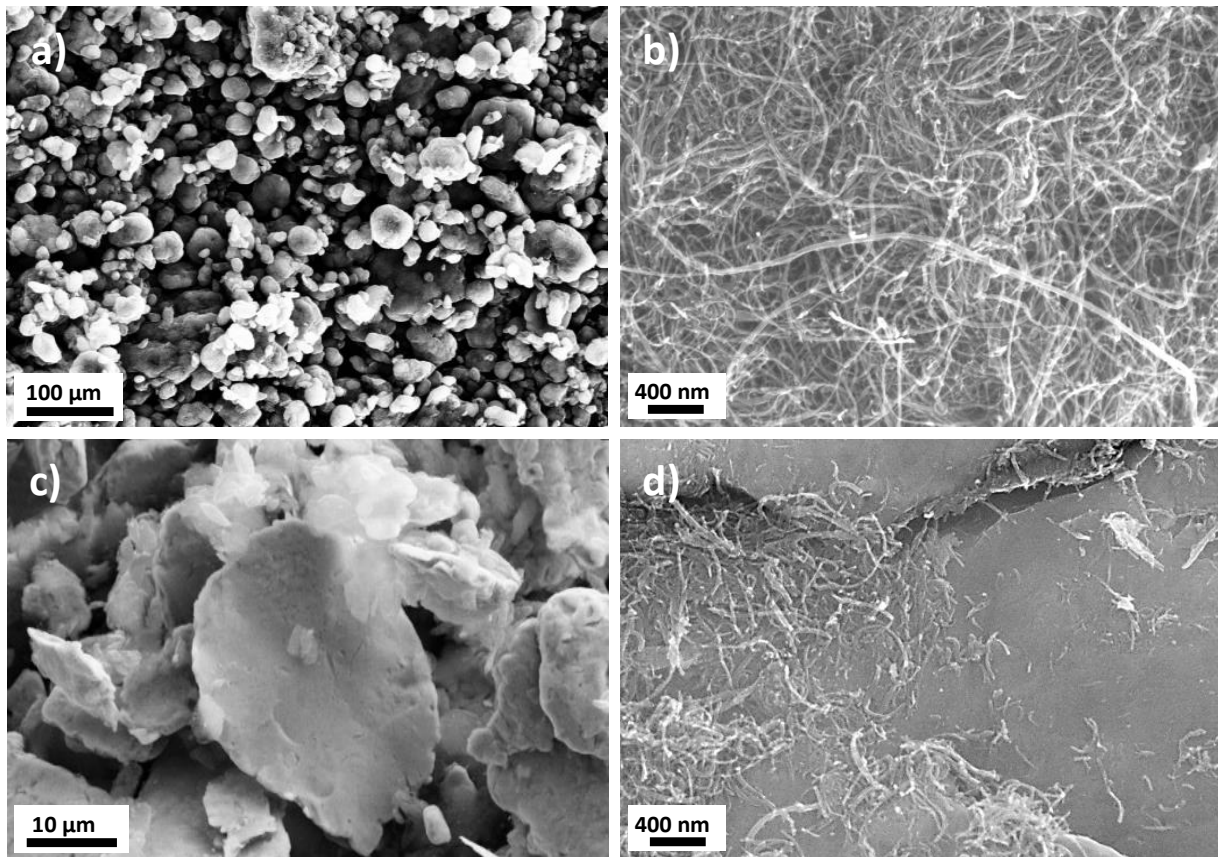**Fig. 4.23.** SEM SE micrographs showing the morphology of the filler: **(a)** and **(b)** as-received (before ball-milling with Cu) S1 MWCNTs, low and high magnification images, respectively; **(c)** and **(d)** composite powder images (after ball-milling) composed of pure Cu ball-milled with 10wt.% of S1 MWCNTs, referred within the thesis as Cu10S1 at low and high magnification, respectively.

Fig. 4.23 d) reveals the flake surface of the Cu10S1 powder, where bundles and individual nanotubes are readily observed. The composite powder was acquired already processed, and therefore its processing is not discussed further in this study.

In order to study the thermal stability of the fillers and predict the effect of the processing temperature on their structure, the as-received S1 MWCNTs and Cu10S1 powders were studied using STA (DSC+TG), Raman spectroscopy and X-ray diffraction techniques.

Fig. 4.24 a) illustrates the normalized differential scanning calorimetry (DSC) curves of the S1 MWCNTs heated up to 900 ºC, in O_2 and He atmospheres at a rate of 10 K/min.

It was found that with increasing temperature the S1 MWCNTs powder when exposed to the O_2 atmosphere exhibits an exothermic peak due to oxidation. The reaction starts at T_{in} = 434.56±19 ºC, reaching a peak at T_{oxi} = 569.28±7.6 ºC and being completely oxidized at T_{end} = 607.69±7.5 ºC (see Table 4.13). In contrast, when heated under a He atmosphere the MWCNTs are stable for the whole heating process (up to 900 ºC). However, in Fig. 4.24 b) a narrow endothermic peak is seen at T_{Peak} = 853.04±5.1 ºC, with T_{in} = 850.54±7 ºC and T_{end} = 855.54±4.9 ºC (see Table 4.14). Nevertheless, this peak occurs at a temperature well above the composite processing temperature (633 ºC). These findings thus indicate that a He protective atmosphere must be used during composite processing to avoid oxidation of the nanotubes at 434.56±19 ºC.

Fig. 4.24 c) gives the normalized TG curves for the S1 MWCNTs that reveal a mass loss when it is subjected to heat under the O_2 and He atmospheres. The MWCNTs, when exposed to O_2, start to lose weight at temperatures as low as ~ 300 °C, which may be attributed to the oxidation of *a*-C. The sample loses almost all of its weight at 607.69±7.5 °C, leaving behind the metal catalyst. When exposed to the He atmosphere, the MWCNTs have a maximum weight loss of 3±1 %. Negligible weight loss is observed up to 593.04 °C (see Table 4.14), after that a steady loss is observed up to 900 °C, which may be related to *a*-C evaporation.
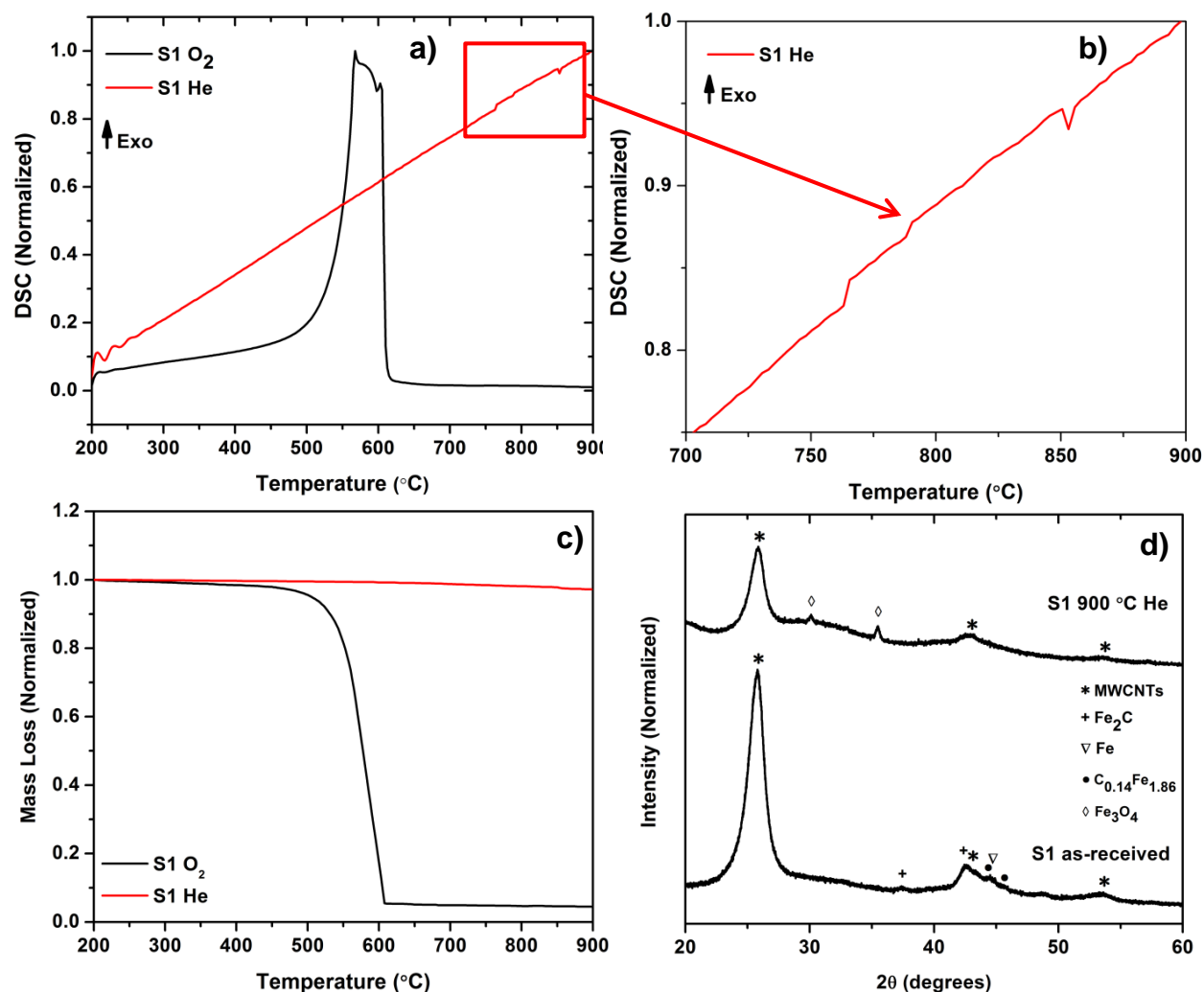
Fig. 4.24 STA + XRD thermal stability assessment of S1 MWCNTs used in the composite processing heated up to 900 ℃, at a rate of 10K/min, in O_2 and He atmospheres. **(a)** DSC curves of S1 MWCNTs heated under O_2 and He atmospheres. **(b)** Magnified view of narrow endothermic peak at 853.04±5.1 ℃ in the S1 MWCNTs samples. **(c)** TG curves from S1 MWCNTs under O_2 and He atmospheres. **(d)** XRD traces from S1 MWCNTs samples in the as-received and after heating at 900 ℃ in He conditions.

Fig. 4.24 d) compares the XRD traces for the S1 MWCNTs in the as-received condition (the trace is also given in Fig. 4.14) and after being subjected to heat under a He atmosphere. The XRD study reveals no structural changes to the nanotubes, as no new compound was observed. Only one new peak arose which appears to be related to the

oxidation of the elemental Fe catalyst, despite the fact that the heating was performed under a protective atmosphere. The crystallographic information is given in Table 4.9.

Table 4.12 gives the Raman results of the as-received and heat-treated S1 MWCNTs under a He atmosphere. There is no significant change in Raman ratios due to the heat treatment, for example, the as-received material shows an I_D/I_G= 0.70 ± 0.03, whereas the heat-treated material shows an I_D/I_G= 0.69 ± 0.08. Therefore, a He atmosphere protects the CNTs from reacting and corroborates the DSC+TG and XRD findings. It is also highly probable that the endothermic peak observed in Fig. 4.24 b) is probably due to a phase transformation related to the Fe based catalyst.

Table 4.12 Raman results for the S1 MWCNTs in the "as-received" and post heating treatment to 900 ºC under a He atmosphere conditions.

Condition	I_D/I_G	$I_{G'}/I_D$	$I_{G'}/I_G$
As-received	0.70 ± 0.03	1.33 ± 0.07	0.93 ± 0.06
900ºC	0.69 ± 0.08	1.39 ± 0.12	0.94 ± 0.04

Fig. 4.25 gives the thermal stability results of the Cu10S1 composite powder when subjected to high temperatures, of up to 900 ºC, again under two different atmospheres, O_2 and He.

Fig. 4.25 a) shows the DSC traces from the Cu10S1 powder indicating its thermal stability, both when exposed to O_2 and He atmospheres. It shows a relatively low stability at high temperatures when exposed to O_2 due to the presence of Cu, which starts to oxidize at T_{in} = 233.16±6.3 ºC and is completely oxidized at T_{end} = 653.16±5 ºC. Three new peaks are observed during the oxidation of the composite powder, the first two are related to the Cu oxidation, probably formation of tenorite (CuO), and the third peak is due to the oxidation of the MWCNTs.

The 1st peak occurs at T_{oxi} = 273.16±2 ºC, the 2nd at T_{oxi} = 478.16±2.2 and the 3rd at T_{oxi} = 535.66±1.5 ºC (see table 4.13). This indicates that the mixing of Cu powder with MWCNTs via high energy ball milling reduces the MWCNTs thermal stability from $T_{oxi, S1}$

$= 569.28 \pm 7.6$ ºC to $T_{oxi, Cu10S1} = 535.66 \pm 1.5$ ºC a reduction of 33.62 ºC). This finding may be related to damage or strain induced within the nanotubes during the mixing.
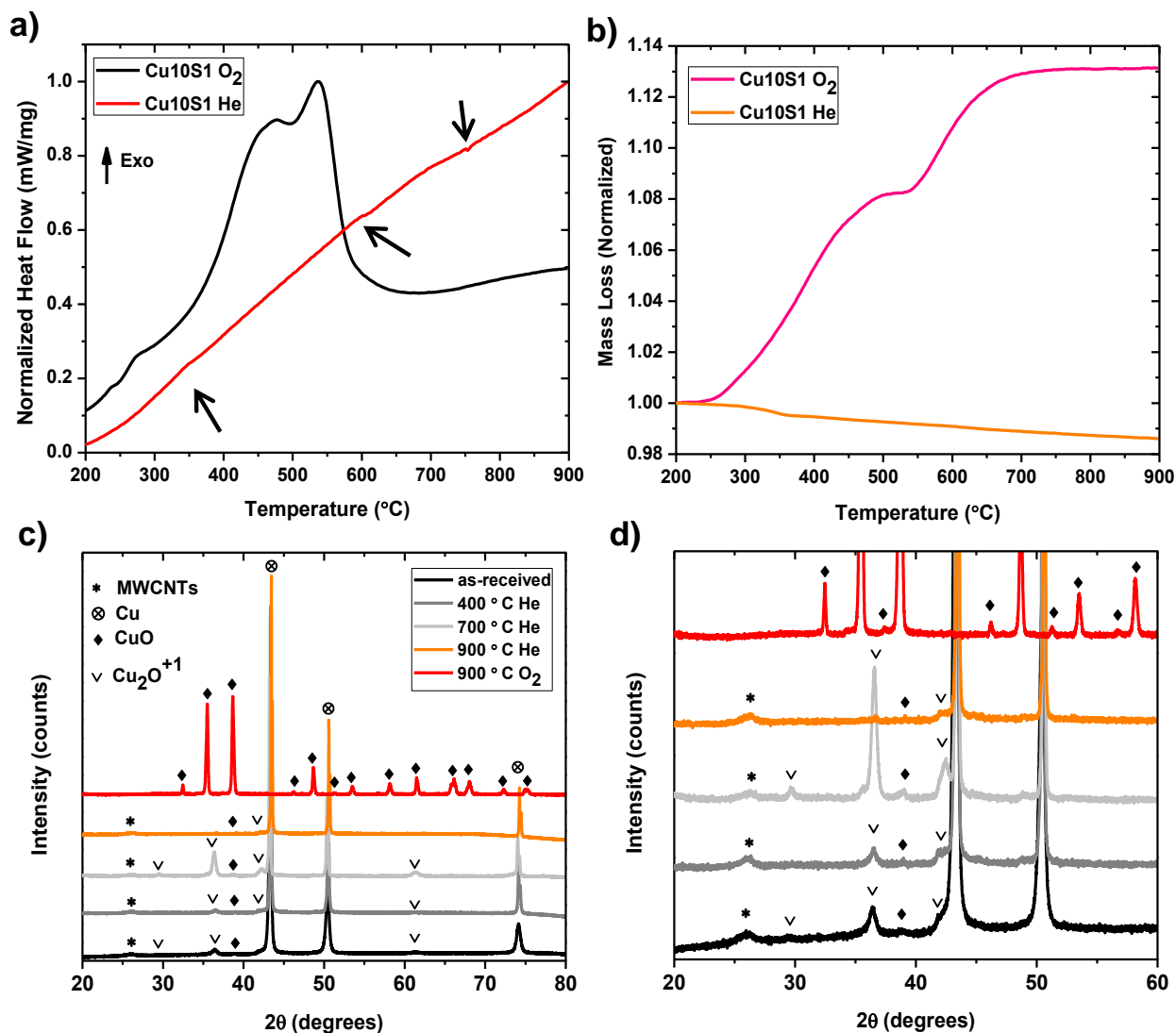
Fig. 4.25 STA (DSC+TG) + XRD thermal stability results for the Cu10S1 composite powder used in the composite processing, heated up to 900 ºC, at a rate of 10K/min, in O_2 and He atmospheres. **(a)** DSC traces for Cu10S1 composite powder in He+O_2 atmospheres. **(b)** TG curves of the Cu10S1 powders **(c)** XRD traces from the Cu10S1 composite powder in the following conditions: as-received, heat-treated in He up to 400 ºC, 700 ºC and 900 ºC and heat–treated in O_2 up to 900 ºC. **(d)** Inset from XRD traces for the Cu10S1 powder shown in (c) to reveal the MWCNT peaks more clearly.

Analogous to what was observed for the S1 MWCNTs powder, the Cu10S1 powder also seems to be stable for temperatures up to 900 ºC under He atmosphere, as no peaks associated with the nanotubes in the DSC+TG traces are observed. Nonetheless, three peaks are observed, two exothermic and one endothermic (arrowed).

The first peak ranges from T_{in} = 323.26±7.2 ºC to T_{end} = 375.76±6.2 ºC, reaching its maximum at T_{peak} = 348.03±3 ºC, whereas the second peak ranges from T_{in} = 572.53±5.5 ºC to T_{end} = 615.93±8.4 ºC, reaching its maximum at T_{peak} = 600.82±2.7 ºC (see Table 4.14). These two peaks may be associated with CuO reduction. The third peak, a very narrow endothermic peak ranges from T_{in} = 750.73±4.1 ºC to T_{end} = 758.18±6 ºC, reaching its maximum at T_{peak} = 753.23±3 ºC.

The third peak shows a similar temperature range and shape to the peak observed for the S1 MWCNTs powder (see Fig. 4.24 b)). This indicates that it is due to the same phenomenon, which again is believed to be related to the presence of the metal catalyst. However, the endothermic peak also appears in the Cu10S1 sample but ~ 100 ºC earlier than for the S1 MWCNTs powder (see Table 4.14). This may be explained by the phase transformation temperature being depressed which is typical for nanoparticles below 100 nm[7]. This is because the ball-milling causes the catalyst particles to break up in smaller ones.

Table 4.13 Phase transformation temperatures and respective mass losses observed in the S1 MWCNTs and Cu10S1 powder samples during heat treatments, of up to 900 ºC in O_2 atmospheres.

Sample	T_{in} (onset) (ºC)	T_{oxi} (peak) (ºC)	T_{end} (offset) (ºC)	Mass Loss (wt.%)
S1	434.56±19	569.28±7.4	607.69±7.5	96.3±1.5
Cu10S1	233.16±6.3	273.16±2	653.16±5	+ 13.14±1
	_ _ _	478.16±2.2	_ _ _	_ _ _
	495.66±3	535.66±1.5	538.17±2	_ _ _

Table 4.14 Phase transformation temperatures and respective mass losses observed in the S1 MWCNTs and Cu10S1 powder samples during heat treatments, of up to 900 ºC in He atmospheres.

Sample	T_{in} (onset) (ºC)	T (peak) (ºC)	T_{end} (offset) (ºC)	Mass Loss (wt.%)
S1	850.54±7	(endo) 853.04±5.1	855.54±4.9	3±1 (900 ºC)
Cu10S1	323.26±7.2	(exo) 348.03±3	375.76±6.2	0.5±0.03
	572.53±5.5	(exo) 600.82±2.7	615.93±8.4	1.0±0.07
	750.73±4.1	(endo) 753.23±3	758.18±6	1.4±0.4 (900 ºC)

Fig. 4.25 b) shows TG curves which give the mass loss of the Cu10S1 powder during exposure to heat under O_2 and He atmosphere curves. Under the O_2 atmosphere, an increase in weight occurs as soon as the powder starts to oxidize at 233.16±6.3 ºC and continues to increase until the MWCNTs starts to oxidize at 495.66±3 ºC, where the weight gain reaches a plateau. After complete oxidation of the nanotubes at 538.17±2 ºC the weight start to increase again and at 653.16±5 ºC the Cu10S1 powder is completely oxidized reaching the maximum weight gain of 13.14±1 %. No further weight increase is registered up to 900 ºC.

When the Cu10S1 composite powder is exposed to the He atmosphere, a mass loss is observed as opposed to the findings for an O_2 atmosphere where a mass gain was seen. The mass starts to decrease at the same time the onset of the first exothermic peak occurs (Fig. 4.25 a)) at 323.26±7.2 ºC. At the end of the peak at 375.76±6.2 ºC, the mass continues to decrease but a lower rate until it reaches the maximum temperature 900 ºC. The maximum weight loss observed was 1.4±0.4%.

In Fig. 4.25 c), the XRD traces from the Cu10S1 composite powder show the effect of temperature on the chemical structure of the powder when subjected to increasing temperature under both O_2 and He atmospheres. The XRD confirms the presence of the MWCNTs and two forms of Cu oxide, cuprite (Cu_2O^{+1}) and tenorite (CuO) for the as-received powder. The same compounds are found in the Cu10S1 powder samples when increasing the temperature up to 900 ºC in He, however their amount decreases. The XRD results also confirm that the powder exposure to high temperatures under O_2

atmosphere cause complete conversion of Cu to CuO and complete oxidation of the MWCNTs (see Fig. 4.25 c)).

Table 4.15 Crystallographic information obtained from the international centre for diffraction data (ICDD) database for the phases found in the XRD thermal study of the Cu10S1 composite powder.

Elements	2θ Angle (º)	{h,k,i,l} {h,k,l} Planes	d(Å)	Reference 2015 ICDD
MWCNTs	**25.9188**	**0002**	**3.434760**	00-058-1638
Cu	43.2966	111	2.088000	00-004-0836
	50.4330	200	1.808000	
	74.1303	220	1.278000	
CuO	35.4170	002	2.532360	00-048-1548
(Tenorite)	35.5431	11$\bar{1}$	2.523670	
	38.7081	111	2.324290	
Cu$_2$O^{+1}	36.4183	111	2.465000	00-005-0667
(Cuprite)	42.2971	200	2.135000	
	61.3435	220	1.510000	

Fig. 4.25 d) shows a magnified view of the XRD traces in c) which clearly reveal the MWCNT and oxides peaks evolution with increasing temperature.

Under a He atmosphere, when increasing the temperature up to 400 ºC, i.e. the temperature range that includes the first exothermic peak and where the powder mass starts to decrease (Fig. 4.25 a)), no significant change is observed in the Cu oxide content in comparison to the as-received material. Further increase in the temperature, up to 700 ºC (above the second exothermic peak with offset at 615.93±8.4 ºC), a substantial increase in the cuprite content is observed, which may indicate that the mass loss is related to the reduction of CuO into Cu$_2$O^{+1}. If the full heat treatment is performed, up to 900 ºC, almost all the oxides are reduced to pure Cu as the oxide peaks almost disappeared.

Regarding the nanotubes, as seen for the S1 MWCNTs powder, the high temperature does not affect their chemical structure. At 400 ºC the Cu10S1 2θ angle corresponding to the MWCNT (0002) plane is 2θ = 26.13º, at 700 ºC is 2θ = 26.17 and at 900 ºC is 2θ

= 26.14⁰. From these results is evident that the temperature does not have an effect on the nanotubes structure as the 2θ angle is nearly constant with increasing temperature.

In contrast, the peak associated with the MWCNT (0002) plane from the as-received Cu10S1 powder shows a 2θ angle of 2θ = 26.09⁰, a higher value in comparison to the that given by the ICCD database and from the S1 MWCNT powder, 2θ = 25.92 ⁰ and 2θ = 25.908⁰, respectively (see section 4.3.2.2). This indicates that the ball milling mixing procedure induces deformation and stresses in the nanotubes walls lattice. This results in imperfections causing the $d_{spacing}$ changes when compared with the S1 MWCNTs.

This study investigating the thermal stability of the filler indicates that it is safe to use the S1 MWCNTs for Al matrix composite processing if only an effective He protective atmosphere is used to avoid nanotube oxidation. However, the high energy ball milling mixing process must be minimal in order to avoid nanotubes damage and a consequent deterioration in their properties.

4.3.4.2 Rheocasting

As the results for the processing of aluminium matrix composites reinforced with Cu-coated carbon fibres (Al/Cu-CFs), described in Section 4.2, were promising the same processing route was adopted for the production of Al/MWCNTs composites. This section details the results of the 1ˢᵗ stage of the processing of these composites, i.e. the rheocasting. The data presented is in the form of optical, scanning and transmission electron microscopy results.

4.3.4.2.1 Composite Microstructure Evolution

The aluminium matrix composites reinforced with the Cu10S1 fillers were processed using the semi-solid metal (SSM) processing method, i.e. rheocasting. The processing is described in detail in Chapter 3, Subsection 3.3.1.

The composite microstructure plays a major role in the properties of the composites. In this case the microstructure is strongly influenced by both the processing method, (rheocasting) and the Cu10S1 filler addition as it increases the content of the MWCNTs but also the content of Cu.

Table 4.16 gives the designation of the composites produced and their final chemical composition acquired by optical emission spectroscopy (OES). Sample M0 (Al3Mg, no filler added) is the reference and has a Cu content of 0.002 wt.%, whereas, sample M1 (Al3Mg, w_f = 0.003, 0.3wt.% MWCNTs added) has a Cu content of 2.86 wt.%. Sample M2 (Al3Mg, w_f = 0.0035, 0.35 wt.% MWCNTs added) has a maximum Cu content of 4.13 wt.%. The analysis of the composite chemical composition clearly demonstrates the increase in Cu content when increasing fillers content. However, the Mg content remains almost stable, with only a small variation between the reference and the composites observed, M1 (- 0.21 wt.%) and M2 (- 0.1 wt.%).

Table 4.16 Al3Mg/Cu10S1 composites samples, designations with respective average chemical composition (wt.%) acquired using OES.

Sample	Designation	Cu10S1 addition (g)	MWCNT addition		Composition (wt%)					
			w_f	v_f (ρ_{bulk})	Al	Si	Fe	Cu	Mn	Mg
M0	Al3Mg	0	0	0	96.5	<0.003	0.13	**0.002**	0.01	**3.35**
M1	Al3Mg/Cu10S1	75	0.003	0.028	93.1	0.08	0.65	**2.86**	0.01	**3.14**
M2	Al3Mg/Cu10S1	87.8	0.0035	0.032	91.4	0.11	0.82	**4.13**	0.01	**3.25**

In Fig. 4.26, the optical micrographs illustrate the microstructure of the reference M0, the M1 and M2 composites, all processed via the semi-solid metal rheocasting method.

Figs. 4.26 a), b), c) and d) (left column) show the microstructure of the M0 sample at 5x, 20x, 50x and 100x magnification, respectively. M0 reveals at least two distinct phases, a nearly globular primary α-Al structure (common for rheocasted metals), the other phase is a grey AlFe needle-like intermetallic normally found at the grain boundaries. The intermetallic originates from Fe contamination and its source is the steel impeller used for stirring the semi-solid slurry during composite processing. This contamination occurs despite a boron nitride protective coating.

Figs. 4.26 e), f) g) and h) (middle column) show the M1 composite microstructure at various magnifications, 5x, 20x, 50x and 100x, respectively. At low magnification the M1 composite is very similar to the M0 material as the same phases are present.
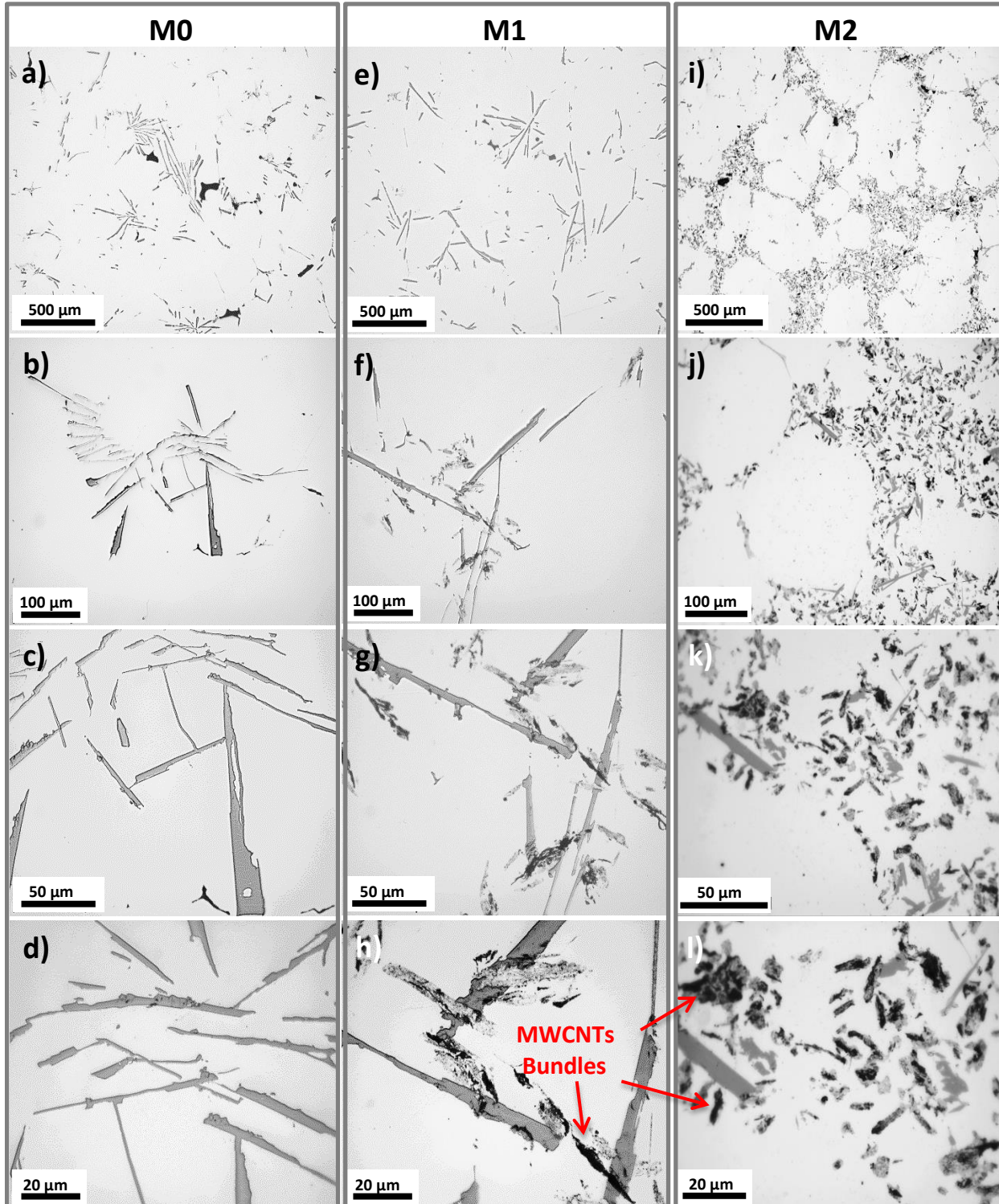
Fig. 4.26 Bright-field optical microscope (O.M.) images illustrating the microstructure of the reference material M0 and the Al3Mg/Cu10S1 composites produced, M1 and M2: **(a)**, **(b), (c)** and **(d)** reference material M0 at 5x, 20x, 50x and 100x mag., respectively.

(e), **(f)**, **(g)** and **(h)**, composite M1 (w_f = 0.003) at 5x, 20x, 50x and 100x mag., respectively and **(i)**, **(j)**, **(k)** and **(l)**, composite M2 (w_f = 0.0035) at 5x, 20x, 50x and 100x mag., respectively.

However, at higher magnifications, dark features are found in the grain boundaries together with the AlFe intermetallic. These features are the multi-walled carbon nanotube bundles formed during composite processing after the Cu10S1 powder was introduced.

Figs. 4.26 i), j), k) and l) (left column) illustrate the M2 composite microstructure at 5x, 20x, 50x and 100x magnification, respectively. In this case, even at lower magnification, the difference in the microstructure in comparison with M0 and M1 is evident. A higher content of dark features (arrowed) is found surrounding the α-Al grains in comparison with the M1 composite despite the MWCNTs content introduced in the M2 metal matrix being only slightly higher (see Table 4.16). This is indicative of more efficient introduction of the MWCNTs in the M2 composite. This is better seen at higher magnification and may indicate that part of the nanotubes introduced into the M1 metal matrix during processing was ejected.

The composite microstructure plays a major role on the properties of the composites. In this case, the microstructure is strongly influenced by the rheocasting processing method, and the Cu10S1 filler addition as the increasing content of MWCNTs also indicates an increasing Cu content.

In order to predict microstructure evolution of the composite alloy, and verify why the M2 composite shows a more efficient introduction of nanotubes into the matrix than the M1, the chemical composition of the composites was obtained by OES (see Table 4.16). These compositions were used to simulate the respective phase diagrams and predict the volume fractions of the phases formed under non-equilibrium conditions using the PANDAT 8 (Pan Al.database) software (methodology described in Chapter 3, Section 3.6).

Scanning electron microscopy together with the energy dispersive spectroscopy (SEM+EDS) was then used to assess the microstructure morphology and chemical composition in samples M0, M1 and M2 to identify the phases present and thus compare the predicted and experimental results.

Fig. 4.27 a) illustrates the simulated phase diagram of the M1 composite alloy (Al-Cu2.86-Mg3.14 wt.%) under non-equilibrium conditions with the dashed line indicating the composition studied.
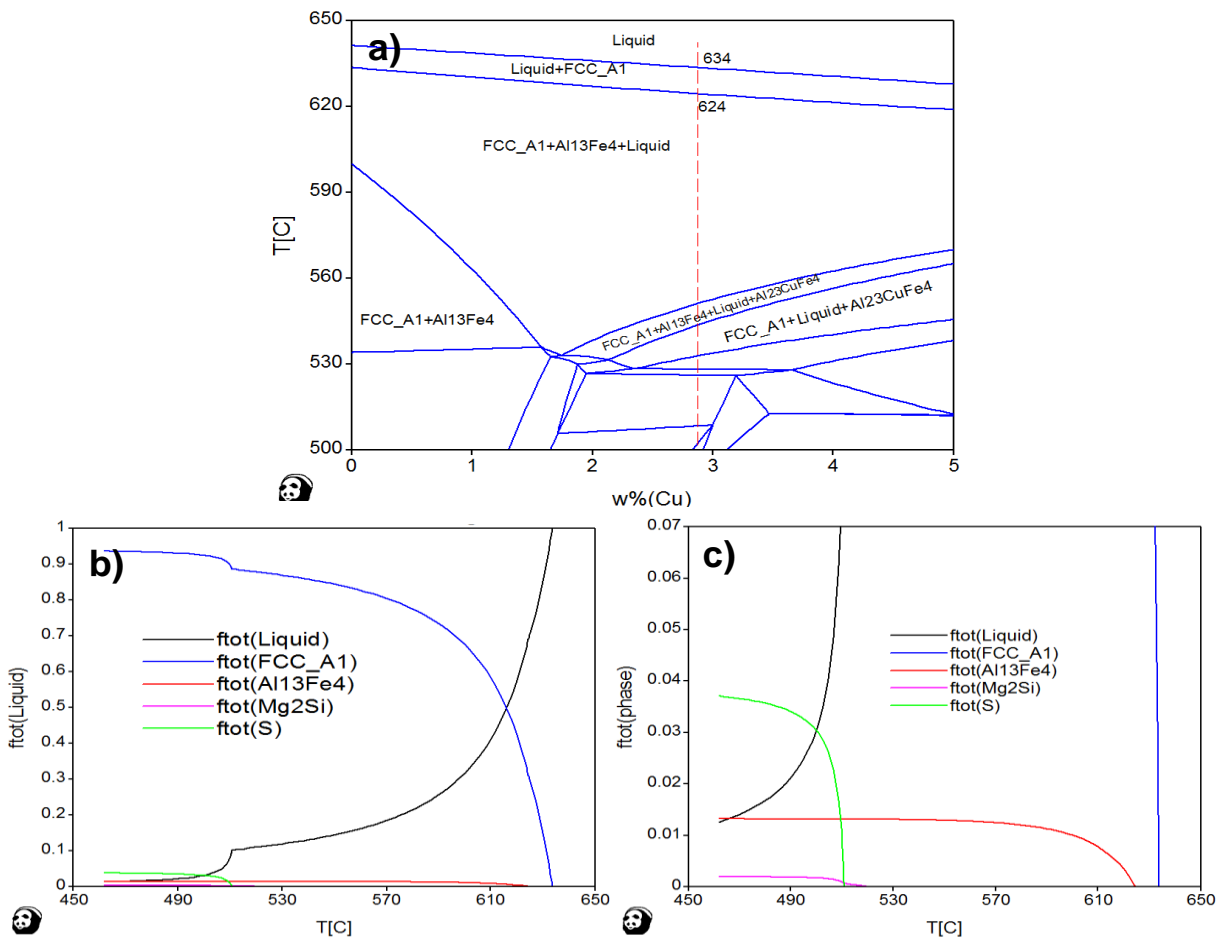

Fig. 4.27. Phase diagram and phase volume fraction simulation for the M1 composite microstructure using the PANDAT 8 Simulation software: **(a)** Non-equilibrium phase diagram; **(b)** Volume fraction evolution for the different phases present during composite alloy solidification and cooling; and, **(c)** volume fraction of the intermetallic phases.

Fig. 4.27 b) and c) give the respective phase formation and phase volume fraction evolution during alloy solidification and cooling. According to the data obtained in the simulation, the phases present at room temperarure are: - the primary Al face centred cubic structure (FCC α-Al) (v_f = 0.948), $Al_{13}Fe_4$ (or $Al_{61}Fe_{39}$ in wt.%, v_f = 0.013), Mg_2Si (or $Mg_{63}Si_{37}$ in wt.%, v_f = 0.0018) and the S phase which is the Al_2CuMg ($Al_{38}Cu_{45}Mg_{17}$ in wt.%, v_f = 0.037).

Fig. 4.28 reveals images of the microstructure for the M1 composite taken using the backscattered electron (BSE) detector to exhibit atomic contrast. Fig. 4.28 a) shows the common phases observed, the FCC α-Al and the $Al_{13}Fe_4$ intermetallic which is the most predominant phase as observed in the optical images (Fig. 4.26 e), f), g), and h)).

The SEM+EDS study reveals that the phase illustrated in Fig. 4.28 a) is in fact the $Al_{13}Fe_4$ ($Al_{61}Fe_{39}$) as the composition retrieved from the EDS measurements is $Al_{64}Fe_{36}$ (see Table 4.17). Two distinct AlCuMg based intermetallics appear to co-exist as shown in Fig. 4.28 c), however, they do not match the simulation, Al_2CuMg ($Al_{38}Mg_{17}Cu_{45}$). This may be due to the nature of the composite processing (non-equilibrium). Experimental results indicate that $Al_{57}Cu_{18}Mg_{25}$ forms first and with increasing amounts of Cu, the Cu replaces Mg forming a $Al_{60}Cu_{25}Mg_{15}$ phase.

The simulation also indicates Mg_2Si ($Mg_{63}Si_{37}$ in wt.%) should form, however this phase may have dissolved during surface polishing due to the use of water and as a consequence was not observed. Nevertheless, the amount of Mg_2Si predicted is relatively small, v_f = 0.0018.

Fig. 4.28 SEM BSE micrographs showing the M1 composite microstructure. **(a)** Common phases observed; FCC α-Al, $Al_{13}Fe_4$ and AlCuMg based intermetallics. **(b)** $Al_{13}Fe_4$ intermetallic morphology and **(c)** Co-existence of two AlCuMg intermetallics $Al_{57}Cu_{18}Mg_{25}$ (dark grey phase) and $Al_{60}Cu_{25}Mg_{15}$ (bright grey phase)

Table 4.17. Comparison of composition between predicted and observed intermetallic phases in M1 + M2 samples.

Predicted Phases wt.%	Observed Phase wt.%	
	M1	**M2**
$Al_{61}Fe_{39}$	$Al_{64}Fe_{36}$	$Al_{62}Fe_{38}$
		$Al_{64}Cu_{2.5}Fe_{33.5}$
		$Al_{56-63}Cu_{21-30}Fe_{9-13}$
$Al_{38}Cu_{45}Mg_{17}$	$Al_{57}Cu_{18}Mg_{25}$	
	$Al_{60}Cu_{25}Mg_{15}$	$Al_{56-59}Cu_{25-30}Mg_{12-13}$
$Mg_{63}Si_{37}$	---	---
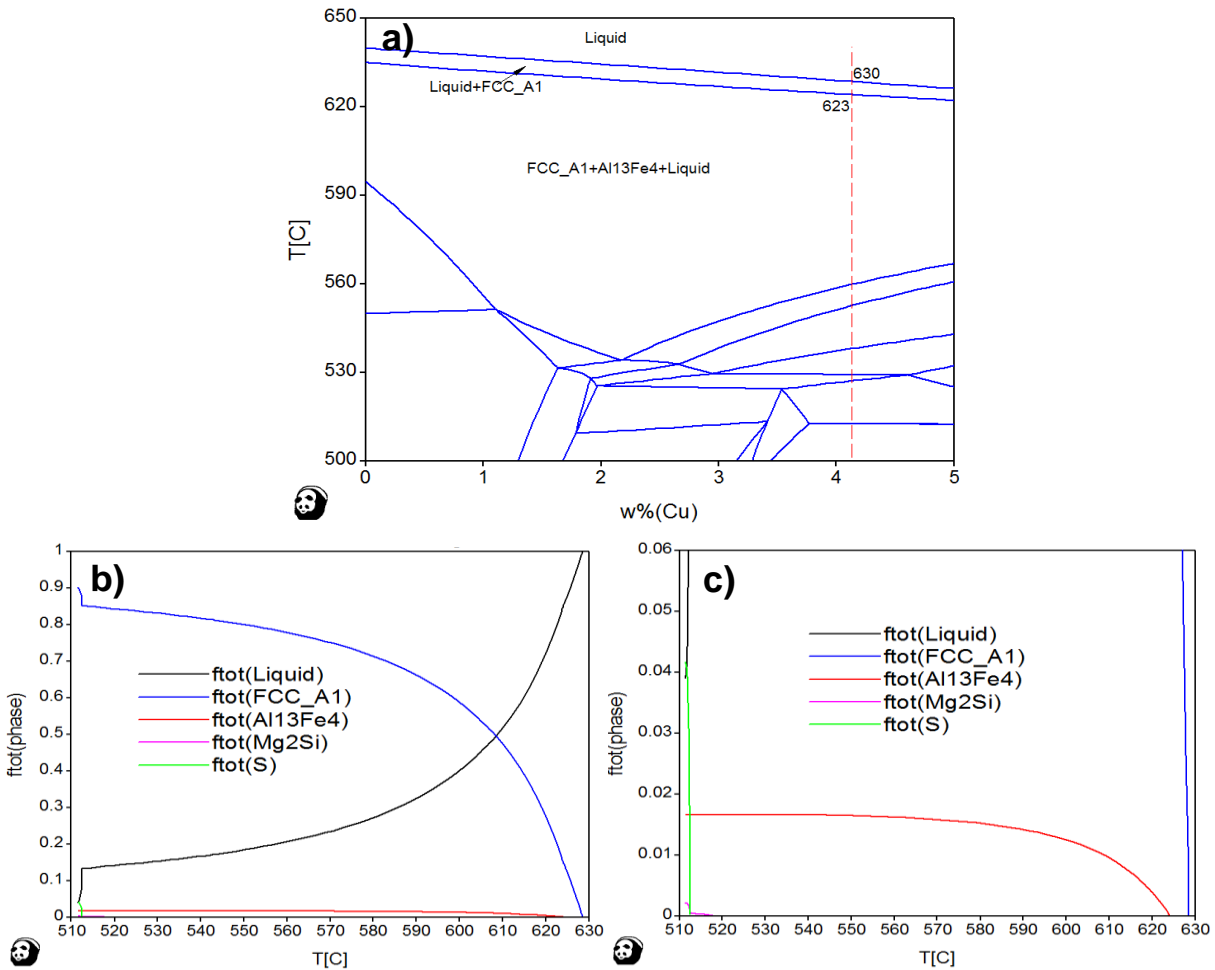
Fig. 4.29 Phase diagram and phase volume fraction estimation for the M2 composite microstructure using PANDAT 8 Simulation software: **(a)** Non-equilibrium phase diagram; **(b)** Volume fraction evolution for the different phases present during composite alloy solidification and cooling; and, **(c)** volume fraction of the intermetallic phases.

Analogous to the Fig. 4.27, the Fig. 4.29 shows the simulated phase diagram for the M2 composite alloy (Al-Cu4.13-Mg3.25 (wt.%)) under non-equilibrium conditions. Figs. 4.29 b) and c) give the respective phases and phase volume fraction evolution during alloy solidification and cooling for the composite composition depicted by the dashed line, in Fig. 4.29 a). The phases present at room temperature are the same as those predicted for the M1 composite with only a marginal variation in phase volume fraction (see Table 4.17): FCC α-Al (v_f = 0.939), $Al_{13}Fe_4$ (or $Al_{61}Fe_{39}$) in wt.%, v_f = 0.017), Mg_2Si (or

$Mg_{63}Si_{37}$ in wt.%, v_f = 0.002) and the S phase which is the Al_2CuMg ($Al_{38}Cu_{45}Mg_{17}$ in wt.%, v_f = 0.042).
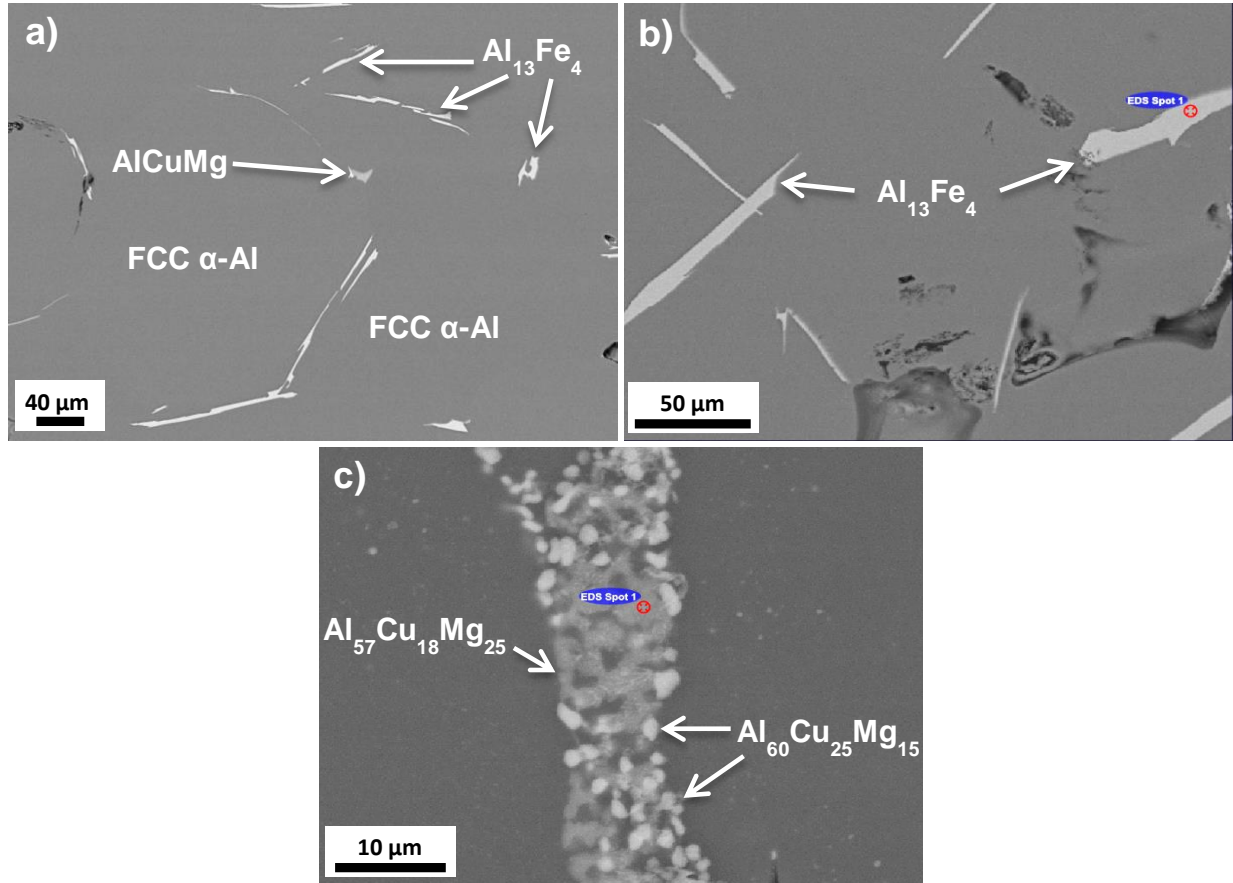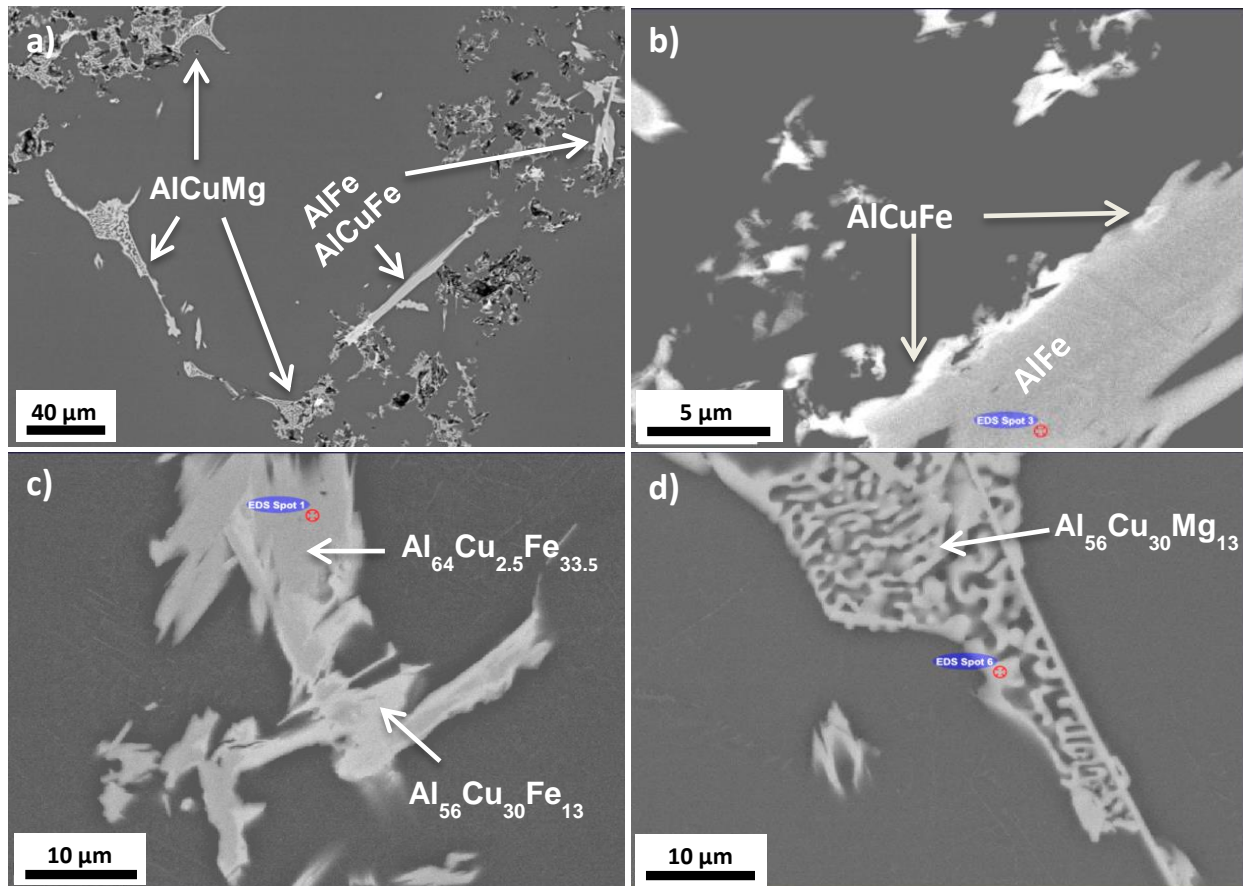

Fig. 4.30 BSE micrograph showing the M2 composite microstructure: **(a)** Common phases observed, FCC α-Al, AlFe, AlCuFe and AlCuMg based intermetallics; **(b)** and **(c)** morphology of an AlCuFe intermetallic composed of two distinct compositions $Al_{64}Cu_{2.5}Fe_{33.5}$ and $Al_{56}Cu_{30}Fe_{13}$ illustratting Cu diffusion into the AlFe intermetallic; and **(d)** an $Al_{56}Cu_{30}Mg_{13}$ intermetallic morphology.

Fig. 4.30 reveals the microstructure morphology of the M2 composite and features studied using EDS point analysis. Fig. 4.30 a) shows the common phases observed, the primary FCC α-Al matrix, and the AlCuFe and AlCuMg based intermetallics. In this composite, the $Al_{61}Fe_{39}$ phase is rarely present alone, however, where found it is in good agreement with the simulation, as it has an average composition of $Al_{62}Fe_{38}$, as shown in Table 4.17. However, due to the higher amount of Cu in the M2 composite

(Cu-4.13wt.%) compared with M1 (Cu-2.86 wt.%), the excess Cu that cannot dissolve in the matrix replaces Fe in the AlFe intermetallic, thus creating the different AlCuFe intermetallic compositions (Table 4.17) and morphologies as shown in Fig. 4.30 b) and c).

It may be possible that AlCuFe quasicrystals form, for example the icosehedral i-AlCuFe ($Al_{63.5}Cu_{23.5}Fe_{13}$) phase or the approximant phases, β-AlCuFe ($Al_{50}Cu_{34.5}Fe_{15.5}$) and ω-AlCuFe ($Al_{70}Cu_{20}Fe_{10}$) as their compositions fall within the AlCuFe intermetallics compositions observed, $Al_{56-63}Cu_{21-30}Fe_{9-13}$. Nevertheless, these intermetallic are not predicted by the simulation.

AlCuMg intermetallics are also easily discerned in the matrix. The Fig.4.30 d) shows an intermetallic with a composition of $Al_{56}Cu_{30}Mg_{13}$. On average, these intermetallics have compositions of $Al_{56-59}Cu_{25-30}Mg_{12-13}$ and are similar to those with higher Cu content found in the M1 composite. However, the composition does not again match the composition predicted by the simulation, $Al_{38}Cu_{45}Mg_{17}$.

It is worth stating the Cu content plays an important role on the successful introduction of the MWCNTs into the Al alloy matrix. The nanotubes were found in substantially higher contents in the M2 composite compared to the M1 (see Fig.4.26), despite the marginally higher amount of MWCNTs (0.3 wt.% in the M1 sample compared 0.35 wt.% in the M2 sample). These nanoparticles were mostly found surrounded or trapped by the AlCuFe and AlCuMg intermetallics.

The Mg_2Si ($Mg_{63}Si_{37}$) phase was also not observed in the M2 composite. Thus, supporting the theory that it was dissolved during specimen surface polishing.

4.3.4.2.2 Filler Identification

In order to verify if the small dark features were in fact MWCNTs, the composites microstructure was analysed by SEM+EDS and TEM (see Chapter 3 Subsection 3.4.1.3 for TEM sample preparation). Fig. 4.31 gives the BSE and In-Lens (IL) mode images of the M1 (left row) and M2 (right row) composites revealing the MWCNT bundles present in the microstructure. Fig. 4.31 a) shows a large MWCNT bundle across the AlFe intermetallic in the M1 composite microstructure. Figs. 4.31 b) and c) show images of the bundles at higher magnifications revealing the nanotubes.

Fig. 4.31 d) shows an In-Lens image from the M2 composite microstructure. It shows the grain boundary area where the dark features (seen in Fig. 4.26 and here are the brighter areas inside the intermetallic) coexist with the AlCuFe and AlCuMg intermetallic. Fig. 4.31 e) shows a MWCNT bundle surrounded by an AlCuFe (needle shape) intermetallic. Fig. 4.31 f) shows bundles of MWCNTs surrounded by AlCuMg intermetallics. The linescan reveals that the bundle is rich in C and therefore is a bundle of MWCNTs.
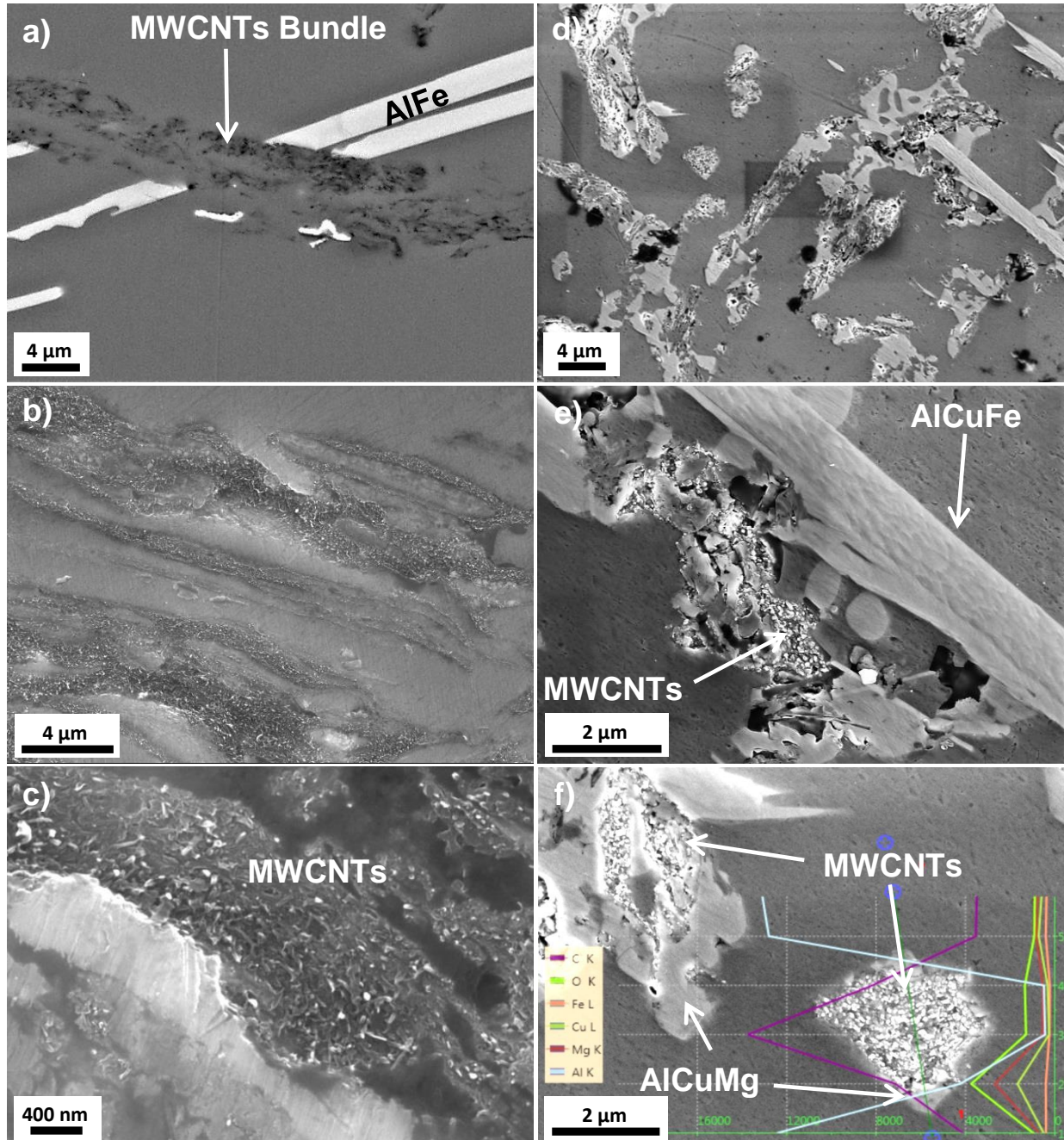
Fig. 4.31 SEM micrographs of the composites microstructures for the M1 (left row) and M2 (right row) samples. **(a)** BSE image revealing a MWCNT bundle crossing an AlFe intermetallic; **(b)** and **(c)** higher magnification images of the MWCNTs bundle; **(d)** In-lens image of an M1 sample grain boundary, **(e)** and **(f)** MWCNT bundles surrounded by AlCuFe and AlCuMg intermetallic and EDS linescan across bundle revealing its C nature.

TEM investigations of the composite microstructure were also performed. Fig. 4.32 shows TEM+EELS+EDS results from the M2 composite sample. Fig.4.32 a) shows a high angle annular dark field STEM image (HAADF images depict Z contrast) of the composite microstructure. The AlMg alloy matrix, the AlCuMg intermetallic and a MWCNT agglomeration located between phases is visible. Individual MWCNTs with an inner core are also observed.

Fig. 4.32 b) presents the MWCNT selected area electron diffraction (SAED) pattern corresponding to the area outlined with the dashed circle. It reveals that is in fact a nanotube and that it have reacted with the Al matrix during processing as 3 diffraction spots were identified as Al_4C_3 (105), (107), (201) and (0012) in addition to the MWCNT planes.

Fig. 4.32 c) gives the characteristic EELS core loss region spectrum for the MWCNT obtained from the same selected area as for the SAED pattern. Once more it confirms the carbon (peak at 284 eV) nature of the nanotube.

Fig. 4.32 d) gives the EDS linescan across the different phases+boundaries shown in Fig. 4.32 a). It confirms that the bright phase is the AlCuMg intermetallic, commonly found surrounding the MWCNTs, and on the other side, (beyond ~ 145 nm) a darker phase rich in Al is observed, which is the AlMg matrix. In between the phases are the MWCNTs. Also at the distance of ~ 145 nm, there is indication of MgO formation and Al_4C_3 formation. The nanotubes are situated between the two metallic phases.

The SEM and TEM characterisation of the composites, produced via the rheocasting technique, show that the MWCNTs can be introduced into the matrix. However, the technique has its limitations as the nanotubes are found in bundles, and also Al_4C_3 formation is not avoided despite the careful selection of the processing conditions. In order to fully harness the properties of these nanoparticles it is crucial that these particles are individually and uniformly dispersed throughout the matrix and any interfacial reactions, in particular the formation of Al_4C_3 are minimized.
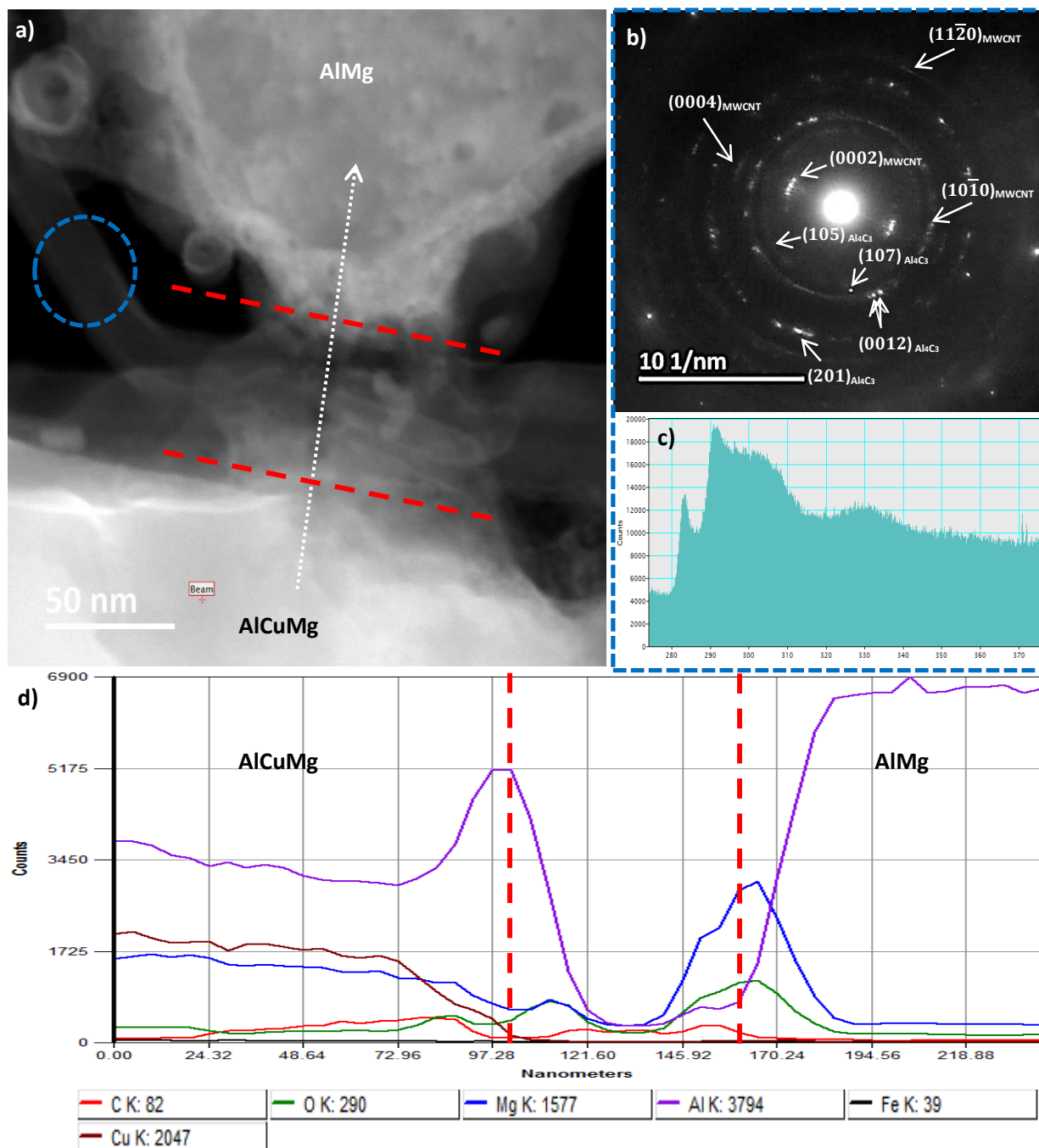
Fig. 4.32 TEM+EELS+EDS study of the M2 composite microstructure: **(a)** STEM HAADF image revealing the distinct phases present, AlMg matrix alloy, AlCuMg intermetallic and the MWCNTs agglomerate between phases; **(b)** and **(c)** SAED pattern and EELS core loss spectrum obtained from the MWCNT selected area (dashed circle), and **(d)** EDS linescan across phases.

4.3.4.3 Equal Channel Angular Extrusion (ECAE)

The composites produced via rheocasting showed that the fillers could be introduced successful into the matrix, however they were found in large randomly oriented bundles. In order to harness the outstanding properties of the MWCNTs, it is necessary that these nanoparticles are individually and uniformly dispersed throughout the matrix. To increase the probability of the MWCNTs improving the thermal conductivity of the matrix, it is important that they are aligned within the matrix, as nanotubes exhibit anisotropic thermal properties.

Equal channel angular extrusion (ECAE) post-processing has been demonstrated to be efficient in aligning CFs within the Al matrix (see Subsection 4.2.1.3), and as a consequence it has also been used to align the MWCNTs after rheocasting. The M1 composite was subjected to ECAE post-processing, see Chapter 3 Subsection 3.3.2 for methodology and description of the samples produced. Only the M1 composite was subjected to the post-processing due to limited access to the ECAE facility as described in the methodology.

The specimens were cut perpendicular to the extrusion direction polished and studied by means of O.M. and SEM, to investigate the composite microstructure evolution with an increase in the number of iterations.

Fig 4.33 shows the microstructure evolution of the M1 composite due to the ECAE post-process after 0 iterations (Fig. 4.33 a)), 4 iterations (Fig. 4.33 b)) and 6 iterations (Fig. 4.33 c)). After 4 iterations, a high degree of microstructure alignment is already observed as the angle ø between the extrusion direction (ED) and deformation direction (DD) $\text{Ø}_{ED\text{-}DD} \approx 7.61°$, which is further reduced after 6 iterations, to $3.24° < \text{Ø}_{ED\text{-}DD} < 3.62°$. Fig. 4.33 d), depicts what is thought to be a MWCNT bundle, deformed and aligned in the deformation direction.

In order to verify if the aligned features observed were indeed the MWCNTs, samples of the M1 composite processed by ECAE after 6 iterations were examined using SEM, and results are shown in Fig. 4.34. Fig. 4.34 a) shows the BSE low magnification image

of the composite microstructure exhibiting long aligned features, similar to that observed in Fig. 4.33 d). Fig. 4.34 b) shows a high magnification In-lens image from a selected area in Fig.4.34 a), revealing the presence of nanotubes.
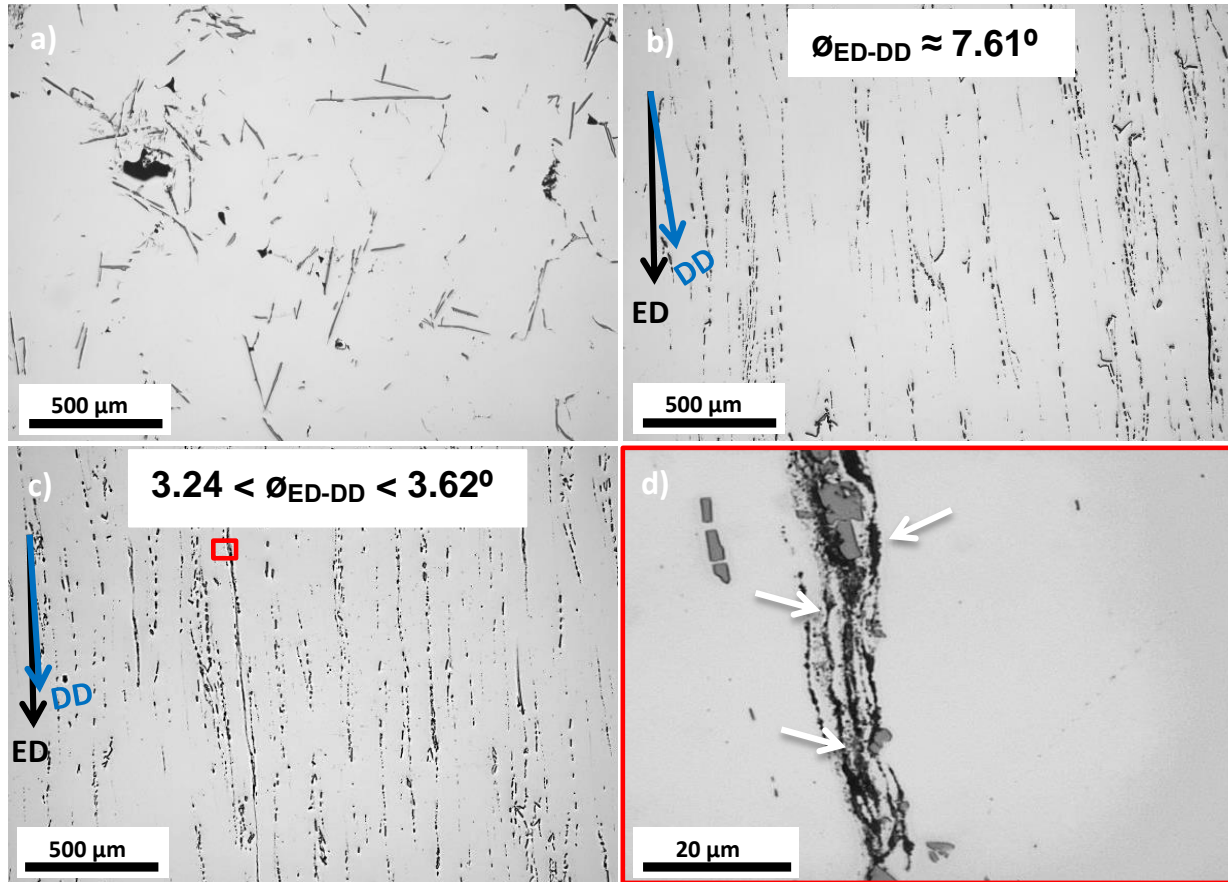
Fig. 4.33 O.M. micrographs of the M1 composite sample displaying the microstructure evolution due to ECAE post-processing: **(a)** 5x, 0 iterations, **(b)** 5x, 4 iterations, $\varnothing_{ED-DD} \approx$ 7.61º, **(c)** 5x, 6 iterations, 3.24º $< \varnothing_{ED-DD} <$ 3.62º and **(d)** 100x, 6 iterations, image from selected area highlighted in (c) showing deformed and aligned MWCNTs bundle (arrowed) in the deformation direction.

As the number of iterations increase, the Al matrix grains are further broken and reduced in size. This also happens to the nanotubes bundles, as illustrated in Fig. 4.34 c), where the bundle become so elongated that they are several nanotubes wide. In some cases the nanotubes were separated from the bundles and became individually dispersed within the metal matrix as shown in Fig. 4.34 d). This indicates that this

technique can be applied to disperse the nanotubes individually within the metal matrix and its effectiveness depends on the initial size of the MWCNTs bundles and the number of iterations executed. In other words, the smaller the bundles the lower the number of iterations needed to achieve individual MWCNT dispersion.
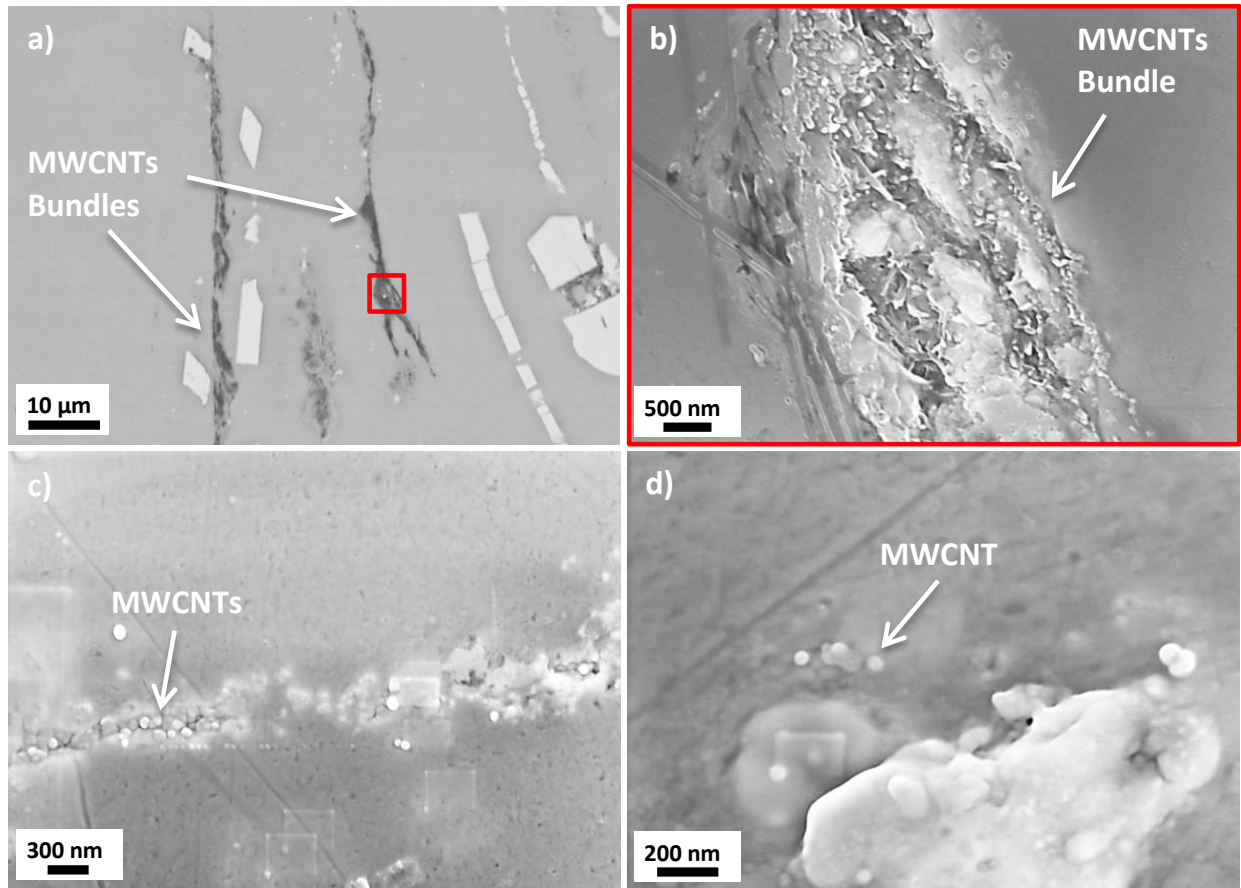
Fig. 4.34 SEM micrographs from the ECAE post-processed M1 composite after 6 iterations: **(a)** BSE image showing the aligned MWCNTs bundles (dark features). **(b)** high magnification In-lens image of area selected in (a) revealing the nanotubes. **(c)** high magnification In-Lens image showing an elongated and very narrow bundle (only a few nanotubes wide) and **(d)** individual nanotubes dispersed within the metal matrix (arrowed).

The ECAE samples were also studied using TEM, in order to verify nanotube alignment and matrix/nanotube interface interaction. Fig. 4.35 shows the TEM characterisation of aligned individual MWCNTs found in an ECAE post-processed M1 composite sample
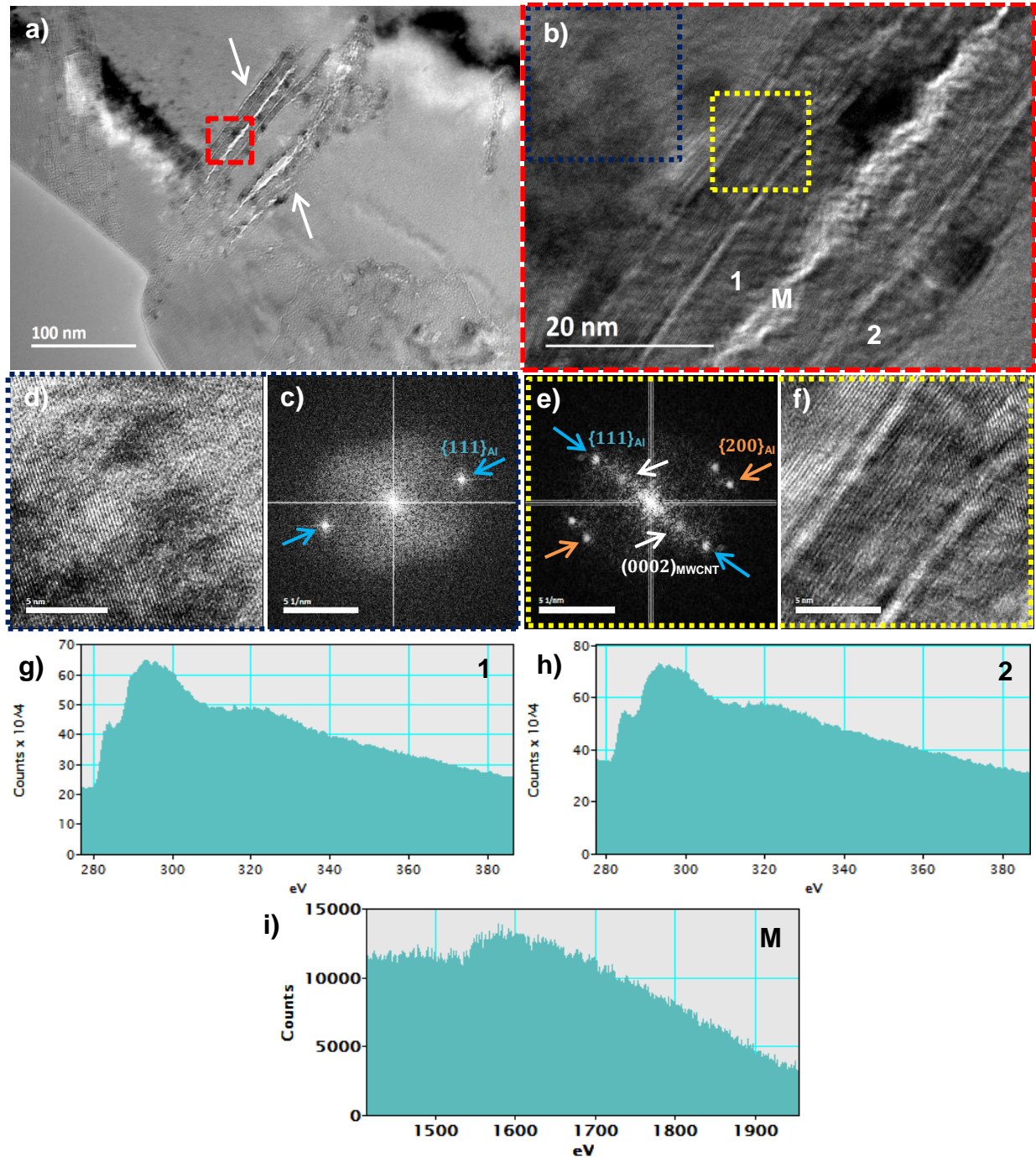
Fig. 4.35 TEM characterisation of aligned individual MWCNTs found in an ECAE post-processed M1 composite sample after 6 iterations. **(a)** BF image (50000 x mag.) of the MWCNTs (arrowed) embedded within the Al matrix. **(b)** BF image (400000 x mag.) of two MWCNTs from the selected area shown in (a). **(c)** FFT generated diffraction pattern obtained from the larger square illustrated in (b) showing Al matrix {111}$_{Al}$ plane and, **(d)**

respective IFFT image revealing the lattice structure. **(e)** FFT generated diffraction pattern obtained from smaller square illustrated in (b) showing Al matrix/MWCNT interface revealing $\{111\}_{Al}$ $\{200\}_{Al}$ $(0002)_{MWCNT}$ planes and, **(f)** corresponding IFFT image revealing the interface lattice structure. **(g)**, **(h)** and **(i)** show the EELS core loss spectrum taken from position 1, 2 and M as illustrated in (b), respectively.

after 6 iterations. Fig 4.35 a), shows a bright field (BF) micrograph where aligned individual MWCNTs (arrowed) can be easily identified. Fig. 4.35 b) depicts a higher magnification (400000x) BF image of two nanotubes, obtained from the selected area highlighted in a). Nanotube 1 has an outer diameter, $d_o = 13.83 \pm 0.58$ nm, and inner diameter $d_{in} = 0.71 \pm 0.21$ nm. Whereas, nanotube 2 revealed outer (d_o) and inner (d_i) tube diameters of $d_o = 12.29 \pm 0.21$ nm, and $d_i = 1.38 \pm 0.11$ nm, respectively.

In both cases the nanotubes appear to be squeezed against one another and aligned in the extrusion direction. This explains why their inner and outer diameters are below the average value for the S1 MWCNTs $d_i = 6.84 \pm 2.45$ nm and $d_o = 26.32 \pm 8.12$ nm, respectively. However, If added the average inner diameter to the squeezed nanotubes, their outer diameter would fall within the average range, proving that they are in fact squeeze against one another. It can also be seen that the adjacent outer walls of the nanotubes (position depicted with letter M in Fig. 4.35 b)) are also severely damaged due to friction during ECAE post-processing.

Fig. 4.35 c) gives the FFT diffraction pattern taken from the Al matrix, i.e. the area delineated by the larger square in b). The $\{111\}_{Al}$ plane is exhibited, being the distance between the points 4.7481 nm^{-1} (i.e. 0.2106 nm). Fig. 4.35 d) shows the IFFT image from the area selected in the matrix, studied with FFT in c). The Al matrix/MWCNT interface was also assessed and the region of the interface selected is depicted as the smaller square in the Fig. 4.35 b) with its corresponding diffraction pattern given in Fig. 4.37 e). The $(0002)_{MWCNT}$ was observed at a distance from the central spot of 2.278 nm^{-1} (0.438 nm), whereas the $\{111\}_{Al}$ and $\{200\}_{Al}$ planes have distance of 4.416 nm^{-1} (0.2264 nm) and 4.895 nm^{-1} (0.2042 nm), respectively. However, in this case no Al_4C_3

presence was observed in the interface. The lattice area of the interface studied with FFT is shown in Fig. 4.35 f).

Figs. 4.35 g) and h) show characteristic EELS spectrum core loss energy edge for the MWCNT obtained from position 1 and 2, respectively (see Fig. 4.35 b)), confirming the presence of C (284 eV). No significant Al energy edge (not shown here) was observed in these positions. Finally, Fig 4.35 i) gives the EELS core loss spectrum from the position M, revealing the Al energy edge (1560 eV) with no significant C energy edge observed (not shown here), thus supporting the statement that they are in fact two nanotubes next to each other.

The TEM study of the M1 composite sample indicates that nanotubes can be individually dispersed and aligned by rheocasting followed by ECAE processing, however, the nanotubes do suffer significant damage. The FFT and EELS study unequivocally proves that the nanofeatures observed in the STEM study are in fact the nanotubes. Al_4C_3 was not observed but, once it nucleates during the rheocasting processing it should also be present after ECAE processing.

4.3.5 Effective Thermal Conductivity of Composite

The same procedure to measure the thermal conductivity is followed in this chapter for the Al/Cu10S1 composites as was described in Subsection 4.2.2 for the Al/Cu-CFs. The thermal conductivity of the composites produced by rheocasting and rheocasting followed by equal channel angular extrusion (ECAE) were measured using the laser flash technique as described in Chapter 3, Subsection 3.5.1.

To predict the real thermal conductivity contribution of the S1 MWCNTs used in the composites, an attempt to obtain a quantitative value for the thermal conductivity from an individual S1 MWCNT was performed using a combination of scanning thermal microscopy (SThM) and finite element method (FEM). The experimental values were then compared with theoretical models to assess the thermal conductivity efficiency of the composite. The results obtained in this study are described hereafter in this chapter.

4.3.5.1 Thermal Conductivity of individual S1 MWCNTs

Testing the real thermal conductivity of the MWCNTs is important in order to be able to verify if the filler has a positive contribution. To measure the thermal conductivity of an individual S1 MWCNT the scanning thermal microscopy (SThM) technique and finite element method (FEM) were used. The results are described in this section. The description of the technique used and methodology followed are described in Chapter 3, Subsection 3.5.2.

The SThM probe measures both the topography and the thermal properties, as shown in Fig. 4.36. Fig. 4.36 a) depicts the topography channel, the brighter the feature the higher is its height. As the probe passes over the nanotube (arrowed), the height profile corresponds to roughly 40 nm in diameter and 3 μm in length. Fig. 4.36 b) gives the thermal channel, the brighter, the lower the thermal conductivity as it corresponds to higher temperature. The data obtained in the thermal channel was recalculated to thermal resistance and subsequently modelled using Finite Element Methods.
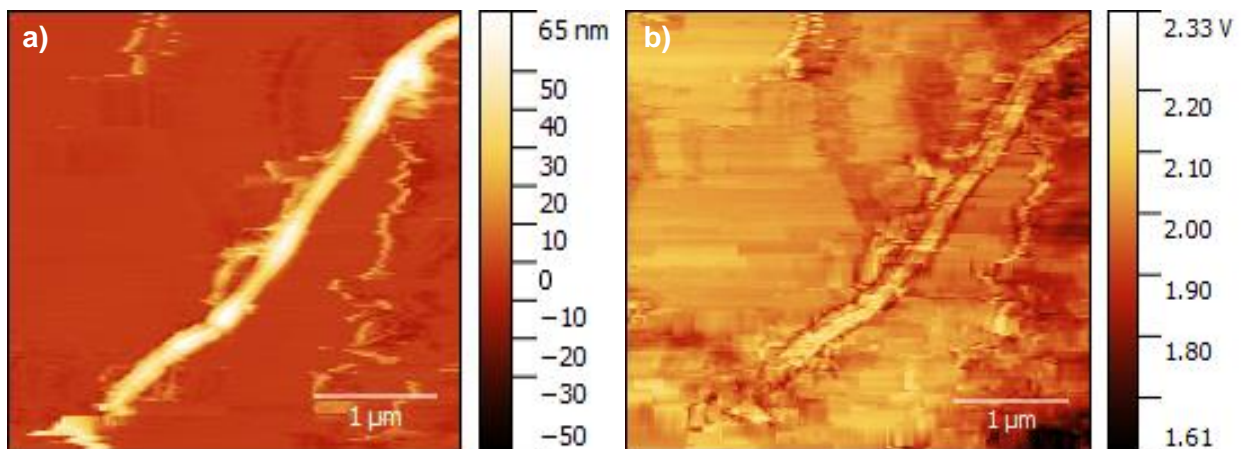
Fig. 4.36 Thermal conductivity assessment of an individual S1 MWCNT using a scanning thermal microscopy device: **(a)** AFM channel giving the nanotube topography; and, **(b)** thermal channel revealing the nanotube thermal properties.

Fig. 4.37 gives the FEM results where the images illustrate two mutual positions of the tip, on top of the substrate and the on top of the nanotube. Fig. 4.37 a) and b) represent the calculated thermal field and the sliced view of the probe in contact with the mica
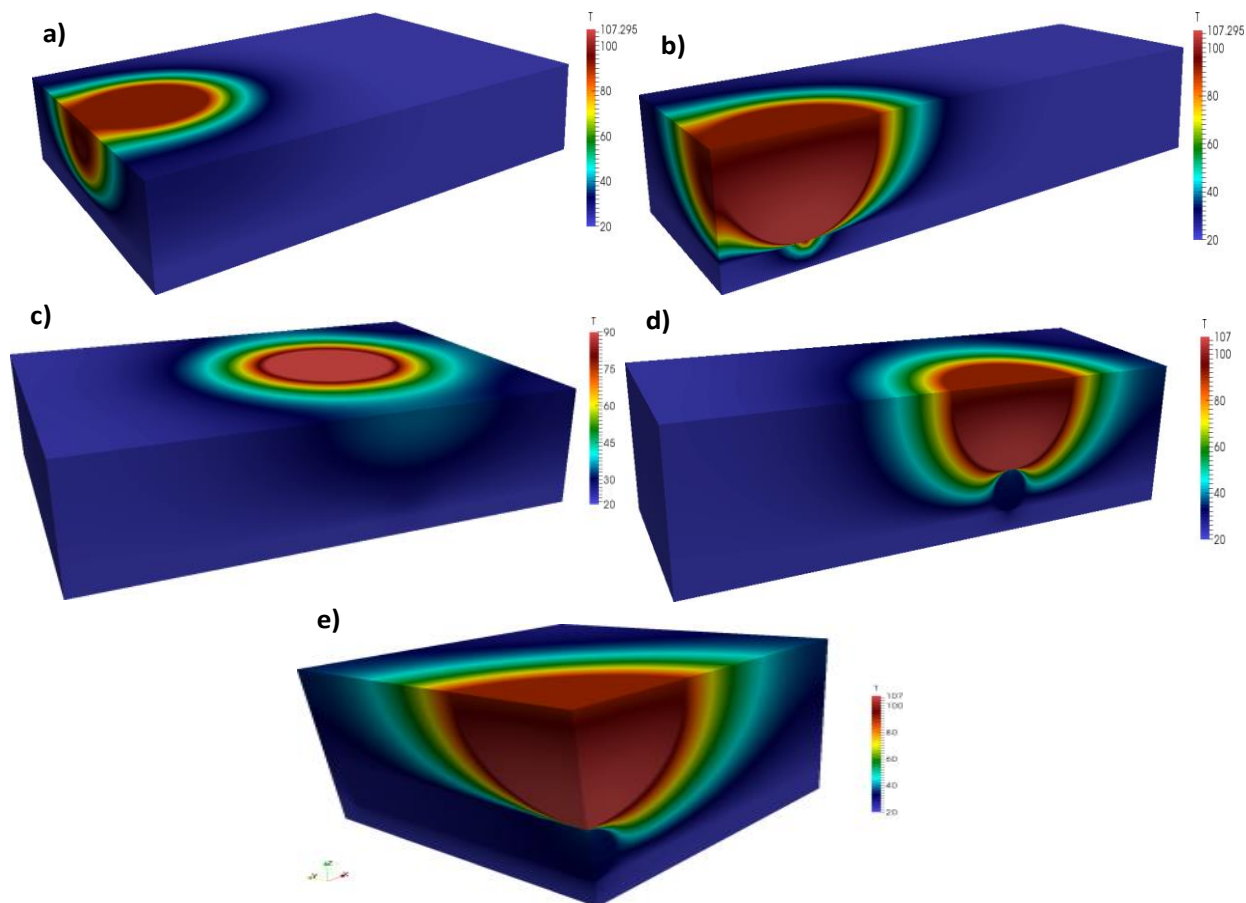
Fig. 4.37 SThM thermal fields calculated using FEM for the following conditions: **(a)** and **(b)** Probe tip placed on top of mica substrate, **(c)**, **(d)** and **(e)** tip placed on top of the nanotube.

substrate. Whereas, Fig. 4.37 c), d) and e) represent the calculated thermal fields and sliced view of the probe on the top of the nanotube lying on the mica substrate.

The computation was run with various parameters and this multi-variate approach narrowed down the possible interval of thermal conductivity. By halving the interval it was found that the lower boundary limit is 19.5 W m^{-1} K^{-1} and the higher boundary limit is 20 W m^{-1} K^{-1}. No further narrowing was performed as this creates high uncertainties caused by other factors. The value obtained is a combination of both, the thermal conductivity along ($K_{MWCNTs,1}$) and across ($K_{MWCNTs,1}$ = 10 W m^{-1} K^{-1}) the nanotube, as the latter value was not deducted during simulation. Therefore, the $K_{MWCNTs,1}$) is definitely higher than 20 W m^{-1} K^{-1}.

4.3.5.2 Rheocasting

The experimental thermal conductivity (K_c) results of the Al3Mg/Cu10S1 composites, as a function of the MWCNTs addition content processed by means rheocasting technique are presented in this section. Fig. 4.38 shows the thermal conductivity evolution as a function of the MWCNTs addition. The variation of the Cu and Mg alloying elements is also shown. Table 4.18 gives the composite sample designation, respective average chemical composition (wt.%) and corresponding measured thermal conductivity data used to produce Fig. 4.38.
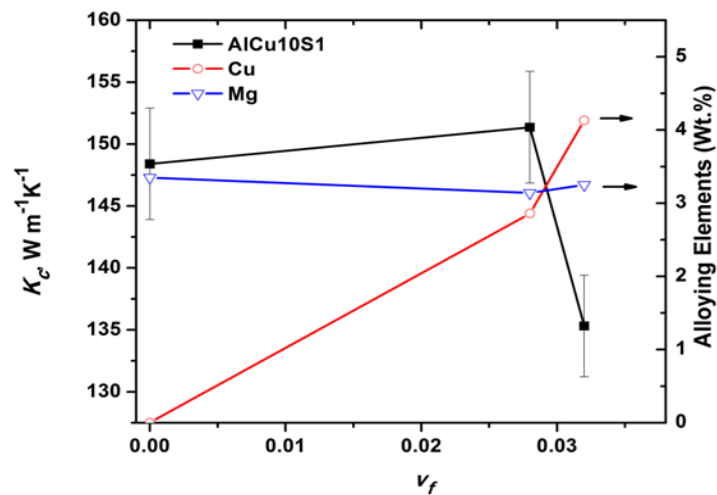
Fig. 4.38 Thermal conductivity of the Al3Mg/Cu10S1 composite versus MWCNTs filler content (wt.%). For reference, Cu and Mg alloying content for the different composites are also plotted.

According to the thermal conductivity results, M0 the reference sample (Al3Mg, no MWCNTs added) has an effective thermal conductivity of $K_{M0} = 148.4 \pm 4.5$ W m^{-1} K^{-1}.

M1 composite ($w_f = 0.003$, $v_f = 0.028$ MWCNTs content) registered a marginal K_c increase, $K_{c,M1} = 151.36 \pm 4.5$ Wm^{-1}K^{-1}, in comparison with the reference M0 (+ 3 W m^{-1} K^{-1}). However, the addition of the powder resulted also in an increase in Cu content (from 0.002 to 2.86 wt.%), whilst the Mg content variation remained minimal, as expected.

Table 4.18. Al3Mg/Cu10S1 composites sample designation, its respective average chemical composition (wt%) and corresponding measured thermal conductivity.

Sample	Cu10S1 addition	MWCNTs addition		Composition (wt%)						Thermal Conductivity, K_c
	g	w_f	v_f (ρ_{bulk})	Al	Si	Fe	Cu	Mn	Mg	W m^{-1} K^{-1}
M0	0	0	0	96.5	<0.003	0.13	0.002	0.01	3.35	148.4 ± 4.5
M1	75	0.003	0.028	93.1	0.08	0.65	2.86	0.01	3.14	151.4 ± 4.5
M2	87.8	0.0035	0.032	91.4	0.11	0.82	4.13	0.01	3.25	135.3 ± 4.1

The M2 composite (w_f= 0.0035, v_f = 0.032 MWCNTs content) has a thermal conductivity of, $K_{c,M2}$ = 135.3 ± 4.1 Wm^{-1}K^{-1}, in comparison with M0 (148.4± 4.5 W m^{-1} K^{-1}, a reduction of 13.1 W m^{-1} K^{-1}) opposing the increment (+ 3 W m^{-1} K^{-1}) observed for the M1 composite. In M2 composite, the Cu content increased even further, to 4.13 wt.% (+ 1.27 wt.% than M1), whilst Mg remained relatively constant.

4.3.5.3 Rheocasting followed by ECAE

Carbon based materials, such as MWCNTs are anisotropic with respect to their properties, and thermal conductivity is no exception. Therefore, the M1 (w_f = 0.003, v_f = 0.028 MWCNTs content) composite was subjected to ECAE post-processing in order to align the filler inside the matrix in an attempt to increase the thermal conductivity. The thermal conductivity results are presented in Fig. 4.39 and further information such as sample designation and respective thermal conductivity to support Fig.4.39 is given in Table 4.19.

In the extrusion direction (ED), the same direction as $K_{c,1}$ (see Figs. 2.17 and 2.18), after 4 iterations the composite M1 showed a small increase in thermal conductivity when compared with the same composite without ECAE processing (0 iterations), $K_{c,4i,1}$ = 156.9 ± 4.7 W m^{-1} K^{-1} (+5.5 W m^{-1} K^{-1}). After 6 iterations, the composite thermal conductivity is $K_{c,6i,1}$ = 147.7 ± 4.4 W m^{-1} K^{-1} (- 9.2 W m^{-1} K^{-1} than for 4 iterations and - 3.7 W m^{-1} K^{-1} than 0 iterations samples), reverting the increase thermal conductivity observed after 4 iterations.
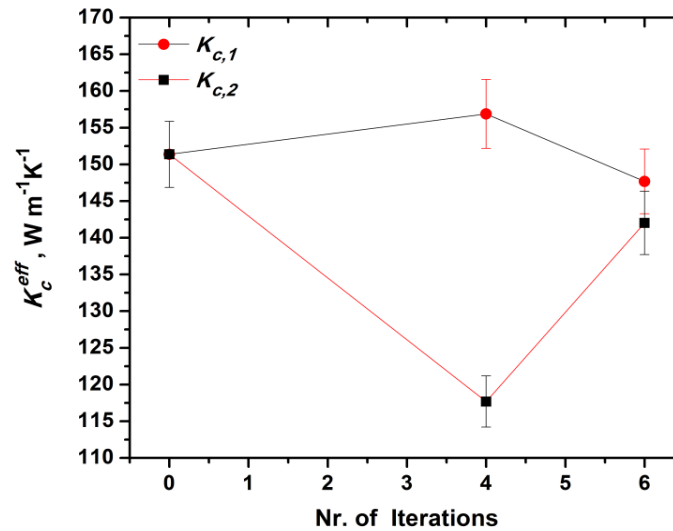
Fig. 4.39. Effect of ECAE post-processing induced deformation on the thermal conductivity of the M1 (Al3Mg/Cu-10S1 (0.3 wt.% MWCNTs)) composite, in the $K_{c,1}$ direction (same direction as the deformation) and $K_{c,2}$, direction (perpendicular direction to deformation) as a function of the ECAE number of passes.

Table 4.19. M1 ECAE post-processed (Al3Mg/Cu10S1 (0.3 wt.% MWCNTs)) composite designation and corresponding measured thermal conductivity.

| | Thermal Conductivity K_c, W m^{-1} K^{-1} | |
| | M1 | |
Iterations	$K_{c,1}$	$K_{c,2}$
0	151.4 ± 4.5	151.4 ± 4.5
4	156.9 ± 4.7	117.7 ± 3.5
6	147.7 ± 4.4	142 ± 4.3

The M1 composite thermal conductivity in the perpendicular direction to ED $K_{c,2}$, dropped to $K_{c,4i,2}$ = 117.7 ± 3.5 W m^{-1} K^{-1} , - 33.7 W m^{-1} K^{-1} for 4 iterations in comparison to the 0 iterations composite sample. After 6 iterations the composite exhibited a thermal conductivity of $K_{c,6i,2}$ = 142 ± 4.3 W m^{-1} K^{-1}, again showing contradictory behaviour in comparison to the declining trend observed in the sample with only 4 iterations , + 24.3 W m^{-1} K^{-1}.

4.3.5.4 Effective Thermal Conductivity of the Al/MWCNTs Composite

The experimental thermal conductivity of the composites produced via rheocasting and rheocasting+ECAE were compared with various theoretical models, in order to help understand if the S1 MWCNTs give a positive thermal contribution to the Al matrix. Three two dimension (2D) thermal conductivity models were used in this comparison; 1) the Maxwell-Garnett effective medium approach (MG-EMA)[8]; 2) Nan et al[8] (an extension of the MG-EMA model) and; 3) Eshelby´s equivalent inclusion model developed by Hatta-Taya et al[2,3] simple models.

MG-EMA and Nan et al models assume the nanotubes are randomly oriented and homogeneously distributed throughout the Al matrix. Hatta-Taya's model was used to simulate spherical particles (sphere shape was selected for simplicity) as the MWCNTs are normally found in big bundles (see Figs 4.26 and 4.33). Hatta-Taya's model was also used to consider aligned MWCNTs within the matrix. For the thermal conductivity theoretical models in depth description see Chapter 2, Section 2.5, and for the parameters used in the models, see Chapter 3, Subsection 3.5.3.

The thermal conductivity comparison was performed according to two circumstances referred to as "theoretical" and "corrected" conditions (see Chapter 3 Subsection 3.5.3), and was similar to the approach used for the Al/Cu-CFs composites (see Subsection 4.2.2.3). However, in this case, the corrected condition only accounted for the effect of the porosity for each composite tested, the v_f used is the theoretical value (i.e. the same as that introduced during composite processing).

The "theoretical" and "corrected" conditions were also calculated for two scenarios (see Figs. 4.40 and 4.41, Tables 4.21, 4.22, 4.23 and 4.24), where the theoretical v_f is calculated as a function of bulk (ρ_{bulk}) and real density (ρ_{real}). Bulk density considers the mass per volume of the material and includes the volume of the pores or void space. However, real density, considers the volume of the material but excludes the pore volume[5]. The bulk density of the nanotubes value used is 0.28 g cm^{-3} and the real density is 2.1 g cm^{-3}.

In order to assess whether the MWCNTs possess high thermal conductivity, two case scenarios were considered in the models. The best case scenario (2000), where the in-plane (along longitudinal axis) thermal conductivity was considered to be the same as that provided by the manufacturer, i.e. $K_{MWCNTs,1}$ = 2000 W m^{-1} K^{-1}, and the worst case scenario (20), where the filler thermal conductivity was considered to be the same as that of the individual nanotube, i.e. $K_{MWCNTs,1}$ = 20 W m^{-1} K^{-1}, obtained from SThM+FEM study (see section 4.3.5.1)

The effect of increasing Cu content (see Fig. 4.38) on the thermal conductivity of the composite was not accounted in the models as it was not possible to obtain experimental thermal conductivity data of the Al3Mg+Cu with Cu content corresponding to that in the composites produced.

4.3.5.4.1 Theoretical Condition

In this subsection, the results of the comparison between the experimental thermal conductivity of the composites (K_c) and the theoretical models considering several factors regarding the MWCNTs, such as: shape; alignment; density and thermal conductivity, according to the "theoretical" condition are outlined.

The K_c value of the composites according to their filler content and filler density type is given in Table. 4.20.

Table 4.20 Composite designation and respective K_c as acquired and after porosity volume faction (φ) correction K_c^{corr} as a function of v_f according to bulk and real MWCNTs density.

Sample	v_f		φ	K_c	K_c^{corr}
	$\rho_{bulk}.$	$\rho_{real}.$			
M0	0	0	0.009 ± 0.005	148.4 ± 4.5	150.5 ± 4.7
M1	0.028	0.0038	0.015 ± 0.004	151.4 ± 4.5	154.8 ± 5.3
M1$_{4i,1}$	0.028	0.0038	0.0003 ± 0.0002	156.9 ± 4.7	157 ± 4.7
M1$_{4i,2}$	0.028	0.0038	0.0003 ± 0.0002	117.7 ± 3.5	117.8 ± 3.5
M1$_{6i,1}$	0.028	0.0038	0.0003 ± 0.0001	147.7 ± 4.4	147.8 ± 4.4
M1$_{6i,2}$	0.028	0.0038	0.0003 ± 0.0001	142 ± 4.3	142.1 ± 4.3
M2	0.032	0.0044	0.04 ± 0.013	135.3 ± 4.1	143.8 ± 7.3

The thermal conductivity of the reference material M0 (no filler addition) obtained experimentally was used as the value of the thermal conductivity of the matrix in all models. (K_m = 148.4 ± 4.5 W m^{-1}K^{-1}).

The MG-EMA and Nan et al models give an estimation of the K_c when individual nanotubes are randomly orientated in the matrix, and since it is only valid for fillers with high thermal conductivity, only the best case scenario (2000) was used in these models. The estimated K_c values according to these models are given in Table 4.21.

Table 4.21 Composite designation and respective K_c obtained according to MG-EMA and Nan et al models for both theoretical and corrected conditions as a function of v_f according to bulk and real MWCNT density.

Sample	$K_{c,MG-EMA}$ ρ_{bulk}.		$K_{c,Nan}$ ρ_{bulk}.		$K_{c,MG-EMA}$ ρ_{real}		$K_{c,Nan}$ ρ_{real}	
	theo	corr	theo	corr	theo	corr	theo	corr
M0	148.4	150.5	148.4	150.5	148.4	150.5	148.4	150.5
M1	173.3	175.4	170.2	172.3	151	153.1	150.7	152.8
M2	176.9	179.1	173.4	175.5	151.9	154	151.5	153.5

Hatta-Taya´s model for composites reinforced with spherical particles described by the eq. 8 was used to predict the contribution of the MWCNTs bundles to the Al matrix for the best (2000) case and worst (20) case scenarios and are designated as, $K_{c,s,2000}$ and $K_{c,s,20}$, respectively. The estimated values are given in Table 4.22.

Table 4.22 Composite designation and respective K_c obtained according to Hatta-Taya's model for a spherical particle for both theoretical and corrected conditions as a function of v_f according to bulk and real MWCNTs density.

Sample	$K_{c,s,2000}$ ρ_{bulk}.		$K_{c,s,20}$ ρ_{bulk}.		$K_{c,s,2000}$ ρ_{real}.		$K_{c,s,20}$ ρ_{real}.	
	theo	*corr*	*theo*	*corr*	*theo*	*corr*	*theo*	*corr*
M0	148.4	150.5	148.4	150.5	148.4	150.5	148.4	150.5
M1	158.7	160.9	143.4	145.4	149.5	151.6	147.9	149.9
M2	160.2	162.4	142.7	144.7	149.8	151.9	147.7	149.7

The Hatta-Taya's model for fillers with the shape of fibres was also used to estimate the effect of nanotube alignment after ECAE using the eqs. 9-13. The in-plane thermal conductivity or higher boundary (HB), was calculated for both, the best (2000) and

worst (20) case scenario, and denoted as $K_{c,1,2000}$, $K_{c,1,r,2000}$, $K_{c,1,20}$, $K_{c,1,r,20}$, respectively.

For the out-plane thermal conductivity or low boundary (LB), in both cases, the best and worst case scenarios depend only on the thermal conductivity across the tube, $K_{MWCNTs,2} = 10$ W m^{-1} K^{-1}, thus, both cases retrieve the same values and therefore designated as $K_{c,2,r}$. For more information about this model see Chapter 2 Section 2.5 Fig. 2.18 and Chapter 3, Subsection 3.5.3. The estimated values for this model are given in Table 4.23 as a function of bulk density (ρ_{bulk}) of MWCNTs and Table 4.24 as a function of real density (ρ_{real}).

Table 4.23 Composites designation and respective K_c according to Hatta-Taya's model for fibres, for best (2000) and worst (20) case scenario in both conditions, "theoretical" and "corrected" using the **bulk density** for the MWCNTs.

Sample	$K_{c,1,2000}$		$K_{c,1,r,2000}$		$K_{c,2,r}$		$K_{c,1,20}$		$K_{c,1,r,20}$	
	theo	*corr*	*theo*	*corr*	*theo*	*corr*	*theo*	*corr*	*theo*	*corr*
M0	148.4	150.5	148.4	150.5	148.4	150.5	148.4	150.5	148.4	150.45
M1	200.2	202.2	176.6	178.7	107	108	144.8	146.8	134.5	136.2
M1$_{4i,1}$	200.2	202.2	176.6	178.7	---	---	144.8	146.8	134.5	136.2
M1$_{4i,2}$	---	---	---	---	107	108	---	---	---	---
M1$_{6i,1}$	200.2	202.2	176.6	178.7	---	---	144.8	146.8	134.5	136.2
M1$_{6i,2}$	----	---	---	---	107	108	---	---	---	---
M2	207.6	209.7	180.7	182.8	102.9	103.8	144.3	146.3	132.7	134.4

Table 4.24 Composites designation and respective K_c according to Eshelby's model for fibres, for best (2000) and worst (20) case scenario in both conditions, "theoretical" and "corrected" using the **real density** for the MWCNTs

Sample	$K_{c,1,2000}$		$K_{c,1,r,2000}$		$K_{c,2,r}$		$K_{c,1,20}$		$K_{c,1,r,20}$	
	theo	*corr*	*theo*	*corr*	*theo*	*corr*	*theo*	*corr*	*theo*	*corr*
M0	148.4	150.5	148.4	150.5	148.4	150.5	148.4	150.5	148.4	150.5
M1	154	156	151.34	153.4	142.5	144.4	148.	150.1	146.8	148.8
M1$_{4i,1}$	154	156	151.4	153.4	---	---	148	150.1	146.8	148.8
M1$_{4i,2}$	---	---	---	---	142.5	144.4	---	---	---	---
M1$_{6i,1}$	154	156	151.4	153.4	---	---	148	150.1	146.8	148.8
M1$_{6i,2}$	---	---	---	---	142.5	144.4	---	---	---	---
M2	155.8	157.9	152.4	154.4	140.7	142.5	147.9	149.9	146.3	148.3

Fig. 4.40 compares the experimental thermal conductivity of the Al/Cu10S1 composites (K_c) processed via rheocasting and rheocasting+ECAE with the MG-EMA, Nan et al and Hatta-Taya´s thermal conductivity models as a function of MWCNT v_f.for the "theoretical" condition.
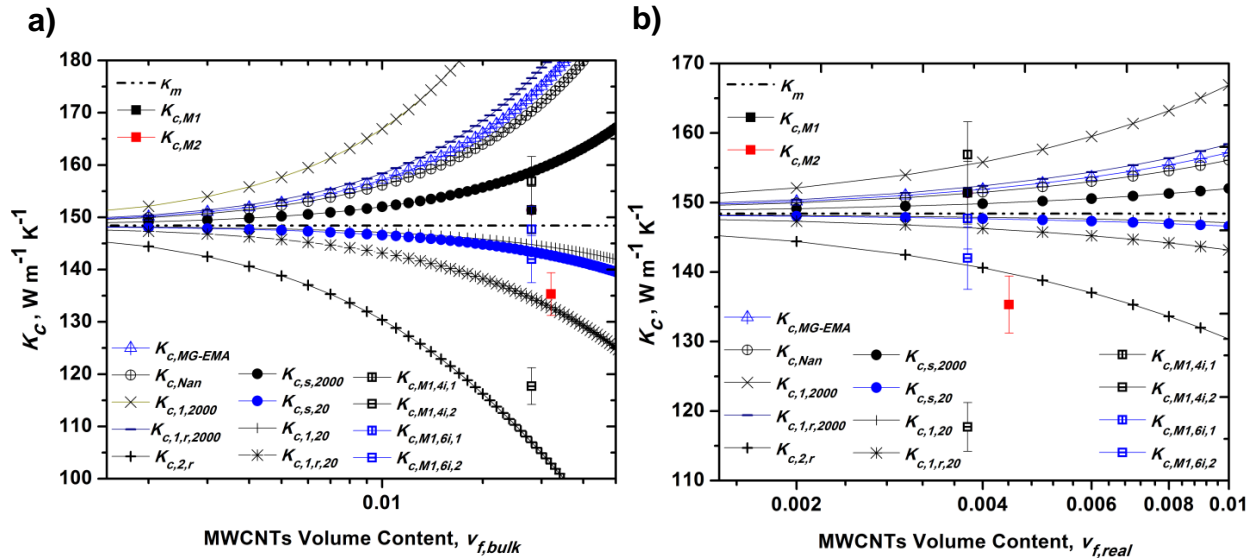
Fig. 4.40 Comparison of the experimental thermal conductivity of the Al/Cu10S1 composites with the Hatta-Taya's, MG-EMA and Nan et al thermal conductivity models as a function of MWCNT content in the "theoretical" condition: **(a)** assuming MWCNTs bulk density, **(b)** MWCNTs real density.

Fig. 4.40 a) gives the estimated thermal conductivity of the composites according to the three models used in the "theoretical" (theo) condition and nanotubes v_f as a function of bulk density, values given in Tables 4.20, 4.21, 4.22 and 4.23.

The K_c value for the M1 composite (v_f = 0.028) is $K_{c,M1}$ = 151.4 ± 4.5 W m^{-1} K^{-1}, which is higher than the reference M0 (no fillers, K_m = K_{M0}), K_m = 148.4 ± 4.5 W m^{-1} K^{-1} (+ 3 W m^{-1} K^{-1}). Whereas, the MG-EMA and Nan et at models, for individually and randomly aligned MWCNT yielded: $K_{c,M1,MG-EMA}$ = 173.3 W m^{-1} K^{-1} (+ 21.9 W m^{-1} K^{-1}) and $K_{c,M1,Nan}$ = 170.2 W m^{-1} K^{-1}(+18.8 W m^{-1} K^{-1}), both models retrieved values significantly above the M1 composite.

The Hatta-Taya's model for spherical particles retrieved values of $K_{c,M1,s,2000}$ = 158.7 W m^{-1} K^{-1} (+ 7.3 W m^{-1} K^{-1}), for the best case scenario and $K_{c,M1,s,20}$ = 143.4 W m^{-1} K^{-1} (- 8 W m^{-1} K^{-1}) for the worst case scenario. Hence, the values are closer to the experimental thermal conductivity when compared with the MG-EMA and Nan et al models.

The M1 samples subjected to ECAE and tested in the in-plane direction ($K_{c,1}$) or extrusion direction (ED) resulted in an increase in composite thermal conductivity after 4 iterations which then subsequently decreases to a value below the reference material M0, $K_{c,M1,4i,1}$ = 156.9 ± 4.7 W m^{-1} K^{-1} and $K_{c,M1,6i,1}$ = 147.7 ± 4.4 W m^{-1} K^{-1}, respectively. Whereas, Hatta-Taya's model for aligned fibres, in the in-plane direction, using the higher boundary, i.e. the best thermal conductivity achievable for the best case scenario estimates composite thermal conductivity values of $K_{c,M1,1,2000}$ = 200.2 W m^{-1} K^{-1} and $K_{c,M1,1,r,2000}$ = 176.6 W m^{-1} K^{-1}. In the worst case scenario, $K_{c,M1,1,20}$ = 144.8 W m^{-1} K^{-1} and $K_{c,M1,1,r,20}$ = 134.5 W m^{-1} K^{-1}.

In the out-of-plane direction ($K_{c,2}$), the ECAE samples revealed the lowest value observed, $K_{c,M1,4i,1}$ = 117.7 ± 3.5 W m^{-1} K^{-1} after 4 iterations and then a substantial increase, $K_{c,M1,6i,2}$ = 142 ± 4.3 W m^{-1} K^{-1}, after 6 iterations. Nevertheless, the Hatta-Taya's model in the out-of-plane direction, lower boundary, predicts a value even below that of the $K_{c,M1,4i,2}$ that is $K_{c,M1,2,r}$ = 108 W m^{-1} K^{-1}.

The M2 composite (v_f = 0.032) thermal conductivity is $K_{c,M2}$ = 135.3 ± 4.1 W m^{-1} K^{-1}, the lowest value among the composites processed via rheocasting, contradicting the idea that higher content of MWCNTs result in larger composite thermal conductivity, in fact it is well below the reference M0 material K_{M0} = 148.4 ± 4.5 W m^{-1} K^{-1} (- 13.1 W m^{-1} K^{-1}). The MG-EMA and Nan et at models predict: $K_{c,M2,MG-EMA}$ = 176.9 W m^{-1} K^{-1} (+ 41.6 W m^{-1} K^{-1}) and $K_{c,M2,Nan}$ = 173.4 W m^{-1} K^{-1} (+38.1 W m^{-1} K^{-1}), values significantly above the M2 experimental value.

If the nanotubes are considered spherical particles, the K_c is estimated to be $K_{c,M2,s,2000}$ = 160.2 W m^{-1} K^{-1} (+ 24.9 W m^{-1} K^{-1}), for the best case scenario and $K_{c,M2,s,2000}$ = 142.7 W m^{-1} K^{-1} (- 7.4 W m^{-1} K^{-1}) for the worst case scenario.

Fig. 4.40 b) gives the estimated thermal conductivity of the composites according to the three models used in the theoretical (theo) condition, as in Fig. 4.40 a), however, in this case, the $v_{f,real}$ of the fillers is computed according to the real density (2.1 g cm^{-3}) of the MWCNTs, see Table 4.20. The thermal conductivity experimental values for the composites are the same, as this only result in a change in their position on the v_f axis.

In the case of the M1 composite, $v_{f,real} = 0.0038$. The MG-EMA and Nan et at models predict: $K_{c,M1,MG-EMA} = 151$ W m^{-1} K^{-1} (- 0.4 W m^{-1} K^{-1}) and $K_{c,M1,Nan} = 150.7$ W m^{-1} K^{-1} (- 0.7 W m^{-1} K^{-1}), values that are now in agreement with the experimental result, $K_{c,M1} = 151.4 \pm 4.5$ W m^{-1} K^{-1}. The Hatta-Taya's model for spherical particles yielded values of $K_{c,M1,s,2000} = 149.5$ W m^{-1} K^{-1} (- 1.9 W m^{-1} K^{-1}), for the best case scenario and $K_{c,M1,s,20} = 147.9$ W m^{-1} K^{-}1 (- 3.5 W m^{-1} K^{-1}) for the worst case scenario.

The Hatta-Taya's model for a fibre in the in-plane direction, high boundary, for the best case scenario estimates composite thermal conductivity values of $K_{c,M1,1,2000} = 154$ W m^{-1} K^{-1} and $K_{c,M1,1,r,2000} = 151.34$ W m^{-1} K^{-1}. In the worst case scenario, these values are $K_{c,M1,1,20} = 148$ W m^{-1} K^{-1} and $K_{c,M1,1,r,20} = 146.8$ W m^{-1} K^{-1}. The thermal conductivity results for the M1 composite after 4 iterations, $K_{c,M1,4i,1} = 156.9 \pm 4.7$ W m^{-1} K^{-1} is marginally higher than the higher boundary in the best case scenario $K_{c,M1,1,2000}$ (+2.9 W m^{-1} K^{-1}). Whereas, the composite with 6 iterations, $K_{c,M1,6i,1} = 147.7 \pm 4.4$ W m^{-1} K^{-1}, has a thermal conductivity in between the higher boundaries for the worst case scenario, $K_{c,M1,1,20}$ (+ 0.3 W m^{-1} K^{-1}) and $K_{c,M1,1,r,20}$ (- 0.9 W m^{-1} K^{-1}).

In the out-of-plane direction ($K_{c,2}$), i.e. lower boundary, the Hatta-Taya's model predicts $K_{c,M1,2,r} = 142.5$ W m^{-1} K^{-1}, a value substantially above the ECAE values observed for the sample after 4 iterations, $K_{c,M1,4i,2} = 117.7 \pm 3.5$ W m^{-1} K^{-1} (+ 24.8 W m^{-1} K^{-1}). However, this value was in agreement with the sample after 6 iterations, $K_{c,M1,6i,2} = 142 \pm 4.3$ W m^{-1} K^{-1} (+ 0.5 . W m^{-1} K^{-1}).

In the case of the M2 composite ($v_{f,real} = 0.0044$, see Table 4.20), i.e. a composite with an experimental thermal conductivity value, $K_{c,M2} = 135.3 \pm 4.1$ W m^{-1} K^{-1}, the MG-EMA and Nan et at models predict: $K_{c,M2,MG-EMA} = 151.9$ W m^{-1} K^{-1} (+ 16.6 W m^{-1} K^{-1}) and

$K_{c,M2,Nan}$ = 151.5 W m^{-1} K^{-1} (+16.2 W m^{-1} K^{-1}). If the nanotubes are considered spherical particles, the $K_{c,}$ is estimated to be $K_{c,M2,s,2000}$ = 149.8 W m^{-1} K^{-1} (+ 14.5 W m^{-1} K^{-1}), for the best case scenario and $K_{c,M2,s,20}$ = 147.7 W m^{-1} K^{-1} (- 12.4 W m^{-1} K^{-1}) for the worst case scenario.

4.3.5.4.2 Corrected Condition

In this subsection, the results of the comparison between the experimental thermal conductivity of the composites (K_c) and the theoretical models considering several factors regarding the MWCNTs, such as: shape; alignment; density and thermal conductivity, according to the "corrected" (accounts the effect of porosity volume faction (φ)) condition are outlined.

Fig. 4.41 a) gives the estimated thermal conductivity of the composites according to the three models used for the corrected condition, K_c^{corr}, and the nanotubes v_f as a function of bulk density (ρ_{bulk}). The porosity volume fraction (φ) present in the composite samples was calculated using the image analysis (see Chapter 3, Subsection 3.4.4) and the thermal conductivity of the composite was corrected (K_c^{corr}) using the eqs. 22 and 23, to remove the effect of porosity content on K_c, resulting in a thermal conductivity increase in all samples. The φ and K_c^{corr} values are given in Table 4.20.

The thermal conductivity of the reference material M0 (no filler addition) obtained experimentally with porosity content (φ_{M0} = 0.01 ± 0.005) was used as the matrix value for all the corrected models. ($K_{c,M0}^{corr}$ = 150.5 ± 4.7 W m^{-1}K^{-1}).

The corrected experimental thermal conductivity value for the M1 composite (v_f = 0.028) with φ_{M1} = 0.015 ± 0.004 is $K_{c,M1}^{corr}$ = 154.8 ± 5.3 W m^{-1} K^{-1}. The MG-EMA and Nan et al models in the corrected condition (see Table 4.21) give a value of to $K_{c,M1,MG-EMA}^{corr}$ = 175.4 W m^{-1} K^{-1} (+ 20.6 W m^{-1} K^{-1}) and $K_{c,M1,Nan}^{corr}$ = 172.3 W m^{-1} K^{-1} (+ 17.5 W m^{-1} K^{-1}), respectively. Despite the porosity correction, the difference between the model and experimental values are still significant.

Fig. 4.41 Comparison of experimental thermal conductivity of the Al/Cu10S1 composites with the Hatta-Taya's, MG-EMA and Nan et al thermal conductivity models as a function of MWCNT content in the "corrected" condition: **(a)** assuming MWCNTs bulk density, **(b)** MWCNTs real density.

The porosity correction applied to the Hatta-Taya's model for spherical particles gave values of $K^{corr}_{c,M1,s,2000}$= 160.9 W m^{-1} K^{-1} (+ 6.1 W m^{-1} K^{-1}), for the best case scenario and $K^{corr}_{c,M1,s,20}$= 145.4 W m^{-1} K^{-1} (- 9.4 W m^{-1} K^{-1}) for the worst case scenario.

The porosity correction applied to the thermal conductivity of the M1 samples subjected to ECAE, in the in-plane direction $K_{c,1}$, resulted in values of $K^{corr}_{c,M1,4i,1}$= 157 ± 4.7 W m^{-1} K^{-1} ($\varphi_{M1,4i,1}$ = 0.0003 ± 0.0002) after 4 iterations and $K^{corr}_{c,M1,6i,1}$= 147.8 ± 4 W m^{-1} K^{-1} ($\varphi_{M1,6i,1}$ = 0.0003 ± 0.0001) for 6 iterations, respectively, a negligible change as the ECAE processing reduced porosity to a near non-existent degree. The correction to the Hatta-Taya´s model for aligned fibres, in the in-plane direction, high boundary, for the best case scenario thus became $K^{corr}_{c,M1,1,2000}$= 202.2 W m^{-1} K^{-1} (+ 47.4 W m^{-1} K^{-1}) and $K^{corr}_{c,M1,1,r,2000}$= 178.7 W m^{-1} K^{-1} (+ 23.9 W m^{-1} K^{-1}). In the worst case scenario, it became $K^{corr}_{c,M1,1,20}$= 146.8 W m^{-1} K^{-1} (- 8 W m^{-1} K^{-1}) and $K^{corr}_{c,M1,1,r,20}$= 136.2 W m^{-1} K^{-1} (- 18.6 W m^{-1} K^{-1}).

187

The K_c values due to the porosity correction of the ECAE samples in the out-of-plane direction ($K_{c,2}$), are $K^{corr}_{c,M1,4i,2}$= 117.8 ± 3.5 W m^{-1} K^{-1} ($\varphi_{M1,4i,2}$ = 0.0003 ± 0.0002) after 4 iterations and $K^{corr}_{c,M1,6i,2}$= 142.1 ± 4.3 W m^{-1} K^{-1} ($\varphi_{M1,6i,2}$ = 0.0003 ± 0.0001) for 6 iterations. The corrected Eshelby´s model in the out-of-plane direction ($K_{c,2}$), lower boundary, in this case predicts $K^{corr}_{c,M1,2,r}$ = 108 W m^{-1} K^{-1}.

The corrected experimental thermal conductivity value for the M2 composite (v_f = 0.032) with φ_{M2} = 0.04 ± 0.013 is $K^{corr}_{c,M2}$= 143.8 ± 7.3 W m^{-1} K^{-1}. The MG-EMA and Nan et al models in the corrected condition (see Table 4.21) however, predict values of $K^{corr}_{c,M2,MG-EMA}$ = 179.1 W m^{-1} K^{-1} (+ 35.3 W m^{-1} K^{-1}) and $K^{corr}_{c,M2,Nan}$ = 175.5 W m^{-1} K^{-1} (+ 31.7 W m^{-1} K^{-1}), respectively. Despite the porosity correction the difference between the model and experimental values are still significant.

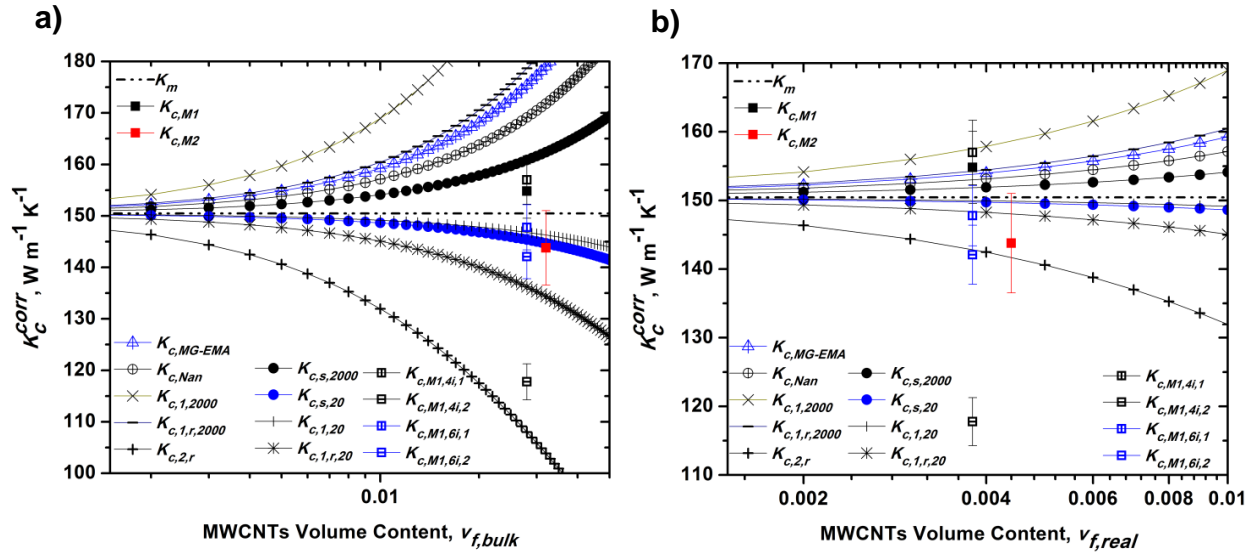The porosity correction applied to the Eshelby´s model for spherical particles gave values of $K^{corr}_{c,M2,s,2000}$= 162.4 W m^{-1} K^{-1} (+ 18.6 W m^{-1} K^{-1}), for the best case scenario and $K^{corr}_{c,M2,s,20}$= 144.7 W m^{-1} K^{-1} (- 0.9 W m^{-1} K^{-1}) for the worst case scenario, the latter value that is in good agreement with given by the experimental results.

Finally, Fig. 4.41 b) demonstrates the estimated thermal conductivity of the composites according to the three models used for the corrected (corr) condition, K^{corr}_c, and the nanotubes content as a function of real density ($v_{f,real}$). Again the only difference between Fig. 4.41 a) and b) is the v_f of the composites as the experimental K^{corr}_c**'s** are the same.

For composite M1, if taking into account the real density ($v_{f,real}$ = 0.0038, Table 4.20), the corrected experimental thermal conductivity is still $K^{corr}_{c,M1}$= 154.8 ± 5.3 W m^{-1} K^{-1}. However, in this case, the MG-EMA and Nan et al models are (see Table 4.21) $K^{corr}_{c,M1,MG-EMA}$ = 153.1 W m^{-1} K^{-1} (- 1.7 W m^{-1} K^{-1}) and $K^{corr}_{c,M1,Nan}$ = 152.8 W m^{-1} K^{-1} (+ 2 W m^{-1} K^{-1}), respectively. These predicted values are in good agreement with the experimental. Applying, the Hatta-Taya's model for spherical particles the values now becomes $K^{corr}_{c,M1,s,2000}$= 151.6 W m^{-1} K^{-1} (- 3.2 W m^{-1} K^{-1}), for the best case scenario and $K^{corr}_{c,M1,s,20}$= 149.9 W m^{-1} K^{-1} (- 4.9 W m^{-1} K^{-1}) for the worst case scenario.

Hatta-Taya's model for aligned fibres in the in-plane direction, high boundary, for the best case scenario estimates composite thermal conductivity values of $K^{corr}_{c,M1,1,2000}$= 156 W m^{-1} K^{-1} and $K^{corr}_{c,M1,1,r,2000}$= 153.4W m^{-1} K^{-1}. In the worst case scenario, $K^{corr}_{c,M1,1,20}$= 150.1 W m^{-1} K^{-1} and $K^{corr}_{c,M1,1,r,20}$= 148.8 W m^{-1} K^{-1}. For the M1 composites after ECAE, the corrected thermal conductivity result, after 4 iterations $K^{corr}_{c,M1,4i,1}$= 157 ± 4.7 W m^{-1} K^{-1} is almost the same as the higher boundary in the best case scenario $K^{corr}_{c,M1,1,2000}$ (+ 1 W m^{-1} K^{-1}). Whereas, the composites with 6 iterations, $K^{corr}_{c,M1,6i,1}$= 147.8 ± 4 W m^{-1} K^{-1} have a thermal conductivity close to the higher boundary value for the worst case scenario, $K^{corr}_{c,M1,1,r,20}$ (- 1 W m^{-1} K^{-1}).

In the out-of-plane direction ($K_{c,2}$), lower boundary, the corrected Hatta-Taya´s model according to the real density predicts $K^{corr}_{c,M1,2,r}$ = 144.4 W m^{-1} K^{-1}, value substantially above the ECAE values observed for the composites after 4 iterations, are $K^{corr}_{c,M1,4i,2}$= 117.8 ± 3.5 W m^{-1} K^{-1} (+ 26.6 W m^{-1} K^{-1}) but in agreement with the composites after 6 iterations, $K^{corr}_{c,M1,6i,2}$= 142.1 ± 4.3 W m^{-1} K^{-1} (+ 2.3 .W m^{-1} K^{-1}).

The corrected experimental thermal conductivity value for the M2 composite according to the real density ($v_{f,real}$ = 0.0044) is $K^{corr}_{c,M2}$= 143.8 ± 7.3 W m^{-1} K^{-1}. However, the MG-EMA and Nan et al models in the corrected condition (see Table 4.21) predict $K^{corr}_{c,M2,MG-EMA}$ = 154 W m^{-1} K^{-1} (+ 10.2 W m^{-1} K^{-1}) and $K^{corr}_{c,M2,Nan}$ = 153.5 W m^{-1} K^{-1} (+ 9.7 W m^{-1} K^{-1}), respectively.

The porosity correction to Hatta-Taya's model for spherical particles retrieved values of $K^{corr}_{c,M2,s,2000}$= 151.9 W m^{-1} K^{-1} (+ 8.1 W m^{-1} K^{-1}), for the best case scenario and $K^{corr}_{c,M2,s,20}$= 149.7 W m^{-1} K^{-1} (+ 5.9 W m^{-1} K^{-1}) for the worst case scenario.

References

1.   Ho, C. Y., Ackerman, M. W., Wu, K. Y., Oh, S. G. & Havill, T. N., Thermal Conductivity of Ten Selected Binary Alloy Systems. J. Phys. Chem. Ref. Data 7, 959–1178 (1978).

2.   Hatta, H. & Taya, M., Effective Thermal Conductivity of a Misoriented Short Fiber Composite. J. Appl. Phys. 58, 2478 (1985).

3.   Hatta, H., Taya, M., Kulacki, F. A. & Harder, J. F., Thermal Diffusivities of Composites with Various Types of Filler. J. Compos. Mater. 26, 612–625 (1992).

4.   DiLeo, R. A., Landi, B. J. & Raffaelle, R. P., Purity Assessment of Multiwalled Carbon Nanotubes by Raman Spectroscopy. J. Appl. Phys. 101, 64307 (2007).

5.   Lehman, J. H., Terrones, M., Mansfield, E., Hurst, K. E. & Meunier, V., Evaluating the Characteristics of Multiwall Carbon Nanotubes. Carbon 49, 2581–2602 (2011).

6.   Cao, A., Xu, C., Liang, J., Wu, D. & Wei, B., X-Ray Diffraction Characterization on the Alignment Degree of Carbon Nanotube. Chem. Phys. Lett. 344, 13–17 (2001).

7.   Cao, G. & Wang, Y., Nanostructures and Nanomaterials: Synthesis, Properties, and Applications. (World Scientific, 2011).

8.   Nan, C.-W., Shi, Z. & Lin, Y., A Simple Model for Thermal Conductivity of Carbon Nanotube-Based Composites. Chem. Phys. Lett. 375, 666–669 (2003).

Chapter 5

Discussion

5.1 Chapter Outline

This chapter assess the viability of producing ultra-high thermal conductivity composites for thermal management applications. It discusses the results presented in chapter 4 with respect to processing + characteristics of the Al/Cu-CFs and Al/MWCNTs composites. It critically analyses the effectiveness of the processing method used to introduce, disperse and align the C-based fillers within the matrix and discuss the formation of interface reactions between the filler + Al alloy matrix.

The discussion also compares the experimental conductivity values obtained for the composites with those found in published literature, presented in the manufacturers data and calculated from theoretical models. This work is one of the first to try to predict the resulting Al/MWCNTs composites thermal conductivity by combining the thermal conductivity of a single MWCNT obtained by SThM+FEM and theoretical models.

5.2 Processing of Composites

In this chapter, the discussion focuses on the interaction of both the CFs and the MWCNTs with the Al matrix processed via rheocasting followed by ECAE. Its purpose is to determine if this combination of techniques, suggested in Chapter 2, Section 2.4.3, can be used to harness the outstanding MWCNTs thermal conductivity in order to produce high thermal conductivity composites.

5.2.1 Rheocasting

In this section the results obtained from the processing of the Al/Cu-CFs (C system) and AlCu10S1 (M system) composites are discussed.

5.2.1.1 Matrix Composition

In this study, an Al3Mg alloy composition (identified by the dashed line on the Al-Mg phase diagram illustrated in Fig. 5.1), was selected as the composite matrix. The main reasons for this selection are as follow:

1. Improve Al wettability of carbon-based fillers
2. Wider semi-solid temperature processing window
3. Simple composition
4. Simple microstructure

Magnesium (Mg) was used as an alloying element in an attempt to improve wettability between Al and carbon-based materials as they have very different surface energy values ((γ_{Mg} = 0.785 J m^{-2} and γ_{Al} = 1.143 J m^{-2})[1], (γ_{MWCNT} = 0.0453 J m^{-2} and γ_{CF} = 0.0459 J m^{-2})[2]). This element reduces the surface tension of the Al sharply, which increases its wettability. This effect was found to be obvious for the initial 1 wt. % of the Mg addition, however it is minimal for any further addition.[3]

According to Patel et al[4] for good processability the freezing range should be within the limit of 10 ºC < T_{SS-S} < 150 °C, for this reason, a further 2 wt.% of Mg was added in order to increase matrix freezing range (i.e. T_{SS-S} ≈ 19 °C, T_{SS} = 633 °C and T_S = 614 ºC), as illustrated in Fig. 5.1, and thus facilitate rheocasting of the composites.
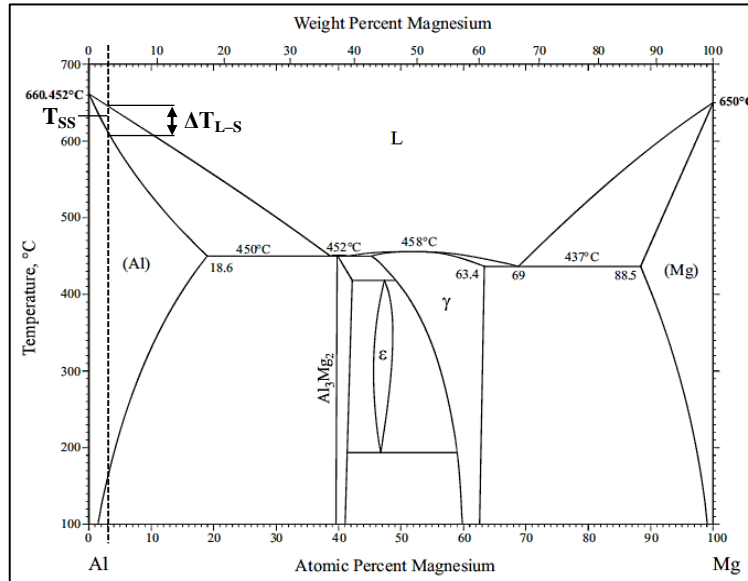
Fig.5.1 Al-Mg phase diagram depicting the semi-solid metal temperature freezing range (ΔT_{L-S}) and processing temperature (T_{SS}) for the Al3Mg alloy selected (dashed line).[5]

The microstructure of the rheocasted Al3Mg alloy is shown in Fig. 4.3 a). Other elements, such as silicon (Si) could be added to avoid the Al_4C_3 (a corrosion susceptible compound) formation that forms as C is thermodynamically unstable in Al above the solidus temperature (T_s). Al_4C_3 formation can be restricted by the addition of at least 8 wt. % of Si promotes the formation of silicon carbide (SiC) instead, as discussed by Lloyd et al[6]. However, the Al_4C_3 formation can be minimized or even avoided by manipulating reaction kinetics, by reducing mixing times and lower processing temperatures. [6–9] This was observed in this study, where the low T_{SS} and short mixing times used during rheocasting helped minimize Al_4C_3 formation and restrict its growth as the Al/Cu-CFs showed no visible Al_4C_3 formation (Fig.4.3), however it was found in the Al/MWCNTs composites but only observable via TEM SAED technique (Fig. 4.32).

In Al/C composites systems it is common to use coatings to avoid direct contact of Al with C with Cu and nickel (Ni) being the most common metal coatings applied.[9] In this study, Cu was the coating metal selected to coat the CFs and embed the MWCNTs in order to avoid Al_4C_3 formation and improve wettability. Again, having a simple composition was important as Cu was added to the matrix as the filler content increased (see Tables 4.1 and 4.16), which resulted in the formation of more complex

intermetallics (see Figs. 4.30 and 4.31). The addition of Si would result in even more complex intermetallic, thus reducing further the thermal conductivity of the matrix.

Keeping the microstructure simple facilitates identification of the filler, which can be difficult for MWCNTs. It also simplifies the investigation of possible matrix/filler interface reactions. The interface reaction products between the filler and matrix are discussed in sections 5.2.1.2.2 and 5.2.1.3.3

The main disadvantage of the alloy selected is its low thermal conductivity in comparison with the Pure Al (237 W m^{-1} K^{-1}). According to the measured laser flash acquired thermal conductivity results, the experimental thermal conductivity of the matrix alloy is $K_m = $ 148.4 ± 4.5 W m^{-1} K^{-1} (Table 4.2), or K_m^{corr} = 150.5 ± 4.8 W m^{-1} K^{-1} (Table 4.5) after applying the correction to neglect the effect of porosity (see eq. 23) on the matrix thermal conductivity. Fig. 5.2 demonstrates the evolution of the Al matrix thermal conductivity as the Mg and Cu alloying element content increases at room temperature (300 K), as given by Ho et al[10].
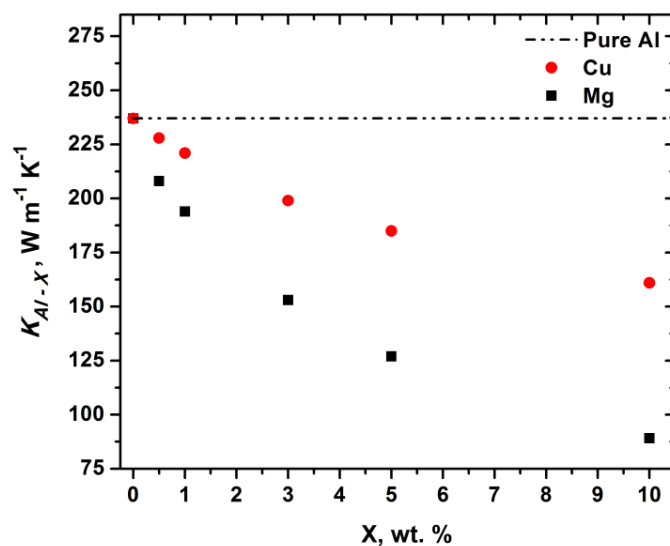
Fig. 5.2 Effect of Cu and Mg alloying element content in wt.% on the thermal conductivity of Al alloys. Reproduced from the work of Ho et al[10].

It shows the strong detrimental effect of Mg on Al thermal conductivity and when Al is alloyed with 3 wt. % of Mg the value is $K_{Al3Mg} = $ 153 W m^{-1} K^{-1}, which is in good agreement with the measured results. Cu also decreases the alloy thermal conductivity, however not to the same degree as that of Mg. Nevertheless, it is expected that this property would further decrease with increasing Cu content on the Al3Mg matrix alloy solid solution.

The effect of matrix composition as discussed does not represent a problem in this study, as the main objective is to assess the thermal contribution of the C-based fillers, CFs and MWCNTs, to the Al composites processed via rheocasting followed by equal channel angular extrusion (ECAE). As, the thermal conductivity phase contrast between the fillers and the matrix is high, even a small amount of fillers should present a noticeable change in thermal conductivity, where this should be more evident for the MWCNTs. The thermal conductivity phase contrast, according to the manufacturers, for the Al/Cu-CFs composites is $K_{CFs,1} / K_m$ = 3.4 ($K_{CFs,1}$ = 500 W m^{-1} K^{-1}, lower value (see Table 3.5), and Al/Cu10S1 composites is $K_{MWCNTs,1} / K_m$= 13.5 ($K_{MWCNTs,1}$= 2000 W m^{-1} K^{-1}, see table 3.6).

5.2.1.2 Al / Cu-CFs

Pitch-based carbon fibres (CFs) are a common reinforcement used in both continuous or short fibre form, that are typically embedded in different metal matrices including Al. These are used to produce composites packaging materials, which are currently widely applied in the electronic industry (see Chapter 2, Table 2.1).

The success of CF usage can be attributed to its high axial thermal conductivity (K_1) and low axial coefficient of thermal expansion (CTE) (see Chapter 2 Subsection 2.3.1).[11–13] In this section, the rheocasting processing of Al/Cu-CF composites is discussed. It is important to emphasize that the CFs were used to test the viability of the processing method and processing parameters in order to attempt the processing of an ultra-high thermal conductivity Al matrix composite (AMC) reinforced with MWCNTs that could used as a thermal management material. The C nature of the fibres is beneficial,

as they can thus be utilized to help predict the effect of the processing route on the MWCNTs.

5.2.1.2.1 Introduction and Dispersion of Fillers

In this study, rheocasting has been demonstrated to be an efficient route to introduce and disperse the pitch based CFs coated with Cu (Cu-CFs). However, the porosity volume fraction content of the composites increases up to 5% with increasing filler content.

The good introduction and dispersion of the Cu-CFs within the Al matrix is demonstrated by the O.M. and SEM micrographs of the C system composites processed by rheocasting, as shown in Figs. 4.3 and 4.4. However, despite the good dispersion, few fibre agglomerates are found, and are more commonly observed in C0.5 and C1 composites, showed in Figs 4.3 b) and c).

The dispersed fibres are mainly located at the grain boundaries of the equiaxed α-Al phase, and in some cases are associated with the AlFe intermetallics, possibly inducing its nucleation (see Fig. 4.4). However, with increasing fibre content more fibres are found within the grains, as illustrated in Figs. 4.3 d) and e), (composites C1.5 and C2, respectively).

The effective fibre introduction into the melt is due to the high melt viscosity generated using carefully selected processing parameters (see Table 3.8) as the viscosity depends on the solid fraction within the Al melt, the stirring shear rate and the time history.[14,15] It allowed the entrapment of the fillers, thus avoiding quick settling and rejection from the melt.

Fig. 4.9 c) shows the relationship between the theoretical fibre volume fraction (v_f) (content of fibres added to the melt slurry) and the real or corrected fibre volume fraction (v_f^{corr}) calculated from the composites using the surface area analysis technique (see Chapter 3 Subsection 3.4.4). The linear trend obtained corroborates the efficiency of the processing method in introducing the fibres within the matrix. However, it was observed that all the composites have a slightly higher v_f^{corr} than the theoretical

values, v_f, this is mainly due to fibre segregation that occurred despite the high viscosity, during melt slurry settling and solidification.

The dispersion of the CFs was facilitated by the use of a helical ribbon type of mixing paddle, illustrated in Fig. 3.1, which promotes laminar flow.

The increase of viscosity, despite being beneficial for filler trapping, reduces filler dispersion effectiveness throughout the metal matrix as the flow velocities rapidly decay away from the impeller, to low values. The laminar flow occurs for high viscous fluids with Reynolds number below 10 (Re < 10). Laminar flow mixing is then achieved due to the composite slurry reorientation and redistribution by cutting, dicing, chopping and then restacking the sectioned material, as the redistribution of the material increases the interfacial area allows diffusion and consequently homogeneous dispersion of the fibres within the matrix.[16]

Fig. 5.3 gives the relationship between the porosity volume fraction (φ) and v_f^{corr} content increase. It reveals that the porosity increases linearly with fibre content increasing up to 5 % (see Table 4.5) of porosity.
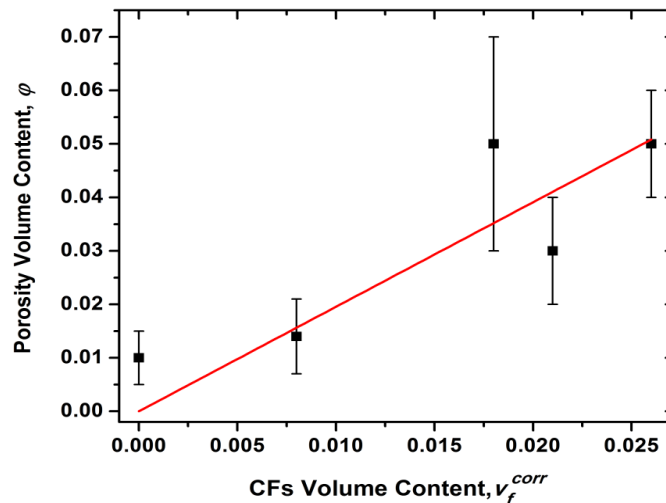

Fig. 5.3 Linear increase in porosity volume fraction (φ) with increase in real (or corrected) fibre v_f^{corr} content (data from Table 4.5).

The ability of the processing method to successfully introduce and disperse the fillers is crucial in harnessing their thermal properties. The porosity content (decrease in density) also has a major effect on the composites final thermal conductivity.

Porosity is a common problem when using stir/vortex casting (mixing in the liquid state) or rheocasting techniques. They are known for the production of composites with high porosity content due to gas dragged into the vortex from the surface of the melt. This enters into the slurry either on its own or in the form of an envelope containing the reinforcement particle, therefore filler content and porosity depend on one another.[17] The increase in melt viscosity due to an increase in filler content may also contribute to increase porosity. These phenomena have also been observed in several studies involving the processing of AMCs with different fillers.[18–20]

Porosity decreases thermal conductivity of the composites, as demonstrated by eqs. 21 and 23. It is therefore important that it is minimized. As a consequence, ECAE was employed as a post-processing technique and the results are discussed in section 5.2.2.

5.2.1.2.2 Wettability and Interfacial Reactions

The Cu coating applied on the pitch-based CFs promoted wettability by the Al melt improving filler introduction and dispersion aided by the formation of an interfacial MgO compound. No clear evidence of the formation of the deleterious Al_4C_3 interfacial compound was found, however, its formation should not be discounted.

As discussed in section 5.2.1.1, the surface energy (γ) difference between the Al and the CFs is significant, resulting in fibres being pushed away by the solidification front, thus forming large agglomerations that can even be pushed out of the melt, if γ difference between them Is not reduced. The Cu coating applied on the fibres, illustrated in Fig. 4.1, promoted wettability and interfacial bonding between fibres and the Al, as can be seen in Fig. 4.4 b). The wetting of the fibres occurred due to the similar surface energies of Al and Cu, γ_{Al} = 1.143 J m^{-2} and γ_{Cu} = 1.825 J m^{-2}, respectively.[1] Fig. 4.4 b), shows a BSE image of an individual CF with good interfacial bonding. The EDS elemental map of the individual fibre and its interface with the matrix

reveals the interfacial reaction products were mainly composed of Mg and O. Mg acts as a powerful surfactant in Al alloys, this means that if an oxygen-containing surface, in this case CuO present in the coating comes into contact with the melt and, the CuO is reduced by the Mg, resulting in the formation Mg-O based compound.[3]

The type of compound to form depends on the Mg content as illustrated in Fig. 5.4 a). In this case, the Mg content of the C system composites is 3 wt.%, and therefore it is highly likely that the interfacial compound formed is MgO, according to the following reaction: [3]

$$2\,Mg_{(l)} + O_{2(g)} \longrightarrow 2MgO_{(s)} \tag{1}$$
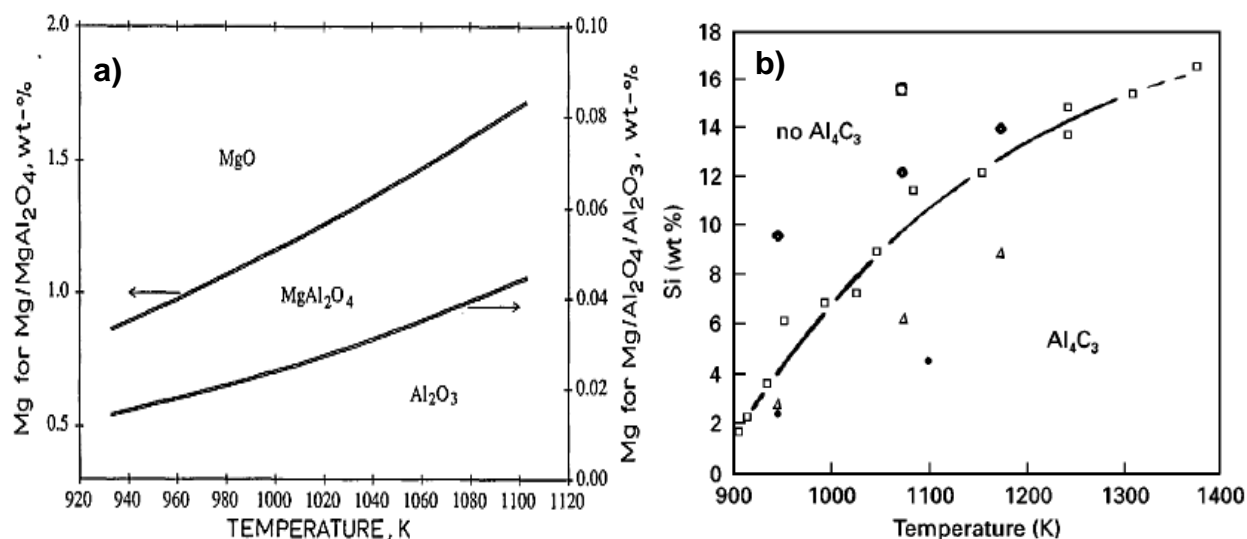
Fig. 5.4 (a) Thermodynamic stabilities of Al-Mg oxides in Al-Mg Alloys[3], and **(b)** silicon levels required in the matrix to prevent the formation of Al_4C_3 as a function of melt temperature[9] (graphs illustrated as per their source).

However, it should be noted that results indicate that the Cu coating appears to diffuse away from the fibre into the matrix solid solution during processing. Despite this, traces of Cu could still be found around the fibres. The Cu content in the matrix increased with increased fibre addition (see Tables 4.1 and Fig. 4.7). For temperatures above ~ 900 K (627 °C), the tendency of the CF when mixed with molten Al is to form Al_4C_3 reaction

products. This formation of Al_4C_3 can be severe if Si is not used, as shown in Fig. 5.4 b).[9]

Nevertheless, in this study no Si was intentionally added in the processing of the C system composites and, hence, at the composite processing temperature of 906.15 K (633 °C) it is expected that carbides will form, according to the following reaction:

$$4\ Al_{(l)} + 3C_{(s)} \longrightarrow Al_4C_{3(s)} \tag{2}$$

However, the microstructural characterisation of the C system composites using O.M. and SEM techniques (Figs. 4.3, 4.4, 4.5 and 4.6) did not reveal any evidence of Al_4C_3 formation. However, although carbides were not observed in the results, their presence should not be dismissed.

Summary:

❖ Rheocasting has been demonstrated to be an efficient method to introduce and disperse the pitch based CFs coated with Cu (Cu-CFs). In contrast, the porosity volume content of the composites increased up to 5% with increasing filler content.

❖ The Cu coating applied on the pitch-based CFs promoted wettability of the fibre by the Al melt improving filler dispersion via the formation of a MgO interfacial compound. There was no clear evidence of the formation of the deleterious interfacial Al_4C_3 compound, however, its formation in the matrix should not be discounted.

5.2.1.3 Al/MWCNTs

Harnessing the outstanding thermal properties of the MWCNTs when added to an Al matrix to produce ultra-high thermal conductivity composites ($K > 400$ w m^{-1} K^{-1}) has long been sought, however, it remains an unresolved desire and it is still far from being achieved. This section discusses the Al/MWCNTs processing results obtained in this study.

5.2.1.3.1 Thermal Stability of Cu10S1 powder

The S1 MWCNTs used as a filler to produce Al/MWCNTs composites are thermally stable for processing temperatures up to 900 ºC when under a He protective atmosphere, either as as-received MWCNTs or when ball-milled with pure Cu (Cu10S1).

As described in Chapter 2 Section 2.3, C-based materials are known to form a variety of allotropes[27] that are unique in terms of thermal conductivity, spanning a very large range, from ~ 0.01 W m^{-1} K^{-1} for amorphous carbon (a-C) to values as high as 3500 W m^{-1} K^{-1} for MWCNTs, at room temperature[28,29]. According to the manufacturer the S1 MWCNTs in-plane thermal conductivity is $K_{MWCNTs,1}$ = 2000 W m^{-1} K^{-1} (see table 3.6). Therefore, ensuring this property does not change due to allotropic transformation, oxidation or damage during composite processing is crucial.

Table 5.1 summarizes the STA (DSC+TG), XRD and Raman results of the thermal stability (chemical and structural properties) study from the S1 MWCNTs and Cu10S1 powders. The idea was to verify whether the MWCNTs are stable during composite processing.

The S1 MWCNTs, either in the as-received or ball-milled with Cu (Cu10S1), when exposed to O$_2$ were found to oxidize when heated to high temperatures (> 400 ºC, see Table 5.1 and Chapter 4, Figs. 4.24 and 4.25), leaving only the metal behind (catalyst and CuO). The thermal stability of the MWCNTs is directly attributed to the aromatic bonding within the MWCNT structure, but it can be influenced by the number of walls, the presence and composition of catalyst, defects within the tubes, and the presence of other materials within the sample (e.g. a-C or graphitic particles)[30–34].

Table 5.1 Summary of results of the thermal stability study of the S1 MWCNTs and Cu10S1 powders when heated up to 900 ºC at 10 K min^{-1} under O_2 and He atmospheres. Obtained from Chapter 4, Subsections 4.3.2 and 4.3.4.

Material	Information
S1 MWCNTs	**O_2 atmosphere: Not stable:**
	DSC: MWCNTs oxidation peak**:** T_{in} = 434.56±19ºC; T_{oxi} = 569.28±7.6ºC, T_{end} = 607.69±7.5ºC.
	TG: 96.3 % mass loss (only catalyst left)
	XRD: As-received: MWCNTs, Fe, Fe_2C, $C_{0.14}Fe_{1.86}$.
	He atmosphere: Stable:
	DSC: No MWCNTs oxidation peak; endothermic peak, T_{endo} = 853.04±5.1 ºC;
	TG: ~ 3% mass loss
	XRD: As-received: MWCNTs, Fe, Fe_2C, $C_{0.14}Fe_{1.86}$. Heat-treated: MWCNTs and Fe_3O_4
	Raman: As-received: I_D/I_G= 0.70±0.03. Heat-treated: I_D/I_G= 0.69±0.08
Cu10S1	**O_2 atmosphere: Not Stable:**
	DSC: MWCNTs oxidation peak: T_{in} = 495.66±3 ºC; T_{oxi} = 535.66±1.5 ºC; T_{end} = 538.17±2 ºC
	TG: 13.14% mass increase.
	XRD: As-received: MWCNTs, Cu, CuO and Cu_2O^{+1}; Heat-treated: CuO
	He atmosphere: Stable:
	DSC: No MWCNTs oxidation peak. CuO reduction exothermic peaks: T_{exo} = 348.03±3 ºC and T_{exo} = 600.82±2.7 ºC. Metal Catalyst endothermic peak, T_{endo} = 753.23±3 ºC
	XRD: As-received: MWCNTs: Cu; CuO; Cu_2O^{+1}. Heat-treated: MWCNTs: Cu; traces of CuO and Cu_2O^{+1}

Defects such as these were found in considerable amounts in the S1 MWCNTs samples (see Chapter 4, section 4.3.2), contributing for their low stability under an O_2 atmosphere.

These findings are in good agreement with literature, where MWCNTs under an O_2 atmosphere are found to burn between 400 to 750 °C.[30–34] Bom et al[31] showed that the oxidation of the as-received MWCNTs synthetized via CCVD (the same method used to synthetize the S1 MWCNTs) started at 420 ºC and finished at 630 ºC, values identical to that obtained in this study (see Table 5.1). However, TG results of the MWCNTs under O_2 (Fig. 4.24 c) show that the mass loss starts at temperatures as low as ~ 300 °C. This

finding may be due to the oxidation of a-C, as this carbonaceous impurity has been reported to burn at temperatures below 400 °C.[30]

Nevertheless, the as-received S1 MWCNTs are more stable than the S1 MWCNTs incorporated in Cu, as the former has higher oxidation temperature (T_{oxi}) than the latter ($T_{oxi, S1}$ = 569.28±7.4 °C > $T_{oxi, Cu10S1}$ = 535.66±1.5 °C (- 33.62±7.6 °C)). This indicates that mixing of MWCNTs with Cu powder via high energy ball-milling reduces the MWCNTs thermal stability. High energy ball-milling is known to induce cutting and damage on the MWCNTs.[35,36] This finding is corroborated by the Cu10S1 powder XRD spectrum (Fig. 4.25 d)) that shows that the S1 MWCNTs (0002) peak is shallower and displaced (i.e. shifted from 2θ = 25.92 ° to 2θ = 26.09°). This is due to a smaller crystallite size and stresses in the lattice structure indicating cutting and damage of the nanotubes. Therefore, ball-milling with MWCNTs must be minimized as the damage induced can be detrimental to their thermal properties.

In contrast, when the atmosphere is changed to He, the as-received S1 MWCNTs and Cu10S1 samples, when heated up to 900 °C at a heating rate of 10 °C min^{-1}, were found to be stable. No MWCNTs oxidation (exothermic) peak was observed in the DSC results (see Table 5.1 and Chapter 4 Figs. 4.24 and 4.25). However, two exothermic peaks were observed for the Cu10S1, due to the reduction of CuO into Cu_2O^{+1} and the latter into pure Cu (see Fig. 4.25). The XRD (Table 4.15) and Raman (Table 4.12) results also confirmed that no chemical or structural changes occur. Therefore, if only taking into account the effect of temperature, the MWCNTs are expected to be stable during composite processing.

The XRD results identified the presence of the nanotubes, in the as-received S1 MWCNTs and Cu10S1 heat-treated samples, and no other C allotropes were identified. It also confirmed the formation of the Cu_2O^{+1} compounds+ Cu due to CuO reduction with the temperature increase.

Raman results were only performed on the S1 MWCNTs sample as the presence of Cu and the small amount of MWCNTs in the Cu10S1 sample limited the acquisition of the data. The results acquired appear to support the findings that no significant change in

the quality of the MWCNTs occurred, as the Raman ratios for the as-received (I_D/I_G = 0.70±0.03) and heat-treated (I_D/I_G = 0.69±0.08) (see Table 4.12) are almost the same. However, the small difference observed maybe related to the weight loss (~ 3 wt.%), probably induced by the a-C sublimation which is the less stable carbonaceous form present.[34]

The thermal stability of the S1 MWCNTs in He for high temperatures is in agreement with literature[31,37], where MWCNTs are reported to be stable, when heated in vacuum or under protective atmospheres up to 3000 ⁰C. In fact, heat treatments are used to purify (remove impurities) and improve quality (improve crystallinity) of the MWCNTs through graphitization (see Chapter 2 Subsection 2.3.2.4), however, no substantial crystallinity improvement is documented at temperatures below 900 ⁰C[38], as was observed in this study.

In both materials, S1 MWCNTs and Cu10S1 powders, a small narrow endothermic peak occurred at 853.04±5.1 ⁰C and 753.23±3 ⁰C, respectively. These peaks are believed to be related to a phase transformation such as the melting of the nano-sized Fe or Fe-C based catalyst (such as cementite (Fe_3C)).

These nanoparticle catalysts have both been found to be present in MWCNTs and are responsible for inducing MWCNTs growth[39–42]. For example, the bulk Fe_3C melting point was found to be about 300 °C below that of the bulk Fe and the same trend should be shown by carbide and pure metal nanoparticles, which melt at lower temperatures which decreases with their decreasing sizes. This can be explained by the phase transformation temperature depression which is typical for nanoparticles below 100 nm. It also explains the lower endothermic peak temperature (~ 100 ⁰C) in the Cu10S1 compared to the S1 MWCNTs sample as the high energy ball-milling causes the catalyst particles to break up in smaller ones, thereby reducing their melting temperature.[39,42,43]

The XRD results (see Fig. 4.24 d)) for the as-received S1 MWCNTs, indicate the presence of catalysts with the following compositions: elemental Fe, hexagonal iron carbide (Fe_2C) and martensite ($C_{0.14}Fe_{1.86}$) before heat-treatment, and only Fe_3O_4 after

the heat-treatment. The only plausible explanation for the oxide formation is that the powders were only tested in the XRD some days after the DSC testing, during this period of time it was exposed to air giving enough time for the oxide form.

The thermal stability study of the S1 MWCNTs and Cu10S1 composite powder reveals that no degradation of MWCNTs occurs in the production of Al/MWCNTs using the composite powder if a noble gas protective atmosphere is used as this prevents oxidation of the nanotubes during mixing. The use of a protective gas during processing of stir mixed composites is already widely used in order to aid insertion of the fillers into the melt, and avoid aluminium oxide formation and hydrogen diffusion in the melt.[44–46] Therefore, no "special" modifications were needed to process the Al/MWCNTs to enhance filler thermal stability further, i.e. the protective atmosphere was therefore employed to guarantee the thermal stability of the MWCNTs while processing.

5.2.1.3.2 Filler Introduction and Dispersion

Rheocasting does allow the incorporation of the MWCNTs into the matrix, however, they are found in bundles and their incorporation and dispersion is relatively dependent on the Cu content, at least for the alloy composition and processing parameters used in this study.

One of the major challenges in processing Al/MWCNTs composites via liquid metal routes, as described in Chapter 2, Subsection 2.4.2.1, is the delivery of the nano-filler into the melt. The density of the MWCNTs is less than the density of the liquid Al alloy and due to the surface tension of the melt, the nano material tends to float to the melt surface.[21,45,47]

Rheocasting is supposed to help overcome this issue due to the higher viscosity of the slurry, however, maintaining a constant processing temperature (T_{SS}) is difficult and can result in a higher or lower solid fraction (f_s), i.e. higher or lower viscosity. To date, to the author's best knowledge, only a few articles have been published about the rheocasting of Al/MWCNTs composites. However, all used a different alloy, filler preparation and delivery method than that used in this study, and none investigated the composites thermal conductivity.[44,46,48,49]

The rheocasting method set-up for the Al/MWCNTs composites, just like that for the Al/Cu-CFs, enabled the MWCNTs to be trapped within the matrix. Fig. 4.26, shows MWCNTs, observed as dark features present within the Al matrix and located at the grain boundaries. This is analogous to the CFs, with the MWCNTs commonly found together with intermetallic phases. The SEM and TEM results shown in Fig. 4.31 and Fig. 4.32, respectively, confirm that the dark features are bundles of nanotubes. In general, bigger bundles that were not well distributed were found in the M1 composite in comparison with the M2 composite, which contained smaller bundles with better distribution.

Figs. 4.26 e), f), g) and h) show the M1 composite (w_f = 0.003) microstructure with few dark features evident when compared with the M2 composite (w_f = 0.0035), shown in Figs. 4.26 i), j), k) and l), despite the small difference (0.05 wt.%) in the MWCNT content. This indicates that some of the MWCNTs added to the M1 composite, may have been ejected from the melt despite the high viscosity. In addition to the number of particles, the M2 composite also showed a better dispersion of the nanotubes bundles at the grain boundaries throughout the matrix.

The processing method is effective in incorporating the MWCNTs into the matrix, however, it is relatively dependent on the Cu content, at least when using this alloy composition and processing parameters.

During processing trials (not documented in this work), composites processed with a MWCNTs content < 0.3 wt.%, resulted in MWCNTs being expelled from the melt during stirring and deposited on the surface of the casting. This could be due to the Cu dissolving in the metal matrix, releasing the nanotubes that subsequently are expunged. Whereas, above 0.35 wt.% bundles of the nanotubes were trapped in the matrix, surrounded by large AlCuMg and AlCuFe based intermetallic phases. These are intermetallics that have very low thermal conductivities, as discussed in section 5.2.1.3.3, and are therefore detrimental for improving the composite thermal conductivity. Hence, for these reasons stated above, the composites with a MWCNTs content below 0.3 wt.% and above 0.35 wt.% were not further studied.

These findings raise another important challenge of processing Al/MWCNTs using liquid metal, which is individual nanotube dispersion throughout the metal matrix. The findings are in agreement with Donthamsetty et al[45], who wrote that it is extremely difficult for the mechanical stirring method to distribute and disperse nano-scale particles uniformly in metal melts due to their large surface-to-volume ratio and their low wettability, which easily induce agglomeration and clustering.

From the few studies published on the Al/MWCNTs composites processed by rheocasting, only Rashad et al[46], claim to have achieved good filler individual dispersion with added contents of up to 1.5 wt.%, above which agglomerations were found. Abbasipour et al[44] and Elshalakany et al[49] also claim to have achieved good dispersion but both fail to give clear microstructural evidence of the presence of MWCNTs, therefore the author is skeptical about their success in dispersing the nanotubes using this method.

Porosity decreases the thermal conductivity of the composites, as demonstrated by eqs. 21 and 23. Analogous to the porosity observed for the Al/Cu-CFs composites processed by rheocasting (see Fig. 5.3), the Al/MWCNTs also revealed an increase of porosity with increasing filler content. Fig. 5.5, shows how the porosity volume fraction (φ) varies with an increase in the theoretical v_f content of the MWCNTs (assuming the nanotube content is the same as that introduced during processing). The porosity increases up to 4 % for the M2 composite ($v_{f,M2}$ = 0.0044, (ρ_{real}) see Table 4.20). This is due to air entrapment during mixing (see Section 5.2.1.2.1) and an increased melt viscosity with increased nanotube content. The increase of Cu from the fillers also increases the alloy viscosity.[50,51]

Rheocasting can be used to introduce the particles into the matrix, however, the introduction efficiency appears to be dependent on the Cu content, at least when using the current set-up and parameters. However, the method is not effective in dispersing individual nanotubes. Rheocasting is therefore more efficient in producing Al/Cu-CFs composites than Al/MWCNTs composites. This is due to the size of the nanotubes and their higher surface area making wettability more difficult. This results in the formation of

agglomerates due to Van der Waals attraction between nanotubes, which are difficult to break apart using this processing route.
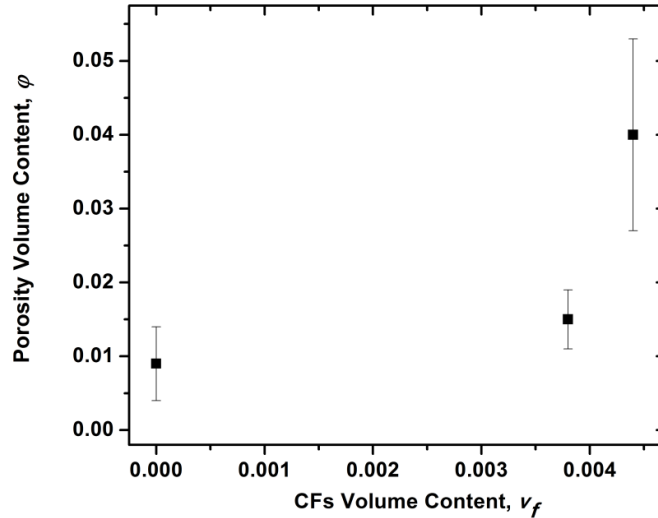
Fig. 5.5 Graph of porosity fraction (φ) vs theoretical MWCNTs volume fraction, v_f, calculated using their real density (ρ_{real}) (data from Table 4.20).

5.2.1.3.3 Wettability and Interfacial Reactions

The ball-milling of the S1 MWCNTs with pure Cu aided the introduction of the MWCNTs within the Al matrix, which was further improved after the Cu solubility in Al was reached, when the MWCNTs begin to get surrounded by low thermal conductivity intermetallics. However, this indicates that rheocasting of Al/MWCNTs composites using the described set-up and parameters is not effective for the production of ultra-high thermal conductivity materials as it does not overcome the main processing challenges, namely, the full control of the introduction and dispersion of the MWCNTs into the matrix.

To facilitate the introduction of MWCNTs into the Al metal matrix the MWCNTs were ball-milled with Cu, resulting in trapped individual nanotubes or bundles of nanotubes as shown in Fig. 4.23 d). The MWCNTs, due to their low surface energy, γ_{MWCNT} = 0.0453 J m^{-2}, in comparison to Al, γ_{Al} = 1.143 J m^{-2}, do not become wetted by the metal. Therefore, Cu (γ_{Cu} = 1.825 J m^{-2}) was used to perform the same role as in the Al/Cu-

CFs composites, promoting their wettability by the Al, thus preventing their immediate rejection from the melt.

In this case, the Cu content was crucial in helping to trap the nanotubes inside the matrix. Table 4.16 gives the chemical composition of the M composite system, showing the clear increase in Cu with an increase in MWCNT content. The M1 composite had a Cu content of 2.86 wt.%, whereas M2 had a content of 4.13 wt.%. As discussed in the previous section, significantly less MWCNTs bundles were observed in the M1 sample compared with M2, despite the small difference in Cu (1.27 wt.%) and MWCNTs (0.05 wt.%) introduced during processing.

Examination of the microstructure of the M1 composite using SEM (see Fig 4.31 a), b) and c)) shows that the MWCNTs are independent of the Cu and are either located in isolation or attached to AlFe intermetallics at the grain boundaries. This indicates that the Cu assists wetting in addition to dissolving in the matrix to release the MWCNTs. However, the M2 composite (Fig. 4.31 d), e), f)) revealed that the MWCNTs were trapped within the matrix mainly inside of AlCuMg and to a lesser extent AlCuFe intermetallics. This could be attributed to the fact that, according to the Al-Cu-Mg system phase diagram[52,53], shown in Fig. 5.6, (for a Mg content between 3 and 4 wt.%) at 507 °C the Cu solubility ranges between 3 to 3.5 wt.%, approximately.

This explains why in the M1 composite (Cu content of 2.86 wt.%) the Cu dissolved in the alloy matrix releasing the MWCNTs. Whereas, in the M2 composite (Cu content of 4.13 wt.%) the solubility limit has been clearly reached. This results in the high content of AlCuMg based intermetallics and AlFe intermetallic forming AlCuFe based intermetallics observed, as listed in Table 4.17.

The presence of intermetallics surrounding the MWCNT is detrimental for the thermal conductivity of the composites. Whatsmore MWCNTs bundles have substantially lower thermal conductivity than individual nanotubes.[54,55] Intermetallics typically have low thermal conductivities and will therefore act as an interfacial thermal barrier resistance between the matrix and the MWCNTs bundles.
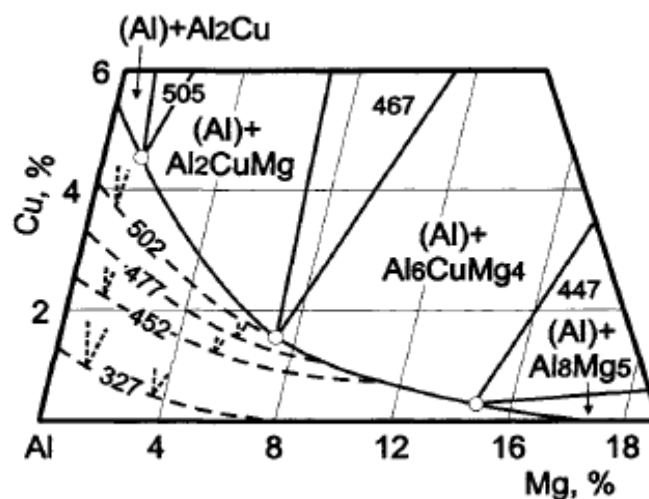
Fig. 5.6 Phase diagram of the ternary Al-Cu-Mg system showing the phase distribution in the solid and solid solubilities at various temperatures.[52,53]

Table 5.2 gives the thermal conductivity of predicted and observed intermetallics found within the microstructure of the composites. When Cu dissolves and replaces Fe in the AlFe intermetallics it may form AlCuFe quasicrystals, such as, the icosehedral i-AlCuFe $(Al_{63.5}Cu_{23.5}Fe_{13})$[56,57] phase or the approximants β-AlCuFe $(Al_{50}Cu_{34.5}Fe_{15.5})$[57] and ω-AlCuFe $(Al_{70}Cu_{20}Fe_{10})$[57,58] phases. The range of compositions of the AlCuFe $(Al_{56-63}Cu_{21-30}Fe_{9-13})$ intermetallics found in the M2 composite (Table 4.17) appear to fall within the compositions of the i- and β-AlCuFe phases that have a reported thermal conductivity ranging from 1.3 to 7 W m^{-1} K^{-1} [56,57].

Without the Cu, intermetallic phases such as $Al_{13}Fe_4$ have a reported thermal conductivity from 4 to 12.8 W m^{-1} K^{-1} [56,59]. Unfortunately, no reliable data has been found in the literature about the thermal conductivity of AlCuMg based intermetallics. However, this property decreases monotonically as the horizontal distance of the constituents of the compound increases in the periodic table. The addition of a third element also decreases the thermal conductivity of an intermetallic compound. It is therefore expected that the AlCuMg based intermetallics will also exhibit low thermal conductivities.[58] Ergo, it is essential that the formation of these intermetallics around the nanotubes is avoided.

Table 5. 2 Thermal Conductivity of selected intermetallics.

Intermetallic	K (W m^{-1} K^{-1})	Reference
$Al_{13}Fe_4$	4.7 - 12.8	Popčević P.[59]
	4	Landauro C.V.[56]
i-$Al_{63.5}Cu_{23.5}Fe_{13}$	1.3	Landauro C.V.[56]
	2.5	Alboni P.N[57]
β-$Al_{50}Cu_{34.5}Fe_{15.5}$	7	Alboni P.N[57]
ω-$Al_{70}Cu_{20}Fe_{10}$	19	Alboni P.N[57]
	≈ 12	Terada Y.[58]
Mg_2Si	≈ 8	Labotz R.J.[60]
	10.93	Wu Li[61]
	11.3	Wu Li[61]
AlCuMg	_ _ _	_ _ _

Addition of Cu10S1 for levels of MWCNTs > 0.3 wt.% will always involve intermetallic formation due to the Cu addition. Although, beneficial for the filler introduction into the matrix, and thus enabling the introduction of the maximum amount of fillers (v_f = 0.3) commonly reported for the described mixing methods[62], the increasing Cu content however will always have a detrimental effect on the maximum thermal conductivity achievable.

Another aspect that detrimentally affects the thermal conductivity of the composites is the Al_4C_3 formation in the filler/matrix interface. The MWCNTs are expected to be chemically stable compared to the CFs when in contact with the molten Al because of their perfect structure. However, the presence of defective sites and *a*-C on their surface, commonly generated during MWCNTs synthesis, promotes Al_4C_3 formation, as observed by many researchers[21,25,26,63,64]. The formation of carbide also depends on the processing techniques and parameters applied.[21]

The quality study of the CCVD synthetized S1 MWCNTs, identified *a*-C and defective sites prior to composite processing, as indicated by the high Raman ratio I_D/I_G=0.7 ± 0.03 (see Fig. 4.13), and the TEM observations (see Fig. 4.17). Ball-milling MWCNTs with metal powders induces damage creating even more defective sites, thereby

making the material even more susceptible to carbide formation during processing.[35,65,66] The presence of the Al_4C_3 was confirmed through the study of the rheocasted M2 composite matrix/filler interface using SAED technique (see Fig. 4.32 a and b)), The Al_4C_3 formation may have been induced by the a-C and defective sites already present before processing.

In the few studies that have been published on the rheocasting of Al/MWCNTs, the composites do not show clear evidence of carbide formation. Abbasipour et al[44], only performed an XRD study on the composites, but since the MWCNT content was about 2 % (volume fraction) neither MWCNT nor Al_4C_3 peaks were observed, as the content was below resolution of the technique.

Elshalakany et al[49] and Rashad et al[46], claimed to have found evidence of Al_4C_3 formation in their Al/MWCNTs composites when higher C peaks were observed using EDS. However, EDS technique is not sufficient to determine the formation of the carbides, due to the low C resolution of the technique. Also, the source of the C signal may arise from the formation of a C-rich film due to the electron beam induced polymerization of hydrocarbon molecules that are adsorbed onto the surface, especially if sample preparation is not properly performed, which can give inaccurate results.[67,68]

According to this study, the rheocasting of Al/MWCNTs composites using the described set-up and parameters is not effective for the production of ultra-high thermal conductivity materials as it has not manage to overcome the main processing challenges, namely, the full control of the introduction and dispersion of the MWCNTs into the matrix. It also promotes the formation of very low thermal conductivity intermetallics around the nanotubes agglomerations when the Cu solubility in the alloy matrix is reached. All the aspects referred above will have a negative thermal conductivity contribution, resulting in a composite with lower thermal conductivity than the monolithic alloy.

Summary:

❖ The incorporation of the S1 MWCNTs with pure Cu aided the introduction of the fillers within the Al matrix, which was further improved after the Cu solubility in Al was reached, when the MWCNTs were surrounded by mainly AlCuMg intermetallics. Deleterious Al_4C_3 was found which may have been induced by the *a*-C and defective sites present in the MWCNTs prior to processing.

❖ The rheocasting of the Al/MWCNTs composites using the described set-up and parameters is not effective for the production of ultra-high thermal conductivity materials as it has not manage to overcome the main processing challenges, namely, the full control of the introduction and dispersion of the MWCNTs into the matrix. This is in contrast to the findings for the Al/Cu-CFs composites.

5.2.2 Equal Channel Angular Extrusion

Deformation processes such as hot extrusion, hot rolling or equal channel angular extrusion (ECAE) have been widely used in powder metallurgy.[69] These methods employ shear force to induce deformation to break-down filler agglomerations and increase their dispersion whist also simultaneously improving the metal composites density. The use of ECAE was employed as a post-processing method to eliminate the porosity created during the rheocasting, and induce fibre/nanotube alignment in the extrusion direction in order to harness the superior thermal conductivity of the C-based fillers in the axial (in-plane) direction.

To date, to the best of the author's knowledge, there is no published work that uses the combination of rheocasting followed by ECAE with an aim to develop Al/MWCNTs composites with ultra-high thermal conductivity.

5.2.2.1 Porosity

The ECAE method was efficient at reducing porosity (down to 0.03%) for both Al/Cu-CFs and Al/Cu10S1 composites.

The porosity generated during rheocasting is strongly detrimental to the thermal conductivity of the composites, as demonstrated by Solórzano et al[70]. The ECAE method is widely used in powder metallurgy to obtain fully dense composites, therefore, it is effective in removing porosity.[71]

Fig. 5.7 shows the decrease in porosity of the C1.5 and M1 composites, thus illustrating the effectiveness of this method in removing porosity. It shows that after 4 iterations the porosity fraction was reduced to 0.03% (see Tables 4.5 and 4.20) for both composites regardless the filler (CFs or MWCNTs), and thus remained unchanged after 6 iterations. Nevertheless, it is important to reiterate that the surface area analysis technique method used to calculate the porosity volume fraction accounts for the porosity in 2D, meaning that in reality (3D) the porosity volume fraction is much higher than that calculated.
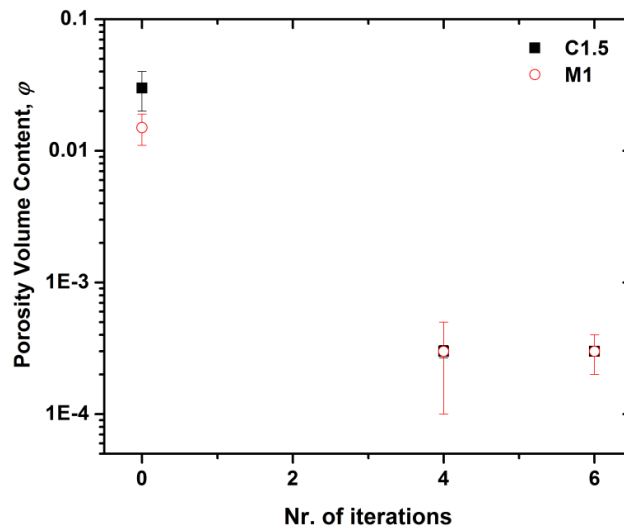
Fig. 5.7 C1.5 and M1 composites porosity volume fraction ($\log_{10}$ scale) evolution with increasing ECAE iterations (data from Tables 4.5 and 4.20).

5.2.2.2 Alignment and Damage

The ECAE method was effective in achieving a high degree of fibre/nanotube alignment with good nanotube/fibre matrix interface surface consolidation. However, the severe deformation induced considerable damage on both fibres and nanotubes, which may counteract the positive effect of the fillers alignment on the thermal conductivity of the composites.

Fig. 4.5 shows the high degree of filler alignment in the C1.5 composite microstructure. Increasing the number of iterations reduced the angle ($\emptyset_{ED-DD}$) between the extrusion direction (ED) and deformation direction (DD), i.e. the microstructure/fibre alignment. The angle was significantly reduced after 4 iterations, $8.51^\circ < \emptyset_{ED-DD} < 9.32^\circ$, and was further reduced to $\emptyset_{ED-DD} \approx 2.69^\circ$ after 6 iterations. Good intimate contact between the matrix and fibres was also achieved (Fig. 4.6). Nevertheless, since the ECAE process is a severe plastic deformation technique damage of the fibres is inevitable, as illustrated in Fig. 4.6. However, not all the fibres suffered damage to the same extent, which could be attributed to the initial fibre orientation before deformation with the worst case scenario for those fibres with a 90° angle between their orientation and deformation direction.

Fig 4.33 shows the degree of microstructure alignment due to ECAE on the M1 composite. After 4 iterations the angle between extrusion direction and deformation direction was $\emptyset_{ED-DD} \approx 7.61°$, which was further reduced to $3.24° < \emptyset_{ED-DD} < 3.62°$ after 6 iterations. Value close to that observed for the Al/Cu-CFs composites.

An SEM micrograph of the M1 composite after 6 iterations is shown in Fig. 4.34. It is evident from the micrograph that the ECAE method does break-up the MWCNT agglomerates, as they become elongated in the shear stress (deformation) direction (DD). It shows smaller agglomerations and the dispersion of individual nanotubes within the matrix, compared with the M1 "as-rheocasted" sample (see Fig. 4.31). This observation is in agreement with the work of Pham et al[72], that reported that the ECAE method could break the MWCNTs agglomerates and achieve a better dispersion in a Cu - 5vol.% MWCNT composite.

Fig. 4.35, shows two individually aligned MWCNTs studied using TEM + EELS, demonstrating that the ECAE technique can be employed to align the nanofillers. Nevertheless, it also shows the severity of the technique as the nanotubes are compressed together showing a high degree of damage. The severity of the observed deformation also indicates that the nanotubes can be broken into smaller lengths. According to Song et al[73], MWCNTs with smaller length (<1 μm) have an enhanced effect on increasing the thermal conductivity compared to longer MWCNTs due to reduced curving or bending. However, the damage observed may counteract any beneficial reduced length effect on the thermal conductivity of the composite. The FFT diffraction patterns and respective IFFT image show that the technique allowed intimate contact between nanotubes and the Al matrix (no voids observed). Intriguingly, Al_4C_3 is not observed, but if this phase forms during rheocasting it will also be present after ECAE.

Summary:

❖ The ECAE method was efficient at removing porosity and achieving a high degree of fibres/nanotubes alignment with good nanotube/fibre matrix interface surface consolidation, for both Al/Cu-CFs and Al/MWCNTs (Al/Cu10S1) composites.

❖ The severe deformation characteristic of the ECAE technique induced considerable damage on both fibres and nanotubes, which may counteract the positive effect of the filler alignment on the composites thermal conductivity.

5.3 Effective Thermal Conductivity of the Composites

The demand for advanced thermal materials with ultra-high thermal conductivity ($K \geq$ 400 W m^{-1} K^{-1}) has increased in order to meet the need to remove excessive heat produced during the operation of electronic components. The amount of heat generated has been steadily increasing over recent years due to the miniaturization of components and the increasing consumption of electrical power in electronic circuits.[13,74]

In this chapter, the discussion is focused on the thermal conductivity contribution of the C-based fillers to the composite in comparison to the monolithic alloy, when processed using a combination of rheocasting and equal channel angular extrusion (ECAE) techniques.

The experimental conductivity of the composites has been compared with published literature and theoretical models. It accounts for the thermal conductivity value according to the manufacturer and also the experimental thermal conductivity values of the S1 MWCNTs samples based on their advanced characterisation results and including that obtained for an individual MWCNT acquired by SThM+FEM. This work is the first to try to combine the thermal conductivity of an individual MWCNT with theoretical models in order to predict the thermal conductivity of the resulting Al/MWCNTs composites.

5.3.1 Effective Thermal Conductivity of Al/Cu-CFs Composites

5.3.1.1 Comparison with Literature

The rheocasting technique alone was not sufficient to improve the thermal conductivity of the composites in comparison with the matrix (Al3Mg). However, after ECAE 6 iterations (C1.5$_{6i,1}$) the composite thermal conductivity improved ~ 20 % with respect to the "as-rheocasted" C1.5 composite, thus overcoming the thermal conductivity of the matrix by 3.6%. This improvement is believed to be due to, porosity reduction, fibre alignment and forced intimate contact of clean CF surfaces (no MgO) with the matrix.

Understanding the effect of the employed processing method on individual phases formed within the composites enable their properties including thermal conductivity to

be controlled. This is important if new composites are to be developed with properties that match those of the ultra-high thermal conductivity materials ($K \geq 400$ W m^{-1} K^{-1}) required for heat management applications especially when utilizing highly anisotropic C-based fillers. Therefore, in this section the effect of the processing method used in this study, i.e. rheocasting + ECAE is discussed with respect to the resultant composites thermal conductivity.

Fig. 5.8 compares the experimental thermal conductivity variation ($\Delta K_c = K_c - K_m$) of the Al/Cu-CFs composites produced in this study (data taken from Table 4.4) in the theoretical condition (i.e. no porosity and no CF v_f correction, described in Chapter 3 Subsection 3.5.3) and the Al/CF composites produced by Silvain et al[75] (triangles), as a function of CF volume fraction.
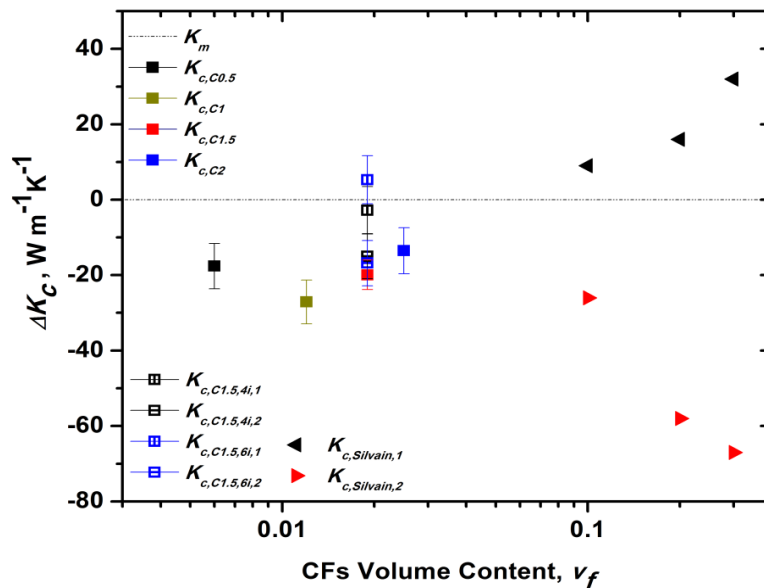

Fig. 5.8 Comparison of experimental thermal conductivity variation in the Al/Cu-CF composites processed via rheocasting and ECAE (data given in Table 4.4) with the reference Al3Mg matrix in the theoretical condition and an Al/CFs composite processed by Silvain et al[75] (no standard deviations were given in the article from which the data was taken).

Fig. 5.8 demonstrates that the rheocasting technique alone was not sufficient to improve the thermal conductivity of the composites in comparison with the matrix (Al3Mg), $\Delta K_{c,C2}$ = -13.5 ± 6.1 W m^{-1} K^{-1} (~ - 9.1%) for a maximum filler content of v_f = 0.025.

The primary reasons for the observed results can be attributed to the associated problems inherent with the rheocasting processing method[14,15,18,20], as discussed in Chapter 5.2, subsection 5.2.1.2.1. These problems are: random fibre orientation in the matrix; fibre agglomerations and high porosity content (see Table 4.5). Nevertheless, for the CFs samples the effective thermal conductivity of the composites increase with increasing fibre content, despite the presence of agglomerates, formation of MgO interface reaction (see Fig. 4.4) and increase in Cu content, a maximum of 2.04 wt.% for the C2 sample (see Fig. 4.7). According to Ho et al[10] (see Fig. 5.1) this increase in Cu content will have a detrimental effect on the thermal conductivity of the composite.

However, after ECAE processing the "as-rheocasted" C1.5 composite thermal conductivity in the in-plane direction greatly improves. The increase was observed with an increasing number of iterations, reaching the maximum thermal conductivity after 6 iterations (C1.5$_{6i,1}$). Thus realised an improvement of ~ 20 % with respect to the "as-rheocasted" C1.5 composite resulting in a higher thermal conductivity then the matrix by 3.6% ($\Delta K_{c,C1.5,6i,1}$ = 5.3 ± 6.4 W m^{-1} K^{-1}).

This is a notable achievement, especially if compared with the work of Silvain et al[75] (see Fig. 5.8). They produced an Al/CF composite via a powder metallurgy hot pressing method and used pitch-based CFs from the same manufacturer as those used in this study. For a CF volume content v_f = 0.1, only an increase of $\Delta K_{c,1}$ = 9 W m^{-1} K^{-1} (~ 4.6%) was observed, only 1% more than the C1.5$_{6i,1}$ sample despite having 5 times more fibres. The difference observed may be due to the fact that the powder metallurgy hot pressing processing method has a limited capability in fibre alignment, when compared, for instance with ECAE.

In the out-of-plane direction, the increase in the number of iterations had almost no effect in the thermal conductivity of the composites in comparison to the "as-rheocasted"

C1.5 composite ($\Delta K_{c,C1.5}$=-19.9 ± 6 W m^{-1} K^{-1} and $\Delta K_{c,C1.5,6i,2}$ = -16.8 ± 6 W m^{-1} K^{-1}). This is likely to be related to the anisotropic behaviour of the CFs due to their crystalline structure which is similar to graphite[76].

ECAE is a severe plastic deformation (SPD) process that produces ultra-fine grain (UFG) materials[77]. After ECAE processing the composite grain size was reduced decreasing atomic order and increasing grain boundary density and dislocations. These factors reduce the electron mean free path (i.e. they decrease the thermal conductivity of the metallic matrix). However, the deformation induced, other than aligning, also brakes fibres, and causes damage as illustrated in Fig. 4.6. The damage reduces the phonon mean free path (i.e. the fibres heat conduction mechanism), resulting in phonon scatter. Despite all the factors referred above, the results indicate that processing Al/CF composites via rheocasting+ECAE seems to be viable for producing composites with an improved thermal conductivity. If the composites microstructure is recovered using heat-treatments it is possible that their attainable thermal conductivity reaches even higher values.

The improvement in the experimental thermal conductivity values is believed to be due to, porosity reduction, fibre alignment and fibre bundles breakage and alignment. However, the author believes that the improvement may also be due to the possibility that severe plastic deformation breaks the fibres and forces an intimate contact with clean CF surfaces (no MgO interface) reducing at the same time the gaps between the fibres and matrix. This idea is based on the following facts:

➢ In real interfaces the asperities present on each of the surfaces (matrix and filler) limit the actual contact between the two solids to a very small fraction of the apparent interfacial surface area. The flow of heat across the gap between two solids in nominal contact occurs by solid conduction in areas of actual contact and gas conduction across the "open" spaces.[78]

➢ The formation of any reaction on the interface is detrimental to thermal conductivity, as clean surfaces have been proven to have higher thermal

conductivity than that with interfacial reactions, and are therefore more desirable.[9]

Despite the improvement observed, it is necessary to assess more composites produced by rheocasting+ECAE techniques that incorporate a wider range of fibre volume fractions in order to validate its effectiveness in improving thermal conductivity.

5.3.1.2 Comparison with Theoretical Models

The "corrected" experimental thermal conductivity of the composite ($K^{corr}_{c,C1.5,6i,1}$) with the highest degree of fibre alignment is in good agreement with the Hatta-Taya's model higher boundary. This indicates that using the rheocasting+ECAE technique to process Al/CF composites gives a direct positive influence in their thermal conductivity by removing porosity and aligning the CFs.

To assess the real contribution of the fibres to the matrix alloy, it is important to account for parameters such as; fibre size and orientation, real fibre content in the matrix and porosity. Unfortunately, due to restrictions in access to thermal conductivity measuring equipment it was not possible to assess experimentally the effect of Cu on the composite thermal conductivity evolution with increasing fibre content.

In order to account for the effects referred above, the "corrected" experimental thermal conductivity of the Al/Cu-CF composites (K^{corr}_c) was compared with the 2D Hatta-Taya Eshelby inclusion model[79,80], with the findings given in Fig 5.9. In the "corrected" condition the porosity volume fraction (φ) is quantified and its effect is subtracted. In addition, the real content of fibres (v^{corr}_f) in the matrix is also accounted as described in Chapter 3 Subsection 3.5.3. All the parameters used in the model are given in Table 3.16.

According to the manufacturer, the CFs used in this study have an in-plane thermal conductivity range of 500 W m^{-1} K^{-1} < $K_{f,1}$ < 600 W m^{-1} K^{-1} (see Table 3.5), for this reason in the model the lower value (500 W m^{-1}K^{-1}) was used to determinate its minimum effect, whereas in the out-of-plane condition $K_{f,2}$ = 10 W m^{-1} K^{-1} was selected.
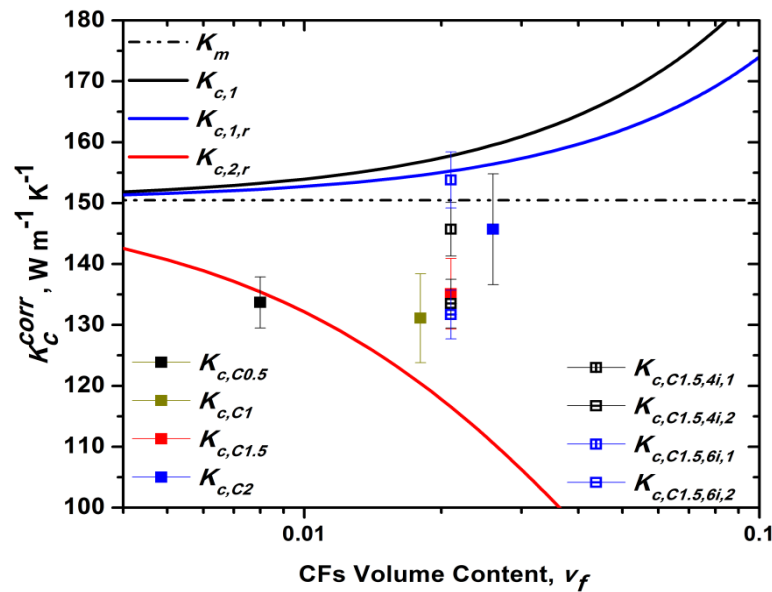
Fig. 5.9 Comparison of the Hatta-Taya Eshelby inclusion model showing the higher ($K_{c,1}$ and $K_{c,1,r}$, fibres aligned in the in-plane direction), and lower ($K_{c,2,r}$, fibres aligned in the out-of-plane direction) thermal conductivity boundaries with the "corrected" experimental thermal conductivity of the composites (K_c^{corr}) accounting for the porosity and real volume fraction, v_f^{corr}.. Data taken from Table 4.5.

Table 5.3 Comparison of agreement between the Hatta-Taya Eshelby inclusion model for different CF configurations within the matrix, and the "corrected" experimental thermal conductivity values (K_c^{corr}). Good agreement (✔) when ≤ ± 2 W m^{-1} K^{-1}, fair (O) when ± 2 < O ≤ ± 4 W m^{-1} K^{-1} and bad (✘) when > ± 4 W m^{-1} K^{-1}

Sample	$K_{c,1}^{corr}$	$K_{c,1,r}^{corr}$	$K_{c,2,r}^{corr}$
C0.5	✘	✘	✔
C1	✘	✘	✘
C1.5	✘	✘	✘
C2	✘	✘	✘
C1.5$_{4i,\,1}$	✘	✘	- - -
C1.5$_{4i,\,2}$	- - -	- - -	✘
C1.5$_{6i,\,1}$	O	✔	- - -
C1.5$_{6i,\,2}$	- - -	- - -	✘

An agreement comparison between theoretical and experimental values was performed with good agreement (✔) considered when the difference between values was ≤ ± 2 W

m^{-1} K^{-1}, fair (o) when $\pm 2 <$ o $\leq \pm 4$ W m^{-1} K^{-1} and bad (✘) when $> \pm 4$ W m^{-1} K^{-1}. The comparison is given in Tables 5.3.

The Hatta-Taya Eshelby inclusion model only considers that the fibres are homogeneously and individually aligned in the matrix, either in the in-plane direction ($K_{c,1}$ and $K_{c,1,r}$) or in the out-of-plane direction ($K_{c,2,r}$) (see Chapter 2 Section 2.5 for K designation description).

Since rheocasting can only disperse fibres randomly (in any orientation/direction) in the matrix, it would be expected that the "as-rheocasted" composites (i.e., C0.5, C1, C1.5 and C2) would not be in agreement with the model but rather, have values in between the higher boundaries $K_{c,1}$ and $K_{c,1,r}$ and the lower boundary $K_{c,2,r}$. This is the case for all the as-rheocasted composites except for the C$_{0.5}$ sample, as seen in Fig. 5.9. Although outside the boundary the value is still in good agreement with $K_{c,2,r}$.(see table 5.3), which may be due to the formation of agglomerates.

Regarding the composites processed via rheocasting+ECAE, only when the highest degree of fibre alignment in the matrix in the in-plane is achieved (C1.5$_{6i,1}$, Ø$_{ED-DD}$ ~ 2.69 ^{0}, see Fig. 4.5 c)) that the experimental value is in fair and good agreement with the Hatta-Taya's Eshelby model high boundaries $K_{c,1}$ and $K_{c,1,r}$, respectively. This may be attributed to the porosity reduction, high degree of fibre alignment and intimate contact of clean CF surfaces with the matrix as discussed in the previous Subsection (5.3.1.1).

Note that the thermal conductivity value of the fibres considered here is 500 W m^{-1} K^{-1} but this value can be higher (500 W m^{-1} K^{-1} $< K_{f,1} <$ 600 W m^{-1} K^{-1}) according to the manufacturer. Even so, the comparison with the theoretical model demonstrated that using the rheocasting+ECAE technique to process the Al/CF composites gives a direct positive influence on their thermal conductivity value by removing porosity and aligning the CFs.

According to Saravanan and Surrappa et al[62], using rheocasting it is possible to a $v_f =$ 0.3 of filler. This would mean that according to Hatta-Taya´s model higher boundary

$K_{c,1,r}$ a composite processed by rheocasting + ECAE with such content may reach a maximum thermal conductivity of $K_{c,1,r}$ = 226.6 W m^{-1} K^{-1}. Despite the improvement (~ 3.6%), the results indicate that the Al/Cu-CF composites produced via rheocasting followed by ECAE are not suitable to produce ultra-high thermal conductivity (K $\geq$ 400 W m^{-1} K^{-1}) composites for thermal management applications. In order to achieve that milestone it would be necessary to have a fibre content of v_f = 0.79.

Summary:

❖ The rheocasting technique alone was not sufficient to improve the thermal conductivity of the composites in comparison with the matrix (Al3Mg). However, after ECAE 6 iterations (C1.5$_{,6i,1}$) the composite thermal conductivity improved ~ 20 % with respect to the "as-rheocasted" C1.5 composite, resulting in an increase in the thermal conductivity of the matrix by 3.6%.

❖ The improvement is believed to be due to, porosity reduction, fibre alignment and forced intimate contact of clean CF surfaces (no MgO) with the matrix. However, it is necessary to assess more composites produced by rheocasting+ECAE techniques for a wider range of fibre volume fractions to fully validate its effectiveness to improve thermal conductivity.

❖ The "corrected" experimental thermal conductivity of the composite ($K^{corr}_{C,C1.5,6i,1}$) with the highest degree of fibre alignment is in good agreement with the Hatta-Taya's model's higher boundary. This shows that using the rheocasting+ECAE technique to process Al/CF composites gives a direct positive influence on their thermal conductivity by removing porosity and aligning the CFs.

❖ Despite the improvement of 3.6%. with respect to the alloy matrix , the results indicate that the Al/Cu-CFs composites produced via rheocasting+ECAE are not suitable to produce ultra-high thermal conductivity (K $\geq$ 400 W m^{-1} K^{-1}) composites for thermal management applications as it would be necessary to have a fibre content of v_f = 0.79 to achieve such a milestone.

5.3.2 Al/MWCNT Composites

5.3.2.1 Thermal Conductivity of MWCNTs

In this section, the discussion is centred on the effect of the S1, S2 and S3 MWCNT characteristics on their thermal conductivity. It focuses on the attempt to obtain the real thermal conductivity of S1 individual nanotubes using a novel combination of scanning thermal microscopy (SThM) and finite element method (FEM) techniques.

5.3.2.1.1 MWCNT Characterisation

The characterisation results demonstrated that the three MWCNT samples acquired from different sources were found to have very distinct morphologies (length, inner and outer diameters), qualities (content of defects) and purities (carbonaceous impurities and metal catalyst content) despite the fact that two samples were synthetized via the same method (CCVD).

According to the literature and the characterisation results, if considering the effect of morphology, quality and purity of the nanotubes, the average thermal conductivity of the individual MWCNTs is expected to be the highest for the S1 sample, followed by the S3 and lastly the S2 sample. Therefore, MWCNTs for high thermal conductivity applications should be carefully selected and must exhibit the smallest lengths and diameters, low defect concentration, and high crystallinity and no impurities.

- **Morphology**

The SEM and TEM characterisation results from the three MWCNTs samples from different sources revealed very distinct morphologies at micro-and nano-scales (see Table 5.4). This was despite the fact that two samples (S1 and S2) were synthetized via the same method (CCVD) (see Chapter 4 Section 4.3.1).

The differences are clear at both, low magnification (powder form) and high magnifications (individual nanotubes). The SEM study (see Fig. 4.10) revealed that the S1 and S2 samples are comprised of highly entangled nanotubes that form agglomerated particles ~ 31 µm and ~ 554.9 µm in size, respectively. S3 samples are

comprised of large carpets (~ 968 µm x 222.2 µm) of vertically aligned nanotubes. In terms of nanotube length (l), S3 nanotubes are the longest, followed by S1 and S2 (~ 219.9 µm, ~ 4.6 µm and ~ 1.5 µm, respectively). The same trend is observed for the nanotubes inner diameter (d_i); S3 ~ 10.9 nm, S1 ~ 6.8 nm and S2 ~ 4.8 nm. The nanotubes outer diameter (d_o) is: - S3 ~ 99.9 nm; S1 ~ 26.3 nm and S2 ~ 14.6 nm.

Table 5.4 Morphology data from S1, S2 and S3 MWCNTs obtained by electron microscopy characterisation.

Method	Result
SEM	S1: shape - rounded low sphericity particles shape, 31 µm (diameter), highly entangled MWCNTs.
	S2: shape - equant particles shape, 554.97 µm (diameter), highly entangled MWCNTs
	S3: shape - large carpets (968 x 222.2 µm), highly aligned MWCNTs
TEM	l: $(1.5\ µm)_{S2} < (4.6\ µm)_{S1} < (219.9\ µm)_{S3}$;
	d_o: $(14.6\ nm)_{S2} < (26.3\ nm)_{S1} < (99.9\ nm)_{S3}$;
	d_i: $(4.8\ nm)_{S2} < (6.8\ nm)_{S1} < (10.9\ nm)_{S3}$

As discussed in Chapter 2, Subsection 2.3.2.6, the thermal conduction in MWCNTs is governed by phonon contribution[28,81] which is affected by several factors such as the number of the phonon active modes, the length of the mean free path of the phonons and inelastic Umklapp scattering. These factors are directly affected by; tube-tube interaction, nanotube type, diameter (inner and outer) and length.[23,82] These are factors that also determine if the MWCNTs are either ballistic or diffusive heat conductors,i.e. high or low thermal conductivity, respectively.[81] As the published literature on whether the chirality affects the thermal conductivity of MWCNTs is ambiguous, this property was not considered in this study.

In published literature, experimental studies have revealed a wide range of thermal conductivities for individual MWCNTs spanning from 17 to above 3000 W m^{-1} K^{-1} [31, 44, 55, 81–90] (see Table 2.2) as depicted in Fig. 5.10. However, bundles of nanotubes exhibit much lower thermal conductivities ranging from 2.5 to 150 W m^{-1}K^{-1} [54,93–95] (see Table 2.3), whilst, the VAMWCNTs carpets exhibit thermal conductivities spanning from 0.145 to 267 W m^{-1} K^{-1}.[81]

Aliev et al[54] demonstrated that individual nanotubes always possess higher thermal conductivities than bundles/arrays of nanotubes with the same individual characteristics. Their results clearly show that the MWCNT powder morphology is important as it can greatly influence the powder thermal conductivity. The larger the bundle's size the lower its thermal conductivity due to tube-tube interaction. Arrays of aligned nanotubes achieve higher thermal conductivity than bundles due to the nanotubes anisotropic thermal properties.

Therefore, neither bundles nor arrays of aligned nanotubes can achieve the values observed for individual nanotubes. Hence, to produce composites for thermal management applications with ultra-high thermal conductivity ($K \geq 400$ W m^{-1}K^{-1}) the morphology of the powder used to deliver the nanotubes within the matrix is important and must allow easy nanotube individual dispersion within it in order to fully harness the nanomaterial thermal conductivity potential.

A more important factor than the MWCNT powder morphology effect on their thermal conductivity which is governed by the tube-tube interaction and alignment, is the effect of the morphology of the individual nanotubes. The length and inner and outer diameters of the nanotubes that comprise the bundles/arrays of the MWCNTs powders, limit the maximum thermal conductivity of the powders.

MWCNT thermal conduction transitions from the ballistic to the diffusive conduction regime as the nanotube length increases[81,88,88]. The increase in length also increases the probability of defect concentration.[81] Song et al[73], found that MWCNTs with lengths below 1 μm have an enhanced effect on increasing the thermal conductivity compared to long MWCNTs due to reduced curving or bending. Pettes and Shi[87] found that the thermal conductivity of MWCNTs decreased with the number of walls, but this is believed to be linked with an increased concentration of defects in nanotubes with more walls.

Fig. 5.10 a) and b) illustrates the published experimental thermal conductivity of individual nanotubes as a function of their length and outer diameter. It shows that the highest values were obtained for nanotubes with shorter lengths and smaller diameters

as expected. However, a large scattering in results demonstrates that other factors may have a more significant impact on nanotubes thermal conductivity than morphology. These factors are the quality and purity of the nanotubes. It is important to note that the techniques used to assess this property are complex and have various limitations, thus, also contributing to the scattering of the results.[96]
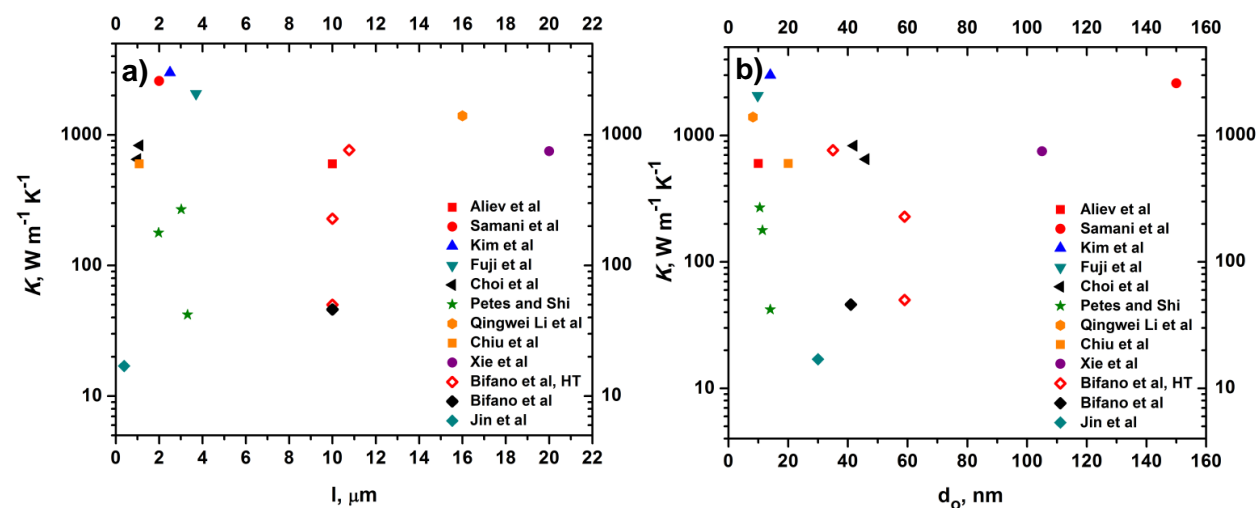
Fig. 5.10 Published experimental results for the thermal conductivity of individual MWCNTs as a function of the nanotubes: **(a)** length (l) and **(b)**. outer diameter (d_o) [31, 44, 55, 81–90]

Finally, if only the nanotubes average length and diameter is taken into account, it would be expected that the individual nanotubes of the S2 sample would possess the highest thermal conductivity amongst all three samples followed by the S1 sample and the S3, respectively. Unfortunately, as discussed the thermal conductivity of the MWCNTs is very complex and it depends not only on nanotubes morphology but also on their quality and purity.

- **Quality and Purity**

The phonon scattering and reduction in the phonon mean free path, which consequently reduces the MWCNTs thermal conductivity, is also highly dependent on the nanotubes degree of crystallinity, defect content (quality) and impurity content (purity) (see Chapter 2, Subsection 2.3.2.6).[81]

The quality and purity results from the three MWCNTs samples are given in Table 5.5 (compilation of the results from Chapter 4 Subsections 4.3.2 and 4.3.3). The three samples, analogous to that observed for the morphology, also exhibit a distinct quality and purity.

Table 5.5 Quality and purity results from all three samples obtained by TEM, Raman, XRD and STA methods.

Method	Information:
TEM	**Defects and Impurities:**
	S1: Structural and lattice disorder defects, presence of Fe-based catalyst, low content of a-C.
	S2: Structural and lattice disorder defects, high content of a-C;
	S3: Best quality among all samples, less structural and lattice defects, presence of nanofibres (no concentric hole), almost no a-C, high Fe-based catalyst content.
	Crystallinity: S2 < S1 < S3
	Stability Under Beam: S2 < S1 < S3
Raman	**Quality** : I_D/I_G: $(0.31\pm0.03)_{S3}$ **<** $(0.7\pm0.03)_{S1}$ **<** $(1.38\pm0.1)_{S2}$
XRD	**Catalyst**:
	S1: Fe, Fe_2C, $C_{0.14}Fe_{1.86}$,
	S2: Fe
	S3: Fe, Fe_2C, $CrFe_7C_{0.45}$
STA	**Thermal Stability**
	T_{oxi}(°C): $(540.47\pm5)_{S2}$ **<** $(560.66\pm2.6)_{S3}$ **<** $(569.28\pm7.6)_{S1}$
	T_{in} (°C): $(369.56\pm10)_{S2}$ **<** $(413.24\pm4)_{S3}$ **<** $(434.56\pm19)_{S1}$
	Width (°C): $(150\pm4.2)_{S3}$ **<** $(173.13\pm20.4)_{S1}$ **<** $(230.01\pm18)_{S2}$
	Catalyst content
	m_r (wt.%): $(1.96\pm1.04)_{S2}$ **<** $(3.68\pm1.59)_{S1}$ **<** $(11.55\pm1.25)_{S3}$

The HRTEM crystallinity study based on the FFT generated diffraction patterns (see Fig. 4.20) the S3 sample exhibited the sharpest peak indicating the highest crystallinity, followed by the S1 sample, and lastly the S2 sample that displayed broader peaks due to the presence of amorphous material.

Regarding the defects, the same types of defects were observed in all three samples (see Figs. 4.17, 4.18 and 4.19). They were structural defects such as heptagons and pentagons and lattice disorder defects, namely bamboo structures, graphite shells and

tapering cylinders. Nevertheless, the S3 sample, despite having larger length and diameter, showed the lowest content of defects, followed by the S1 sample, with the S2 sample again the worst. This is corroborated by the ratio of the Raman D/G bands intensity (I_D/I_G: $(0.31\pm 0.03)_{S3}$ < $(0.7\pm 0.03)_{S1}$ < $(1.38\pm0.1)_{S2}$, see Fig. 4.13 and Table 5.5), where the D band indicates the presence of defects due to broken sp^2 bonds in the MWCNTs sidewalls and impurities with sp^3 bonding such as carbonaceous impurities, whereas, the G band indicates the crystallinity present within the MWCNT sample.[33,34]

Theoretical work[81] (see Chapter 2 Subsection 2.3.2.6) on single-walled carbon nanotubes (SWCNTs) has demonstrated that defects significantly reduce their thermal conductivity and that the thermal conductivity saturated with increasing defect concentration above ~ 0.5% at ~ 160 W m^{-1} K^{-1} for all types of defects studied. The theoretical studies of the effect of defects on carbon nanotubes has been primarily conducted on SWCNTs, with the findings suggesting that defects should also have a strong impact on MWCNTs. This indicates that the defect content must be minimized.

The impurities present in all samples are carbonaceous impurities and metal catalysts. The S2 sample has a large amount of carbonaceous impurities present as a thick layer on top of the nanotubes (see Fig. 4.18), and has the highest content amongst the samples, followed by the S1 and lastly the S3 sample. This is the primary reason why this sample has the highest Raman D/G ratio.

This can also be demonstrated by analysing the width (temperature range) of the DSC peaks[34] for each sample $((150\pm4.2 \ ^oC)_{S3}$ < $(173.13\pm20.4 \ ^oC)_{S1}$ < $(230.01\pm18 \ ^oC)_{S2})$. The wider the peaks, the higher the content and variety of carbonaceous impurities (see Fig. 4.15).[34] Nevertheless, the S3 sample has the highest content of metal catalysts (11.55 ± 1.25 wt. %) which according to the XRD results are elemental Fe, Fe_2C and $CrFe_7C_{0.45}$. The S1 sample has 3.68 ± 1.59 wt. % of catalyst identified as elemental Fe, Fe_2C, $C_{0.14}Fe_{1.86}$ and, S2 has only 1.96 ± 1.04 wt. % consisting of only elemental Fe.

The presence of carbonaceous impurities on the MWCNTs resulting from the nanotubes synthesis decreases their thermal conductivity.[97] For instance, a-C has very low thermal

conductivity, spanning from 0.1 to 10 W m^{-1} K^{-1}. [28,82] Therefore, the presence of C-based impurities must also be minimized.

It is well known that the catalyst nature (i.e. composition) plays a major role on the morphology and quality of the nanotubes during synthesis/growth. This influences parameters such as length, number of walls, defects content and chirality. It is also known that its presence after synthesis reduces the nanotubes thermal stability as it can catalyze an oxidation reaction. [98]

Fortunately, after MWCNTs synthesis purification can be applied to reduce the amount of defects and impurities present. [99–101] The importance of purification on the individual carbon nanotubes thermal conductivity has been demonstrated by Bifano et al[37] who found that a heat treatment at 3000 ºC for 20h increased the thermal conductivity nearly 5 times for most samples when compared with "as-received material". In this study, the MWCNTs samples were not subjected to purification because it was not possible to get access to the facilities with the high temperatures required for this effect.

The stability study of the MWCNTs under a plasma atmosphere and under an electron beam (see chapter 4 Subsections 4.3.3.1 and 4.3.3.2), i.e. conditions which the nanotubes are subjected to during characterisation, show that special care needs to be taken when analysing the samples. During sample preparation, handling and investigation of the MWCNTs powders may cause further degradation and lead to false quantification results for the quality of the nanotubes.

According to the quality and purity results, if we consider that crystallinity and carbonaceous impurities are the factors that affect the thermal conductivity of the individual nanotubes the most, and the metal catalyst content is less detrimental, then one would expect the S3 individual MWCNTs to exhibit the highest thermal conductivity followed by the S1 sample, and the S2 MWCNTs to have the worst performance. If this is true, the thermal conductivity performance sequence of the samples would then be the reverse of that expected according to the individual nanotubes morphology. Therefore, knowledge of the morphology, quality and purity is essential when acquiring MWCNTS for thermal management applications.

An attempt to identify which of the MWCNTs samples provides the best thermal conductivity with respect to its individual nanotubes is difficult at this stage as there are no studies that confirm which of the factors influences this property the most. However, the author believes that the crystallinity/defect concentration plays the major role followed by the carbonaceous impurities sitting on top of the nanotubes impairing the heat transfer with the nanotube morphology with the metal catalyst content the least important. Therefore, if this were the case, one would expect that the individual MWCNTs from S1 sample to have the highest average thermal conductivity followed by S3, with the S2 sample being the worst.

In conclusion, MWCNTs for high thermal conductivity applications should be carefully selected and they must exhibit the following attributes:

- Smallest lengths and diameters (i.e. contain a low number of walls)
- Low defect concentration and high crystallinity
- No Impurities (carbonaceous and metal catalyst).

This study emphasizes the potential of the use of characterisation techniques to quantify the morphology, quality and purity of the MWCNTs in order to attempt to predict the thermal conductivity of a given MWCNT sample. This is still not possible as there are no models to predict the thermal conductivity of a given MWCNT sample by taking into account each factor (i.e. length, diameter, crystallinity, carbonaceous and catalyst impurities). There is also no data to attribute a "power factor" or weight to each of their contributions depending on their impact on thermal conductivity.

The development of such model would enable the thermal conductivity to be estimated through the characterisation of the MWCNTs from any source.

5.3.2.1.2 Thermal Conductivity of an individual S1 MWCNT

The combination of SThM + FEM enabled the acquisition of the thermal conductivity (K) of an individual S1 MWCNT that resulted a combined thermal conductivity ($K_{MWCNT,1,2}$) value of ~ 20 W m^{-1} K^{-1}.

The K of an individual MWCNT from the S1 sample was obtained by using a combination of scanning thermal microscopy (SThM) and finite element analysis (FEM). Due to the complexity of the measurements unreliable data may result mainly due to nanotube movement whilst the probe scans its surface in the contact mode. As a consequence only one measurement from the S1 MWCNT was considered valid (see Chapter 4 Subsection 4.3.5.1).

The nanotube tested was ~ 3 µm length and 40 nm in diameter, and the K value was determined to be within 19.5 W m^{-1} K^{-1} (lower boundary limit) and 20 W m^{-1} K^{-1} (higher boundary limit). The value acquired was very low compared to many of those reported in literature (> 3000 W m^{-1}K^{-1}) [29,37,54,83–92], however it was not the lowest (17 W m^{-1} K^{-1})[83] (see Fig. 5.11). The result and value obtained is a combination of the K parallel to the longitudinal ($K_{MWCNT,1}$) and perpendicular ($K_{MWCNT,2}$) to the nanotube axis. During FEM modelling it was not possible to deduct the K perpendicular to the nanotube axis ($K_{MWCNT,2}$= 10 W m^{-1} K^{-1}), therefore, it can be deduced that the K value along the nanotube, $K_{MWCNT,1}$, is substantially higher than the 20 W m^{-1} K^{-1} value calculated, however much lower than the 2000 W m^{-1}K^{-1} claimed by the manufacturer (see Chapter 3 Table 3.6).

The low K obtained can be explained by the nanotube's long length and large outer diameter indicating a diffusive heat conduction regime[81] and possible low quality (see Chapter 2, Subsection 2.3.2.6). It was not possible to characterise the tested nanotube by Raman spectroscopy or electron microscopy to assess its defect content. Nevertheless, it can be assumed that the nanotube, as it was taken from the S1 sample, has a length which is within the average for the S1 sample (i.e. l$_{mean}$ = 4.6 ± 2.75 µm), whilst its outer diameter (40 nm) is larger than the average (d$_{o, mean}$ = 26.3 ± 8.1 nm). As discussed in Subsection 5.3.2.1.1, the longer the length and larger the diameter the

greater the probability of defects occurring. Consequently, there is a high probability that the type+content of defects in the nanotube tested is similar to that observed for the S1 sample. That is, the nanotube contains structural and lattice disorder defects, Fe-based catalyst, low content of a-C and a Raman ratio $I_D/I_G = 0.7 \pm 0.03$.
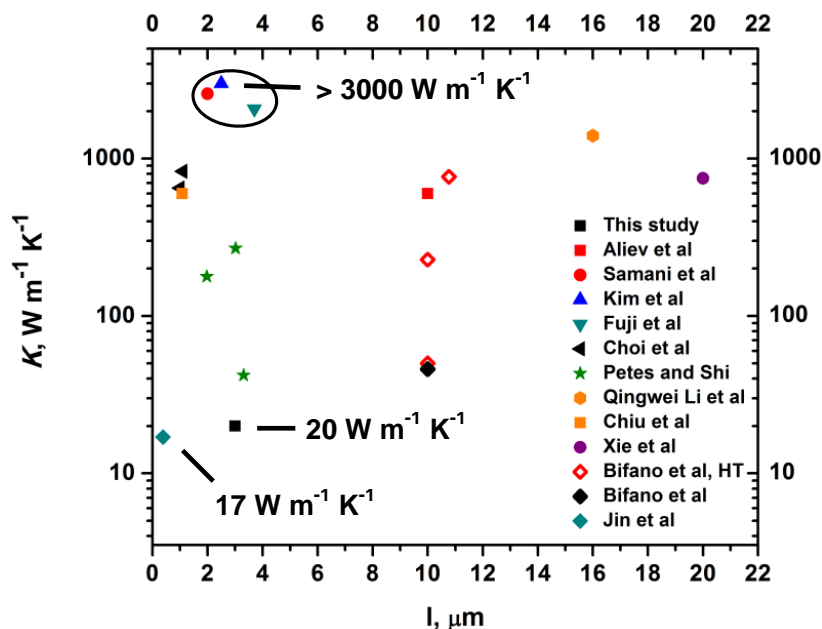
Fig. 5.11 Comparison between the thermal conductivity of the S1 MWCNT tested in this study with the published experimental thermal conductivity of individual MWCNTs[29,37,54,83–92]. Open symbols represent heat-treated (HT) individual MWCNTs.

Bifano et al[37] tested the thermal conductivity of individual CVD MWCNTs via the "T-type probe method", which is an extension of the self-heating technique. The thermal conductivity was obtained for "as-received" and "heat-treated" (at 3000 °C for 20h) MWCNTs, as given in Fig. 5.11 (denoted as closed and open rhombohedral symbols, respectively).

In their study the "as-received" individual MWCNTs gave a Raman ratio (I_D/I_G) of 0.7 ± 0.15 (similar to that of the S1 sample in this study) and an average thermal conductivity of 46 ± 29 W m^{-1} K^{-1}, therefore it was expected that the average K of the S1 MWCNTs would be similar.

In contrast, the heat-treated MWCNTs, exhibited a Raman ratio (I_D/I_G) of 0.2 ± 0.05 and an average thermal conductivity of 228 ± 149 W m^{-1} K^{-1}. In fact, the highest thermal conductivity in their study was 765 ± 153 W m^{-1} K^{-1} for a heat-treated nanotube with an outer diameter of 35 ± 4 nm, a 10.15 nm inner diameter, and a length of 10.77 ± 0.04 μm. Also, it was the straightest of all samples measured and had the least number of visible physical defects. Nevertheless, (despite heat-treatment) a sample of individual nanotubes where severe defects were not removed gave an average thermal conductivity of 50 ± 28 W m^{-1} K^{-1}. This show how detrimental is the effect of defects on thermal conductivity of the nanotubes.

In Bifano's et al study the quality of the "as-received" nanotubes and their resultant thermal conductivity are similar to that of the S1 sample. This emphasises the effect of a high content of defects and impurities present, in common CVD synthetized MWCNTs on their thermal conductivity. This limits the capabilities of these MWCNTs in attaining values as high as those reported in the literature (>3000 W m^{-1} K^{-1}) and restricts their suitability for use in heat management applications.

Comparing the value obtained in this study with that from Bifano et al's study demonstrates the potential of the SThM and FEM technique in obtaining thermal conductivity values for individual nanotubes. This technique also has several advantages, given in Table 5.6, in comparison to most of the current techniques employed (see Chapter 2, Subsection 2.3.2.6.1). The main advantage is that it is a less complex, laborious and cheaper method than those typically used for this purpose, as there is no need for the fabrication of microdevices.[96] However, several problems still need to be solved, such as nanotube movement during scanning. The technique is only in its infancy and, therefore, further development and optimization is still required.

Currently there are no standard procedures to acquire the thermal conductivity of nanomaterials due to the complex nature of this class of materials.[34] The author believes that advanced characterisation results from MWCNTs in order to acquire data on the morphology, quality and purity to input into a model to determine thermal conductivity of individual MWCNTs can be combined with the SThM +FEM results (as

suggested in Subsection 5.3.2.1.1). These methods could be employed together to develop a standard method to acquire not only the thermal conductivity of MWCNTs but the thermal conductivity of many other types of nanomaterials.

Table 5.6 Advantages and disadvantages of the SThM+FEM technique to determine the thermal conductivity of individual MWCNTs**.**

Advantages
• Simpler and less laborious method
• No need for expensive microdevices
• Simple sample preparation
• No need for stable, repeatable thermal contact to the ends of the sample
• No need for nanotubes alignment to the thermal probe
• Possible to determine nanotube geometry (length and outer diameter only)
• No need for high thermal isolation
• Determines heat loss both through the sample and surroundings

Disadvantages
• Nanotubes movement during scanning (sample preparation needs improvement)
• Not possible for in-situ assessment of the nanotube quality and purity.
• Not possible to determine nanotube inner diameter
• It is still in the preliminary stage.

Summary:

Morphology and quality

❖ The characterisation results demonstrate that the three MWCNT samples acquired from different sources were found to have very distinct morphologies, qualities and purities despite the fact that two samples were synthetized using the same technique (CCVD).

❖ If considering only the effect of morphology, quality and purity of the nanotubes studied, the average K of the individual MWCNTs is expected to be the highest for the S1 sample, followed by the S3 and lastly the S2 sample. Therefore, MWCNTs for high K applications should be carefully selected and must exhibit the smallest lengths and diameters possible, and contain a low defect concentration and have high crystallinity with no impurities.

❖ The development of a model using the characterisation results would enable the K of a sample of MWCNTs from any source to be estimated only through their characterisation.

Thermal Conductivity of an individual S1 MWCNT

❖ The use of the SThM + FEM technique allowed the K of an individual S1 MWCNT to be determined. From the data a combined value of $K_{MWCNT,1,2}$ ~ 20 W m^{-1} K^{-1} was obtained. The low value was attributed to the nanotube large length and outer diameter of the nanotube which increases the probability of defects thus resulting in diffusive heat conduction regime.

❖ The main advantage of the SThM + FEM technique is that it is less complex and laborious, and id a cheaper method than those typically used for this purpose. However, further development and optimization is still required.

❖ A thermal conductivity model based on the characterisation and SThM + FEM of the nanotubes could be used to develop a standard method to acquire not only the thermal conductivity of MWCNTs but also many other types of nanomaterials.

5.3.2.2 Effective Thermal Conductivity of Al/MWCNT Composites

In this section the experimental thermal conductivity (K_c) of the Al/MWCNT composites, also denoted Al/Cu10S1 (i.e. Al3Mg alloy reinforced with pure Cu ball-milled with 10wt.% S1 MWCNTs) produced via rheocasting and rheocasting followed by equal channel extrusion (ECAE) are discussed by comparing findings with the published in existing literature.

The experimental data was also compared with various theoretical models to determine if the models can predict the effect of filler thermal conductivity according to the value given by the manufacturer and that acquired in this study using the SThM+FEM technique. The filler density types are also compared in order to determine whether or not the S1 MWCNTs give a positive thermal contribution to the Al3Mg composite material. Three thermal conductivity models were used in this study; the Maxwell-Garnett effective medium approach (MG-EMA), Nan et al simple model, and the Hatta-Taya Eshelby model. Both the MG-EMA and Nan et al simple models simulate individual MWCNTs dispersed+orientated randomly within the Al matrix, whereas, the Hatta-Taya Eshelby model is used to simulate aligned nanotubes and spherical particles (bundles).

5.3.2.2.1 Comparison with Literature

The experimental thermal conductivity results from the Al/MWCNT composites processed via rheocasting + ECAE indicate that it is possible to improve the thermal conductivity of the Al3Mg alloy by adding MWCNTs as results show that an improvement of ~ 5.7 % was achieved.

In order to produce ultra-high thermal conductivity composites via rheocasting + ECAE, it is clear that to obtain the best thermal contribution from the nanotubes, they need to be fully dispersed within the matrix. The formation of intermetallics around the nanotubes, and nanotube damage during ECAE must also be avoided.

Only a few studies have examined the thermal conductivity of Al matrix composites reinforced with MWCNTs and to the author's best knowledge there has been no data published on Al/MWCNTs composites produced via rheocasting or rheocasting followed

by ECAE. Determining the real thermal conductivity of a sample of MWCNTs that are used to produce Al matrix composites and using it in theoretical models to compare with the experimental results in order to understand the real contribution of these fillers to Al alloys, has also to the author's best knowledge, not been reported. This highlights the novelty and importance of the work undertaken in this thesis.

Fig. 5.12 shows a comparison of the variation in experimental thermal conductivity (K_c) attained in this study with the limited published thermal conductivity values for Al/MWCNTs composites. The data used to plot the graph is given in Table 5.7.
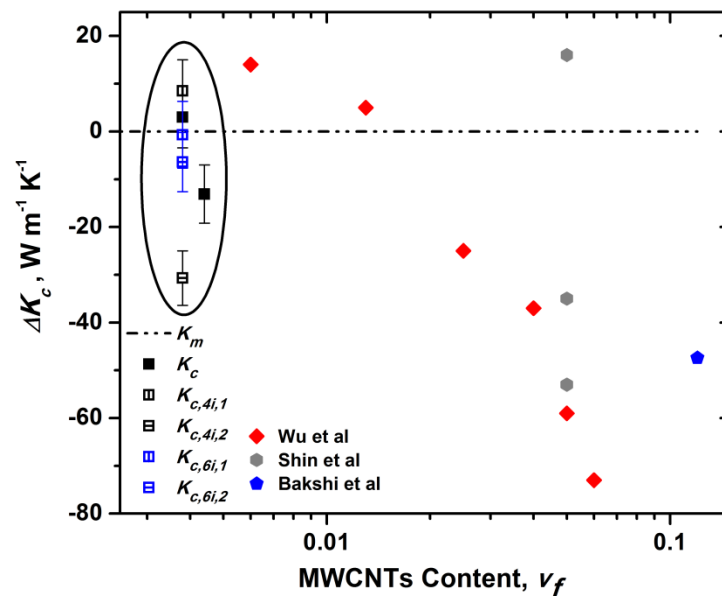
Fig. 5.12 Experimental thermal conductivity variation in the Al/Cu10S1 composites processed via rheocasting and ECAE (data given in Tables 4.18 and 4.19 and 5.7) compared with the reference Al3Mg alloy and the thermal conductivity variation of other published Al/MWCNTs composites (note: no standard deviations were given in the published articles).[102–104]

The M1 composite with a MWCNT content of v_f = 0.0038 produced via rheocasting registered an increase, $\varDelta K_c$ = 3 ± 6.4 W m^{-1} K^{-1} (~ 2 %), in comparison with the reference (M0 = K_m) (see Table 5.7 and Fig. 5.12). Whereas, the M2 composite with higher MWCNTs content, v_f = 0.0044, showed a substantial decrease, $\varDelta K_c$ = - 13.1 ±

6.1 W m^{-1} K^{-1} (~ - 8.8%). A similar trend, i.e. decrease in K_c with an increase in MWCNT content (v_f) was observed by Wu et al[102] (see Table 5.7). In their study the Al/MWCNTs were produced via spark plasma sintering (SPS) and the MWCNTs filler content (v_f) ranged from 0 to 0.06 (according to ρ_{real}). A maximum contribution of ΔK_c = 14 W m^{-1} K^{-1} (~ 7.6 %) was achieved for a MWCNT content of v_f = 0.006, however, for further filler content increases the thermal conductivity decreased, reaching a negative contribution of ΔK_c = - 59 W m^{-1} K^{-1} (~ - 32 %)) for a MWCNT content of v_f = 0.06.

Table 5.7 Experimental thermal conductivity of the Al/MWCNTs composites from this study and the few values obtained from the published literature.[102–104]

Sample	ΔK_c, W m^{-1} K^{-1}	K_c, W m^{-1} K^{-1}	K_m, W m^{-1} K^{-1}	S1 MWCNTs		Material	Method
				v_f (ρ_{real})	w_f		
M0	---	---	148.4 ± 4.5	---	---	Al3Mg	Rheocasting
M1	3 ± 6.4	151.4 ± 4.5	148.4 ± 4.5	0.0038	0.0030	Al3Mg	Rheocasting
M1$_{4i,1}$	8.5 ± 6.5	156.9 ± 4.7	148.4 ± 4.5	0.0038	0.0030	Al3Mg +	Rheocasting
M1$_{4i,2}$	- 30 ± 5.7	117.7 ± 3.5	148.4 ± 4.5	0.0038	0.0030	Cu10S1	+
M1$_{6i,1}$	- 0.7 ± 7.0	147.7 ± 4.4	148.4 ± 4.5	0.0038	0.0030	Al3Mg +	ECAE
M1$_{6i,2}$	- 6.4 ± 6.2	142 ± 4.3	148.4 ± 4.5	0.0038	0.0030	Cu10S1	
M2	- 13.1 ± 6.1	135.3 ± 4.1	148.4 ± 4.5	0.0044	0.0035	Al3Mg + Cu10S1	Rheocasting
Bakshi et al	- 47.6	25.4	73	0.12	0.1	Al12Si	Plasma spraying
Shin et al	- 53	103	156	0.05	0.04	Pure Al	PM + Deformation
	+ 16	172	156	0.05	0.04		process
Wu et al	+ 14	199	185	0.006	0.005	Pure Al	SPS
	- 73	112	5	0.06	0.05		

Wu et al[102] claimed that the enhanced K_c was due to the bridging effect of the MWCNTs dispersed amongst the Al grains for the low filler content as the interfacial thermal resistance is still low. However, for higher v_f the formation of bundles and increase in thermal resistance reduces the thermal conductivity.

Bakshi et al[104] produced an Al/MWCNT composite via the plasma spray method, where a MWCNT addition of v_f = 0.12 resulted in a decrease in thermal conductivity of ΔK_c = - 47.6 W m^{-1} K^{-1} (~ -65 %) which was also attributed to the presence of MWCNT clusters. As demonstrated by Aliev et al[54], tube-tube interaction decreases the thermal

conductivity of the nanotubes at room temperature (see Chapter 2 Subsection 2.3.2.6). Thus, consequently, individual nanotubes conduct the thermal conductivity better and hence the larger the MWCNT bundle the lower its thermal conductivity. This phenomenon explains why the MWCNT agglomerations have a detrimental effect on the Al/MWCNTs K_c.

The O.M. and SEM observations for the M1 composite processed via rheocasting (Figs. 4.26 and 4.31) demonstrate that the improvement in K_c (~ 2%) occurred despite the MWCNTs being found in micron-sized agglomerates. It should thus be noted that the thermal conductivity improved irrespective of the expected detrimental effect due to the increase in Cu in solid solution (2.86 wt.%) as demonstrated in Fig. 5.2.[10]

The M2 composite, produced only by the rheocasting alone showed a K_c decrease of 8.8 % in comparison to the matrix alloy. According to the microscopy results the decrease is due to the nanotubes being dispersed throughout the matrix in agglomerates, even though they are smaller and better distributed in this composite than the M1 composite (see Fig. 4.26 and 4.31). The agglomerates were normally found inside low thermal conductivity intermetallics, mainly AlCuMg and to lesser extent AlCuFe intermetallics (see Figs 4.31 d), e) and f) and Tables 4.17 and 5.2). The presence of the intermetallic further increases the thermal resistance between the filler and the matrix leading to a further decrease in the thermal conductivity of the composite.

The M1 composite was also subjected to ECAE post-processing. Here, the thermal conductivity increases even further after processing with 4 iterations in the in-plane direction (M1$_{4i,1}$), ($\Delta K_{c,M1,4i,1}$= 8.5 ± 6.5 W m^{-1} K^{-1}), (see Table 5.7), resulting in an increase of ~ 5.7% in comparison to the reference M0, and ~ 3% in comparison to the same sample that was only subjected to rheocasting. It can therefore be deduced that, the improvement observed is mainly due to micro-porosity removal, as verified in Fig. 5.7. However, the effect of agglomerate deformation and alignment, aligning the nanotubes within the composite in the deformation direction, as shown in Fig. 4.34 a) and b), may also play a role.

Shin et al[103] produced Al/MWCNTs with a MWCNT content of v_f = 0.05 via a powder metallurgy route involving a ball-milling technique. They managed to achieve a 10.2 % increase in thermal conductivity (ΔK_c = 16 W m^{-1} K^{-1}) accompanied also by an increase in electrical conductivity in comparison to the pure Al powder (matrix). This was achieved as the MWCNTs were dispersed in a "network", acting as channels for the conduction of electrons or phonons. A similar phenomenon may also occur for the M1$_{4i,1}$ composite as the nanotubes agglomerates are aligned during deformation. However, Shin's results contradict Aliev's[54] study that proves that tube-tube interaction decreases the thermal conductivity of the MWCNTs.

Shin and Aliev works indicate that it may be beneficial to have a percolation network comprised of a small number of MWCNTs where their thermal conductivity contribution is still higher than that for individual nanotubes dispersed in the matrix, as the latter means more boundaries/phonon scattering. Therefore, it is necessary to determine if better to have individually dispersed nanotubes in the matrix or a percolation network, and if the latter, what would be the ideal number of nanotubes in mutual contact contained in the network.

A significant drop (20.7 %) in the thermal conductivity is observed for the M1 composite after 4 iterations in the out-of-plane direction (M1$_{4i,2}$) , $\Delta K_{c,M1,4i,2}$ = - 30.7 W m^{-1} K^{-1}, which may be attributed to the anisotropic nature of the MWCNTs. However, after 6 iterations the thermal conductivity of the composites, both M1$_{6i,1}$ and M1$_{6i,2}$ evolve in the opposite direction (in comparison to M1$_{4i,1}$ and M1$_{4i,2}$) (see Fig. 4.39). The thermal conductivity of the M1$_{6i,1}$ is basically the same as the matrix ($\Delta K_{c,M1,6i,1}$ = - 0.7 W m^{-1} K^{-1}). Whereas, M1$_{6i,2}$ sample despite showing a higher thermal conductivity than M1$_{4i,2,}$ is still ~ 4.3 % below the value of the reference ($\Delta K_{c,M1,6i,2}$ = - 6.4 W m^{-1} K^{-1}).

In the ECAE processed samples, the porosity content remains unchanged after 4 iterations, but the increased deformation causes further deformation of the agglomerates and alignment of the nanoparticles. In both M1$_{6i,1}$ and M1$_{6i,2}$ samples, agglomerates less than 100 nm thick and even individual nanotubes were observed dispersed within the matrix (see Figs. 4.34 c) and d) and Fig. 4.35). As discussed in the

Subsection 5.3.2.1.1, the reduced bundle size and individual nanotubes dispersed in the matrix should increase the thermal conductivity. Nevertheless, this does not occur and could be due to the result of damage induced on the MWCNTs by the ECAE method as depicted in Fig. 4.35. This was despite the nanotubes matrix intimate contact which was expected to improve electron and phonon scattering.

The thermal conductivity results from the Al/Cu10S1 composites appear to indicate that it is possible to improve the thermal conductivity of the Al3Mg alloy by processing Al/MWCNTs via combining rheocasting with ECAE, however it is not fully understood why this happens Nevertheless, it is clear that to obtain the best thermal contribution from the nanotubes, it is necessary to: determinate which is more beneficial to the composite thermal conductivity, if individual or a network of nanotubes within the matrix; a trade-off between porosity closure, matrix deformation and nanotube damage during ECAE and; no intermetallics formation around the nanotubes

Therefore, it is necessary to perform detailed experiments to acquire more data, to fully understand the mechanism of how the thermal conductivity of Al and Al alloys can be increased using MWCNTs.

Finally, this discussion exposes the premature stage of the development and understanding of the effect of MWCNTs fillers within Al and its alloys on the thermal conductivity of Al/MWCNTs composites as a means to potentially produce future ultra-high thermal conductivity ($K \geq 400$ W m^{-1} K^{-1}) material for heat management applications.

5.3.2.2.2 Comparison with Theoretical Models

The comparison of the "corrected" (porosity excluded) experimental thermal conductivity of the composites with the theoretical models, taking into account the models limitations, the composites microstructure characterisation results, the quality and purity of the MWCNTs and the SThM+FEM results, indicate that the comparison assuming a bulk density for the worst case scenario (i.e. $K_{MWCNTs,1} = 20$ W m^{-1} K^{-1}) are the realistic conditions. Therefore, it further supports the results that indicate that the K of the

MWCNTs used for the composite processing is much lower than that claimed by the manufacturer. However, its value is higher than the thermal conductivity of the matrix (K_m), which is possible as the value obtained by the SThM+FEM is a combined value, therefore the in-plane value is higher than 20 W m^{-1} K^{-1}.

In the previous section the experimental conductivity of the Al/Cu10S1 was discussed without any correction factor (no porosity volume fraction correction). In this section, the effect of porosity content (φ) in the Al3Mg matrix and for each composite sample was accounted for according to eq. 23 (Chapter 3 Subsection 3.5.3) and designated as the corrected experimental thermal conductivity of the composites, K_c^{corr}, (see Table 4.20). The theoretical condition (no porosity correction) was not discussed here, as in general, the corrected condition is in better agreement with the models, as demonstrated in Chapter 4 Subsection 4.3.5.4.

This discussion involves the use of namely the Hatta-Taya[79,80], MG-EMA[105] and Nan et al[105] (which is an extension of the MG-EMA model, see Chapter 2 Section 2.5) two dimensional (2D) theoretical models for two scenarios according to the MWCNTs in-plane thermal conductivity: 1) Best case scenario (2000), when the in-plane (longitudinal) K of the MWCNTs ($K_{MWCNTs,1}$) is 2000 W m^{-1} K^{-1}, value given by the manufacturer; 2)Worst case scenario (20), when the $K_{MWCNTs,1}$ is 20 W m^{-1} K^{-1}, the value obtained using the SThM+FEM method. The designation for the different models used according to the MWCNTs configuration within the matrix (see Chapter 2 section 2.5 for designations description) is given in Table 5.8.

The theoretical values were compared with the K_c^{corr} which considers the MWCNTs real (ρ_{real}) and bulk (ρ_{bulk}) densities, as shown in Fig. 5.13. Real density accounts for volume of the nanotubes but excludes the pore/open space volume, whereas bulk density considers the volume of the nanotubes and the volume of the pores/void space between nanotubes.[34]

Table 5.8 The theoretical K models and designations used to simulate different MWCNTs configurations distributed homogeneously and individually within the matrix for the best (2000) and the worst (20) case scenarios: Hatta-Taya model for aligned nanotubes in the in-plane, high boundary ($K_{c,1}$, HB); out-of-plane direction, low boundary ($K_{c,2} = K_{c,2,r}$, LB); nanotubes randomly aligned within in-plane direction, high boundary ($K_{c,1,r}$, HB); spheres to represent bundles of nanotubes high boundary ($K_{c,s,2000}$, HB); and low boundary ($K_{c,s,20}$, LB); and MG-EMA and Nan et al models for randomly orientated nanotubes ($K_{c,MG-EMA}$ and $K_{c,Nan}$).

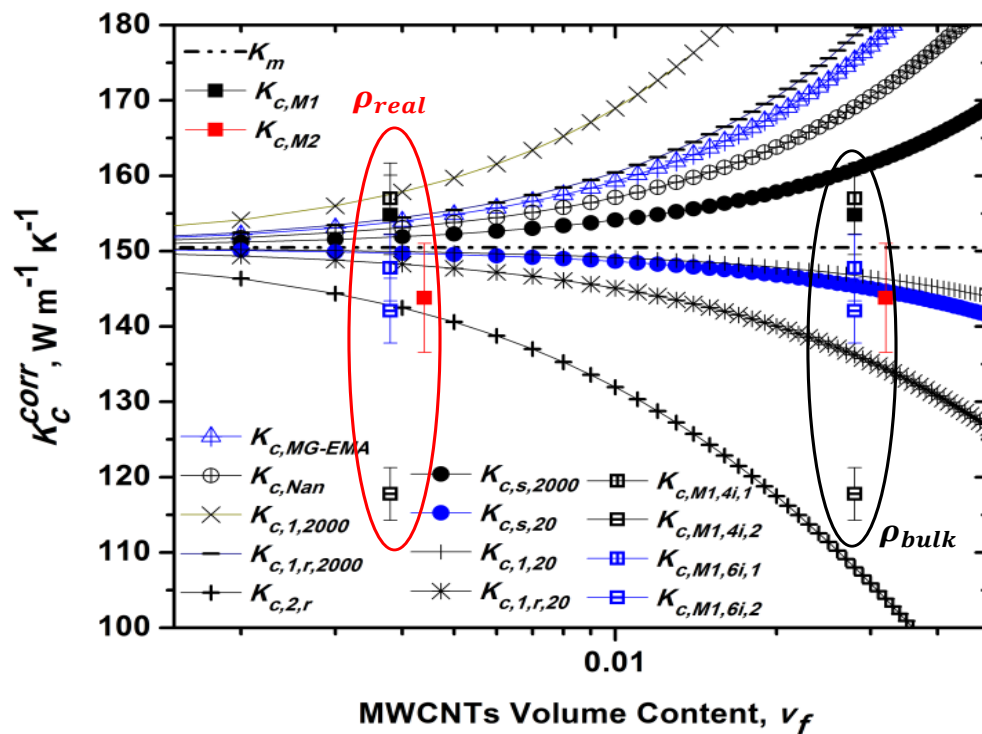| Models	Aligned		Random	Spheres (Bundles)	
	HB	LB		HB	LB
Hatta-Taya	$K_{c,1,2000}$	$K_{c,2,r}$	---	$K_{c,s,2000}$	$K_{c,s,20}$
	$K_{c,1,20}$	---	---	---	---
	$K_{c,1,r,2000}$	---	---	---	---
	$K_{c,1,r,20}$	---	---	---	---
Nan	---	---	$K_{c,Nan}$	---	---
MG-EMA	---	---	$K_{c,MG-EMA}$	---	---

Fig. 5.13 Comparison of K_c^{corr} according to ρ_{real} and ρ_{bulk} densities with respect to the 2D thermal conductivity Hatta-Taya, and MG-EMA and Nan et al (extension of MG-EMA model) models. Data extracted from Tables 4.20, 4.21, 4.22, 4.23 and 4.24.

Comparison of the agreement between the theoretical and experimental values was performed and the results are given in Tables 5.9 and 5.10 with respect to ρ_{real} and ρ_{bulk} densities, respectively. Results were considered to be in good agreement (✔) when the difference between values is ≤ ± 2 W m^{-1} K^{-1}, fair (O) when ± 2 < O ≤ ± 4 W m^{-1} K^{-1} and bad (✗) when > ± 4 W m^{-1} K^{-1}. The comparison

Table 5.9 Comparison of the agreement between the theoretical thermal conductivity models for different MWCNTs configurations within the matrix with the corrected experimental thermal conductivity values (K_c^{corr}) according to the real density (ρ_{real}). Good (✔) when ≤ ± 2 W m^{-1} K^{-1}, fair (O) when ± 2 < O ≤ ± 4 W m^{-1} K^{-1} and bad (✗) agreement when > ± 4 W m^{-1} K^{-1}.

Sample	Hatta-Taya							MG-EMA	Nan
	$K_{c,1,2000}$	$K_{c,1,r,2000}$	$K_{c,s,2000}$	$K_{c,1,20}$	$K_{c,1,r,20}$	$K_{c,s,20}$	$K_{c,2,r}$	$K_{c,MG-EMA}$	$K_{c,Nan}$
M1	✔	✔	O	✗	✗	✗	✗	✔	✔
M2	✗	✗	✗	✗	✗	✗	✔	✗	✗
M1$_{4i,1}$	✔	O	---	✗	✗	---	---	---	---
M1$_{4i,2}$	---	---	---	---	---	---	✗	---	---
M1$_{6i,1}$	✗	✗	---	O	✔	---	---	---	---
M1$_{6i,2}$	---	---	---	---	---	---	O	---	---

Table 5.10 Comparison of the agreement between the theoretical thermal conductivity models for different MWCNTs configurations within the matrix, with the corrected experimental thermal conductivity values (K_c^{corr}) according to the bulk density (ρ_{bulk}). Good (✔) when ≤ ± 2 W m^{-1} K^{-1}, fair (O) when ± 2 < O ≤ ± 4 W m^{-1} K^{-1} and bad (✗) agreement when > ± 4 W m^{-1} K^{-1}.

Sample	Hatta-Taya							MG-EMA	Nan
	$K_{c,1,2000}$	$K_{c,1,r,2000}$	$K_{c,s,2000}$	$K_{c,1,20}$	$K_{c,1,r,20}$	$K_{c,s,20}$	$K_{c,2,r}$	$K_{c,MG-EMA}$	$K_{c,Nan}$
M1	✗	✗	✗	✗	✗	✗	✗	✗	✗
M2	✗	✗	✗	O	✗	✔	✗	✗	✗
M1$_{4i,1}$	✗	✗	---	✗	✗	---	---	---	---
M1$_{4i,2}$	---	---	---	---	---	---	✗	---	---
M1$_{6i,1}$	✗	✗	---	✔	✗	---	---	---	---
M1$_{6i,2}$	---	---	---	---	---	---	✗	---	---

Let us assume that, in an ideal situation the rheocasting technique was able to individually disperse the MWCNTs within the Al matrix and that the MWCNTs had a thermal conductivity of 2000 W m^{-1} K^{-1} (best case scenario), then one would expect the M1 and M2 sample to be in good agreement with $K_{c,MG-EMA}$ and $K_{c,Nan}$ predictions.

However, microscopy characterisation has shown that the nanotubes are found in agglomerates, therefore, one would expect the samples to be in good agreement with Hatta-Taya's $K_{c,s,2000}$.

However, the M1 sample is in good agreement with the $K_{c,MG-EMA}$ and $K_{c,Nan}$ which both consider the best case scenario according to ρ_{real} (see Fig. 5.13 red ellipse) no pores between nanotubes. Whereas, the M2 sample is in good agreement with $K_{c,s,20}$, that considers that the MWCNTs are in bundles having a thermal conductivity of 20 W m^{-1} K^{-1}, worst case scenario according to ρ_{bulk} (see Fig. 5.13 black ellipse), i.e. the presence of pores between nanotubes).

Now, if we assume that using the combination of rheocasting+ECAE techniques it was possible to disperse and align individually the nanotubes within the matrix. In the best case scenario, one would expect that the M1$_{4i,1}$ and M1$_{6i,1}$ samples, for the in-plane direction to be in good agreement with $K_{c,1,2000}$ and $K_{c,1,r,2000}$. Whereas, the M1$_{4i,2}$ and M1$_{6i,2}$ samples for the out-of-plane direction should be in good agreement with the $K_{c,2,r}$ (only 10 W m^{-1}K^{-1}). This is the case for M1$_{4i,1,}$ result which was found to be in good agreement with $K_{c,1,2000}$ according to the ρ_{real}, even though some MWCNTs were found in bundles but elongated due to deformation. However, M1$_{4i,2}$ was not in agreement with any models for both ρ_{real} and ρ_{bulk}.

Sample M2, also shows good agreement in accordance with ρ_{bulk}. Whereas, the samples M1$_{6i,1}$ and M1$_{6i,2}$ show good agreement with $K_{c,1,20}$ (worst case scenario) and $K_{c,2,r}$, respectively.

The comparison of M1 and M1$_{4i,1}$ samples with the theoretical models suggest that it is possible that the MWCNTs have $K_{MWCNTs,1}$ = 2000 W m^{-1} K^{-1}. However, the models consider that the nanotubes are homogeneously and individually dispersed within the matrix, and also do not take into account the interfacial thermal barrier resistance (R_{BD}), which does not correspond to the reality.[79,80,105] Also, when assuming the real density condition, it is assumed that there is no pores and open spaces between nanotubes, which is not true as they are found in bundles, and even after ECAE not all the

nanotubes will become individually dispersed and have an intimate contact with the matrix resulting in micro and nano pores.

Additionally, the characterisation of the S1 MWCNTs, discussed in Subsection 5.3.2.1.1, indicates that according to the morphology and quality results the nanotubes should have very low thermal conductivity. This is supported by the SThM+FEM technique (Subsection 5.3.2.1.2), which gives a combined thermal conductivity of $K_{MWCNT,1-2}$ = 20 W m^{-1} K^{-1}. The facts described above give strong evidence that the MWCNTs in-plane thermal conductivity is definitely smaller than that claimed by the manufacturer (2000 W m^{-1} K^{-1}).

The results discussed above in general indicate that the comparison according to ρ_{bulk} as shown in Fig. 5.13 within a black ellipse for the worst case scenario are more realistic. For example, the M2 sample, as expected, was in good agreement with this condition since the nanotubes were in bundles. These bundles according to the published literature should a have low K, between 2.5 to 150 W m^{-1}K^{-1} [54,93–95] (see Table 2.3), and are also surrounded by low K (ranging from 1.3 to 19 W m^{-1} K^{-1} [56,57]) intermetallics (see Table 5.2), therefore more realistic. The M1$_{6i,1}$ and M1$_{6i,2}$ are also closer to the reality because the increased ECAE iterations caused damage to the nanotubes (see Fig. 4.35) decreasing their K even though they were found individually aligned and in intimate contact with the Al matrix.

Note that the K of the M1 and M1$_{6i,1}$ samples are still above K_m (reference M0), which also indicates that the nanotubes give a positive contribution to the composites. Therefore, the measured K of the nanotubes is higher than the matrix, which is possible as the value obtained by the ShTM+FEM is a combined value, i.e. the in-plane value is higher than 20 W m^{-1} K^{-1} but still lower than the 2000 W m^{-1}K^{-1} claimed by the manufacturer.

Despite the fact that the models seems to be in better agreement when considering bulk density, due to the reduced number of experimental results it is not possible to validate

this claim. Therefore, the processing set-up needs to be improved and more data (from individual nanotubes and composites) needs to be collected.

Nevertheless, the comparison of the experimental data with the models exposed two main limitations that hinder the prediction of the thermal conductivity by the models:

- I.   Lack of the real thermal conductivity of the MWCNTs sample to be used in the composite

- II. Type of density (real or bulk) to be used in the model due to the presence of micro and nano porosity.

According to Saravanan and Surrappa et al[62], using rheocasting it is possible to add up to v_f = 0.3 of fillers. If the nanotubes have a thermal conductivity of $K_{MWCNTs,1}$= 2000 W m^{-1}K^{-1} and are homogeneously and individually dispersed in the Al3Mg matrix then the composite thermal conductivity is predicted to be between $K_{c,Nan}$~ 351 W m^{-1} K^{-1} and $K_{c,MG-EMA}$~ 480 W m^{-1} K^{-1} which can be even higher if the nanotubes are aligned within the matrix $K_{c,1,r,2000}$ ~ 497 W m^{-1}K^{-1}. Therefore, in order to process ultra-high ($K \geq 400$ W m^{-1} K^{-1}) thermal conductivity materials via rheocasting+ECAE it is imperative that the $K_{MWCNTs,1} \geq 2000$ W m^{-1} K^{-1}.

Therefore, this study indicates that in order to produce Al/MWCNTs with an ultra-high thermal conductivity (i.e. $K > 400$ W m^{-1} K^{-1}) it is essential to overcome the following milestones:

- I.   The selection of high quality/thermal conductivity MWCNTs according to description in Subsection 5.3.2.1.1 and acquisition of the real (measured) thermal conductivity of the MWCNTs.

- II. Selection of a processing method capable to homogeneously disperse and align individual nanotubes with an intimate contact with matrix.

- III. Elimination or reduction of MWCNT/matrix interfacial resistance, i.e. interfacial reaction products that hinders electron and phonon mean free path.

Summary:

Comparison with literature

❖ The thermal conductivity (K) of the Al/MWCNTs composites has to date not been studied in depth and to the author's best knowledge there is no published data on Al/MWCNTs composites produced via rheocasting and rheocasting+ECAE. Therefore, this work is deemed to be highly novel and at the forefront of current scientific knowledge in this particular field.

❖ The attempt to obtain the real K from a MWCNT sample that have subsequently been used to produce Al/MWCNTs composites and from which experimental results were compared with theoretical models in order to understand the real contribution of these fillers to Al alloys, has to the author´s best knowledge, also never been reported.

❖ The experimental results from the Al/MWCNTs composites processed via rheocasting + ECAE appears to indicate that it is possible to improve the K of the Al3Mg alloy by adding MWCNTs as an improvement of ~ 5.7 % was achieved.

❖ In order to produce ultra-high thermal conductivity composites via rheocasting + ECAE, it is necessary to: 1) Determine which is more beneficial to the composite thermal conductivity, if individual or a network of nanotubes within the matrix; 2) A trade-off between porosity closure, matrix deformation and nanotube damage during ECAE; 3) No intermetallics formation around the nanotubes.

Comparison with Theoretical Models

❖ The comparison of the "corrected" (porosity excluded) experimental thermal conductivity of the composites with the theoretical models, taking into account the models limitations, the characteristics of composites microstructure, the quality and purity of the MWCNTs and the SThM+FEM findings, indicate that the comparison assuming the bulk density for the worst case scenario ($K_{MWCNTs,1}$ = 20 W m^{-1} K^{-1}) is the most realistic.

❖ This finding supports the hypothesis that the K of the MWCNTs used in the processing of the composite is much lower than that claimed by the manufacturer. However, its value is higher than the thermal conductivity of the matrix (K_m), which is possible as the value obtained by the ShM+FEM is a combined value, therefore the in-plane value must be higher than 20 W m^{-1} K^{-1}

❖ The models show that in order to produce ultra-high ($K \geq 400$ W m^{-1} K^{-1}) thermal conductivity materials via rheocasting+ECAE (for maximum volume of filler v_f = 0.3) it is imperative that the $K_{MWCNTs,1} \geq 2000$ W m^{-1} K^{-1}.

❖ This study thus indicates that in order to produce Al/MWCNTs with ultra-high thermal conductivity (K $\geq$ 400 W m^{-1} K^{-1}) it is essential to overcome the following milestones:

      I.   The selection of high quality/thermal conductivity MWCNTs.

     II.   Selection of a processing method capable to uniformly disperse and align individual nanotubes with intimate contact with matrix

    III.   Elimination or reduction of MWCNT/matrix interfacial resistance interfacial reaction products) that hinders the electron and phonon mean free path.

References

1.   Vitos, L., Ruban, A. V., Skriver, H. L. & Kollar, J. The Surface Energy of Metals. Surf. Sci. 411, 186–202 (1998).

2.   Nuriel, S., Liu, L., Barber, A. H. & Wagner, H. D. Direct Measurement of Multiwall Nanotube Surface Tension. Chem. Phys. Lett. 404, 263–266 (2005).

3.   Pai, B. C., Ramani, G., Pillai, R. M. & Satyanarayana, K. G. Role of Magnesium in Cast Aluminium Alloy Matrix Composites. J. Mater. Sci. 30, 1903–1911 (1995).

4.   Patel, J. B., Liu, Y. Q., Shao, G. & Fan, Z. Rheo-Processing of an Alloy Specifically Designed for Semi-Solid Metal Processing Based on the Al–Mg–Si System. Mater. Sci. Eng. A 476, 341–349 (2008).

5.   Okamoto, H. Supplemental Literature Review of Binary Phase Diagrams: Al-Mg, Bi-Sr, Ce-Cu, Co-Nd, Cu-Nd, Dy-Pb, Fe-Nb, Nd-Pb, Pb-Pr, Pb-Tb, Pd-Sb, and Si-W. J. Phase Equilibria Diffus. 36, 183–195 (2015).

6.   Lloyd, D. J. The Solidification Microstructure of Particulate Reinforced Aluminium/SiC composites. Compos. Sci. Technol. 35, 159–179 (1989).

7.   Lloyd, D. J. Particle Reinforced Aluminium and Magnesium Matrix Composites. Int. Mater. Rev. 39, 1–23 (1994).

8.   Lloyd, D. J., Lagacé, H. P. & Mcleod, A. D. in Controlled Interphases in Composite Materials (ed. Ishida, H.) 359–376 (Springer Netherlands, 1990).

9.   Rajan, T. P. D., Pillai, R. M. & Pai, B. C. Reinforcement Coatings and Interfaces in Aluminium Metal Matrix Composites. J. Mater. Sci. 33, 3491–3503 (1998).

10.   Ho, C. Y., Ackerman, M. W., Wu, K. Y., Oh, S. G. & Havill, T. N. Thermal Conductivity of Ten Selected Binary Alloy Systems. J. Phys. Chem. Ref. Data 7, 959–1178 (1978).

11.   Electronic Materials Handbook Volume 1: Packaging. (ASM International, 1989).

12.   Zweben, C. Advances in Composite Materials for Thermal Management in Electronic Packaging. Jom 50, 47–51 (1998).

13.   Davim, J. P. Metal Matrix Composites: Materials, Manufacturing and Engineering. (Walter de Gruyter GmbH & Co KG, 2014).

14.   Spencer, D. B., Mehrabian, R. & Flemings, M. C. Rheological Behavior of Sn-15 pct Pb in the Crystallization Range. Metall. Trans. 3, 1925–1932 (1972).

15.   Hirt, G., Kopp, R., Thixoforming: Semi-solid Metal Processing. (Wiley-VCH, 2009).

16.   Paul, E. L., Atiemo-Obeng, V. A. & Kresta, S. M. Handbook of Industrial Mixing: Science and Practice. (John Wiley & Sons, 2004).

17.   Ghosh, P. K. & Ray, S. Fabrication and Properties of Compocast Aluminium-Alumina Particulate Composite. Indian J. Technol. 26, 83–94 (1988).

18.   Bindumadhavan, P. N. et al. Effect of Particle-Porosity Clusters on Tribological Behavior of Cast Aluminum Alloy A356-SiCp Metal Matrix Composites. Mater. Sci. Eng. A 315, 217–226 (2001).

19.   Aqida, S. N., Ghazali, M. I. & Hashim, J. Effect of Porosity on Mechanical Properties of Metal Matrix Composite: An Overview. J. Teknol. 40, 17–32 (2012).

20.   Ahmad, S. N. The Effects of Porosity on Mechanical Properties of Cast Discontinuous Reinforced Metal-Matrix Composite. J. Compos. Mater. 39, 451–466 (2005).

21.   Bakshi, S. R., Lahiri, D. & Agarwal, A. Carbon Nanotube Reinforced Metal Matrix Composites - A Review. Int. Mater. Rev. 55, 41–64 (2010).

22.   Neubauer, E., Kitzmantel, M., Hulman, M. & Angerer, P. Potential and Challenges of Metal Matrix Composites Reinforced with Carbon Nanofibers and Carbon Nanotubes. Compos. Sci. Technol. 70, 2228–2236 (2010).

23.   Tjong, S. C., Recent Progress in the Development and Properties of Novel Metal Matrix Nanocomposites Reinforced with Carbon Nanotubes and Graphene Nanosheets. Mater. Sci. Eng. R Rep. 74, 281–350 (2013).

24.   Koppad, P. G., Singh, V. K., Ramesh, C. S., Koppad, R. G. & Kashyap, K. T. Metal Matrix Nanocomposites Reinforced with Carbon Nanotubes. Adv. Carbon Mater. Technol. 331–376 (2013).

25.   Deng, C. F., Wang, D. Z., Zhang, X. X. & Li, A. B. Processing and Properties of Carbon Nanotubes Reinforced Aluminum Composites. Mater. Sci. Eng. A 444, 138–145 (2007).

26.   Ci, L., Ryu, Z., Jin-Phillipp, N. Y. & Rühle, M. Investigation of the Interfacial Reaction Between Multi-Walled Carbon Nanotubes and Aluminum. Acta Mater. 54, 5367–5375 (2006).

27.   Dresselhaus, M. S., Dresselhaus, G. & Eklund, P. C. Science of Fullerenes and Carbon Nanotubes: Their Properties and Applications. (Academic Press, 1996).

28.   Balandin, A. A. Thermal Properties of Graphene and Nanostructured Carbon Materials. Nat. Mater. 10, 569–581 (2011).

29.   Kim, P., Shi, L., Majumdar, A. & McEuen, P. L. Thermal Transport Measurements of Individual Multiwalled Nanotubes. Phys. Rev. Lett. 87, (2001).

30.   Dillon, A. C. et al. A simple and Complete Purification of Single-walled Carbon Nanotube Materials. Adv. Mater. 11, 1354–1358 (1999).

31.   Bom, D. et al. Thermogravimetric Analysis of the Oxidation of Multiwalled Carbon Nanotubes: Evidence for the Role of Defect Sites in Carbon Nanotube Chemistry. Nano Lett. 2, 615–619 (2002).

32.   Lin, C.-P., Lin, J.-Z., Shu, C.-M. & Tseng, J.-M. Multi-Walled Carbon Nanotube Thermal Stability Characteristics Evaluation by DSC Tests. J. Loss Prev. Process Ind. 25, 302–308 (2012).

33.   DiLeo, R. A., Landi, B. J. & Raffaelle, R. P. Purity Assessment of Multiwalled Carbon Nanotubes by Raman Spectroscopy. J. Appl. Phys. 101, 64307 (2007).

34.   Lehman, J. H., Terrones, M., Mansfield, E., Hurst, K. E. & Meunier, V. Evaluating the Characteristics of Multiwall Carbon Nanotubes. Carbon 49, 2581–2602 (2011).

35.   Tucho, W. M. et al. The Effects of Ball Milling Intensity on Morphology of Multiwall Carbon Nanotubes. Scr. Mater. 63, 637–640 (2010).

36.   Poirier, D., Gauvin, R. & Drew, R. A. L. Structural Characterization of a Mechanically Milled Carbon Nanotube/Aluminum Mixture. Compos. Part Appl. Sci. Manuf. 40, 1482–1489 (2009).

37.   Bifano, M. F. P., Park, J., Kaul, P. B., Roy, A. K. & Prakash, V. Effects of Heat Treatment and Contact Resistance on the Thermal Conductivity of Individual Multiwalled Carbon Nanotubes Using a Wollaston Wire Thermal Probe. J. Appl. Phys. 111, 54321 (2012).

38.   Mahajan, A., Kingon, A., Kukovecz, Á., Konya, Z. & Vilarinho, P. M. Studies on the Thermal Decomposition of Multiwall Carbon Nanotubes Under Different Atmospheres. Mater. Lett. 90, 165–168 (2013).

39.   Ding, F., Bolton, K. & Rosén, A. Iron-Carbide Cluster Thermal Dynamics for Catalyzed Carbon Nanotube Growth. J. Vac. Sci. Technol. A 22, 1471–1476 (2004).

40.   Liu, J. et al. Synthesis and Magnetic Properties of Fe_3C–C Core–Shell Nanoparticles. Nanotechnology 26, 85601 (2015).

41.   He, Z. et al. Iron Catalysts for the Growth of Carbon Nanofibers: Fe, Fe_3C or Both?. Chem. Mater. 23, 5379–5387 (2011).

42.   Pellegrino, L. & Mazzocchia. Searching for Rate Determining Step of CNT Formation: The Role of Cementite. Chem. Eng. Trans. 32, 739–744 (2013).

43.   Cao, G. & Wang, Y. Nanostructures and Nanomaterials: Synthesis, Properties, and Applications. (World Scientific, 2011).

44.   Abbasipour, B., Niroumand, B. & Monir Vaghefi, S. M. Compocasting of A356-CNT Composite. Trans. Nonferrous Met. Soc. China 20, 1561–1566 (2010).

45.   Donthamsetty, S., Damera, N. R. & Jain, P. K. Ultrasonic Cavitation Assisted Fabrication and Characterization of A356 Metal Matrix Nanocomposite Reinforced with SiC, B_4C, CNTs. Asian Int. J. Sci. Technol. Prod. Manuf. Eng. 2, 27–34 (2009).

46.   Rashad, R. M., Awadallah, O. M. & Wifi, A. S. Effect of MWCNTs Content on the Characteristics of A356 Nanocomposite. J. Achiev. Mater. Manuf. Eng. 2, 74–80 (2013).

47.   Miranda, A. et al. Study of Mechanical Properties of an LM24 Composite Alloy Reinforced with Cu-CNT Nanofillers, Processed Using Ultrasonic Cavitation. Mater. Sci. Forum 765, 245–249 (2013).

48.   Marini, C. D. & Fatchurrohman, N. A Review on the Fabrication Techniques of Aluminium Matrix Nanocomposites. J. Teknol. 74, (2015).

49.   Elshalakany, A. B., Osman, T. A., Khattab, A., Azzam, B. & Zaki, M. Microstructure and Mechanical Properties of MWCNTs Reinforced A356 Aluminum Alloys Cast Nanocomposites Fabricated by Using a Combination of Rheocasting and Squeeze Casting Techniques. J. Nanomater. 2014, 1–14 (2014).

50.   Di Sabatino, M., Fluidity of Aluminium Foundry Alloys. (Norwegian University of Science and Technology, 2005).

51.   Mills, K. C., Recommended Values of Thermophysical Properties for Selected Commercial Alloys. (Woodhead, 2002).

52.   Belov, N. A., Eskin, D. G. & Aksenov, A. A., Multicomponent Phase Diagrams: Applications for Commercial Aluminum Alloys. (Elsevier, 2005).

53.   Mondolfo, L. F. Al–Cu–Mg Aluminum–Copper–Magnesium System. 497–505 (Butterworth-Heinemann, 1976).

54.   Aliev, A. E., Lima, M. H., Silverman, E. M. & Baughman, R. H. Thermal Conductivity of Multi-walled Carbon Nanotube Sheets: Radiation Losses and Quenching of Phonon Modes. Nanotechnology 21, 35709 (2010).

55.   Hsu, I.-K. et al., Optical Absorption and Thermal Transport of Individual Suspended Carbon Nanotube Bundles. Nano Lett. 9, 590–594 (2009).

56.   Landauro, C. V. & Solbrig, H., Modeling the Electronic Transport Properties of Al-Cu-Fe phases. Phys. B Condens. Matter 301, 267–275 (2001).

57.   Alboni, P. N. et al., Investigation of i-AlCuFe Quasicrystals and their ω and β Approximants as Thermoelectric Materials. in (2002).

58.   Terada, Y., Ohkubo, K., Mohri, T., Suzuki, T., Thermal Conductivity of Intermetallic Compounds with Metallic Bonding, Japan Inst. of Metals, Vol.43 No.12, pp.3167-3176 (2002)

59.   Popčević, P., Smontara, A., Dolinšek, J. & Gille, P., Anisotropic Transport Properties of the $Al_{13}Fe_4$ Decagonal Approximant. Croat. Chem. Acta 83, 101–105 (2010).

60.   LaBotz, R. J. & Mason, D. R., The Thermal Conductivities of Mg_2Si and Mg_2Ge. J. Electrochem. Soc. 110, 121–126 (1963).

61.   Li, W., Lindsay, L., Broido, D. A., Stewart, D. A. & Mingo, N. Thermal Conductivity of Bulk and Nanowire $Mg_2Si_xSn_{1-x}$ Alloys from First Principles. Phys Rev B 86, 174307 (2012).

62.   Saravanan, R. & Surappa, M., Fabrication and Characterisation of Pure Magnesium-30 vol.% SiC_P Particle Composite. Mater. Sci. Eng. A 276, 108–116 (2000).

63.   Bakshi, S. R., Keshri, A. K., Singh, V., Seal, S. & Agarwal, A., Interface in Carbon Nanotube Reinforced Aluminum Silicon Composites: Thermodynamic Analysis and Experimental Verification. J. Alloys Compd. 481, 207–213 (2009).

64.   Laha, T., Kuchibhatla, S., Seal, S., Li, W. & Agarwal, A., Interfacial Phenomena in Thermally Sprayed Multiwalled Carbon Nanotube Reinforced Aluminum Nanocomposite. Acta Mater. 55, 1059–1066 (2007).

65.   Zhu, X., Zhao, Y., Wu, M., Wang, H. & Jiang, Q., Effect of Initial Aluminum Alloy Particle Size on the Damage of Carbon Nanotubes during Ball Milling. Materials 9, 173 (2016).

66.   Forró, L. et al., Tuning the Length Dispersion of Multi-walled Carbon Nanotubes by Ball Milling. AIP Adv. 3, 92117 (2013).

67.   Soong, C., Woo, P. & Hoyle, D., Contamination Cleaning of TEM/SEM Samples with the ZONE Cleaner. Microsc. Today 20, 44–48 (2012).

68.   Amman, M. et al., Atomic Force Microscopy Study of Electron Beam Written Contamination Structures. J. Vac. Sci. Technol. B 14, 54–62 (1996).

69.   Agarwal, A., Bakshi, S. R. & Lahiri, D., Carbon Nanotubes: Reinforced Metal Matrix Composites. (CRC Press, 2010).

70.   Solórzano, E., Rodriguez-Perez, M. A. & de Saja, J. A., Thermal Conductivity of Cellular Metals Measured by the Transient Plane Sour Method. Adv. Eng. Mater. 10, 371–377 (2008).

71.   Casati, R. & Vedani, M., Metal Matrix Composites Reinforced by Nano-Particles - A Review. Metals 4, 65–83 (2014).

72. Pham, Q., Jeong, Y. G., Hong, S. H. & Kim, H. S., Equal Channel Angular Pressing of Carbon Nanotube Reinforced Metal Matrix Nanocomposites. Key Eng. Mater. 326–328, 325–328 (2006).

73. Song, P. C., Liu, C. H. & Fan, S. S., Improving the Thermal Conductivity of Nanocomposites by Increasing the Length Efficiency of Loading Carbon Nanotubes. Appl. Phys. Lett. 88, 153111 (2006).

74. ZwebenConsulting. Available at: https://sites.google.com/site/zwebenconsulting/. (Accessed: 15th March 2016)

75. Silvain, J.-F., Veillère, A. & Lu, Y., Copper-Carbon and Aluminum-Carbon Composites Fabricated by Powder Metallurgy Processes. J. Phys. Conf. Ser. 525, 12015 (2014).

76. Huang, X., Fabrication and Properties of Carbon Fibers. Materials 2, 2369–2403 (2009).

77. Prokofiev, E. A., Junior, A. M. J., Botta, W. J., Valiev, R. Z., Development of Ultrafine-Grained Metals by Equal-Channel Angular Pressing. Comp. Mat. Proc., Elsevier (2014)

78. Zhang, Y., Shen, Z. & Tong, Z., Thermal Conductivity and Interfacial Thermal Barrier Resistance of the Particle Reinforced Metal Matrix Composites. in Electronic Packaging Technology, 2007. ICEPT 2007. 8th International Conference on 1–4 (IEEE, 2007).

79. Hatta, H. & Taya, M., Effective Thermal Conductivity of a Misoriented Short Fiber Composite. J. Appl. Phys. 58, 2478 (1985).

80. Hatta, H., Taya, M., Kulacki, F. A. & Harder, J. F., Thermal Diffusivities of Composites with Various Types of Filler. J. Compos. Mater. 26, 612–625 (1992).

81. Marconnet, A. M., Panzer, M. A. & Goodson, K. E., Thermal Conduction Phenomena in Carbon Nanotubes and Related Nanostructured Materials. Rev. Mod. Phys. 85, 1295–1326 (2013).

82. Han, Z. & Fina, A., Thermal Conductivity of Carbon Nanotubes and their Polymer Nanocomposites: A review. Prog. Polym. Sci. 36, 914–944 (2011).

83. Dames, C. et al., A Hot-wire Probe for Thermal Measurements of Nanowires and Nanotubes Inside a Transmission Electron Microscope. Rev. Sci. Instrum. 78, 104903 (2007).

84. Xie, H., Cai, A. & Wang, X., Thermal Diffusivity and Conductivity of Multiwalled Carbon Nanotube Arrays. Phys. Lett. A 369, 120–123 (2007).

85. Chiu, H.-Y. et al., Ballistic Phonon Thermal Transport in Multiwalled Carbon Nanotubes. Phys. Rev. Lett. 95, (2005).

86.   Li, Q., Liu, C., Wang, X. & Fan, S., Measuring the Thermal Conductivity of Individual Carbon Nanotubes by the Raman Shift Method. Nanotechnology 20, 145702 (2009).

87.   Pettes, M. T. & Shi, L., Thermal and Structural Characterizations of Individual Single-, Double-, and Multi-Walled Carbon Nanotubes. Adv. Funct. Mater. 19, 3918–3925 (2009).

88.   Choi, T.-Y., Poulikakos, D., Tharian, J. & Sennhauser, U., Measurement of the Thermal Conductivity of Individual Carbon Nanotubes by the Four-Point Three-ω Method. Nano Lett. 6, 1589–1593 (2006).

89.   Choi, T. Y., Poulikakos, D., Tharian, J. & Sennhauser, U., Measurement of thermal conductivity of individual multiwalled carbon nanotubes by the 3-ω method. Appl. Phys. Lett. 87, 13108 (2005).

90.   Fujii, M. et al. ,Measuring the Thermal Conductivity of a Single Carbon Nanotube. Phys. Rev. Lett. 95, (2005).

91.   Kim, P., Shi, L., Majumdar, A. & McEuen, P. L., Mesoscopic Thermal Transport and Energy Dissipation in Carbon Nanotubes. Phys. B Condens. Matter 323, 67–70 (2002).

92.   Samani, M. K. et al., Thermal Conductivity of Individual Multiwalled Carbon Nanotubes. Int. J. Therm. Sci. 62, 40–43 (2012).

93.   Jin, R. et al., The Effect of Annealing on the Electrical and Thermal Transport Properties of Macroscopic Bundles of Long Multi-Wall Carbon Nanotubes. Phys. B Condens. Matter 388, 326–330 (2007).

94.   Yang, D. J. et al., Thermal Conductivity of Multiwalled Carbon Nanotubes. Phys. Rev. B 66, (2002).

95.   Yi, W., Lu, L., Dian-lin, Z., Pan, Z. W. & Xie, S. S., Linear Specific Heat of Carbon Nanotubes. Phys. Rev. B 59, R9015–R9018 (1999).

96.   Cahill, D. G., Goodson, K. & Majumdar, A., Thermometry and Thermal Transport in Micro/Nanoscale Solid-State Devices and Structures. J. Heat Transf. 124, 223 (2002).

97.   Zhang, G. & Li, B., Thermal Conductivity of Nanotubes Revisited: Effects of Chirality, Isotope Impurity, Tube Length, and Temperature. J. Chem. Phys. 123, 114714 (2005).

98.   Wang, C., Guo, S., Pan, X., Chen, W. & Bao, X., Tailored Cutting of Carbon Nanotubes and Controlled Dispersion of Metal Nanoparticles Inside Their Channels. J. Mater. Chem. 18, 5782 (2008).

99.   Andrews, R., Jacques, D., Qian, D. & Dickey, E. C., Purification and Structural Annealing of Multiwalled Carbon Nanotubes at Graphitization Temperatures. Carbon 39, 1681–1687 (2001).

100.   Hou, P.-X., Liu, C. & Cheng, H.-M., Purification of Carbon Nanotubes. Carbon 46, 2003–2025 (2008).

101.   Collins, P. G., Defects and Disorder in Carbon Nanotubes. Oxf. Handb. Nanosci. Technol. Front. Adv. (2010).

102.   Wu, J., Zhang, H., Zhang, Y. & Wang, X., Mechanical and Thermal Properties of Carbon Nanotube/Aluminum Composites Consolidated by Spark Plasma Sintering. Mater. Des. 41, 344–348 (2012).

103.   Shin, S., Choi, H. & Bae, D., Electrical and Thermal Conductivities of Aluminum-Based Composites Containing Multi-Walled Carbon Nanotubes. J. Compos. Mater. 47, 2249–2256 (2013).

104.   Bakshi, S. R., Patel, R. R. & Agarwal, A., Thermal Conductivity of Carbon Nanotube Reinforced Aluminum Composites: A Multi-Scale Study using Object Oriented Finite Element Method. Comput. Mater. Sci. 50, 419–428 (2010).

105.   Nan, C.-W., Shi, Z. & Lin, Y., A Simple Model for Thermal Conductivity of Carbon Nanotube-Based Composites. Chem. Phys. Lett. 375, 666–669 (2003).

Chapter 6

Conclusions and Future Work

6.1 Chapter Outline

This chapter outlines the conclusions drawn from the work presented in Chapters 4 and 5. Suggestions for further work have also been identified and are also outlined herein.

6.2 Conclusions

The overall goal of the thesis was to study the possibility of using multi-walled carbon nanotubes (MWCNTs) as composite fillers. They have an unusually high thermal conductivity (K ~ 3000 to 3500 W m^{-1} K^{-1}), suitable to produce ultra-high thermal conductivity ($K \geq$ 400 W m^{-1} K^{-1}) aluminium matrix composites (Al/MWCNTs) for advanced thermal management applications such HPLEDs. To produce the composites, a combination of rheocasting and ECAE techniques was employed.

The thermal conductivity of Al/MWCNTs composites has been scarcely studied in the past and to the author's best knowledge there is no data published on Al/MWCNTs composites produced via rheocasting and rheocasting+ECAE. Therefore, this underlines the novelty and importance of this work.

The attempt to obtain the real K (via the SThM+FEM technique) from the MWCNTs used to produce the Al/MWCNTs and to use this value in theoretical models in order to compare with the experimental results so as to understand the real contribution of these fillers to Al alloys, has to the author´s best knowledge, also not been reported, and is thus also novel.

263

6.2.1 Processing of the Composites

6.2.1.1 Rheocasting+ECAE

In this study, in order to assess the possibility of producing Al/MWCNTs composites with an ultra-high thermal conductivity ($K \geq 400$ W m^{-1} K^{-1}), a processing method consisting of two steps was tested. The 1st step, involved the use of the rheocasting technique to overcome the common difficulties found to introduce these fillers within the Al matrix. In the 2nd step, the ECAE technique was used to promote the alignment of the anisotropic MWCNTs within the matrix (which is randomly oriented after the rheocasting process) and also induce porosity closure which is highly detrimental to the thermal conductivity.

The work began by investigating Al matrix composites reinforced with Cu-coated pitch-based carbon fibres (Al/Cu-CFs) in order to test the suitability of the method selected. The CFs were selected because they are similar to the MWCNTs in several aspects such as; chemical composition, and thus have similar Al$_4$C$_3$ reaction products; reinforcing geometries; and, anisotropic thermal properties.

This study demonstrated that the rheocasting was efficient in introducing and dispersing the Cu-coated CFs (Cu-CFs) within the Al3Mg matrix. However, the porosity content of the composites produced increased by up to 5% for a CF filler content of up to 2 wt.%. It was found that the Cu coating promoted wettability of the fibres by the Al melt, improving filler dispersion via the formation of a MgO interfacial compound. There was no clear evidence of the formation of the deleterious interfacial Al$_4$C$_3$ compound, however, its formation in the matrix should not be discounted.

The subsequent processing of the Al/Cu-CFs composites (C1.5 composite samples) using the ECAE method showed good efficiency in removing porosity and achieving a high degree of fibre alignment with good fibre matrix interface surface consolidation. However, the severe deformation characteristic of the ECAE technique induced considerable damage on the fibres.

After the promising results of the processing of the Al/Cu-CFs composites, the same processing method was employed to produce Al/MWCNTs. The results showed that the use of rheocasting was also effective in introducing the mechanically alloyed composite powders (MWCNTs embedded in pure Cu denoted as Cu10S1) produced using the high energy ball-milling, within the Al matrix. However, the MWCNTs were found in large agglomerates.

The incorporation of the MWCNTs with pure Cu aided the introduction of the fillers within the Al matrix, which was further improved after the Cu solubility limit in Al was reached, when the MWCNTs agglomerates were surrounded by mainly AlCuMg intermetallics. However, deleterious Al_4C_3 was found in the composites which may have been induced by the *a*-C and defective sites present in the MWCNTs, prior to processing.

The rheocasting of the Al/MWCNTs composites using the described set-up and parameters in this study, was not effective for the production of ultra-high thermal conductivity materials as it did not manage to overcome the main processing challenges, namely, the full control of the introduction and dispersion of the MWCNTs into the matrix. This is in contrast to the findings for the Al/Cu-CFs composites.

The subsequent processing of the Al/MWCNTs composites (M1 composite samples) by ECAE, analogous to the results obtained for the Al/Cu-CFs composite samples, was also efficient at removing porosity and achieving a high degree of nanotubes alignment, with good nanotube matrix interface surface consolidation. However, the technique also induced considerable damage on the nanotubes, which may counteract the positive effect of the filler alignment on the composites thermal conductivity.

6.2.2 Thermal conductivity of the Composites

Understanding the effect of the employed processing method on individual phases formed within the composites has enabled their properties including thermal conductivity to be controlled. This is important if new composites are to be developed with properties that match that of the ultra-high thermal conductivity materials (required for heat management applications) especially when utilizing highly anisotropic C-based fillers.

For this, the thermal conductivity of the two composites systems produced in this study, Al/Cu-CFs and Al/MWCNTs, via rheocasting and rheocasting+ECAE, were assessed using the laser flash technique. Moreover, in order to assess the real thermal conductivity contribution of the fillers (CFs and MWCNTs) to the matrix alloy, the experimental thermal conductivity was compared with various theoretical models that take into account filler geometry, anisotropy and orientation.

6.2.2.1 Thermal Conductivity of the Al/Cu-CF Composites

The Al/Cu-CFs composites when processed by rheocasting alone did not improve the thermal conductivity of the composites when compared with the matrix alloy. In fact, the thermal conductivity of the composite with the highest filler content (C2 composite sample, 2 wt.%) was ~ 9% lower ($K_{c,C2}$ = 134.9 ± 4.1 W m^{-1} K^{-1}) than that of the reference matrix (Al3Mg, K_m = 148.4 ± 4.5 W m^{-1} K^{-1}). However, after 6 iterations of ECAE the composite thermal conductivity improved ~ 20 % (C1.5$_{6i,1}$ composite sample, $K_{c,C1.5,6i,1}$ = 153.7 ± 4.6 W m^{-1} K^{-1}) with respect to the "as-rheocasted" C1.5 composite ($K_{c,C1.5}$ = 128.5 ± 3.9 W m^{-1} K^{-1}). This value was also greater than the thermal conductivity of the matrix by 3.6%.

This improvement is believed to be due to, porosity reduction, fibre alignment and forced intimate contact of clean CF surfaces (no MgO) with the matrix. However, it is necessary to assess more composites produced by rheocasting+ECAE techniques for a wider range of fibre volume fractions, to fully validate its effectiveness in improving the thermal conductivity.

For comparison with the theoretical models the "corrected" experimental thermal conductivity condition (which accounts for the porosity volume fraction and real content of fibres within the matrix) of the composites was selected. The "corrected" experimental thermal conductivity of the composite ($K^{corr}_{C,C1.5,6i,1}$) with the highest degree of fibre alignment was in good agreement with the Hatta-Taya model's higher boundary. This shows that using the rheocasting+ECAE technique to process Al/CF composites gives a direct positive influence on their thermal conductivity by removing porosity and aligning the CFs.

Despite the improvement in thermal conductivity of 3.6% with respect to the alloy matrix, the results indicate that the Al/Cu-CFs composites produced via rheocasting+ECAE are not suitable to produce ultra-high thermal conductivity ($K \geq 400$ W m^{-1} K^{-1}) composites for thermal management applications as it would be necessary to have a fibre content of $v_f = 0.79$ to achieve such milestone. This is because it is only possible to add $v_f = 0.3$ using rheocasting.

6.2.2.2 Thermal Conductivity of the Al/MWCNT Composites:

6.2.2.2.1 MWCNTs Morphology, Quality and Purity

The exceptional thermal conductivity reported for MWCNTs is attributed to the covalent sp^2 bonds strong harmonic nature that results in the efficient transfer of heat by lattice vibrations (phonons). In contrast, the electrons contribution is so low that in comparison to phonons it is considered negligible. However, the morphology, quality and purity of the MWCNTs play a key role in their thermal conductivity. Therefore, in this study, an extensive characterisation of three MWCNTs samples (S1, S2 and S3) from different sources, including the one used for composite processing (S1) was performed and their thermal conductivities qualitatively assessed regarding their morphology, quality and purity.

The characterisation results demonstrated that the three MWCNTs samples acquired from different sources were found to have very distinct morphologies, qualities and

purities despite the fact that two samples were synthetized via same method (CCVD). Therefore, care must be taken when acquiring this material from the manufacturer.

If considering the effect of morphology, quality and purity on the K of the nanotubes studied, the average K of the individual MWCNTs is expected to be the highest for sample S1, followed by S3 and I S2 respectively. Therefore, MWCNTs for high K applications should be carefully selected and must exhibit the following attributes:

 ➢ Smallest lengths and diameters
 ➢ Low defect concentration and high crystallinity
 ➢ No impurities (carbonaceous and metal catalysts).

This study emphasizes the potential of the use of characterisation techniques to quantify the morphology, quality and purity of the MWCNTs in order to attempt to predict the thermal conductivity of a given MWCNT sample. However, this is still not possible as no models currently take into account one or more of these factors (i.e. length, diameter, crystallinity, carbonaceous and catalyst impurities). There is also no data available to attribute a "power factor" or "weighing" to each of their contributions depending on their impact on thermal conductivity. Hence, there is a real need to develop such model, that will enable the thermal conductivity to be estimated through the characterisation of the MWCNTs contribution from any manufacturing source.

6.2.2.2.2 Thermal Conductivity of an Individual S1 MWCNT

The use of the SThM + FEM technique allowed the acquisition of the K of an individual S1 MWCNT that resulted in a combined (in-plane + out-of-plane) thermal conductivity of $K_{MWCNT,1,2}$ ~ 20 W m^{-1} K^{-1}. The low value is due to the long length and large outer diameter of the nanotube that increases the probability of a higher defect content. This results in a diffusive heat conduction regime, and thus a lower thermal conductivity.

The main advantage of the SThM + FEM technique developed in this study is that it is less complex and laborious, and less expensive than other methods typically used for this purpose. However, further development and optimization is still required.

A thermal conductivity model based on the characterisation results of the MWCNTs, as suggested above, together with the SThM + FEM technique could be used to develop a standard method to acquire not only the thermal conductivity of MWCNTs but many other types of nanomaterials.

6.2.2.2.3 Thermal Conductivity of the Composite

The thermal conductivity of the Al/MWCNTs composites has been scarcely studied and to the author's best knowledge there is no data published on Al/MWCNTs composites produced via rheocasting and rheocasting +ECAE. Also, any attempt to obtain the real K of a sample of MWCNTs used to produce an Al/MWCNTs composite and employing it in theoretical models to compare with the experimental results in order to understand the real contribution of these fillers to Al alloys, has to the author´s best knowledge, also not been reported. This clearly demonstrates the importance and novelty of the scientific work undertaken herein.

The experimental results of the Al/MWCNTs composites processed via rheocasting+ECAE appear to indicate that it is possible to improve the K of the Al3Mg alloy (K_m = 148.4 ± 4.5 W m^{-1} K^{-1}) by adding MWCNTs as results indicate an increase in ~ 5.7 % in thermal conductivity ($K_{M1,4i,1}$ = 156.9 ± 4.7 W m^{-1} K^{-1}) was achieved. This finding may be related to the porosity removal and MWCNTs bundle alignment forming a percolation network.

In order to assess the real thermal conductivity contribution of the MWCNTs to the Al alloys, the experimental thermal conductivity of the composites was compared with various thermal conductivity models for two case scenarios. The best case scenario where the MWCNTs thermal conductivity was considered to be 2000 W m^{-1} K^{-1} (value provided by the manufacturer) and worst case scenario, 20 W m^{-1} K^{-1} (value obtained in this study using the SThM+FEM study).

The comparison of the experimental thermal conductivity of the composites in the "corrected" (porosity volume fraction accounted) condition with the various thermal conductivity theoretical models, taking into account the models limitations, the characterisation results from the composites microstructure, the MWCNTs quality and

purity, and the SThM+FEM results, indicates that the comparison that assumes the bulk density for the worst case scenario (i.e. $K_{MWCNTs,1}$ = 20 W m^{-1} K^{-1}) is probably the most realistic condition.

This therefore supports the idea that the K of the MWCNTs used in the composite processing is much lower than that claimed by the manufacturer, however, its value is higher than the thermal conductivity of the matrix (K_m = 148.4 ± 4.5 W m^{-1} K^{-1}), which is possible as the value obtained by the SThM+FEM is a combined value, therefore the in-plane value is higher than 20 W m^{-1} K^{-1}.

The theoretical models also showed that it should be possible to achieve thermal conductivities between ~ 351 W m^{-1} K^{-1} to ~ 497 W m^{-1}K^{-1} for Al/MWCNTs composites processed via rheocasting+ECAE for a filler volume content of v_f = 0.3. However, in order to process ultra-high ($K \geq$ 400 W m^{-1} K^{-1}) thermal conductivity via rheocasting+ECAE it is imperative that the $K_{MWCNTs,1} \geq$ 2000 W m^{-1} K^{-1}.

This study indicates that, using rheocasting+ECAE, and assuming that the MWCNTs have high thermal conductivity, to produce ultra-high thermal conductivity composites, it is necessary to: 1) Determine whether individual or a network of nanotubes within the matrix is more beneficial to the composite thermal conductivity; 2) A trade-off between porosity closure, matrix deformation and nanotube damage during ECAE; 3) No intermetallics formation around the nanotubes.

Finally, this study indicates that in general, in order to produce Al/MWCNTs with ultra-high thermal conductivity (K ≥ 400 W m^{-1} K^{-1}) it is necessary to:

    I.   Select high quality/thermal conductivity MWCNTs.

    II.   Select a processing method capable of dispersing and aligning individual nanotubes with each having an intimate contact with the matrix.

    III.   Eliminate or reduce MWCNT/matrix interfacial resistance that hinders electron and phonon mean free path.

6.3 Suggestions for Future Work

Analysis of the results and discussion supported by relevant literature, have revealed aspects of this work which require further clarification and investigation. Areas for potential future investigations for research have been identified as:

❖ Acquire and perform advanced characterisation on high quality MWCNTs. Assess the necessity to perform purification to ensure the fillers have the highest as possible thermal conductivity when added to the Al matrix.

❖ Study the possibility of improving nanotube incorporation and dispersion within the matrix by using high shearing technology in the semi-solid state in order to overcome the problem of nanotube agglomeration, a problem detailed in Chapter 4 Subsection 4.3.4.2 and Chapter 5 Subsection 5.2.1.3.2.

❖ Explore other methods to deliver the MWCNTs into the melt without the use of Cu as it significantly affects the microstructure of the matrix and consequently the thermal properties.

❖ Perform ECAE in the semi-solid state (immediately after mixing), in order to promote the breaking-up of bundles, pore size reduction, nanotube alignment and intimate interface interaction whilst minimizing damage of the nanotubes.

❖ Assess which case, whether having a MWCNT percolation network or individual nanotubes dispersed within the matrix provides the best thermal contribution to the composite.

❖ Produce composites via rheocasting + ECAE with higher filler contents to verify if it is possible to produce ultra-high thermal conductivity ($K \geq 400$ W m^{-1} K^{-1}) composites for thermal management applications using MWCNTs.

❖ Perform heat treatments to recover the composites microstructure in order to reduce the number of grain boundaries and other defects that cause electron/phonon dispersion thus potentially achieve even higher thermal conductivities.

❖ Assess the actual volume of MWCNTs introduced and the porosity (micro and nano) by means of high resolution absorption tomography (holotomography) and phase contrast tomography in order to improve the accuracy of the thermal conductivity theoretical models.

❖ Employ and validate thermal conductivity models that account for the interfacial thermal barrier resistance (R_{BD}).

❖ Improve and optimize the SThM + FEM technique in order to obtain consistent consecutive measurements for the intrinsic thermal conductivity of individual nanotubes allowing an average value to be calculated for the bulk MWCNT sample.

❖ Combine both the advanced characterisation and the SThM + FEM techniques to obtain the thermal conductivity of MWCNTs samples with various morphologies (length, outer and inner diameters) and qualities (defects, carbonaceous impurities, metal catalyst impurities). Once the parameters that affect the thermal conductivity of the MWCNTs (morphology and quality) are quantified, models can be developed that incorporate a "weighting factor" for each parameter, so that the thermal conductivity (or a range of thermal conductivities) for a given MWCNTs sample can be predicted using this advanced characterisation methodology.

❖ A standard technique to obtain the thermal conductivity could thus be devised through advanced characterisation and SThM+FEM techniques, not only for MWCNTs but for other nanomaterials.